



May 1996 • NREL/TP-442-8161

Effects of Grit Roughness and Pitch Oscillations on the S814 Airfoil

Airfoil Performance Report, Revised (12/99)

J. M. Janiszewska
R. Reuss Ramsay
M. J. Hoffmann
G. M. Gregorek
The Ohio State University
Columbus, Ohio

National Renewable Energy Laboratory
1617 Cole Boulevard
Golden, Colorado 80401-3393
A national laboratory of the U.S. Department of Energy
Managed by Midwest Research Institute
for the U.S. Department of Energy
under contract No. DE-AC36-83CH10093

Foreword

Airfoils for wind turbines have been selected by comparing data from different wind tunnels, tested under different conditions, making it difficult to make accurate comparisons. Most wind tunnel data sets do not contain airfoil performance in stall commonly experienced by turbines operating in the field. Wind turbines commonly experience extreme roughness for which there is very little data. Finally, recent tests have shown that dynamic stall is a common occurrence for most wind turbines operating in yawed, stall or turbulent conditions. Very little dynamic stall data exists for the airfoils of interest to a wind turbine designer. In summary, very little airfoil performance data exists which is appropriate for wind turbine design.

Recognizing the need for a wind turbine airfoil performance data base, the National Renewable Energy Laboratory (NREL), funded by the U.S. Department of Energy, awarded a contract to Ohio State University (OSU) to conduct a wind tunnel test program. Under this program, OSU tested a series of popular wind turbine airfoils. A standard test matrix was developed to assure that each airfoil was tested under the same conditions. The test matrix was developed in partnership with industry and is intended to include all of the operating conditions experienced by wind turbines. These conditions include airfoil performance at high angles of attack, rough leading edge (bug simulation), steady and unsteady angles of attack.

Special care has been taken to report as much of the test conditions and raw data as practical so that designers can make their own comparisons and focus on details of the data relevant to their design goals. Some of the airfoil coordinates are proprietary to NREL or an industry partner. To protect the information which defines the exact shape of the airfoil, the coordinates have not been included in the report. Instructions on how to obtain these coordinates may be obtained by contacting C.P. (Sandy) Butterfield at NREL.

C. P. (Sandy) Butterfield
Wind Technology Division
National Renewable Energy Laboratory
1617 Cole Blvd.
Golden, Colorado, 80401 USA
Internet Address: Sandy_Butterfield@NREL.GOV
Phone 303-384-6902
FAX 303-384-6901

Preface

The Ohio State University Aeronautical and Astronautical Research Laboratory is conducting a series of steady state and unsteady wind tunnel tests on a set of airfoils which have been or will be used for horizontal-axis wind turbines. The purpose is to investigate the effect of pitch oscillations and leading edge grit roughness on airfoil performance. The study of pitch oscillation effects can help to understand the behavior of horizontal-axis wind turbines in yaw. The results of these tests will aid in the development of new airfoil performance codes that account for unsteady behavior and also aid in the design of new airfoils for wind turbines. The application of leading edge grit roughness (LEGR) simulates surface irregularities that occur on wind turbines. These irregularities on the blades are due to the accumulation of insect debris, ice, and/or the aging process and can significantly reduce the output of the horizontal axis wind turbines. The experimental results from the application of leading edge grit roughness will help the development of airfoils that are less sensitive to roughness.

This work was made possible by the efforts and financial support of the National Renewable Energy Laboratory which provided major funding and technical monitoring, the U.S. Department of Energy is credited for its funding of this document through the National Renewable Energy Laboratory under contract number DE-AC36-83CH10093. The staff of The Ohio State University Aeronautical and Astronautical Research Laboratory appreciates the contributions made by personnel from that organization. In addition the authors would like to recognize the efforts of the following student research assistants, Fernando Falasca, and Mònica Angelats i Coll.

Summary

An S814 airfoil model was tested in The Ohio State University Aeronautical and Astronautical Research Laboratory 3×5 subsonic wind tunnel under steady state and unsteady conditions. The test defined baseline conditions for steady state angles of attack from -20° to +40° and examined unsteady behavior by oscillating the model about its quarter chord pitch axis for three mean angles, three frequencies, and two amplitudes. For all oscillating cases, Reynolds numbers of 0.75, 1, 1.25, and 1.5 million were used. In addition, the above conditions were repeated after the application of leading edge grit roughness (LEGR) to determine contamination effects on the airfoil performance.

Typical steady state results of the S814 testing showed a baseline maximum lift coefficient of 1.29 at 11.2° angle of attack for a 1 million Reynolds number. The application of LEGR reduced the maximum lift coefficient by 25% and increased the 0.0108 minimum drag coefficient value by more than 45%. The zero lift pitching moment of -0.1345 showed a 42% reduction in magnitude to -0.0786 with LEGR applied.

Data were also obtained for two pitch oscillation amplitudes, ±5.5° and ±10°. The larger amplitude consistently gave a higher maximum lift coefficient than the smaller amplitude, and both sets of unsteady maximum lift coefficients were greater than the steady state values. Stall was delayed on the airfoil while the angle of attack was increasing, thereby causing an increase in maximum lift coefficient. A hysteresis behavior was exhibited for all the unsteady test cases. The hysteresis loops were larger for the higher reduced frequencies and for the larger amplitude oscillations. As in the steady case, the effect of LEGR in the unsteady case was to reduce the lift coefficient at high angles of attack. In addition, with LEGR, the hysteresis behavior persisted into lower angles of attack than with the clean case.

In general, the unsteady maximum lift coefficient was from 9% to 110% higher than the steady state maximum lift coefficient, and variation in the quarter chord pitching moment coefficient magnitude was from 7% to more than 200% larger than the steady state values at high angles of attack. These findings indicate the importance of considering the unsteady flow behavior occurring in wind turbine operation because use of steady state results could greatly underestimate the loads.

Table of Contents

	Page
Preface	iv
Summary	v
List of Symbols	ix
Introduction	1
Experimental Facility	2
Wind Tunnel	2
Oscillation System	3
Model Details	4
Test Equipment and Procedures	6
Data Acquisition	6
Data Reduction	7
Test Matrix	8
Results and Discussion	10
Comparison with Theory	10
Steady State Data	11
Unsteady Data	13
Summary of Results	20
References	23
Appendix A: Surface Pressure Tap Coordinates	A-1
Appendix B: Steady State Data	B-1
Appendix C: Unsteady Integrated Coefficients	C-1

List of Figures

Page

1. 3×5 Subsonic wind tunnel, top view	2
2. 3×5 Subsonic wind tunnel, side view	2
3. 3×5 Wind tunnel oscillation system	3
4. S814 airfoil section	4
5. Measured-to-desired model coordinates difference curves.	4
6. Roughness pattern	5
7. Data acquisition schematic	6
8. Comparison with theory, C_l vs α	10
9. Comparison with theory, C_m vs α	10
10. Comparison with theory, C_p vs x/c , $\alpha=0.0^\circ$	10
11. Comparison with theory, C_p vs x/c , $\alpha=6.2^\circ$	10
12. C_l vs α , clean	11
13. C_l vs α , LEGR, $k/c=0.0019$	11
14. C_m vs α , clean	11
15. C_m vs α , LEGR, $k/c=0.0019$	11
16. Clean, drag polar	12
17. LEGR, drag polar	12
18. Pressure distribution, $\alpha=2.0^\circ$	12
19. Pressure distribution, $\alpha=12.3^\circ$	12
20. Clean, C_l vs α , $\omega_{red}=0.028, \pm 5.5^\circ$	13
21. Clean, C_l vs α , $\omega_{red}=0.084, \pm 5.5^\circ$	13
22. Clean, C_m vs α , $\omega_{red}=0.028, \pm 5.5^\circ$	14
23. Clean, C_m vs α , $\omega_{red}=0.084, \pm 5.5^\circ$	14
24. LEGR, C_l vs α , $\omega_{red}=0.028, \pm 5.5^\circ$	14
25. LEGR, C_l vs α , $\omega_{red}=0.087, \pm 5.5^\circ$	14
26. LEGR, C_m vs α , $\omega_{red}=0.028, \pm 5.5^\circ$	15
27. LEGR, C_m vs α , $\omega_{red}=0.087, \pm 5.5^\circ$	15
28. Clean, C_l vs α , $\omega_{red}=0.030, \pm 10^\circ$	15
29. Clean, C_l vs α , $\omega_{red}=0.091, \pm 10^\circ$	15
30. Clean, C_m vs α , $\omega_{red}=0.030, \pm 10^\circ$	16
31. Clean, C_m vs α , $\omega_{red}=0.091, \pm 10^\circ$	16
32. LEGR, C_l vs α , $\omega_{red}=0.032, \pm 10^\circ$	16
33. LEGR, C_l vs α , $\omega_{red}=0.096, \pm 10^\circ$	16
34. LEGR, C_m vs α , $\omega_{red}=0.032, \pm 10^\circ$	17
35. LEGR, C_m vs α , $\omega_{red}=0.096, \pm 10^\circ$	17
36. Unsteady pressure distribution, clean, $\omega_{red}=0.055, 14\pm 5.5^\circ$	18
37. Unsteady pressure distribution, LEGR, $\omega_{red}=0.056, 14\pm 5.5^\circ$	18
38. Unsteady pressure distribution, clean, $\omega_{red}=0.060, 14\pm 10^\circ$	19

List of Tables

	Page
1. S814 Steady State Parameters Summary	20
2. S814, Unsteady, Clean, $\pm 5.5^\circ$	20
3. S814, Unsteady, LEGR, $\pm 5.5^\circ$	21
4. S814, Unsteady, Clean, $\pm 10^\circ$	21
5. S814, Unsteady, LEGR, $\pm 10^\circ$	22

List of Symbols

AOA	Angle of attack
A/C, a.c.	Alternating current
c	Model chord length
C_d	Drag coefficient
$C_{d\min}$	Minimum drag coefficient
C_{dp}	Pressure drag coefficient
C_{dw}	Wake drag coefficient
C_{du}	Uncorrected drag coefficient
C_l	Lift coefficient
$C_{l\max}$	Maximum lift coefficient
$C_{l\text{ dec}}$	Lift coefficient at angle of maximum lift, but with angle of attack decreasing
C_{lu}	Uncorrected lift coefficient
$C_m, C_{m\frac{1}{4}}$	Pitching moment coefficient about the quarter chord
$C_{m\text{ dec}}$	Pitching moment coefficient at angle of maximum lift, but with angle of attack decreasing
$C_{m\text{ inc}}$	Pitching moment coefficient at angle of maximum lift, but with angle of attack increasing
C_{mo}	Pitching moment coefficient about the quarter chord, at zero lift
$C_{m\frac{1}{4}u}$	Uncorrected pitching moment coefficient about the quarter chord
C_p	Pressure coefficient, $(p - p_\infty)/q_\infty$
$C_{p\min}$	Minimum pressure coefficient
f	Frequency
h	Wind tunnel test section height
hp, Hp, HP	Horsepower
Hz	Hertz
k	Grit particle size
k/c	Grit particle size divided by airfoil model chord length
p	Pressure
q	Dynamic pressure
q_u	Uncorrected dynamic pressure
q_w	Dynamic pressure through the model wake
q_∞	Free stream dynamic pressure
Re	Reynolds number
Re_u	Uncorrected Reynolds number
t	Time
U_∞	Corrected free stream velocity
V	Velocity
V_u	Uncorrected velocity
x	Axis parallel to model reference line
y	Axis perpendicular to model reference line

α	Angle of attack
α_{dec}	Decreasing angle of attack
α_{inc}	Increasing angle of attack
α_m	Median angle of attack
α_{mean}	Mean angle of attack
α_u	Uncorrected angle of attack
ϵ	Tunnel solid wall correction scalar
ϵ_{sb}	Solid blockage correction scalar
ϵ_{wb}	Wake blockage correction scalar
Λ	Body-shape factor (0.305 used)
π	3.1416
σ	Tunnel solid wall correction parameter
$\omega_{\text{red}}, \omega_{\text{reduced}}$	Reduced frequency, $\pi f_c/U_\infty$

Introduction

Horizontal-axis wind turbine rotors experience unsteady aerodynamics when the rotor is yawed, when rotor blades pass through the support tower wake, and when the wind is gusting. An understanding of this unsteady behavior is necessary to assist in the design of new rotor airfoils. The rotors also experience performance degradation due to surface roughness. These surface irregularities are due to the accumulation of insect debris, ice, and/or the aging process. Wind tunnel studies that examine both the steady and unsteady behavior of airfoils can help define pertinent flow phenomena, and the resultant data can also be used to validate analytical computer codes.

An S814 airfoil model was tested in The Ohio State University Aeronautical and Astronautical Research Laboratory (OSU/AARL) 3×5 subsonic wind tunnel (3×5) under steady flow with both stationary model conditions and pitch oscillations. To study the extent of performance loss due to surface roughness, a leading edge grit roughness pattern (LEGR) was used to simulate leading edge contamination. After baseline cases were completed, the LEGR was applied for both steady state and model pitch oscillation cases. The Reynolds numbers for steady state conditions were 0.75, 1, 1.25 and 1.5 million, while the angle of attack ranged from -20° to +40°. While the model underwent pitch oscillations, data were acquired at Reynolds numbers of 0.75, 1, 1.25, and 1.5 million, at frequencies of 0.6, 1.2, and 1.8 Hz. Two sine wave forcing functions $\pm 5.5^\circ$ and $\pm 10^\circ$, were used; at mean angles of attack of 8°, 14°, and 20°. For purposes herein, any reference to unsteady conditions means the model was in pitch oscillation.

Experimental Facility

Wind Tunnel

The OSU/AARL 3×5 subsonic wind tunnel (3×5) was used to conduct tests on the S814 airfoil section. Schematics of the top and side views of the tunnel are shown in Figure 1 and Figure 2, respectively. This open-circuit tunnel has a velocity range of 0 to 55-m/s (180-ft/s) produced by a 2.4-m (8-ft) diameter,

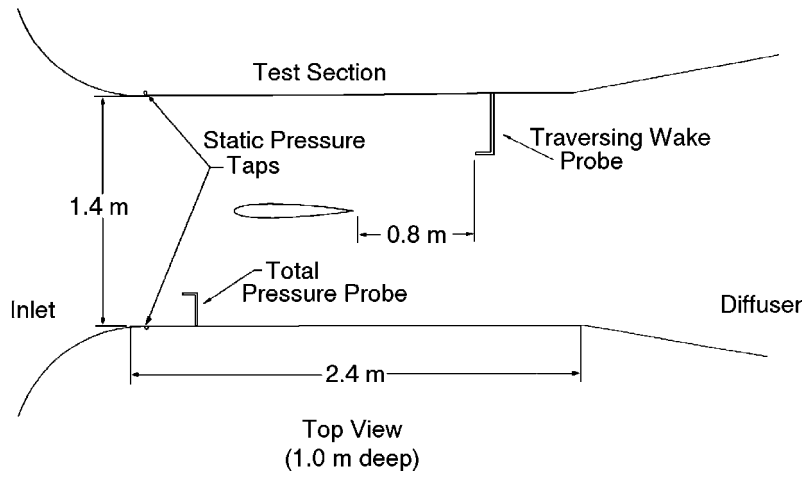


Figure 1. 3×5 Subsonic wind tunnel, top view

six-bladed fan. The fan is belt driven by a 93.2-kw (125-hp) three phase a.c. motor connected to a variable frequency motor controller. Nominal test section dimensions are 1.0 m (39 inch) high by 1.4-m (55-in) wide by 2.4-m (96-in) long. The 457-mm (18-in) chord airfoil model was mounted vertically in the test section.

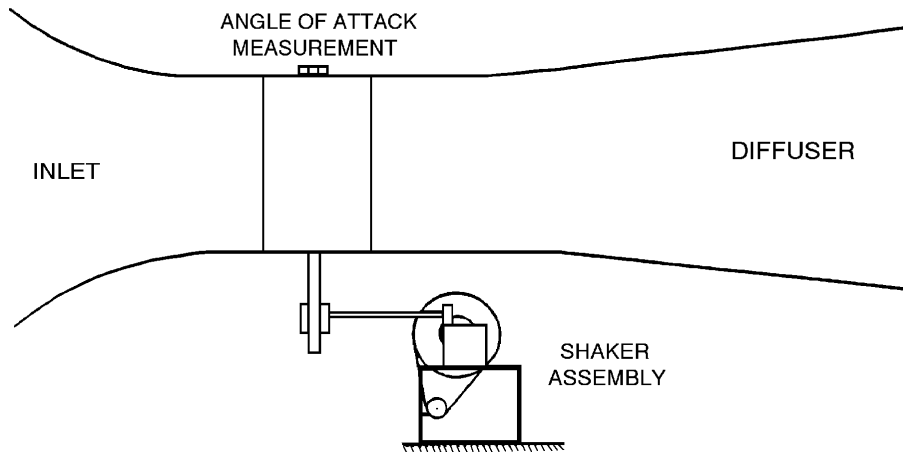


Figure 2. 3×5 Subsonic wind tunnel, side view

A steel tube through the quarter chord of the model was used to attach the model to the tunnel during testing. An angle of attack potentiometer was fastened to the model at the top of the tunnel as shown in Figure 2. The steady state angle of attack was adjusted with a worm gear drive attached to the model strut below the tunnel floor.

Oscillation System

Portions of the testing required the use of a reliable model pitch oscillation system. The OSU/AARL "shaker" system incorporated a face cam and follower arm attached to the model support tube below the wind tunnel floor, is shown in Figure 3. The choice of cam governed the type and amplitude of the wave form produced. Sine wave forms having amplitudes of $\pm 5.5^\circ$ and $\pm 10^\circ$ were used for these tests; the wave form is defined by the equation

$$\alpha = \alpha_m + A \sin(2\pi ft)$$

where A is the respective amplitude. The shaker system was powered by a 5-hp a.c. motor with a variable line frequency controller. The useable oscillating frequency range was 0.1 - 2.0 Hz, and three frequencies were used for this test: 0.6, 1.2, and 1.8 Hz.

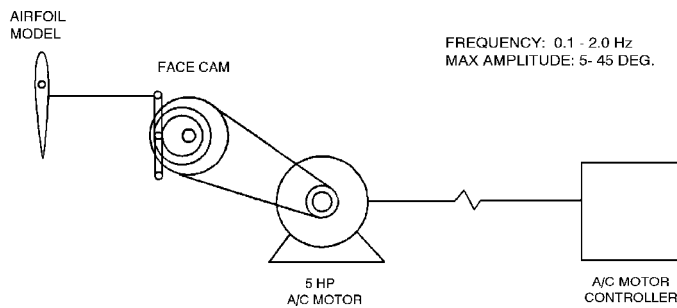


Figure 3. 3x5 Wind tunnel oscillation system

Model Details

A 457-mm (18-in) constant chord S814 airfoil model was designed by AARL/OSU personnel and manufactured by others. Figure 4 shows the airfoil section. Due to their proprietary nature, model coordinates are not presented in tabular form. The model trailing edge was thickened to 1.25 mm (0.05-in)

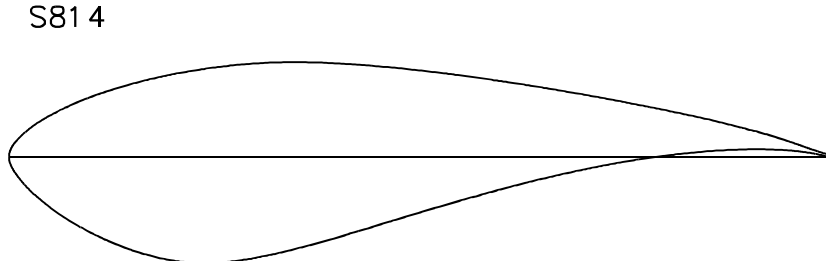


Figure 4. S814 airfoil section

for fabrication purposes. The model was made of a nine layer composite lay up of alternating fiberglass and carbon fiber over ribs. The main load bearing member was a 38-mm (1.5-in) diameter steel tube which passed through the model quarter chord station. Ribs and end plates were used to transfer loads from the composite skin to the steel tube. The final surface was filled, painted, and wet sanded to attain given coordinates within a requested tolerance of $\pm 0.25\text{-mm}$ ($\pm 0.01\text{-in}$). The completed model was measured at

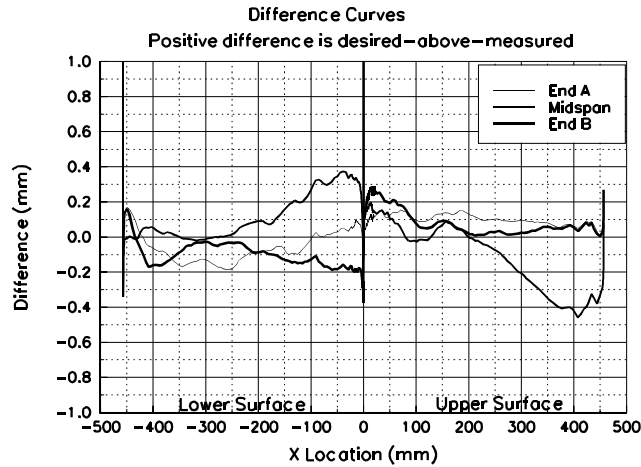


Figure 5. Measured-to-desired model coordinates difference curves.

three spanwise locations using a Sheffield-Cordax coordinate measurement machine. Measurements were made in English units and later converted to metric. Figure 5 shows the results of comparing measured-to-desired coordinates by calculating differences normal to the profiled surface at three stations on the model. The "spikes" showing near the trailing edge and at the leading edge are due to the numerical methods and are not real. Although not all of the surface was within tolerance, this model was accepted because the discrepancy was small and over a narrow range.

To minimize pressure response times, which is important for the unsteady testing, the lengths of surface pressure tap lead-out lines had to be as short as possible. Consequently, a compartment was built into the model so pressure scanning modules could be installed inside the model. This compartment was accessed through a panel door fitted flush with the model contour on the lower (pressure) surface.

For test cases involving roughness, a standard roughness pattern developed for the National Renewable Energy Laboratory airfoil test program was employed. The pattern was generated using a molded insect pattern taken from a wind turbine in the field. The particle density was 5 particles per cm^2 (32 particles per square inch) in the middle of the pattern, thinning to 1.25 particles per cm^2 (8 particles per square inch) at the edge of the pattern. Figure 6 shows the pattern. To make a usable template, the pattern was repeatedly cut into a steel sheet 102-mm (4-in) wide and 91-cm (3-ft) long with holes just large enough for one piece of grit. Based on average particle size from the field specimen, standard #40 lapidary grit was chosen for the roughness elements, giving $k/c=0.0019$ for a 457-mm (18-in) chord model.

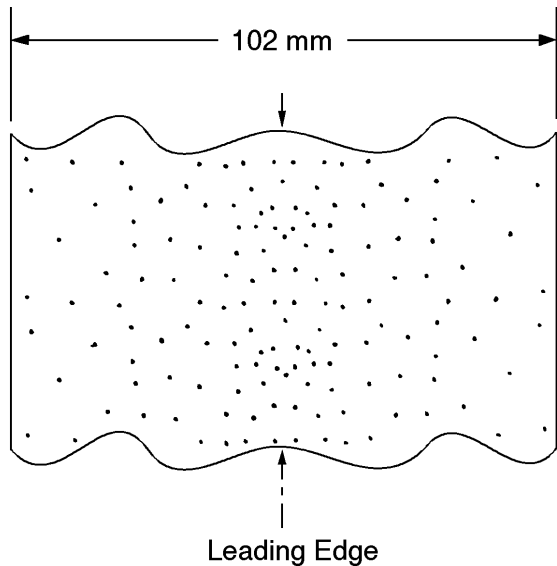


Figure 6. Roughness pattern

To use the template, 102-mm (4-in) wide double-tack tape was applied to one side of the template, and grit was poured and brushed from the opposite side. The tape was then removed from the template and transferred to the model. This method allows the same roughness pattern to be replicated for any test.

Test Equipment and Procedures

Data Acquisition

Data was acquired and processed from 60 surface pressure taps, four individual tunnel pressure transducers, an angle of attack potentiometer, a wake probe position potentiometer, and a tunnel thermocouple. The data acquisition system included an IBM PC compatible 80486-based computer connected to a Pressure Systems Incorporated (PSI) data scanning system. The PSI system included a 780B Data Acquisition and Control Unit (DACU), 780B Pressure Calibration Unit (PCU), 81-IFC scanning module interface, two 2.5-psid pressure scanning modules (ESPs), one 20-in water column range pressure scanning module, and a 30 channel Remotely Addressed Millivolt Module (RAMM-30). Figure 7 shows the data acquisition system schematic.

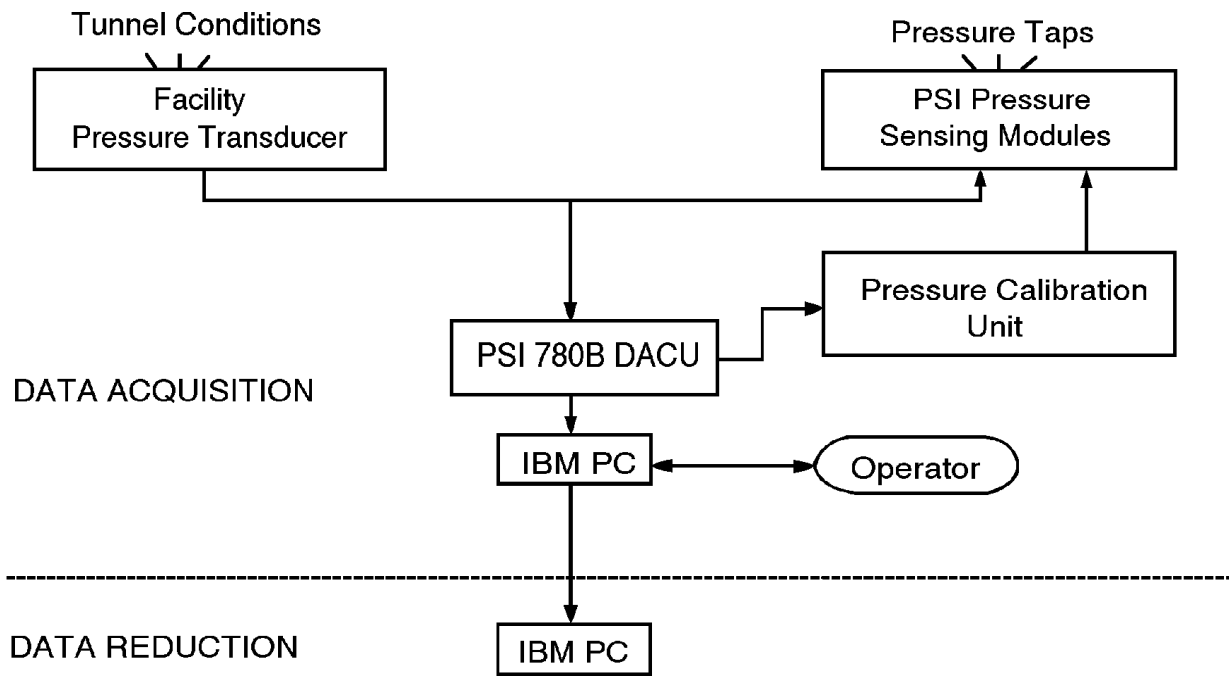


Figure 7. Data acquisition schematic

Four individual pressure transducers read tunnel total pressure, tunnel north static pressure, tunnel south static pressure, and wake dynamic pressure. Before the test began, these transducers were bench calibrated using a water manometer to determine their sensitivities and offsets. Related values were entered into the data acquisition and reduction program so the transducers could be shunt resistor calibrated before each series of wind tunnel runs.

The rotary angle of attack potentiometer of 0.5% linearity was regularly calibrated during the tunnel pressure transducers shunt calibration. The angle of attack calibration was accomplished by taking voltage readings at known values of set angle of attack. This calibration method gave angle of attack readings within $\pm 0.25^\circ$ over the entire angle range. The wake probe position potentiometer was a linear potentiometer, and it was also regularly calibrated during the shunt calibration of the tunnel pressure transducers.

Calibration of the three ESPs was done simultaneously using the DACU and PCU. At operator request, the DACU commanded the PCU to apply known regulated pressures to the ESPs and read the output voltages from each integrated pressure sensor. From these values, the DACU calculated the calibration coefficients and stored them internally until the coefficients were requested by the controlling computer. This calibration

was done several times during a run set because the ESPs were installed inside the model, and their outputs tended to drift with temperature changes during a test sequence. Frequent on-line calibrations minimized the effect.

For steady state cases, the model was set to angle of attack, and the tunnel conditions were adjusted. At operator request, pressure measurements from the airfoil surface taps and all other channels of information were acquired and stored by the DACU and subsequently passed to the controlling computer for final processing. The angles of attack were always set in the same progression from 0° to -20° then from 0° to +40°.

For model oscillating cases, the tunnel conditions were set while the model was stationary at the desired mean angle of attack. The "shaker" was started, the model was allowed to oscillate through at least five cycles to set up the flow field, and then the model surface pressure and tunnel condition data were acquired. Generally, 120 data scans were acquired over three model oscillation cycles. Since surface pressures were scanned sequentially, the data rate was set so the model rotated through less than 0.50° during any data burst. Finally, due to the unsteady and complex nature of the pitch oscillation cases, model wake surveys (for drag) were not conducted.

Data Reduction

The data reduction routine was included as a section of the data acquisition program. This combination of data acquisition and reduction routines allowed data to be reduced on-line during a test. By quickly reducing selected runs, integrity checks could be made to ensure that the equipment was working properly and to allow timely decisions about the test matrix.

The ambient pressure was manually input into the computer and was updated regularly. This value, as well as the measurements from the tunnel pressure transducers and the tunnel thermocouple, were used to calculate tunnel airspeed. As a continuous check of readings, the tunnel total and static pressures were read by both the tunnel individual pressure transducers and the 20-in water column ESP.

A typical steady state data point was derived by acquiring 10 data scans of all channels over a 10 second window at each angle of attack and tunnel condition. The reduction portion of the program processed each data scan to coefficient forms C_p , C_l , $C_{m\frac{1}{4}}$, and C_{dp} using the measured surface pressure voltages, calibration coefficients, tap locations, and wind tunnel conditions. Then, all scan sets for a given condition were ensemble averaged to provide one data set and that data set was then corrected for the effects of solid tunnel walls. All data were saved in electronic form.

Corrections due to solid tunnel sidewalls were applied to the wind tunnel data. As described by Pope and Harper (1966), tunnel conditions are represented by the following equations:

$$q = q_u(1 + \epsilon)$$

$$V = V_u(1 + \epsilon)$$

$$R_e = R_{e_u}(1 + \epsilon)$$

Airfoil aerodynamic characteristics are corrected by:

$$\alpha = \alpha_u + \frac{57.3\sigma}{2\pi} (C_{l_u} + 4C_{m\frac{1}{4}_u})$$

$$C_l = C_{l_u}(1 - \sigma - 2\epsilon)$$

$$C_{m_{\frac{1}{4}}} = C_{m_{\frac{1}{4}_u}} (1 - 2\epsilon) + \frac{\sigma}{4} C_l$$

$$C_d = C_{d_u} (1 - 3\epsilon_{sb} - 2\epsilon_{wb})$$

where

$$\sigma = \frac{\pi^2}{48} \left(\frac{c}{h} \right)^2$$

$$\epsilon = \epsilon_{sb} + \epsilon_{wb}$$

$$\epsilon_{sb} = \Lambda \sigma$$

$$\epsilon_{wb} = \frac{c}{h4} C_{d_u}$$

Model wake data were taken for steady state cases when the wake could be completely traversed. Pressures were acquired from a pitot-static probe which was connected to measure incompressible dynamic pressure through the wake. These pressure measurements were used to calculate drag coefficient using a form of the Jones equation derived from Schlichting (1979).

$$C_{dw} = \frac{2}{c} \int \sqrt{\frac{q_w}{q_\infty}} \left(1 - \sqrt{\frac{q_w}{q_\infty}} \right) dy$$

This equation assumes that static pressure at the measurement site is the free-stream value. The integration was done automatically except the computer operator chose the end points of the integration from a plot of the wake survey displayed on the computer screen.

For pitch oscillation cases, model surface pressures were reduced to pressure coefficient form with subsequent integrations and angle of attack considerations giving lift, moment, and pressure drag coefficients. There was no calibration available for unsteady model pitch conditions; therefore, the unsteady pressure data were not corrected for any possible effects due to time dependent pitching or solid tunnel walls. Also for these cases, the wind tunnel contraction pressures (used for steady state cases) could not be used to calculate instantaneous freestream conditions due to slow response. The tunnel conditions were obtained from a total pressure probe and the average of opposing static taps in the test section entrance; thereby giving near instantaneous flow pressure conditions for the pitching frequencies used.

Test Matrix

The test was designed to study steady state and unsteady pitch oscillation data. Steady state data were acquired at Reynolds numbers of 0.75, 1, 1.25, and 1.5 million, with and without LEGR. Refer to the tabular data in Appendix B for the actual Reynolds number for each angle of attack for the steady state data. The angle of attack increment was two degrees when $-20^\circ < \alpha < +10^\circ$ or $+20^\circ < \alpha < +40^\circ$, and one degree when $+10^\circ < \alpha < +20^\circ$. Wake surveys were conducted to find total airfoil drag over an approximate angle of attack range of -10° to $+10^\circ$. Unsteady data were taken for Reynolds numbers of 0.75, 1, 1.25, and 1.5 million. Sine wave cams having amplitudes $\pm 5.5^\circ$ and $\pm 10^\circ$ were used for pitch oscillations, and the mean angles for

both these amplitudes were 8° , 14° , and 20° . For all these conditions, the frequencies were varied to 0.6, 1.2, and 1.8 Hz. All data points for the unsteady cases were acquired for both clean and LEGR cases.

Results and Discussion

The S814 airfoil model was tested under steady state and pitch oscillation conditions. A brief discussion of the results follows, including a comparison of experimental data and computational predictions, steady state results, and unsteady results.

Comparison with Theory

Comparisons were made between present wind tunnel steady state data and computed predictions made using the North Carolina State Airfoil Analysis Code. This analysis code has proven to be accurate for moderate angles of attack. The analysis was made with specifications set to allow free transition from laminar to turbulent flow, and the pressure distribution comparisons were matched to the same angle of attack as the wind tunnel cases.

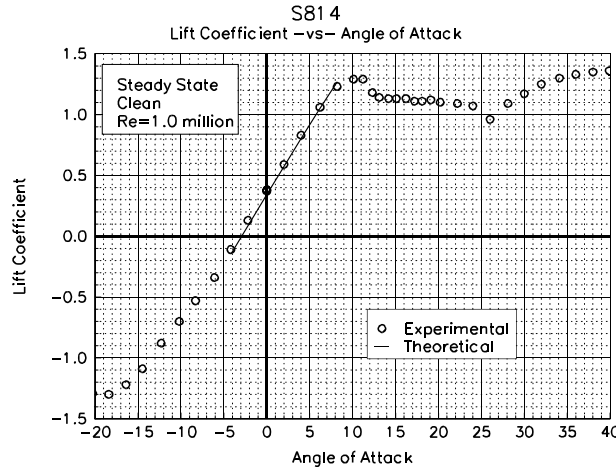


Figure 8. Comparison with theory, C_l vs α

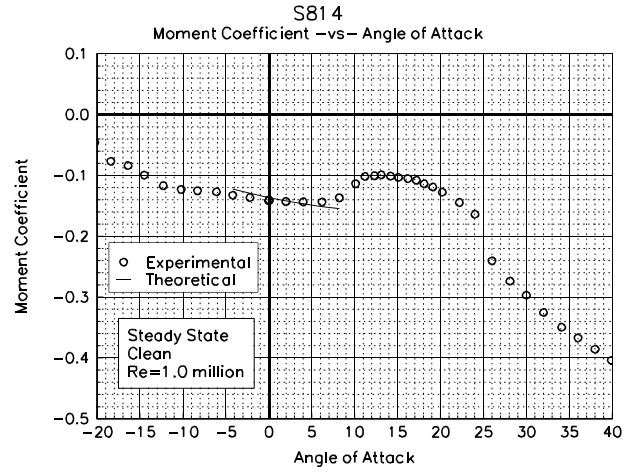


Figure 9. Comparison with theory, C_m vs α

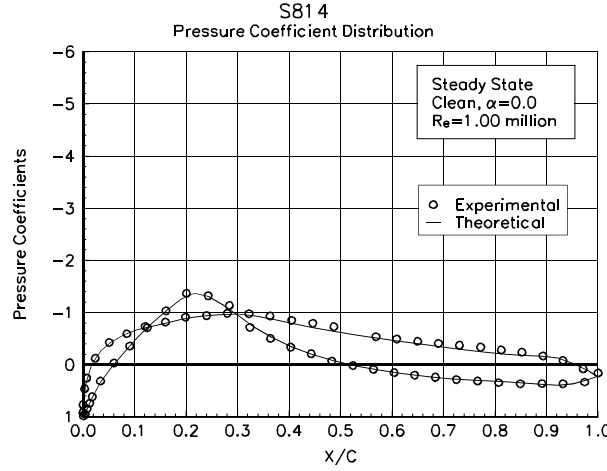


Figure 10. Comparison with theory, C_p vs x/c , $\alpha=0.0^\circ$

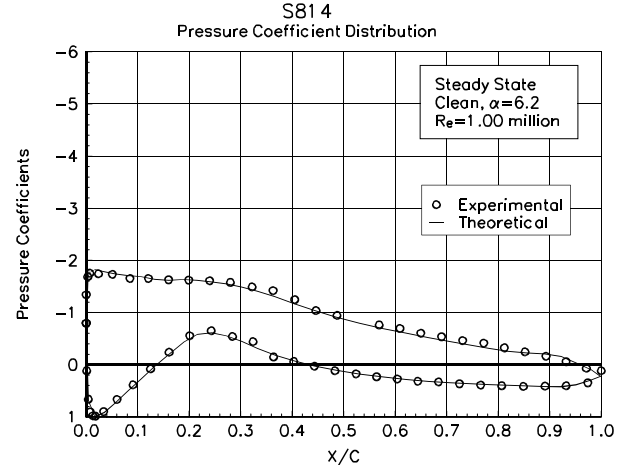


Figure 11. Comparison with theory, C_p vs x/c , $\alpha=6.2^\circ$

Figure 8 shows the lift coefficient versus angle of attack for the 1 million Reynolds number case. For moderate angles of attack in which the analysis code is valid, the comparison shows good agreement. The pitching moment about the quarter chord, Figure 9, shows adequate agreement for angles of attack from $+0^\circ$ to $+5^\circ$. The pressure distributions shown in Figure 10 and Figure 11 are for angles of attack of 0.0° and 6.2° ,

respectively, and include clean wind tunnel data as compared to computed free transition pressure distributions. For both angles of attack, there is excellent correlation between the experimental and the predicted values.

Steady State Data

The S814 airfoil model was tested at four Reynolds numbers at nominal angles of attack from -20° to $+40^\circ$. Figure 12 and Figure 13 show lift coefficients for all the test Reynolds numbers for both clean model and

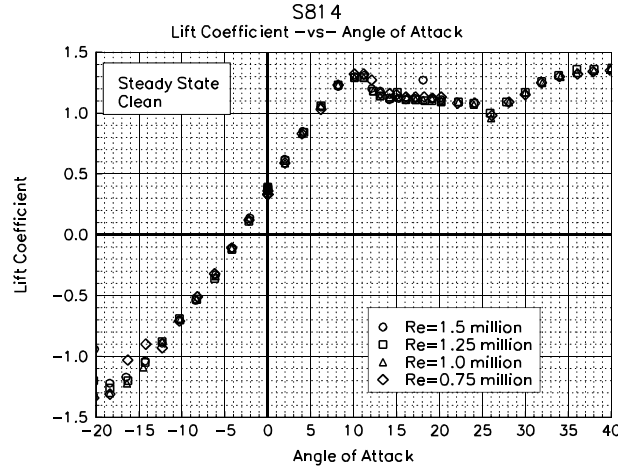


Figure 12. C_l vs α , clean

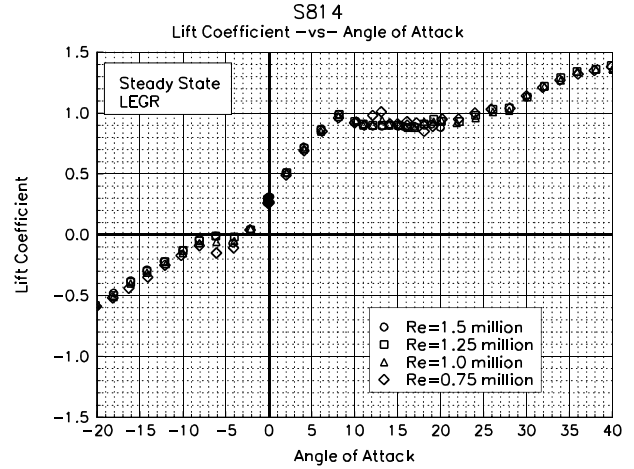


Figure 13. C_l vs α , LEGR, $k/c=0.0019$

with LEGR applied, respectively. The maximum positive lift coefficient for the clean cases is about 1.32 and 0.99 for the LEGR cases, a 25% reduction. The clean cases have a positive stall at 11° while the LEGR cases stall at 8° angle of attack. Both clean and LEGR cases have nearly constant lift coefficient in early post stall, which is only 0.2 lower than the maximum lift coefficient. The negative stall with the LEGR applied occurs much sooner than in the clean model, therefore shortening the linear portion of the lift curve slope. Finally, the average lift curve slope is about 0.110 for clean data and slightly lower at 0.093 for the LEGR case. The associated average lift coefficients at zero angle of attack are 0.38 for the clean case and 0.30 for the LEGR case.

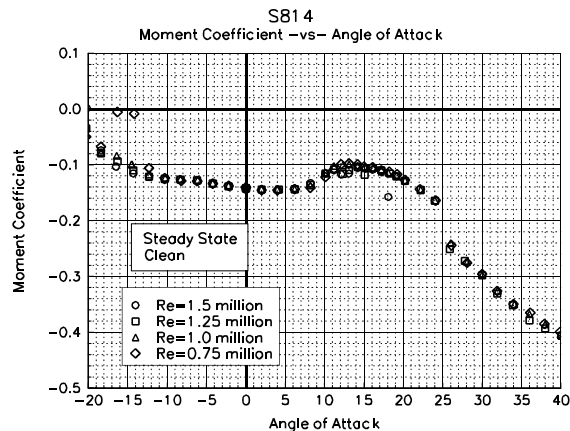


Figure 14. C_m vs α , clean

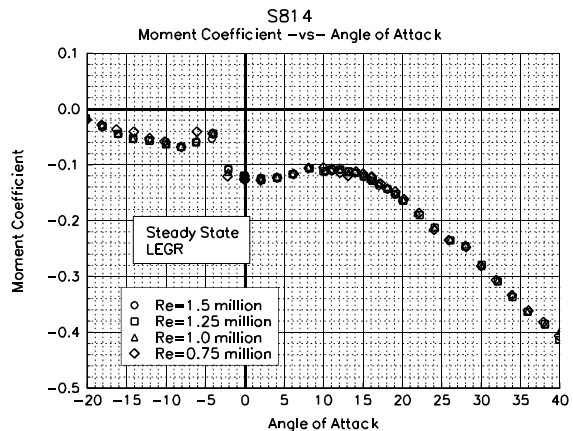


Figure 15. C_m vs α , LEGR, $k/c=0.0019$

Figure 14 shows the pitching moment about the quarter chord for the clean cases and Figure 15 shows the same for the LEGR cases. The LEGR data have slightly more positive pitching moment at low angles of attack, and a drastic jump at -4° angle of attack, which corresponds to the negative stall. The moment coefficient about the quarter chord for the 1 million Reynolds number, is for the clean case -0.1345 and -0.0786 for the LEGR case.

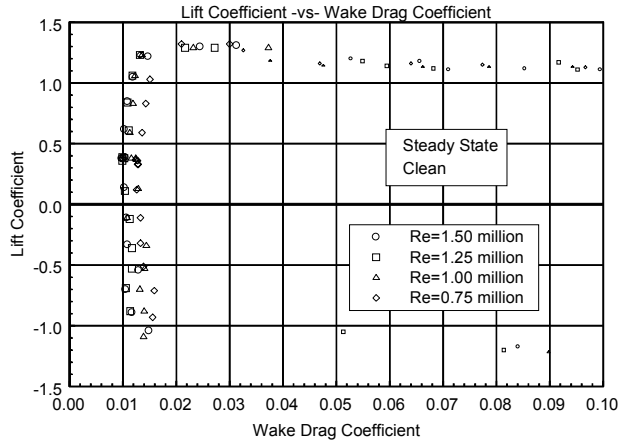


Figure 16. Clean, drag polar

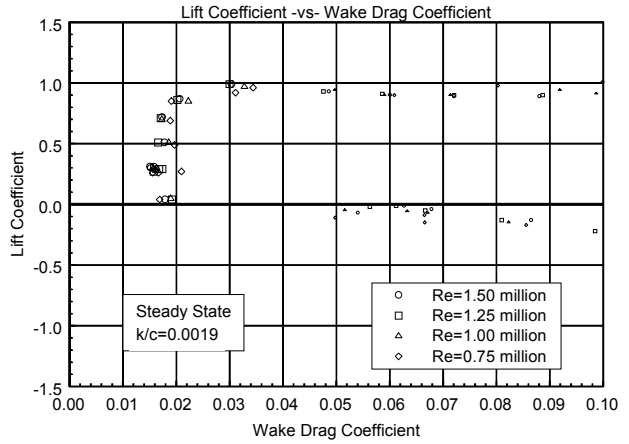


Figure 17. LEGR, drag polar

Total wake drag data were obtained for both the clean and the LEGR cases over an angle of attack range of -10° to $+10^\circ$. A pitot-static probe was used to describe the wake profile. This method is reliable when there is relatively low turbulence in the wake flow; therefore, only moderate angles of attack have reliable total drag coefficient data. At angles of attack other than -10° to $+10^\circ$, surface pressure data was integrated to give C_{dp} and is shown in the drag polars as small symbols. The model clean drag data are shown in Figure 16, and the LEGR case data are shown in Figure 17. At 1.25 million Reynolds number, minimum drag coefficient for the clean cases was measured as 0.0099, and for LEGR as 0.0158, a 60% increase. The general effect of LEGR is to increase drag consistently through most angles of attack. The LEGR cases show a much narrower drag bucket than do the clean data due to the early negative stall.

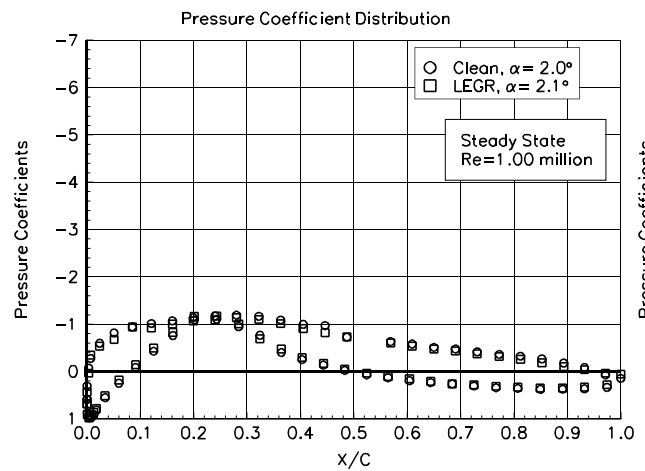


Figure 18. Pressure distribution, $\alpha=2.0^\circ$

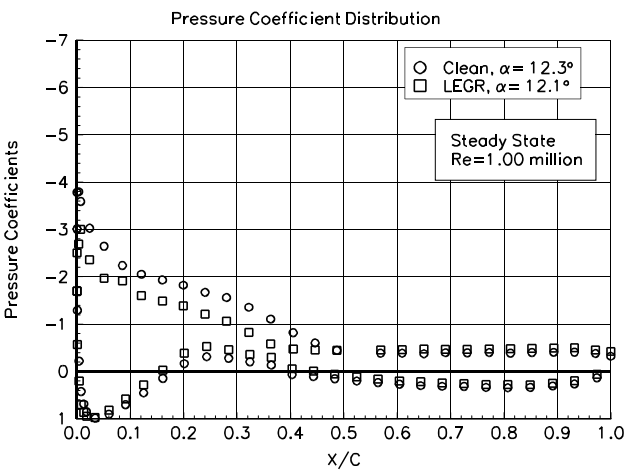


Figure 19. Pressure distribution, $\alpha=12.3^\circ$

Two examples of the surface pressure distributions are shown in Figure 18 and Figure 19 for 2.0° and 12.3° , respectively, for 1 million Reynolds number. At the angles of attack close to zero degrees, the effect of LEGR does not appear to significantly affect the pressure distribution in comparison with that of clean case distribution; however, there is a small effect apparent in the lift coefficient with values of 0.51 for the LEGR case and 0.59 for the clean case. For the higher angle of attack case, shown in Figure 19, the effect of LEGR is to reduce the magnitude of the pressure peak from -3.8 to -3.0, increase the pressures on the upper (suction) surface over the forward 45% of the chord, and increase trailing edge separation. The net effect is a reduction in lift coefficient from 1.18 to 0.90, a 24% decrease.

Unsteady Data

Unsteady experimental data were obtained for the S814 airfoil model undergoing sinusoidal pitch oscillations. As mentioned earlier, no calibration was available for the unsteady oscillating model conditions; the steady state tunnel calibration was used to set the flow conditions while the model was stationary at its mean angle of attack. A comprehensive set of test conditions was used to describe unsteady behavior of the airfoil including two angle of attack amplitudes, $\pm 5.5^\circ$ and $\pm 10^\circ$; four Reynolds numbers, 0.75, 1, 1.25, and 1.5 million; three pitch oscillation frequencies, 0.6, 1.2, and 1.8; and three mean angles of attack, 8° , 14° , and 20° .

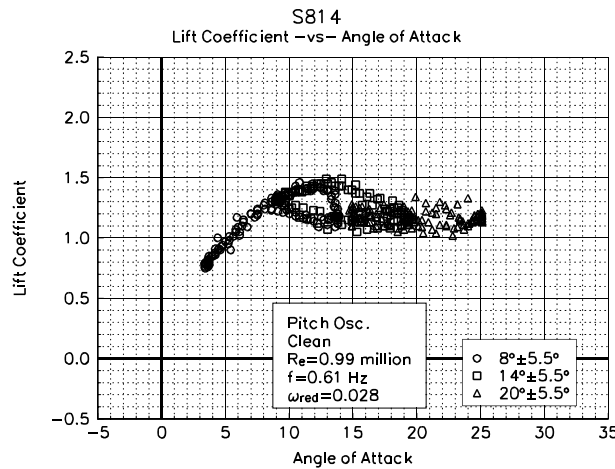


Figure 20. Clean, C_l vs α , $\omega_{red}=0.028$, $\pm 5.5^\circ$

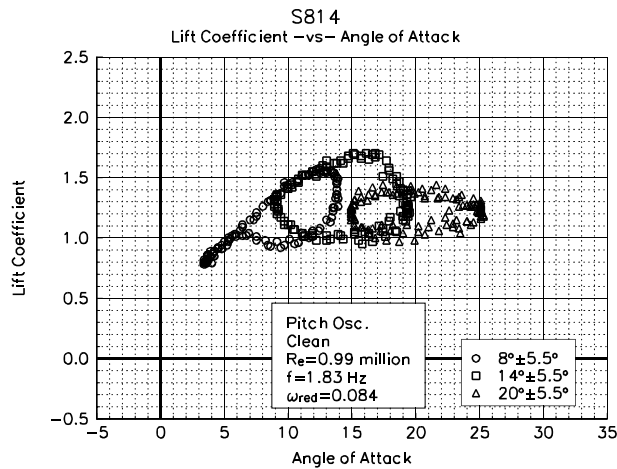


Figure 21. Clean, C_l vs α , $\omega_{red}=0.084$, $\pm 5.5^\circ$

Figure 20 shows the lift coefficient versus angle of attack for the $\pm 5.5^\circ$ amplitude model clean case, at reduced frequency of 0.028 and 1 million Reynolds number. Note that all three mean angles of attack are plotted on the same figure. The maximum prestall lift coefficient for this case is near 1.49 and occurs when the airfoil is traveling with the angle of attack increasing. In contrast, when the model is traveling through decreasing angles of attack, the stall recovery is delayed, and a hysteresis behavior is exhibited in the lift coefficient that can be seen throughout all of the unsteady data. To obtain some measure of this hysteresis behavior, the lift coefficient on the "return" portion of the curve, at the angle of attack where maximum lift coefficient occurs, can be used. For the case discussed here, the hysteresis lift coefficient is 1.11, a 26% decrease from the 1.49 unsteady maximum value. In comparison, the steady state maximum lift coefficient is 1.29. At a higher reduced frequency of 0.084, the hysteresis behavior is more pronounced, as seen in Figure 21. In addition to greater hysteresis, the maximum lift coefficient is increased to about 1.70, which is an 62% increase over the steady state value. The corresponding hysteresis lift coefficient is 0.97. This difference between steady state behavior and unsteady hysteresis behavior is a main reason that unsteady testing should be required for airfoils used in wind turbine applications.

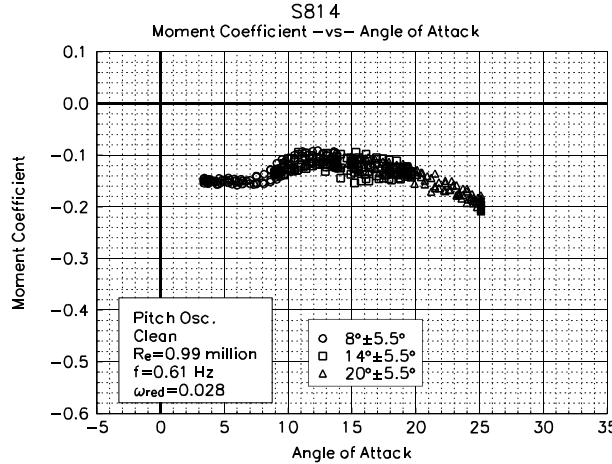


Figure 22. Clean, C_m vs α , $\omega_{red}=0.028, \pm 5.5^\circ$

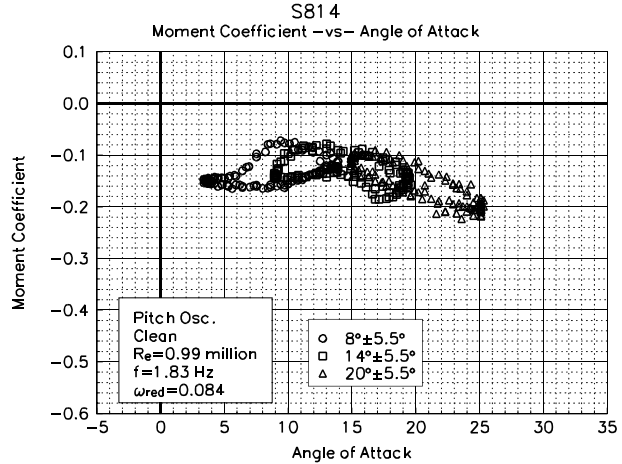


Figure 23. Clean, C_m vs α , $\omega_{red}=0.084, \pm 5.5^\circ$

The pitching moment in Figure 22 and Figure 23 corresponds to the same conditions as in the two lift coefficient plots previously discussed. There is an indication that the hysteresis behavior is present, but it is not as apparent as in the lift coefficient plots; but the higher reduced frequency case does show hysteresis more than the lower reduced frequency case. For reference, the steady state maximum lift occurs near 11° angle of attack, and the steady state pitching moment at this maximum lift point is -0.1019 . In comparison, when the airfoil is undergoing pitch oscillation for the lower frequency, pitching moment varies from -0.1446 to -0.0982 (at the angle of attack where maximum lift occurs), a 41% increase to 4% decrease in magnitude from the steady state value. Note that the angle of attack where the maximum lift coefficient occurs does not necessarily show the "greatest" hysteresis behavior but does give a relative indication of the effect.

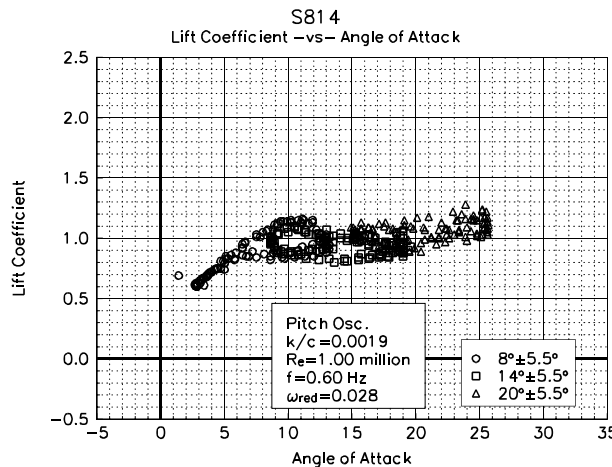


Figure 24. LEGR, C_l vs α , $\omega_{red}=0.028, \pm 5.5^\circ$

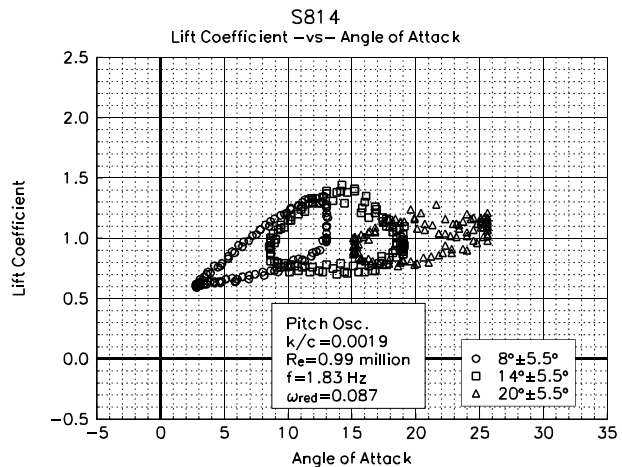


Figure 25. LEGR, C_l vs α , $\omega_{red}=0.087, \pm 5.5^\circ$

In comparison to the clean data, the application of LEGR reduces the maximum lift coefficient in the pitch oscillation cases. Lift coefficient versus angle of attack with LEGR applied is shown in Figure 24 for the 0.028 reduced frequency case. The 0.087 reduced frequency case is in Figure 25. Both correspond to the same run conditions that were described earlier for the clean cases. For the lower reduced frequency, the maximum unsteady lift coefficient is reduced to 1.16 from the corresponding clean case of 1.49, a 22% decrease. Hysteresis behavior is apparent at this frequency but it is of slightly smaller order than the clean case; the corresponding hysteresis lift coefficient is 1.03 when LEGR is applied. In contrast, the higher frequency LEGR case has a maximum lift coefficient of 1.44 while the model is increasing in angle of attack,

and the corresponding decreasing angle of attack lift coefficient is 0.79. Again in this case, the application of LEGR slightly reduces the hysteresis loop behavior for larger angles of attack in comparison with that of the clean case at the same run conditions.

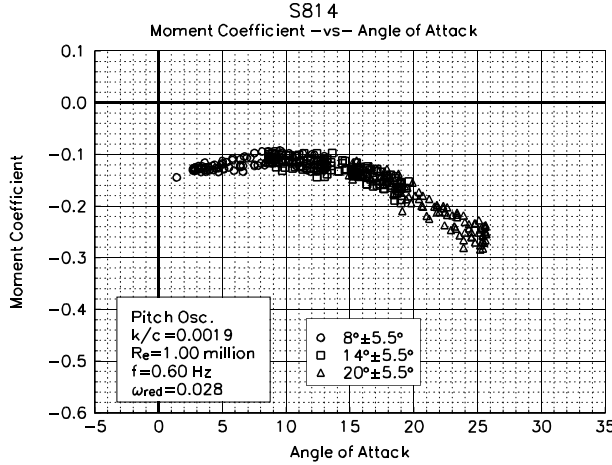


Figure 26. LEGR, C_m vs α , $w_{red}=0.028, \pm 5.5^\circ$

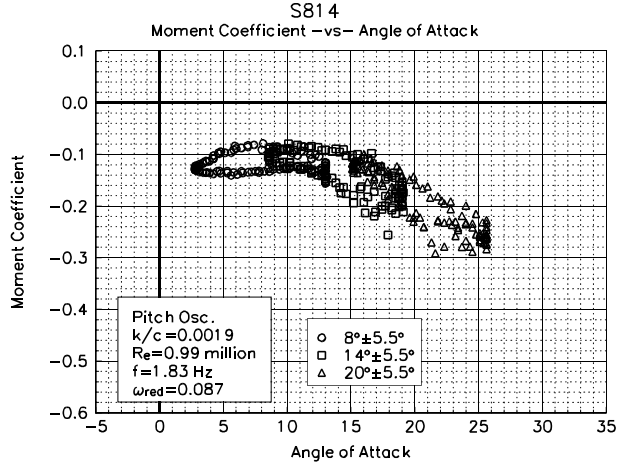


Figure 27. LEGR, C_m vs α , $w_{red}=0.087, \pm 5.5^\circ$

The pitching moment coefficient shown in Figure 26 is for 0.028 reduced frequency with LEGR applied. At the angle of unsteady maximum lift, the pitching moment ranges from -0.1239 to -0.1119, while the steady state LEGR pitching moment is -0.1040 at the steady state stall angle of attack (8.1°). The higher reduced frequency of 0.087 with LEGR application is shown in Figure 27. As was seen with the lift coefficient, pitching moment hysteresis is more apparent at the higher reduced frequency than the corresponding low reduced frequency case. Unsteady maximum lift angle of attack for this reduced frequency occurs at 14.2° , and the pitching moment ranges from -0.1752 to -0.0958 at that angle. Throughout the higher angle of attack range, the magnitude of the unsteady pitching moment can be very different than that of the steady state clean case (steady state pitching moment at maximum lift is -0.1040). It seems that these differences can have significant impact on the fatigue life predictions of a wind turbine system.

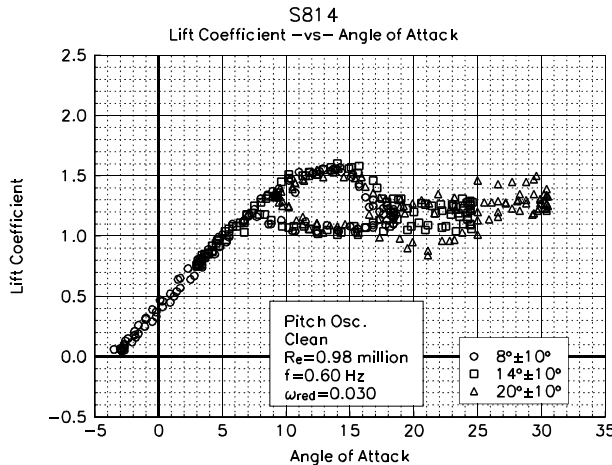


Figure 28. Clean, C_l vs α , $w_{red}=0.030, \pm 10^\circ$

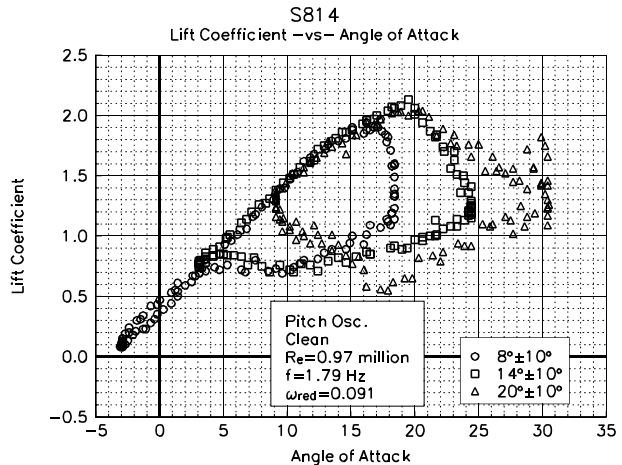


Figure 29. Clean, C_l vs α , $w_{red}=0.091, \pm 10^\circ$

In addition to the $\pm 5.5^\circ$ unsteady experimental data, $\pm 10^\circ$ unsteady data were obtained with and without LEGR. The data were taken at 1 million Reynolds number using the same mean angles and frequencies as those of the 5.5° amplitude cases. Figure 28 and Figure 29 show the $\pm 10^\circ$, unsteady, clean, lift coefficient

for the reduced frequencies of 0.030 and 0.091, respectively. The maximum lift coefficient for the lower frequency is 1.60 and occurs, as expected, when the airfoil is traveling through increasing angle of attack. The hysteresis lift coefficient (at 14.0°) is 1.01. At the higher reduced frequency, the maximum lift coefficient occurs at a higher angle of attack, 19.5°, and is 2.13. The corresponding hysteresis lift coefficient is 0.90. A much greater hysteresis response is experienced for the lower reduced frequency than the higher ones. The steady state, clean, maximum lift coefficient is 1.29; therefore, the unsteady behavior created lift coefficients as much as 65% higher than those of the steady state conditions.

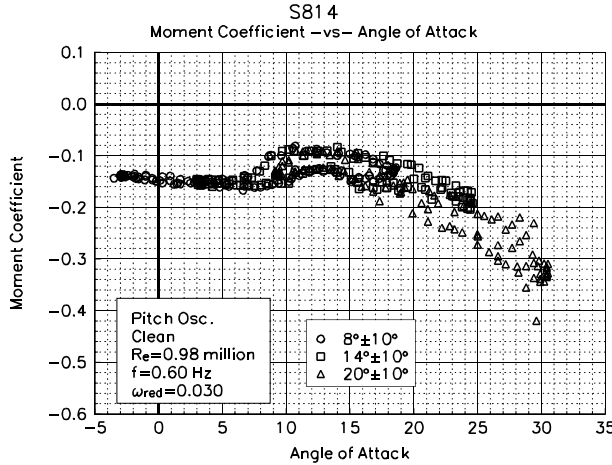


Figure 30. Clean, C_m vs α , $\omega_{red}=0.030, \pm 10^\circ$

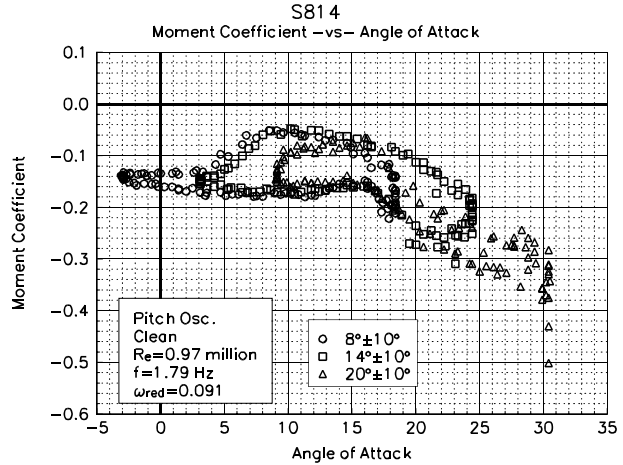


Figure 31. Clean, C_m vs α , $\omega_{red}=0.091, \pm 10^\circ$

The quarter chord pitching moments having the same reduced frequencies as the lift coefficient cases are shown in Figure 30 and Figure 31. The hysteresis behavior observed in the lift coefficient plots is also reflected in this pitching moment data. Near the maximum lift angle, 14.0° for the lower frequency, the pitching moment coefficient ranges from -0.1320 to -0.0835; whereas the 0.091 reduced frequency case has maximum lift near 19.5° and pitching moment ranges from -0.2701 to -0.0969. In comparison, the steady state pitching moment is -0.1019 near the steady state maximum lift coefficient angle of attack of 11°. The higher reduced frequency again shows large hysteresis loops for all three mean angles of attack.

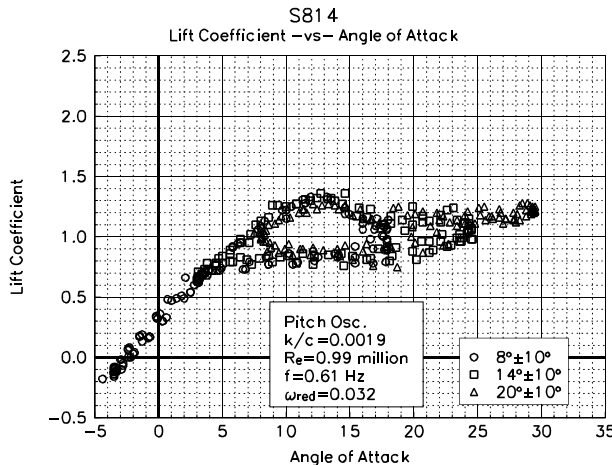


Figure 32. LEGR, C_l vs α , $\omega_{red}=0.032, \pm 10^\circ$

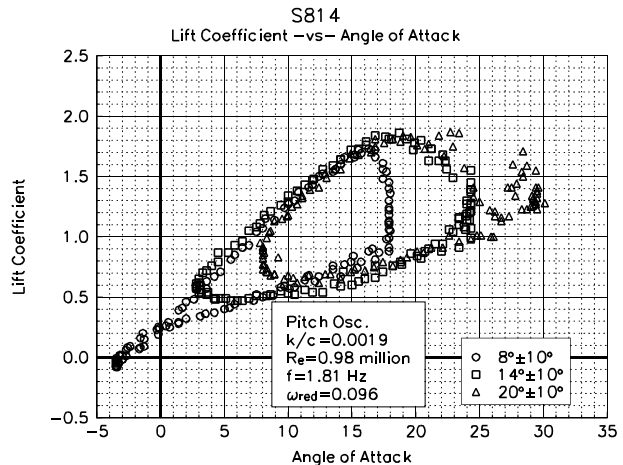


Figure 33. LEGR, C_l vs α , $\omega_{red}=0.096, \pm 10^\circ$

The application of LEGR degrades the lift performance of the airfoil as would be expected from the results discussed previously. The LEGR lift coefficient data for reduced frequencies of 0.032 and 0.096 are shown

in Figure 32 and Figure 33, respectively. The maximum lift coefficient is reduced to 1.36 from 1.60 for the low frequency clean case. Although there is a reduction, this value is still significantly higher than that of the LEGR steady state case, which has a maximum lift coefficient of 0.97 at 8.1° angle of attack. The higher reduced frequency has a maximum lift coefficient of 1.86, which occurs near 19° angle of attack. The corresponding lift coefficient at 19° for the airfoil traveling with decreasing angle of attack is 0.79, a 57% reduction from the maximum.

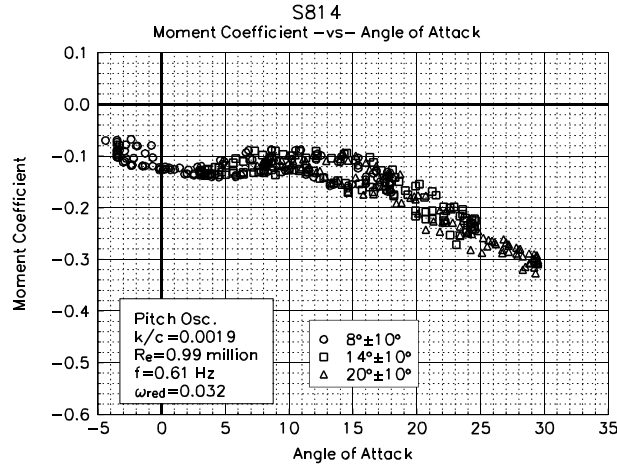


Figure 34. LEGR, C_m vs α , $\omega_{red}=0.032, \pm 10^\circ$

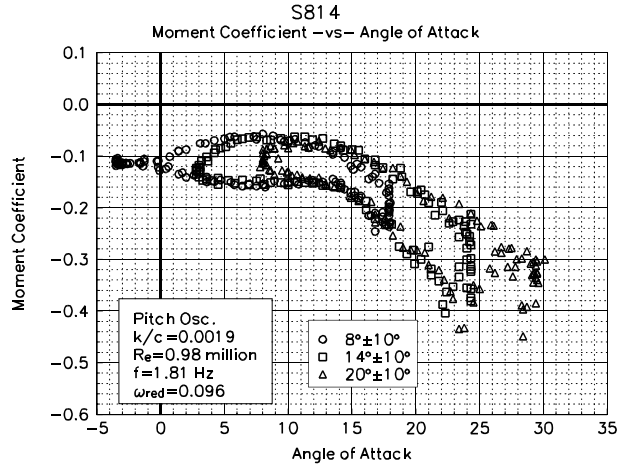


Figure 35. LEGR, C_m vs α , $\omega_{red}=0.096, \pm 10^\circ$

Figure 34 and Figure 35 show the corresponding pitching moment coefficients for the reduced frequencies of 0.032 and 0.096. For the 0.032 reduced frequency case, the pitching moment varies from -0.1709 to -0.0941 at 14.6° (where the maximum lift occurs). The hysteresis behavior is more pronounced for the higher reduced frequency case, where the range of pitching moments at the maximum lift angle of 18.7° is from -0.2753 to -0.1232. These values can then be compared to the steady state LEGR value of -0.1040.

Although all the unsteady data have not been discussed here, the previous discussion included typical examples of the wind tunnel data. The remaining cases of the $\pm 5.5^\circ$ and $\pm 10^\circ$ oscillation data for all the Reynolds numbers are included in Appendix C.

The following four unsteady pressure distributions show examples of the data used to calculate the lift, the pressure drag, and the pitching moment coefficients. Figure 36 shows the distribution for a clean model, with a reduced frequency of 0.055, a mean angle of attack of 14° , and a $\pm 5.5^\circ$ pitch oscillation. For plotting clarity, the model pressures were "unwrapped" about the trailing edge. The upper surface pressures are depicted on the right of the surface plot, and the lower surface values are on the left. The trailing edge is then at the midpoint of the x-axis with the leading edge at each extreme. Additionally, the pressure coefficients were linearly interpolated to create evenly spaced x positions, thus making an evenly spaced grid. The time scale corresponds to angle of attack. For this case, the pressure peak is at approximately -4.5. Figure 37 shows the LEGR case for the same test conditions as in the previous figure. The application of LEGR reduces the pressure peak to -3. Separated flow is defined as the irregular, "rough" areas on the upper surface, which are more widely noticeable for the LEGR case than for the clean case. Also note that the lower surface stays attached through the airfoil travel.

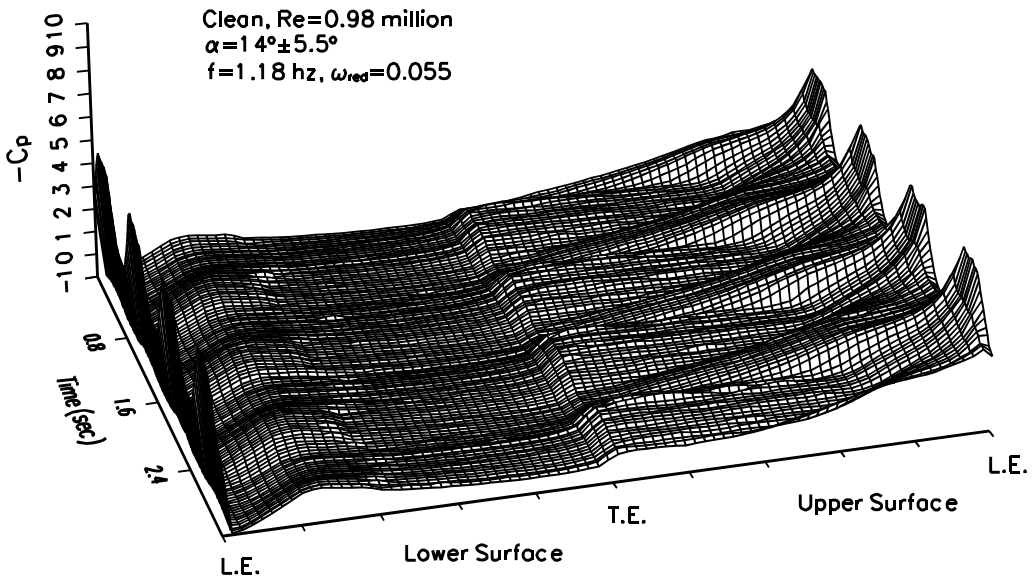


Figure 36. Unsteady pressure distribution, clean, $\omega_{red}=0.055$, $14\pm 5.5^\circ$

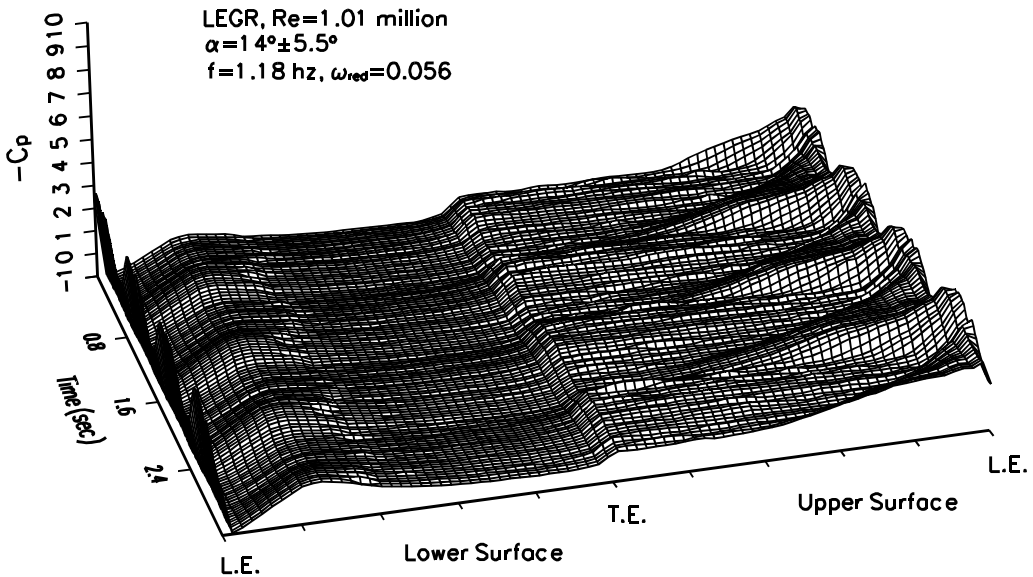


Figure 37. Unsteady pressure distribution, LEGR, $\omega_{red}=0.056$, $14\pm 5.5^\circ$

Figure 38 shows the same clean run conditions as above except with the $\pm 10^\circ$ amplitude oscillation. This case is characterized by significant portions of the upper surface in stall and high pressure peaks. The pressure coefficient peaks are about -6.5 for this case although they were near -4.5 for the previous clean, 14° mean angle of attack case.

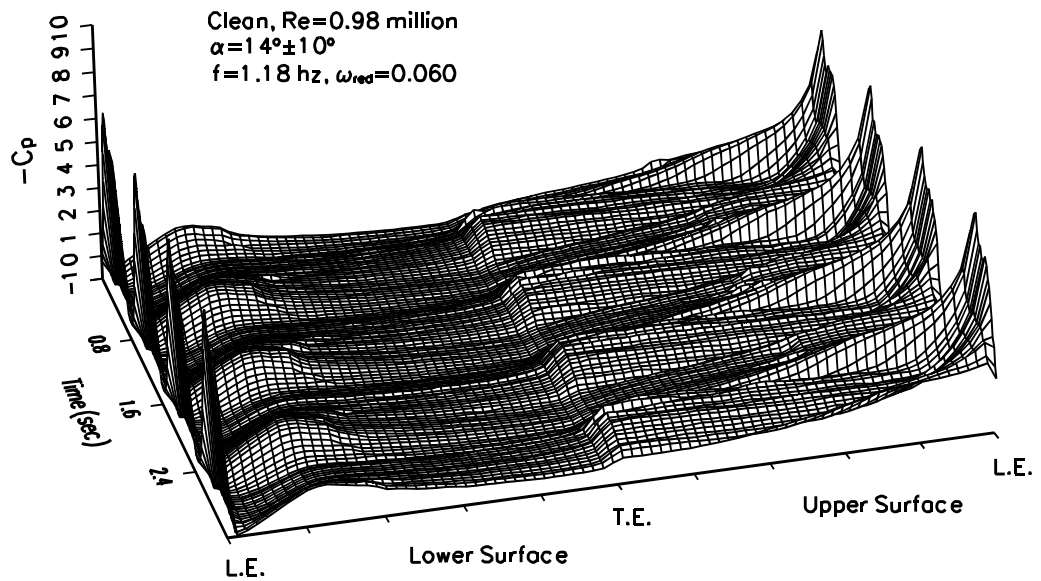


Figure 38. Unsteady pressure distribution, clean, $\omega_{red}=0.060$, $14\pm10^\circ$

Summary of Results

An S814 airfoil model was tested under steady state and pitch oscillation conditions. Baseline tests were made while the model was clean, and then corresponding tests were conducted with leading edge grit roughness (LEGR) applied.

A summary of the steady state aerodynamic parameters is shown in Table 1. As observed, the application of LEGR reduced the maximum lift of the airfoil up to 25%, and the minimum drag coefficient increased more than 24%. The zero lift pitching moment coefficient was also affected by application of LEGR, which reduced the magnitude an average of 35%.

Table 1. S814 Steady State Parameters Summary

Grit Pattern	Re x 10 ⁻⁶	C _{lmax}	C _{dmin}	C _{mo}
Clean	0.75	1.32 @ 11.2°	0.0126	-0.1356
k/c=0.0019	0.75	0.96 @ 8.1°	0.0156	-0.1209
Clean	1.00	1.29 @ 11.2°	0.0108	-0.1345
k/c=0.0019	1.00	0.97 @ 8.1°	0.0157	-0.0786
Clean	1.25	1.29 @ 11.2°	0.0099	-0.1363
k/c=0.0019	1.25	0.99 @ 8.2°	0.0158	-0.0656
Clean	1.50	1.31 @ 11.2°	0.0098	-0.1368
k/c=0.0019	1.50	0.99 @ 8.1°	0.0151	-0.0880

Table 2. S814, Unsteady, Clean, ±5.5°

ω _{red}	Re x 10 ⁻⁶	f	C _{lmax}	α _{max}	C _{l dec}	C _{m inc}	C _{m dec}
0.037	0.74	0.61	1.54	14.8	1.17	-0.1431	-0.1055
0.073	0.74	1.18	1.68	16.3	1.06	-0.1658	-0.1012
0.114	0.74	1.85	1.91	17.9	1.14	-0.2354	-0.1151
0.028	0.99	0.61	1.49	14.1	1.11	-0.1446	-0.0982
0.055	0.99	1.19	1.59	14.9	1.03	-0.1404	-0.0874
0.084	0.99	1.83	1.70	16.8	0.97	-0.1655	-0.0941
0.022	1.24	0.60	1.44	12.6	1.15	-0.1195	-0.1069
0.044	1.24	1.19	1.57	13.8	1.15	-0.1274	-0.1134
0.068	1.23	1.85	1.64	15.7	1.05	-0.1568	-0.1032
0.018	1.49	0.60	1.43	13.1	1.19	-0.1156	-0.1130
0.036	1.49	1.19	1.51	14.4	1.08	-0.1541	-0.1076
0.055	1.49	1.83	1.61	14.1	1.03	-0.1361	-0.0924

The pitch oscillation data can be divided into two groups, the ±5.5° amplitude and the ±10° amplitude oscillations which show similar trends. For both ±5.5° and ±10°, the unsteady test conditions and some parameters are listed in Tables 2, 3, 4, and 5. As the reduced frequency, which takes oscillation and tunnel speed into account, is increased, the maximum lift coefficient also increases. In addition, the hysteresis behavior becomes increasingly apparent with increased reduced frequency.

Table 3. S814, Unsteady, LEGR, $\pm 5.5^\circ$

ω_{red}	$\text{Re} \times 10^{-6}$	f	$C_{l\max}$	α_{\max}	$C_{l\text{dec}}$	$C_{m\text{ inc}}$	$C_{m\text{ dec}}$
0.038	0.75	0.60	1.25	12.5	0.94	-0.1629	-0.1141
0.075	0.75	1.19	1.33	13.0	0.74	-0.1400	-0.0819
0.115	0.75	1.83	1.57	15.7	0.74	-0.2193	-0.1154
0.028	1.00	0.60	1.16	11.1	0.93	-0.1239	-0.1119
0.057	1.00	1.19	1.29	13.6	0.86	-0.1646	-0.1076
0.087	0.99	1.83	1.44	14.2	0.79	-0.1752	-0.0958
0.022	1.25	0.60	1.14	10.5	0.88	-0.1185	-0.1079
0.045	1.24	1.19	1.27	12.4	0.92	-0.1710	-0.1074
0.070	1.24	1.85	1.33	13.6	0.78	-0.1677	-0.0951
0.019	1.50	0.61	1.13	9.5	0.95	-0.1141	-0.1049
0.038	1.49	1.21	1.21	11.1	0.80	-0.1250	-0.0943
0.057	1.47	1.83	1.30	13.8	0.87	-0.1549	-0.1142

Table 4. S814, Unsteady, Clean, $\pm 10^\circ$

ω_{red}	$\text{Re} \times 10^{-6}$	f	$C_{l\max}$	α_{\max}	$C_{l\text{dec}}$	$C_{m\text{ inc}}$	$C_{m\text{ dec}}$
0.040	0.73	0.59	1.72	14.0	1.04	-0.1470	-0.0869
0.081	0.73	1.19	2.04	18.7	1.07	-0.2229	-0.1109
0.125	0.72	1.83	2.42	22.2	0.93	-0.3615	-0.2184
0.030	0.98	0.60	1.60	14.0	1.01	-0.1320	-0.0835
0.061	0.97	1.19	1.88	17.1	1.01	-0.1872	-0.1024
0.091	0.97	1.79	2.13	19.5	0.90	-0.2701	-0.0969
0.024	1.22	0.60	1.55	13.7	1.04	-0.1278	-0.1001
0.048	1.22	1.18	1.75	15.7	0.94	-0.1521	-0.0852
0.073	1.22	1.79	2.05	17.7	0.92	-0.1934	-0.0991
0.020	1.47	0.59	1.52	13.5	1.11	-0.1275	-0.1015
0.040	1.46	1.19	1.70	16.2	0.97	-0.1672	-0.0928
0.061	1.46	1.83	1.87	16.8	0.90	-0.1772	-0.0939

As expected the application of LEGR reduces the aerodynamic performance of the airfoil. The unsteady maximum lift coefficient is reduced from 15% to 21% for the $\pm 5.5^\circ$ case and 11% to 18% for the $\pm 10^\circ$ case. As well as following the same trends as the clean, unsteady data discussed previously, the LEGR causes the hysteresis behavior to persist into lower angles of attack than do the clean cases. Overall, the unsteady wind tunnel data show hysteresis behavior that becomes more apparent with increased, reduced frequency. The maximum unsteady lift coefficient can be as much as 55% higher for the $\pm 5.5^\circ$ amplitude and as much as 110% higher for the $\pm 10^\circ$ amplitude than the steady state maximum lift coefficient. In addition, variation in the quarter chord pitching moment coefficient can be more than two times greater than that indicated by steady state results. These findings indicate that it is very important to consider the unsteady loading that will occur in wind turbine operation because steady state results can greatly underestimate the forces.

Table 5. S814, Unsteady, LEGR, $\pm 10^\circ$

ω_{red}	$\text{Re} \times 10^{-6}$	ω	$C_{l\max}$	α_{\max}	$C_{l\text{ dec}}$	$C_{m\text{ inc}}$	$C_{m\text{ dec}}$
0.042	0.74	0.61	1.48	13.8	0.73	-0.1566	-0.0873
0.083	0.74	1.19	1.80	17.4	0.67	-0.2480	-0.1133
0.128	0.74	1.81	2.12	19.9	0.82	-0.3108	-0.1876
0.032	0.99	0.61	1.36	14.6	0.76	-0.1709	-0.0941
0.064	0.99	1.21	1.60	15.7	0.74	-0.2017	-0.0941
0.096	0.98	1.81	1.86	18.7	0.79	-0.2753	-0.1232
0.025	1.24	0.61	1.31	12.4	0.88	-0.1391	-0.1005
0.051	1.23	1.22	1.55	14.9	0.81	-0.1916	-0.1048
0.076	1.23	1.81	1.71	18.2	0.78	-0.2550	-0.1352
0.021	1.49	0.61	1.25	12.1	0.93	-0.1357	-0.1010
0.042	1.48	1.19	1.47	14.8	0.82	-0.1866	-0.1010
0.064	1.48	1.83	1.66	15.2	0.76	-0.1985	-0.1047

References

- Pope, A.; Harper, J.J. (1966). *Low Speed Wind Tunnel Testing*. New York, NY: John Wiley & Sons, Inc.
- Schlichting, H. (1979). *Boundary Layer Theory*. New York, NY: McGraw-Hill Inc.
- Smetana, F., Summey D., et-al. 1975. *Light Aircraft Lift, Drag, Moment Prediction - a Review and Analysis*. North Carolina State University. NASA-CR2523.

Appendix A: Surface Pressure Tap Coordinates

**Table A1. S814 Surface Pressure Taps,
Non-Dimensional Coordinates**

Tap Number	Chord Station	Ordinate
1	1.0003	--
2	0.9740	--
3	0.9321	--
4	0.8910	--
5	0.8489	--
6	0.8075	--
7	0.7663	--
8	0.7254	--
9	0.6843	--
10	0.6440	--
11	0.6037	--
12	0.5635	--
13	0.5240	--
14	0.4833	--
15	0.4432	--
16	0.4033	--
17	0.3641	--
18	0.3238	--
19	0.2836	--
20	0.2426	--
21	0.2006	--
22	0.1613	--
23	0.1249	--
24	0.0914	--
25	0.0596	--
26	0.0344	--
27	0.0176	--
28	0.0127	--
29	0.0081	--
30	0.0039	--
31	0.0009	--
32	0.0000	--
33	0.0004	--
34	0.0035	--

**Table A1. S814 Surface Pressure Taps,
Non-Dimensional Coordinates**

Tap Number	Chord Station	Ordinate
35	0.0070	--
36	0.0237	--
37	0.0513	--
38	0.0848	--
39	0.1213	--
40	0.1597	--
41	0.1991	--
42	0.2396	--
43	0.2798	--
44	0.3217	--
45	0.3635	--
46	0.4048	--
47	0.4459	--
48	0.4873	--
49	0.5275	--
50	0.5688	--
51	0.6090	--
52	0.6502	--
53	0.6904	--
54	0.7310	--
55	0.7715	--
56	0.8120	--
57	0.8522	--
58	0.8925	--
59	0.9324	--
60	0.9707	--
End of Table A1		

Appendix B: Steady State Data Integrated Coefficients and Pressure Distributions

List of Figures

Page

Pressure Distributions, Steady State, Re = 0.75 million	B-20
1. $\alpha = -20.3^\circ$	B-21
2. $\alpha = -18.4^\circ$	B-21
3. $\alpha = -16.3^\circ$	B-21
4. $\alpha = -14.2^\circ$	B-21
5. $\alpha = -12.3^\circ$	B-22
6. $\alpha = -10.3^\circ$	B-22
7. $\alpha = -8.2^\circ$	B-22
8. $\alpha = -6.2^\circ$	B-22
9. $\alpha = -4.2^\circ$	B-23
10. $\alpha = -2.2^\circ$	B-23
11. $\alpha = 0.0^\circ$	B-23
12. $\alpha = 2.0^\circ$	B-23
13. $\alpha = 4.0^\circ$	B-24
14. $\alpha = 6.2^\circ$	B-24
15. $\alpha = 8.2^\circ$	B-24
16. $\alpha = 10.1^\circ$	B-24
17. $\alpha = 11.2^\circ$	B-25
18. $\alpha = 12.1^\circ$	B-25
19. $\alpha = 13.1^\circ$	B-25
20. $\alpha = 14.2^\circ$	B-25
21. $\alpha = 15.0^\circ$	B-26
22. $\alpha = 16.1^\circ$	B-26
23. $\alpha = 17.2^\circ$	B-26
24. $\alpha = 18.2^\circ$	B-26
25. $\alpha = 19.2^\circ$	B-27
26. $\alpha = 20.2^\circ$	B-27
27. $\alpha = 22.1^\circ$	B-27
28. $\alpha = 24.1^\circ$	B-27
29. $\alpha = 26.1^\circ$	B-28
30. $\alpha = 28.1^\circ$	B-28
31. $\alpha = 30.0^\circ$	B-28
32. $\alpha = 31.9^\circ$	B-28
33. $\alpha = 34.0^\circ$	B-29
34. $\alpha = 36.1^\circ$	B-29
35. $\alpha = 37.9^\circ$	B-29
36. $\alpha = 39.9^\circ$	B-29
 Pressure Distributions, Steady State, Re = 1 million	 B-30
37. $\alpha = -20.3^\circ$	B-31
38. $\alpha = -18.4^\circ$	B-31
39. $\alpha = -16.4^\circ$	B-31
40. $\alpha = -14.5^\circ$	B-31
41. $\alpha = -12.3^\circ$	B-32
42. $\alpha = -10.2^\circ$	B-32
43. $\alpha = -8.3^\circ$	B-32
44. $\alpha = -6.1^\circ$	B-32

45. $\alpha = -4.2^\circ$	B-33
46. $\alpha = -2.2^\circ$	B-33
47. $\alpha = 0.0^\circ$	B-33
48. $\alpha = 2.0^\circ$	B-33
49. $\alpha = 4.0^\circ$	B-34
50. $\alpha = 6.2^\circ$	B-34
51. $\alpha = 8.2^\circ$	B-34
52. $\alpha = 10.1^\circ$	B-34
53. $\alpha = 11.2^\circ$	B-35
54. $\alpha = 12.3^\circ$	B-35
55. $\alpha = 13.1^\circ$	B-35
56. $\alpha = 14.2^\circ$	B-35
57. $\alpha = 15.1^\circ$	B-36
58. $\alpha = 16.2^\circ$	B-36
59. $\alpha = 17.2^\circ$	B-36
60. $\alpha = 18.1^\circ$	B-36
61. $\alpha = 19.1^\circ$	B-37
62. $\alpha = 20.2^\circ$	B-37
63. $\alpha = 22.2^\circ$	B-37
64. $\alpha = 24.0^\circ$	B-37
65. $\alpha = 26.0^\circ$	B-38
66. $\alpha = 28.1^\circ$	B-38
67. $\alpha = 30.0^\circ$	B-38
68. $\alpha = 32.0^\circ$	B-38
69. $\alpha = 34.1^\circ$	B-39
70. $\alpha = 36.0^\circ$	B-39
71. $\alpha = 38.0^\circ$	B-39
72. $\alpha = 39.9^\circ$	B-39

Pressure Distributions, Steady State, $Re = 1.25$ million	B-40
73. $\alpha = -20.3^\circ$	B-41
74. $\alpha = -18.4^\circ$	B-41
75. $\alpha = -16.3^\circ$	B-41
76. $\alpha = -14.3^\circ$	B-41
77. $\alpha = -12.3^\circ$	B-42
78. $\alpha = -10.3^\circ$	B-42
79. $\alpha = -8.3^\circ$	B-42
80. $\alpha = -6.2^\circ$	B-42
81. $\alpha = -4.2^\circ$	B-43
82. $\alpha = -2.2^\circ$	B-43
83. $\alpha = 0.0^\circ$	B-43
84. $\alpha = 2.0^\circ$	B-43
85. $\alpha = 4.2^\circ$	B-44
86. $\alpha = 6.2^\circ$	B-44
87. $\alpha = 8.2^\circ$	B-44
88. $\alpha = 10.1^\circ$	B-44
89. $\alpha = 11.2^\circ$	B-45
90. $\alpha = 12.3^\circ$	B-45
91. $\alpha = 13.1^\circ$	B-45
92. $\alpha = 14.2^\circ$	B-45

93. $\alpha = 15.1^\circ$	B-46
94. $\alpha = 16.1^\circ$	B-46
95. $\alpha = 17.2^\circ$	B-46
96. $\alpha = 18.3^\circ$	B-46
97. $\alpha = 19.1^\circ$	B-47
98. $\alpha = 20.2^\circ$	B-47
99. $\alpha = 22.2^\circ$	B-47
100. $\alpha = 24.0^\circ$	B-47
101. $\alpha = 25.9^\circ$	B-48
102. $\alpha = 27.8^\circ$	B-48
103. $\alpha = 30.0^\circ$	B-48
104. $\alpha = 31.9^\circ$	B-48
105. $\alpha = 33.9^\circ$	B-49
106. $\alpha = 36.0^\circ$	B-49
107. $\alpha = 38.0^\circ$	B-49
108. $\alpha = 40.1^\circ$	B-49
Pressure Distributions, Steady State, Re = 1.5 million	B-50
109. $\alpha = -20.2^\circ$	B-51
110. $\alpha = -18.4^\circ$	B-51
111. $\alpha = -16.5^\circ$	B-51
112. $\alpha = -14.3^\circ$	B-51
113. $\alpha = -12.3^\circ$	B-52
114. $\alpha = -10.3^\circ$	B-52
115. $\alpha = -8.4^\circ$	B-52
116. $\alpha = -6.1^\circ$	B-52
117. $\alpha = -4.2^\circ$	B-53
118. $\alpha = -2.1^\circ$	B-53
119. $\alpha = 0.0^\circ$	B-53
120. $\alpha = 2.0^\circ$	B-53
121. $\alpha = 4.1^\circ$	B-54
122. $\alpha = 6.2^\circ$	B-54
123. $\alpha = 8.2^\circ$	B-54
124. $\alpha = 10.1^\circ$	B-54
125. $\alpha = 11.2^\circ$	B-55
126. $\alpha = 12.1^\circ$	B-55
127. $\alpha = 13.1^\circ$	B-55
128. $\alpha = 14.2^\circ$	B-55
129. $\alpha = 15.2^\circ$	B-56
130. $\alpha = 16.1^\circ$	B-56
131. $\alpha = 17.2^\circ$	B-56
132. $\alpha = 18.1^\circ$	B-56
133. $\alpha = 19.1^\circ$	B-57
134. $\alpha = 20.2^\circ$	B-57

List of Tables

	Page
--	-------------

B1. S814, Clean, $Re = 0.75 \times 10^6$	B-6
B2. S814, Clean, $Re = 1.0 \times 10^6$	B-8
B3. S814, Clean, $Re = 1.25 \times 10^6$	B-10
B4. S814, Clean, $Re = 1.5 \times 10^6$	B-12
B5. S814, LEGR, $Re = 0.75 \times 10^6$	B-13
B6. S814, LEGR, $Re = 1.0 \times 10^6$	B-15
B7. S814, LEGR, $Re = 1.25 \times 10^6$	B-17
B8. S814, LEGR, $Re = 1.5 \times 10^6$	B-19

Table B1. S814, Clean, Re = 0.75 x 10⁶

RUN	AOA	C _I	C _{dp}	C _{m^{1/4}}	Re x 10 ⁻⁶	C _{dw}
77	-20.3	-1.34	0.1697	-0.0499	0.74	--
76	-18.4	-1.31	0.1246	-0.0679	0.74	--
75	-16.3	-1.03	0.1575	-0.0055	0.75	--
74	-14.2	-0.90	0.1559	-0.0085	0.76	--
73	-12.3	-0.93	0.0482	-0.1061	0.75	0.0156
72	-10.3	-0.71	0.0301	-0.1239	0.74	0.0159
71	-8.2	-0.51	0.0191	-0.1290	0.74	0.0139
70	-6.2	-0.32	0.0099	-0.1293	0.74	0.0133
69	-4.2	-0.11	0.0066	-0.1339	0.75	0.0133
68	-2.2	0.12	0.0072	-0.1374	0.75	0.0126
67	0.0	0.36	0.0098	-0.1407	0.75	0.0128
78	0.0	0.33	0.0113	-0.1403	0.75	0.0129
104	0.0	0.33	0.0110	-0.1409	0.75	0.0128
79	2.0	0.59	0.0122	-0.1454	0.75	0.0136
80	4.0	0.83	0.0093	-0.1458	0.75	0.0143
81	6.2	1.03	0.0182	-0.1439	0.74	0.0151
82	8.2	1.23	0.0208	-0.1412	0.74	0.0132
83	10.1	1.32	0.0267	-0.1222	0.74	0.0210
84	11.2	1.32	0.0328	-0.1081	0.75	0.0300
85	12.1	1.27	0.0326	-0.0991	0.74	--
86	13.1	1.16	0.0469	-0.0976	0.75	--
87	14.2	1.16	0.0640	-0.0995	0.75	--
88	15.0	1.15	0.0774	-0.1033	0.75	--
89	16.1	1.13	0.0967	-0.1044	0.75	--
90	17.2	1.13	0.1153	-0.1100	0.75	--
91	18.2	1.13	0.1279	-0.1127	0.75	--
92	19.2	1.12	0.1485	-0.1172	0.75	--
93	20.2	1.13	0.1752	-0.1271	0.75	--

Table B1. S814, Clean, Re = 0.75×10^6

RUN	AOA	C _I	C _{dp}	C _{m^{1/4}}	Re x 10 ⁻⁶	C _{dw}
94	22.1	1.08	0.2240	-0.1437	0.75	--
95	24.1	1.08	0.2832	-0.1640	0.75	--
96	26.1	0.98	0.5531	-0.2442	0.76	--
97	28.1	1.09	0.6512	-0.2757	0.75	--
98	30.0	1.15	0.7325	-0.2958	0.74	--
99	31.9	1.25	0.8358	-0.3260	0.73	--
100	34.0	1.30	0.9295	-0.3500	0.74	--
101	36.1	1.32	1.0081	-0.3652	0.73	--
102	37.9	1.34	1.0872	-0.3853	0.73	--
103	39.9	1.35	1.1584	-0.3994	0.73	--

End of Table B1

Table B2. S814, Clean, Re = 1.0 x 10⁶

RUN	AOA	C _I	C _{dp}	C _{m^{1/4}}	Re x 10 ⁻⁶	C _{dw}
11	-20.3	-1.29	0.1793	-0.0456	0.99	--
10	-18.4	-1.30	0.1226	-0.0767	0.99	--
9	-16.4	-1.22	0.0898	-0.0839	0.99	--
8	-14.5	-1.09	0.0634	-0.0994	0.99	0.0139
7	-12.3	-0.88	0.0396	-0.1172	0.99	0.0140
6	-10.2	-0.70	0.0267	-0.1231	1.00	0.0132
5	-8.3	-0.53	0.0209	-0.1254	0.99	0.0141
4	-6.1	-0.34	0.0098	-0.1273	1.00	0.0144
3	-4.2	-0.11	0.0074	-0.1327	1.00	0.0108
2	-2.2	0.13	0.0066	-0.1366	1.00	0.0129
1	0.0	0.37	0.0075	-0.1408	1.00	0.0125
12	0.0	0.38	0.0073	-0.1415	1.00	0.0124
38	0.0	0.38	0.0066	-0.1414	0.99	0.0116
13	2.0	0.59	0.0098	-0.1431	1.00	0.0113
14	4.0	0.83	0.0087	-0.1436	1.00	0.0119
15	6.2	1.06	0.0137	-0.1437	1.00	0.0123
16	8.2	1.23	0.0186	-0.1369	1.00	0.0136
17	10.1	1.29	0.0227	-0.1138	1.00	0.0232
18	11.2	1.29	0.0263	-0.1019	1.00	0.0373
19	12.3	1.18	0.0376	-0.1009	1.00	--
20	13.1	1.14	0.0476	-0.0991	1.00	--
21	14.2	1.13	0.0662	-0.1014	1.00	--
22	15.1	1.13	0.0786	-0.1034	1.00	--
23	16.2	1.13	0.0943	-0.1053	1.00	--
24	17.2	1.11	0.1113	-0.1083	1.00	--
25	18.1	1.11	0.1267	-0.1141	1.00	--
26	19.1	1.12	0.1499	-0.1192	1.00	--
27	20.2	1.10	0.1749	-0.1278	1.00	--

Table B2. S814, Clean, Re = 1.0 x 10⁶

RUN	AOA	C _I	C _{dp}	C _{m¼}	Re x 10 ⁻⁶	C _{dw}
28	22.2	1.09	0.2263	-0.1446	0.99	--
29	24.0	1.07	0.2823	-0.1639	0.99	--
30	26.0	0.96	0.5458	-0.2405	1.01	--
31	28.1	1.09	0.6515	-0.2738	1.01	--
32	30.0	1.17	0.7379	-0.2972	1.00	--
33	32.0	1.25	0.8367	-0.3254	1.01	--
34	34.1	1.30	0.9326	-0.3497	1.01	--
35	36.0	1.33	1.0134	-0.3672	1.00	--
36	38.0	1.35	1.0926	-0.3857	0.99	--
37	39.9	1.36	1.1699	-0.4039	1.00	--

End of Table B2

Table B3. S814, Clean, Re = 1.25 x 10⁶

RUN	AOA	C _I	C _{dp}	C _{m^{1/4}}	Re x 10 ⁻⁶	C _{dw}
115	-20.3	-1.20	0.1922	-0.0351	1.26	--
114	-18.4	-1.26	0.1274	-0.0794	1.24	--
113	-16.3	-1.20	0.0814	-0.0940	1.23	--
112	-14.3	-1.05	0.0513	-0.1099	1.24	--
111	-12.3	-0.88	0.0336	-0.1215	1.25	0.0114
110	-10.3	-0.69	0.0237	-0.1253	1.25	0.0106
109	-8.3	-0.53	0.0175	-0.1267	1.25	0.0117
108	-6.2	-0.36	0.0073	-0.1280	1.25	0.0117
107	-4.2	-0.12	0.0067	-0.1339	1.25	0.0113
106	-2.2	0.11	0.0068	-0.1385	1.25	0.0104
105	0.0	0.36	0.0077	-0.1420	1.26	0.0099
116	0.0	0.38	0.0069	-0.1423	1.24	0.0103
142	0.0	0.39	0.0062	-0.1419	1.25	0.0099
117	2.0	0.61	0.0075	-0.1444	1.25	0.0111
118	4.2	0.84	0.0106	-0.1443	1.25	0.0109
119	6.2	1.06	0.0131	-0.1439	1.24	0.0118
120	8.2	1.23	0.0162	-0.1355	1.25	0.0132
121	10.1	1.29	0.0232	-0.1157	1.25	0.0217
122	11.2	1.29	0.0306	-0.1083	1.25	0.0272
123	12.3	1.18	0.0549	-0.1162	1.26	--
124	13.1	1.14	0.0595	-0.1092	1.25	--
125	14.2	1.12	0.0682	-0.1036	1.25	--
126	15.1	1.17	0.0917	-0.1182	1.25	--
127	16.1	1.11	0.0952	-0.1062	1.25	--
128	17.2	1.11	0.1149	-0.1103	1.24	--
129	18.3	1.10	0.1325	-0.1156	1.25	--
130	19.1	1.10	0.1507	-0.1208	1.25	--
131	20.2	1.09	0.1751	-0.1287	1.24	--

Table B3. S814, Clean, Re = 1.25×10^6

RUN	AOA	C _I	C _{dp}	C _{m^{1/4}}	Re x 10 ⁻⁶	C _{dw}
132	22.2	1.09	0.2258	-0.1453	1.25	--
133	24.0	1.08	0.2830	-0.1646	1.23	--
134	25.9	1.00	0.5566	-0.2508	1.25	--
135	27.8	1.09	0.6432	-0.2722	1.25	--
136	30.0	1.17	0.7392	-0.2982	1.24	--
137	31.9	1.26	0.8464	-0.3308	1.23	--
138	33.9	1.31	0.9303	-0.3512	1.24	--
139	36.0	1.36	1.0329	-0.3790	1.25	--
140	38.0	1.36	1.1063	-0.3931	1.23	--
141	40.1	1.37	1.1814	-0.4067	1.21	--

End of Table B3

Table B4. S814, Clean, Re = 1.5×10^6

RUN	AOA	C _l	C _{dp}	C _{m^{1/4}}	Re x 10 ⁻⁶	C _{dw}
49	-20.2	-0.94	0.2003	0.0011	1.50	--
48	-18.4	-1.22	0.1335	-0.0739	1.49	--
47	-16.5	-1.17	0.0840	-0.1034	1.48	--
46	-14.3	-1.04	0.0513	-0.1155	1.49	0.0149
45	-12.3	-0.89	0.0307	-0.1222	1.50	0.0117
44	-10.3	-0.70	0.0203	-0.1270	1.49	0.0105
43	-8.4	-0.54	0.0106	-0.1260	1.51	0.0129
42	-6.1	-0.33	0.0064	-0.1295	1.50	0.0109
41	-4.2	-0.11	0.0071	-0.1347	1.50	0.0107
40	-2.1	0.14	0.0061	-0.1395	1.51	0.0103
39	0.0	0.38	0.0072	-0.1440	1.50	0.0098
50	0.0	0.39	0.0072	-0.1447	1.50	0.0104
66	0.0	0.38	0.0061	-0.1438	1.51	0.0101
51	2.0	0.62	0.0065	-0.1459	1.51	0.0103
52	4.1	0.85	0.0100	-0.1456	1.50	0.0109
53	6.2	1.05	0.0135	-0.1423	1.51	0.0119
54	8.2	1.22	0.0156	-0.1332	1.50	0.0147
55	10.1	1.30	0.0226	-0.1157	1.50	0.0245
56	11.2	1.31	0.0300	-0.1076	1.50	0.0313
57	12.1	1.20	0.0527	-0.1171	1.50	--
58	13.1	1.18	0.0656	-0.1157	1.50	--
59	14.2	1.11	0.0710	-0.1061	1.50	--
60	15.2	1.12	0.0853	-0.1069	1.50	--
61	16.1	1.11	0.0994	-0.1090	1.49	--
62	17.2	1.12	0.1182	-0.1135	1.49	--
63	18.1	1.27	0.1778	-0.1576	1.50	--
64	19.1	1.12	0.1500	-0.1208	1.50	--
65	20.2	1.11	0.1750	-0.1290	1.50	--

End of Table B4

Table B5. S814, LEGR, Re = 0.75 x 10⁶

RUN	AOA	C _I	C _{dp}	C _{m^{1/4}}	Re x 10 ⁻⁶	C _{dw}
293	-20.1	-0.59	0.1901	-0.0192	0.75	--
292	-18.2	-0.52	0.1659	-0.0284	0.76	--
291	-16.3	-0.44	0.1381	-0.0369	0.75	--
290	-14.1	-0.35	0.1234	-0.0410	0.75	--
289	-12.1	-0.25	0.1021	-0.0525	0.75	--
288	-10.2	-0.17	0.0856	-0.0585	0.75	--
287	-8.1	-0.09	0.0665	-0.0682	0.74	--
286	-6.1	-0.15	0.0666	-0.0408	0.75	--
285	-4.1	-0.11	0.0498	-0.0441	0.75	--
284	-2.2	0.04	0.0097	-0.1209	0.75	0.0169
283	-0.1	0.26	0.0111	-0.1261	0.75	0.0167
294	0.0	0.26	0.0102	-0.1262	0.75	0.0156
321	0.0	0.27	0.0107	-0.1272	0.75	0.0210
295	2.0	0.49	0.0110	-0.1279	0.76	0.0197
296	4.1	0.69	0.0125	-0.1231	0.74	0.0189
297	6.2	0.85	0.0197	-0.1167	0.74	0.0191
298	8.1	0.96	0.0256	-0.1058	0.75	0.0344
299	10.0	0.92	0.0456	-0.1049	0.75	0.0311
300	11.1	0.90	0.0609	-0.1076	0.75	--
301	12.1	0.98	0.0803	-0.1145	0.74	--
302	13.1	1.01	0.0999	-0.1203	0.75	--
303	14.1	0.91	0.1012	-0.1121	0.73	--
304	15.0	0.91	0.1153	-0.1159	0.76	--
305	16.1	0.90	0.1369	-0.1210	0.75	--
306	16.1	0.93	0.1406	-0.1232	0.77	--
307	17.2	0.92	0.1679	-0.1335	0.76	--
308	18.1	0.85	0.1955	-0.1433	0.75	--
309	19.1	0.89	0.2189	-0.1484	0.75	--

Table B5. S814, LEGR, Re = 0.75 x 10⁶

RUN	AOA	C _I	C _{dp}	C _{m¼}	Re x 10 ⁻⁶	C _{dw}
310	20.2	0.95	0.2573	-0.1620	0.74	--
311	22.1	0.95	0.3259	-0.1865	0.76	--
312	24.0	1.00	0.4153	-0.2166	0.75	--
313	25.9	1.03	0.4909	-0.2351	0.75	--
314	28.1	1.04	0.5680	-0.2475	0.74	--
315	30.0	1.14	0.6833	-0.2814	0.73	--
316	31.9	1.21	0.7803	-0.3065	0.75	--
317	33.9	1.27	0.8818	-0.3336	0.74	--
318	36.0	1.32	0.9900	-0.3615	0.74	--
319	37.9	1.35	1.0742	-0.3821	0.73	--
320	39.9	1.38	1.1694	-0.4067	0.74	--

End of Table B5

Table B6. S814, LEGR, Re = 1.0 x 10⁶

RUN	AOA	C _I	C _{dp}	C _{m^{1/4}}	Re x 10 ⁻⁶	C _{dw}
189	-20.3	-0.58	0.1927	-0.0188	1.00	--
188	-18.1	-0.51	0.1643	-0.0286	1.00	--
187	-16.1	-0.40	0.1364	-0.0435	1.00	--
186	-14.2	-0.31	0.1143	-0.0535	1.00	--
185	-12.0	-0.24	0.1001	-0.0545	1.01	--
184	-10.0	-0.15	0.0823	-0.0618	1.00	--
183	-8.1	-0.07	0.0671	-0.0669	1.00	--
182	-6.1	-0.06	0.0633	-0.0538	1.00	--
181	-4.0	-0.05	0.0516	-0.0443	1.00	--
180	-2.1	0.05	0.0117	-0.1128	1.00	0.0190
179	-0.1	0.30	0.0075	-0.1248	1.00	0.0157
216	-0.1	0.28	0.0081	-0.1236	1.00	0.0162
190	0.0	0.30	0.0076	-0.1244	0.99	0.0163
191	2.1	0.51	0.0091	-0.1269	1.00	0.0186
192	4.1	0.70	0.0106	-0.1218	1.00	0.0173
193	6.1	0.85	0.0149	-0.1161	1.00	0.0223
194	8.1	0.97	0.0197	-0.1040	1.00	0.0328
195	10.2	0.94	0.0497	-0.1098	1.00	--
196	11.0	0.90	0.0590	-0.1091	1.00	--
197	12.1	0.90	0.0714	-0.1079	1.00	--
198	13.2	0.94	0.0919	-0.1137	1.00	--
199	14.0	0.91	0.0987	-0.1120	1.00	--
200	15.1	0.90	0.1186	-0.1173	1.00	--
201	15.9	0.89	0.1387	-0.1256	0.99	--
202	17.0	0.88	0.1625	-0.1321	0.99	--
203	18.1	0.93	0.1915	-0.1401	0.99	--
204	19.2	0.93	0.2233	-0.1512	0.99	--
205	20.1	0.94	0.2557	-0.1628	1.00	--

Table B6. S814, LEGR, Re = 1.0 x 10⁶

RUN	AOA	C _I	C _{dp}	C _{m¼}	Re x 10 ⁻⁶	C _{dw}
206	21.9	0.92	0.3289	-0.1863	1.00	--
207	24.1	0.96	0.4131	-0.2115	0.99	--
208	26.1	1.01	0.4964	-0.2337	1.00	--
209	28.0	1.02	0.5568	-0.2428	1.00	--
210	30.1	1.15	0.6841	-0.2814	1.00	--
211	32.1	1.22	0.7831	-0.3082	1.00	--
212	34.0	1.27	0.8773	-0.3317	1.00	--
213	35.9	1.34	0.9875	-0.3630	0.99	--
214	38.1	1.36	1.0851	-0.3862	0.99	--
215	40.0	1.36	1.1510	-0.3977	0.98	--

End of Table B6

Table B7. S814, LEGR, Re = 1.25 x 10⁶

RUN	AOA	C _I	C _{dp}	C _{m^{1/4}}	Re x 10 ⁻⁶	C _{dw}
281	-20.2	-0.58	0.1949	-0.0169	1.24	--
280	-18.1	-0.50	0.1639	-0.0305	1.25	--
279	-16.1	-0.39	0.1352	-0.0445	1.24	--
278	-14.2	-0.30	0.1151	-0.0528	1.25	--
277	-12.1	-0.22	0.0985	-0.0572	1.25	--
276	-10.0	-0.13	0.0810	-0.0637	1.26	--
275	-8.1	-0.05	0.0667	-0.0681	1.26	--
274	-6.2	-0.01	0.0612	-0.0605	1.26	--
273	-4.0	-0.02	0.0563	-0.0443	1.26	--
272	-2.1	0.04	0.0129	-0.1083	1.24	0.0192
245	-0.1	0.29	0.0088	-0.1201	1.25	0.0168
271	-0.1	0.29	0.0090	-0.1214	1.25	0.0174
282	-0.1	0.27	0.0095	-0.1201	1.25	0.0158
246	2.1	0.51	0.0091	-0.1253	1.25	0.0166
247	4.1	0.71	0.0102	-0.1236	1.25	0.0171
248	6.1	0.86	0.0149	-0.1170	1.25	0.0202
249	8.2	0.99	0.0234	-0.1065	1.25	0.0300
250	10.0	0.93	0.0476	-0.1120	1.25	--
251	11.0	0.91	0.0586	-0.1085	1.25	--
252	12.1	0.90	0.0721	-0.1085	1.26	--
253	13.2	0.90	0.0887	-0.1118	1.26	--
254	14.0	0.90	0.1019	-0.1145	1.25	--
255	15.1	0.90	0.1216	-0.1206	1.25	--
256	16.2	0.88	0.1478	-0.1290	1.25	--
257	17.0	0.88	0.1659	-0.1340	1.25	--
258	18.1	0.91	0.1950	-0.1434	1.26	--
259	19.2	0.95	0.2243	-0.1527	1.26	--
260	20.1	0.93	0.2575	-0.1645	1.25	--

Table B7. S814, LEGR, Re = 1.25 x 10⁶

RUN	AOA	C _I	C _{dp}	C _{m¼}	Re x 10 ⁻⁶	C _{dw}
261	22.2	0.93	0.3394	-0.1904	1.26	--
262	24.1	0.98	0.4157	-0.2126	1.25	--
263	26.1	1.03	0.5006	-0.2355	1.24	--
264	28.0	1.04	0.5636	-0.2463	1.25	--
265	30.1	1.13	0.6782	-0.2791	1.23	--
266	32.1	1.22	0.7836	-0.3090	1.24	--
267	34.0	1.29	0.8825	-0.3370	1.23	--
268	35.9	1.34	0.9853	-0.3632	1.23	--
269	38.1	1.36	1.0810	-0.3851	1.22	--
270	39.9	1.39	1.1772	-0.4140	1.21	--

End of Table B7

Table B8. S814, LEGR, $Re = 1.5 \times 10^6$

RUN	AOA	C _l	C _{dp}	C _{m^{1/4}}	Re x 10 ⁻⁶	C _{dw}
227	-20.3	-0.59	0.1984	-0.0163	1.49	--
226	-18.1	-0.48	0.1623	-0.0330	1.49	--
225	-16.1	-0.38	0.1357	-0.0452	1.49	--
224	-14.2	-0.29	0.1162	-0.0532	1.49	--
223	-12.2	-0.22	0.1012	-0.0556	1.51	--
222	-10.0	-0.13	0.0865	-0.0586	1.52	--
221	-8.1	-0.04	0.0679	-0.0685	1.51	--
220	-6.2	-0.01	0.0627	-0.0591	1.50	--
219	-4.2	-0.07	0.0541	-0.0535	1.51	--
218	-2.1	0.04	0.0126	-0.1077	1.51	0.0180
217	-0.1	0.30	0.0076	-0.1199	1.51	0.0153
244	0.0	0.31	0.0074	-0.1212	1.50	0.0151
228	0.1	0.31	0.0080	-0.1204	1.51	0.0159
229	2.0	0.51	0.0078	-0.1234	1.51	0.0179
230	4.1	0.72	0.0085	-0.1228	1.51	0.0174
231	6.1	0.87	0.0125	-0.1166	1.51	0.0207
232	8.1	0.99	0.0172	-0.1047	1.50	0.0304
233	10.2	0.93	0.0486	-0.1127	1.50	--
234	11.0	0.90	0.0601	-0.1117	1.51	--
235	12.1	0.89	0.0721	-0.1095	1.50	--
236	13.2	0.89	0.0881	-0.1122	1.50	--
237	14.0	0.90	0.1008	-0.1153	1.51	--
238	15.1	0.89	0.1239	-0.1224	1.50	--
239	16.1	0.88	0.1446	-0.1285	1.50	--
240	17.0	0.89	0.1693	-0.1383	1.50	--
241	18.1	0.90	0.1934	-0.1435	1.49	--
242	19.0	0.91	0.2223	-0.1533	1.51	--
243	20.0	0.88	0.2595	-0.1649	1.50	--

End of Table B8

S814

Pressure Distributions, Steady State, Re = 0.75 million

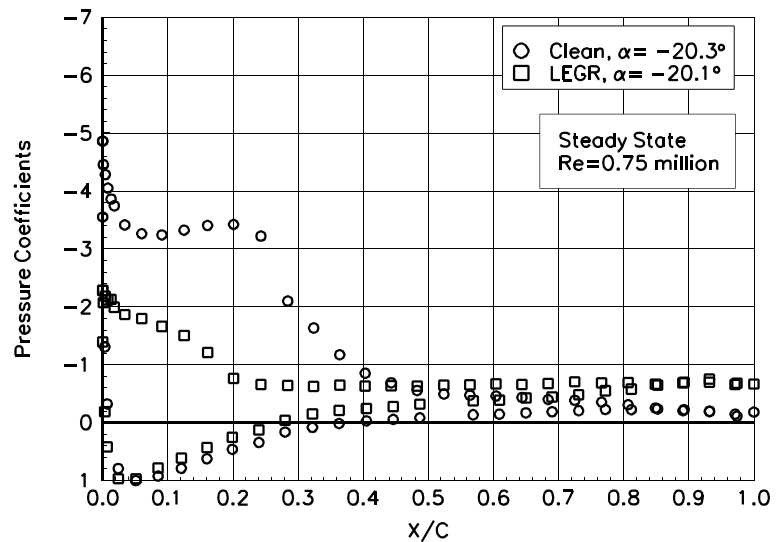


Figure 1. $\alpha = -20.3^\circ$

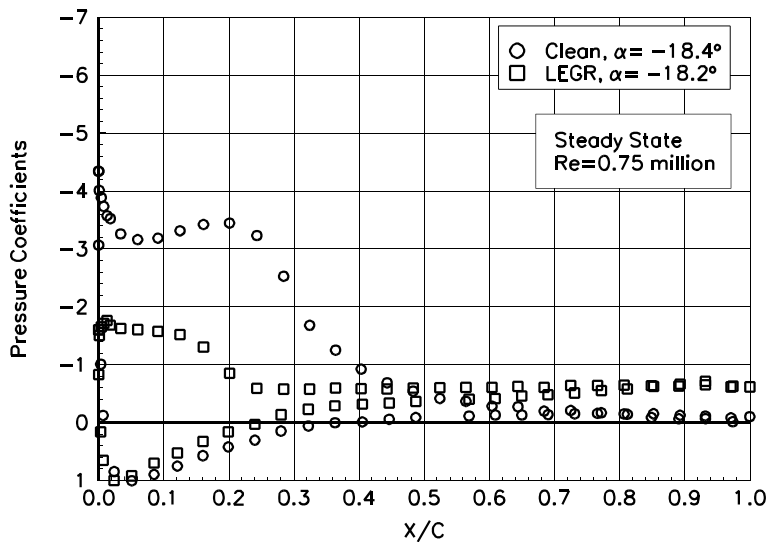


Figure 2. $\alpha = -18.4^\circ$

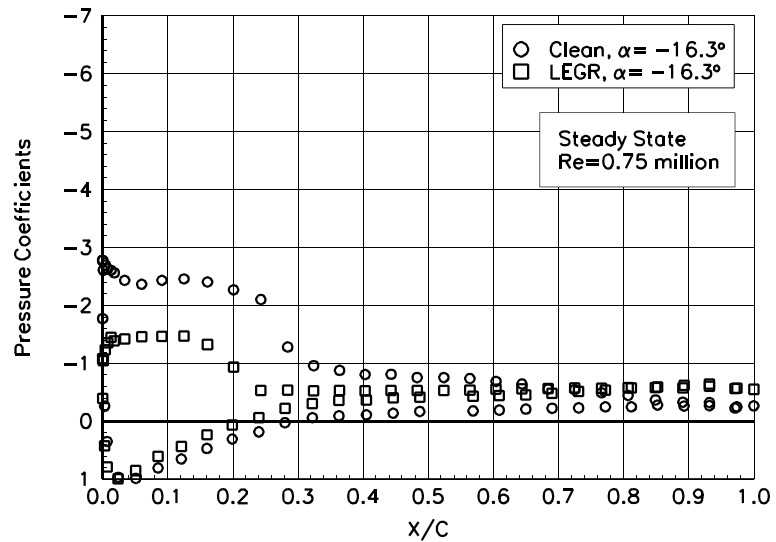


Figure 3. $\alpha = -16.3^\circ$

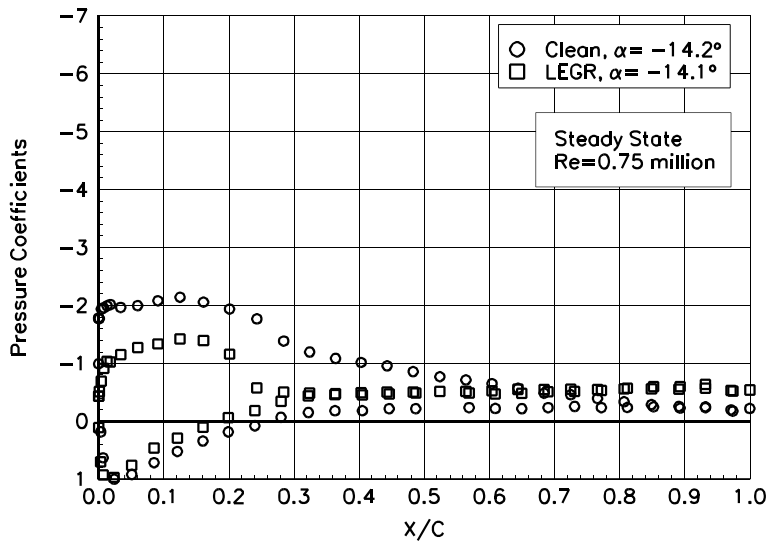


Figure 4. $\alpha = -14.2^\circ$

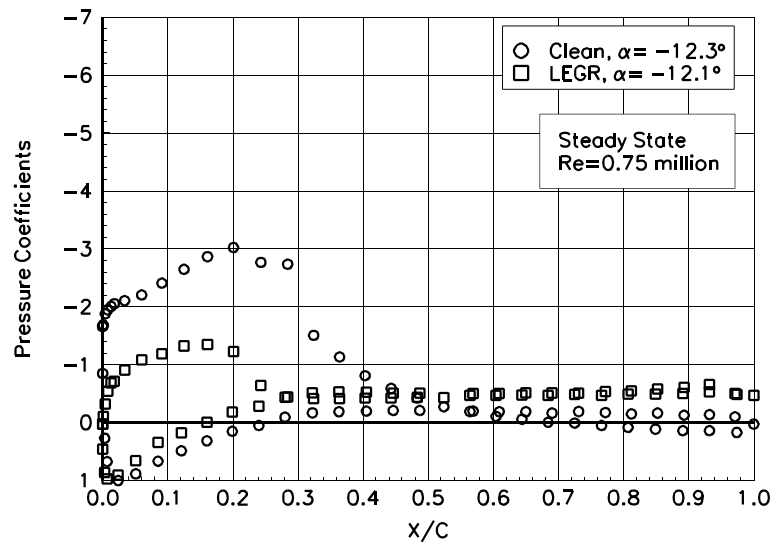


Figure 5. $\alpha = -12.3^\circ$

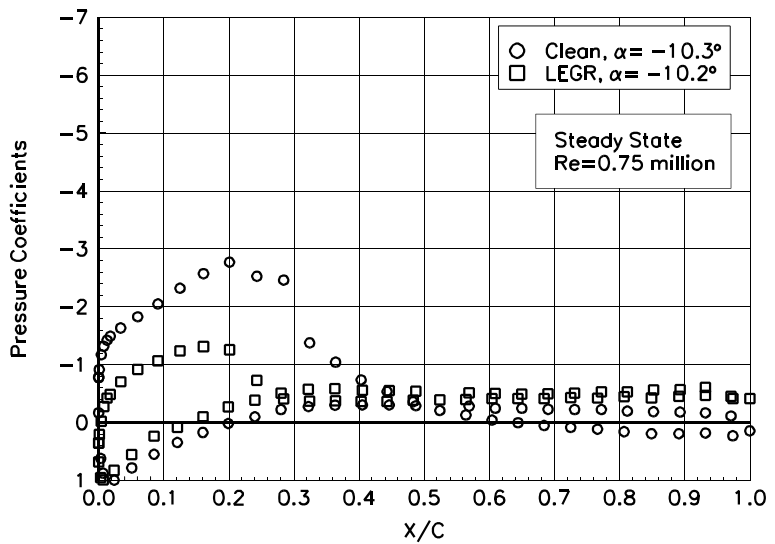


Figure 6. $\alpha = -10.3^\circ$

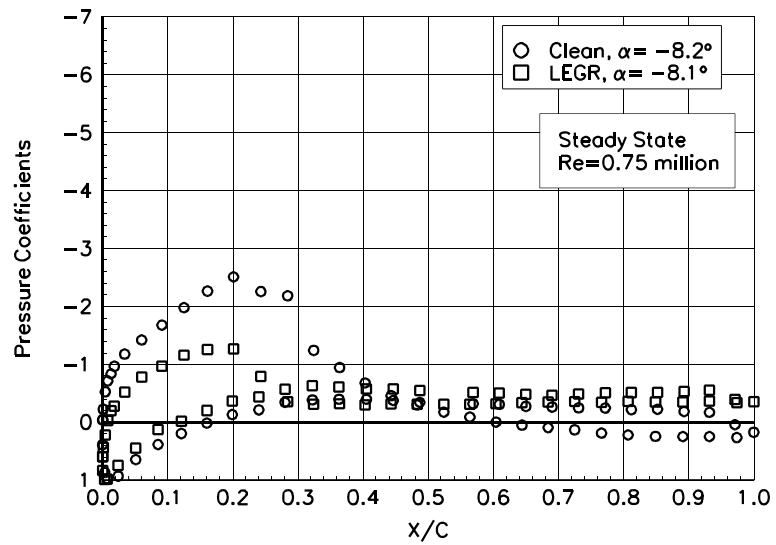


Figure 7. $\alpha = -8.2^\circ$

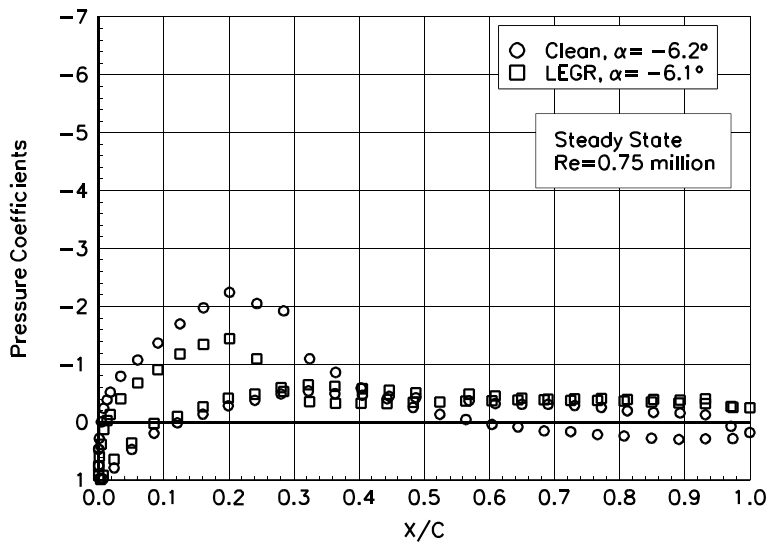


Figure 8. $\alpha = -6.2^\circ$

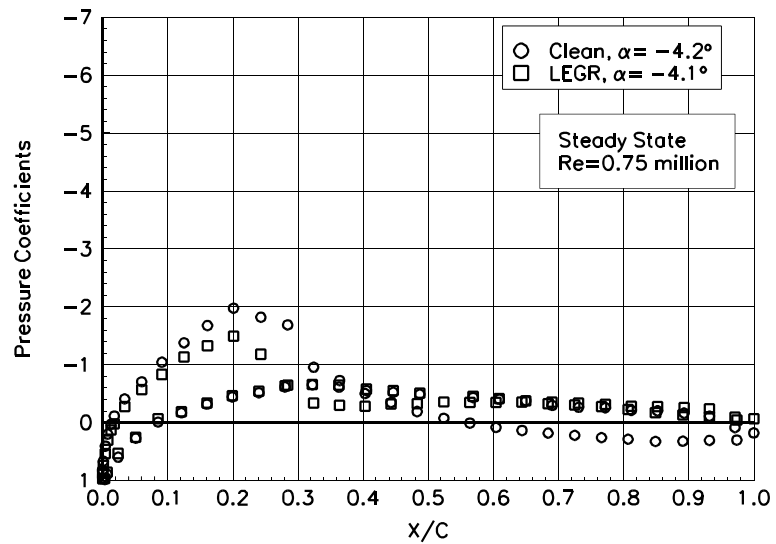


Figure 9. $\alpha = -4.2^\circ$

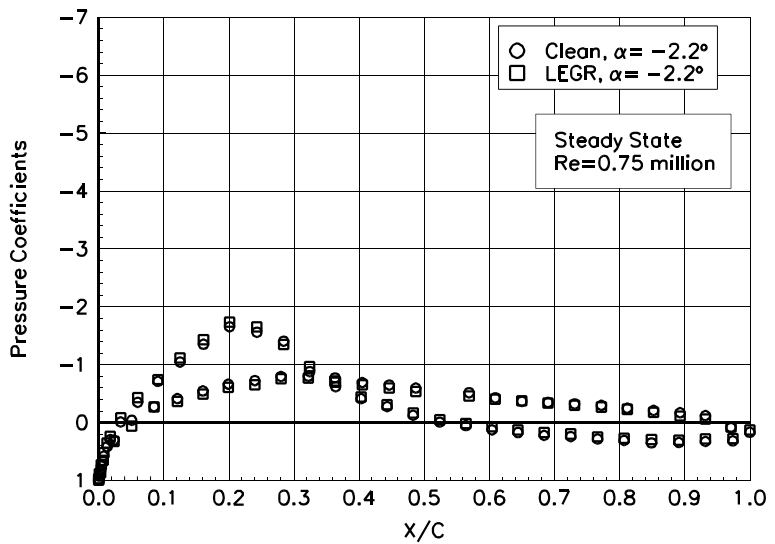


Figure 10. $\alpha = -2.2^\circ$

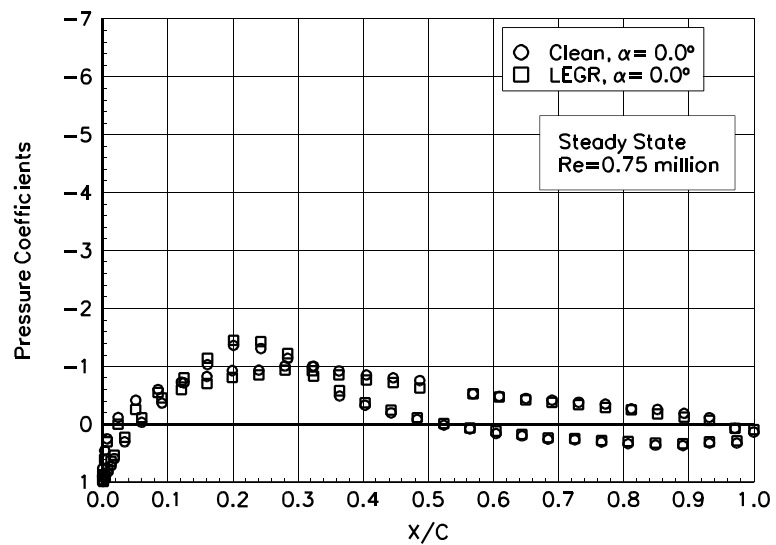


Figure 11. $\alpha = 0.0^\circ$

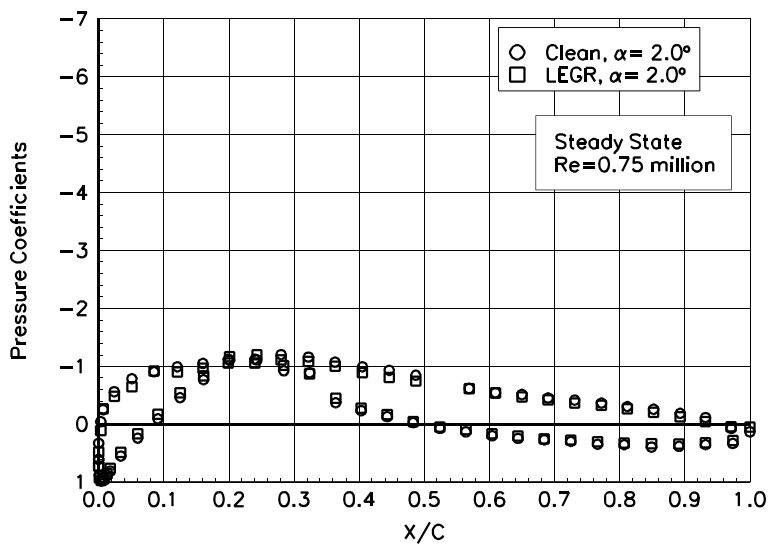


Figure 12. $\alpha = 2.0^\circ$

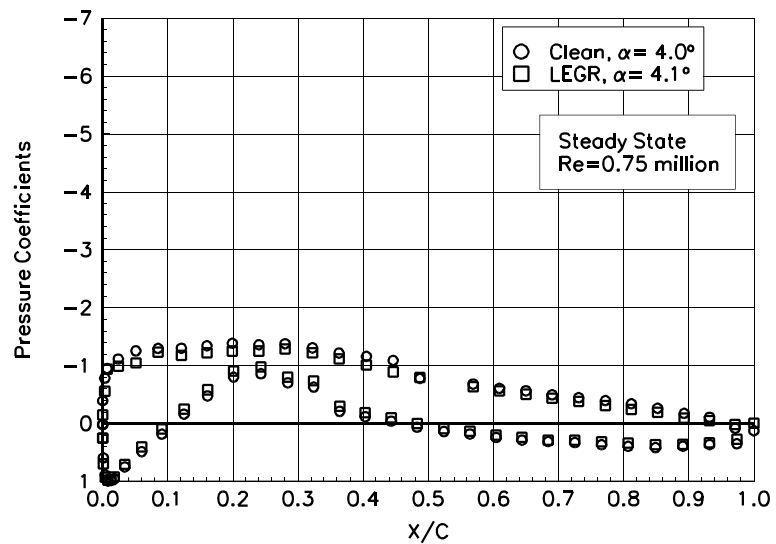


Figure 13. $\alpha = 4.0^\circ$

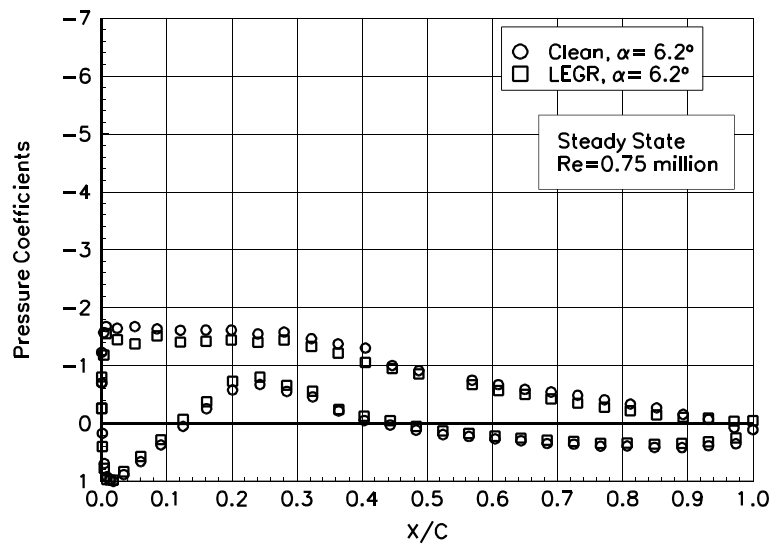


Figure 14. $\alpha = 6.2^\circ$

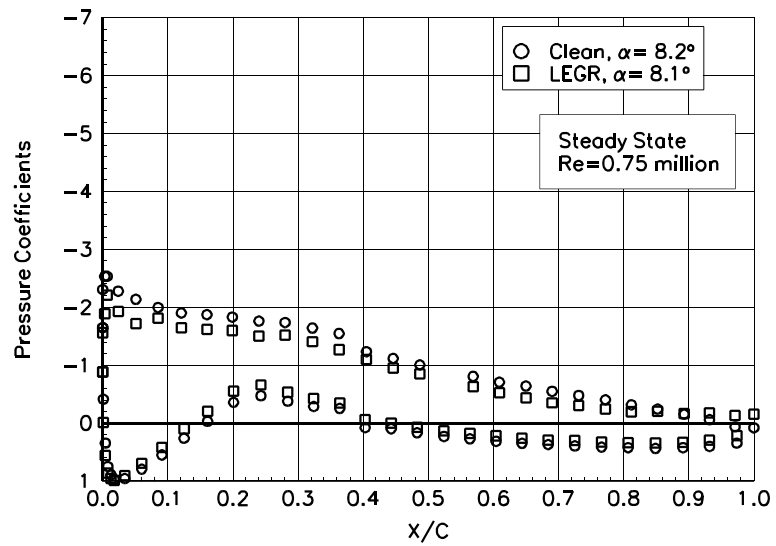


Figure 15. $\alpha = 8.2^\circ$

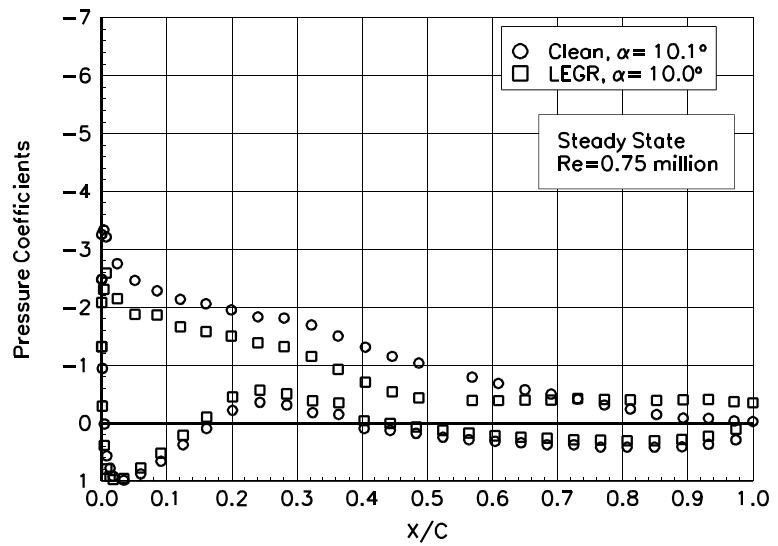


Figure 16. $\alpha = 10.1^\circ$

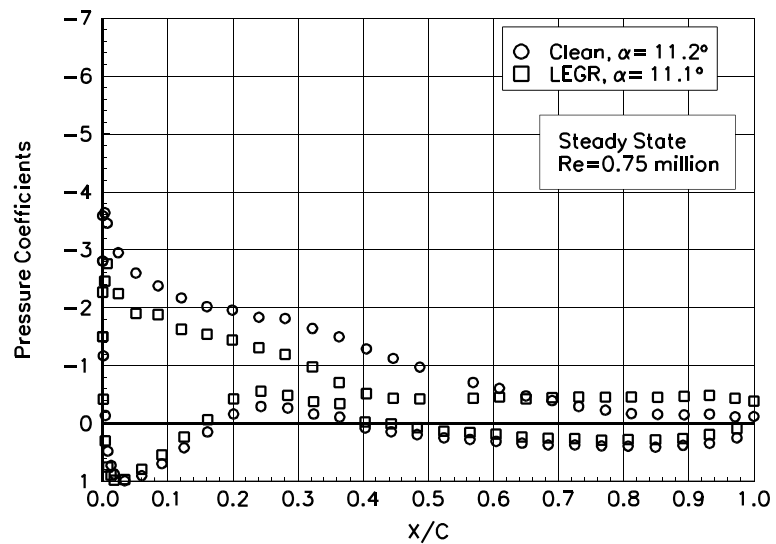


Figure 17. $\alpha = 11.2^\circ$

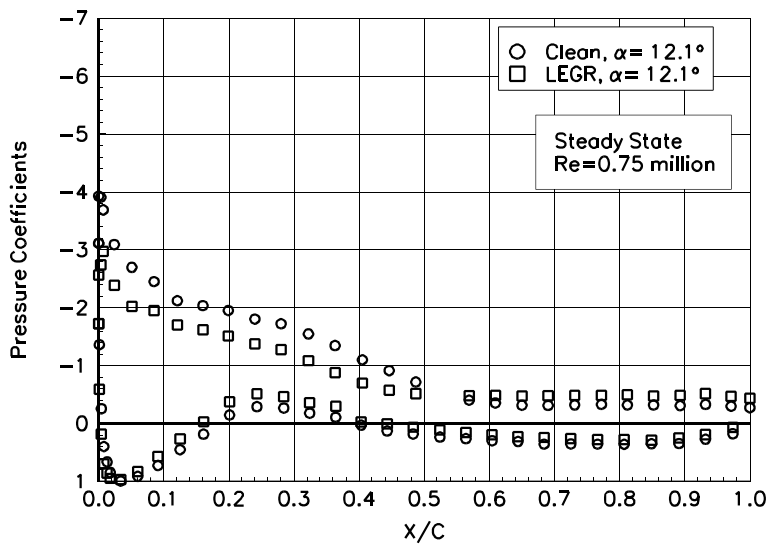


Figure 18. $\alpha = 12.1^\circ$

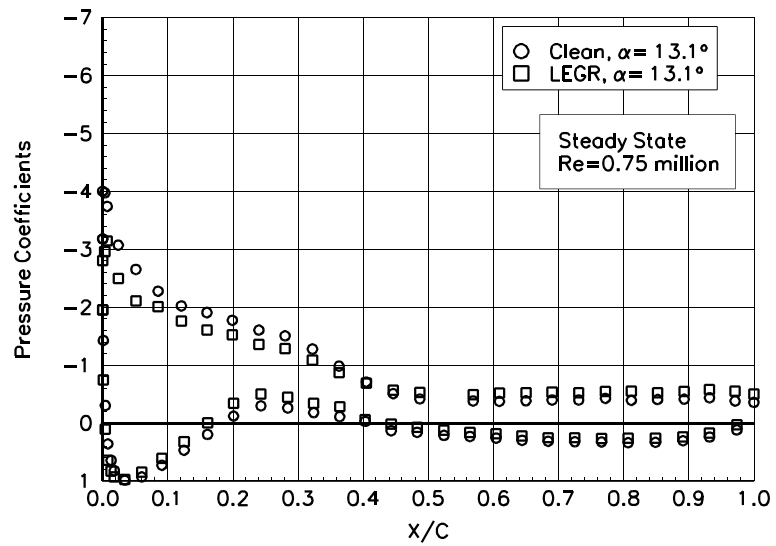


Figure 19. $\alpha = 13.1^\circ$

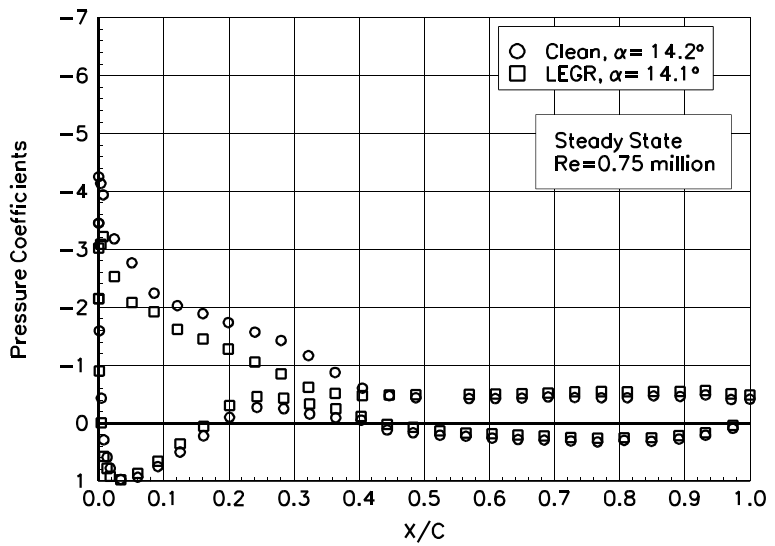


Figure 20. $\alpha = 14.2^\circ$

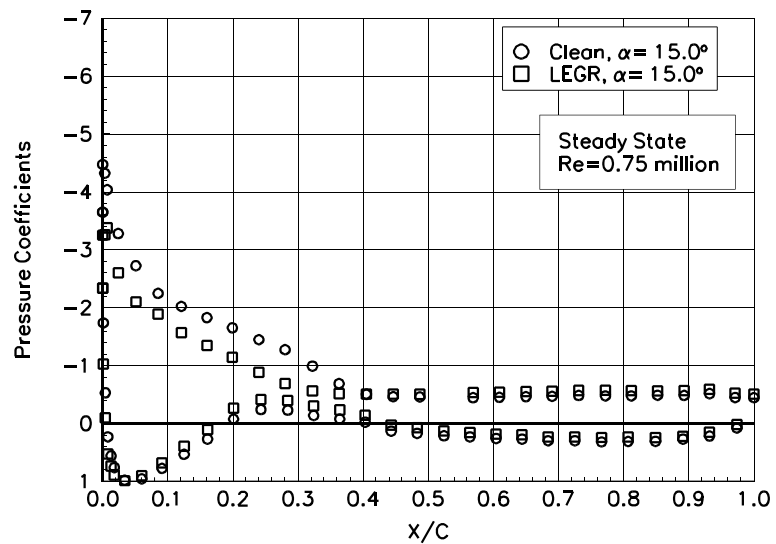


Figure 21. $\alpha = 15.0^\circ$

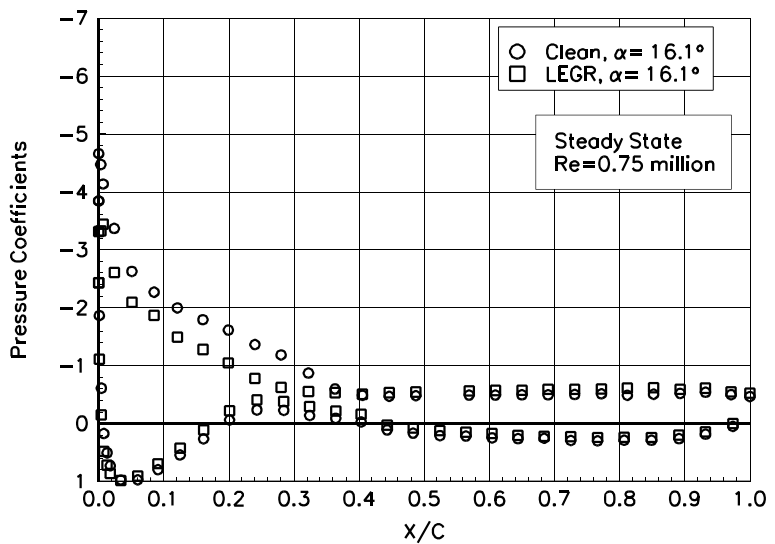


Figure 22. $\alpha = 16.1^\circ$

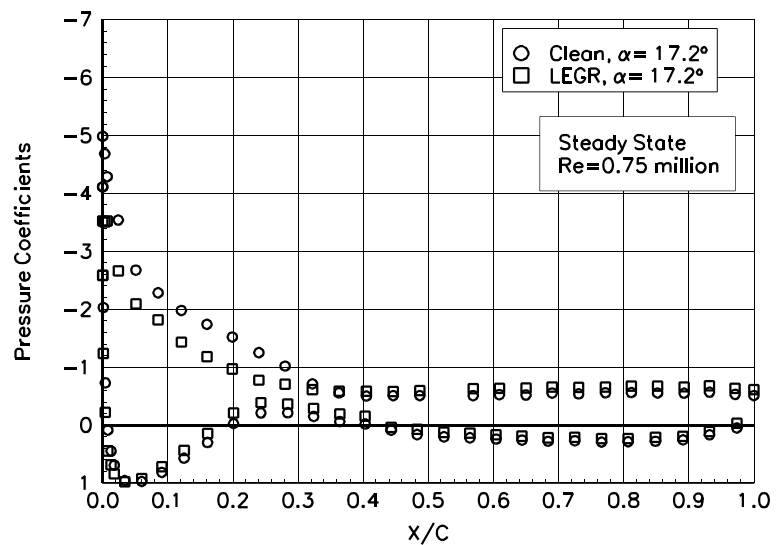


Figure 23. $\alpha = 17.2^\circ$

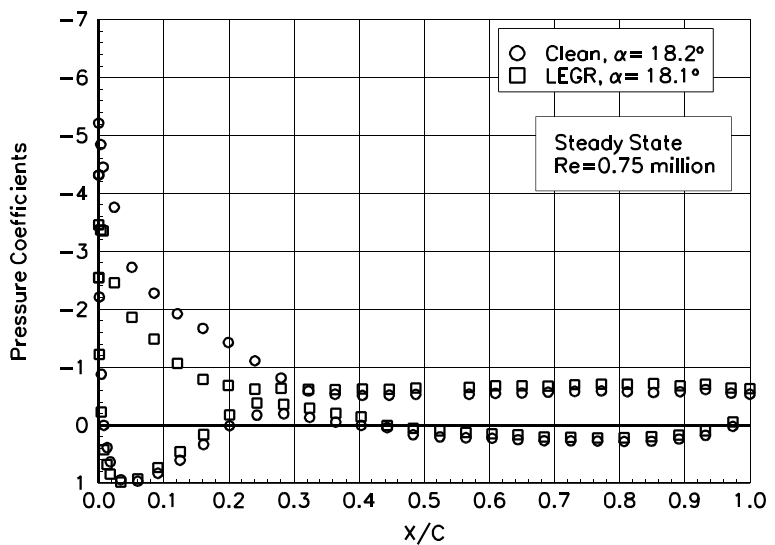


Figure 24. $\alpha = 18.2^\circ$

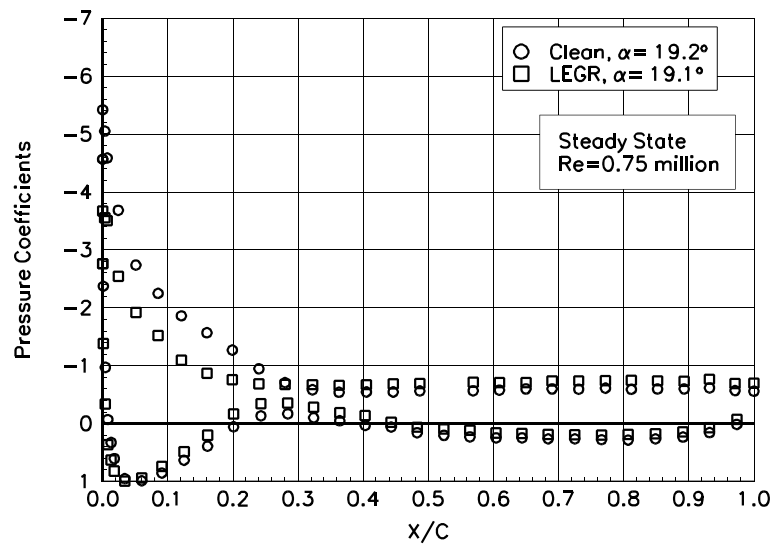


Figure 25. $\alpha = 19.2^\circ$

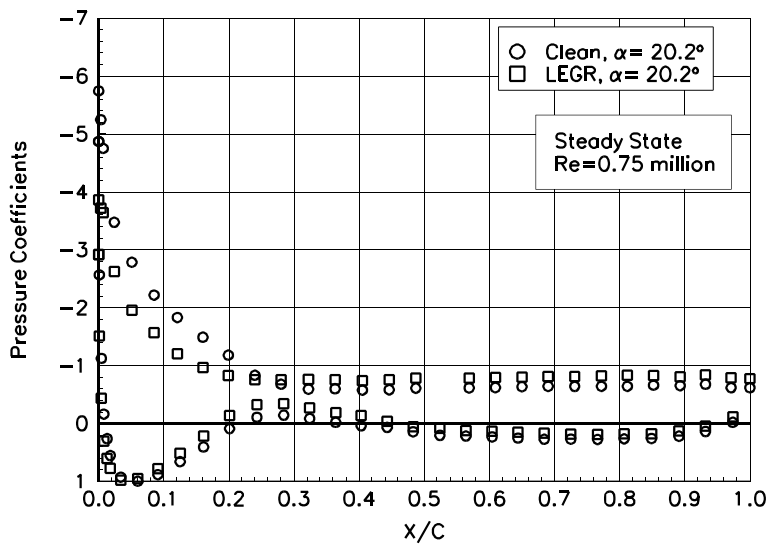


Figure 26. $\alpha = 20.2^\circ$

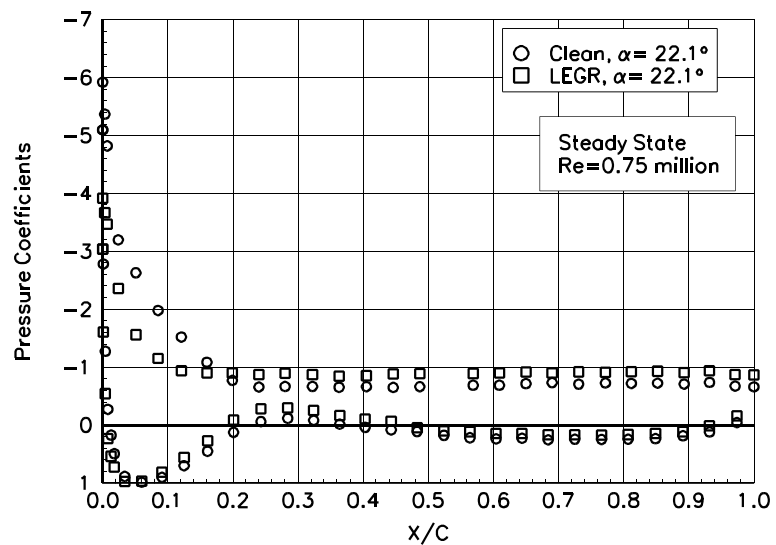


Figure 27. $\alpha = 22.1^\circ$

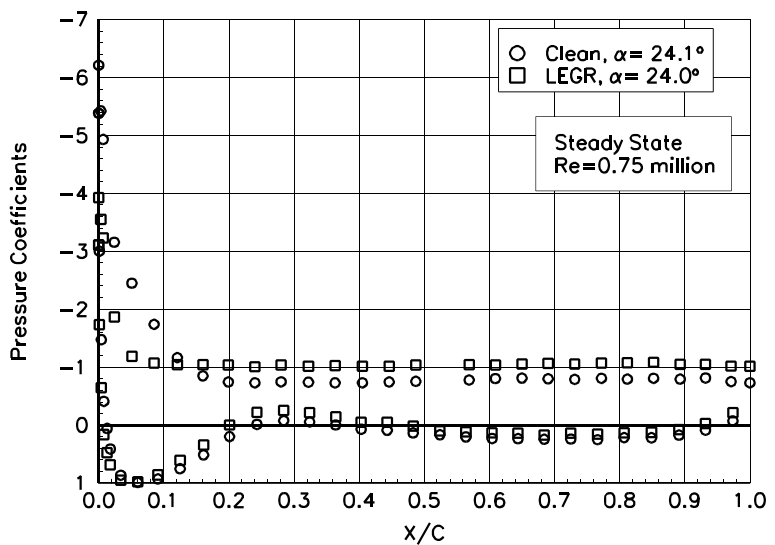


Figure 28. $\alpha = 24.1^\circ$

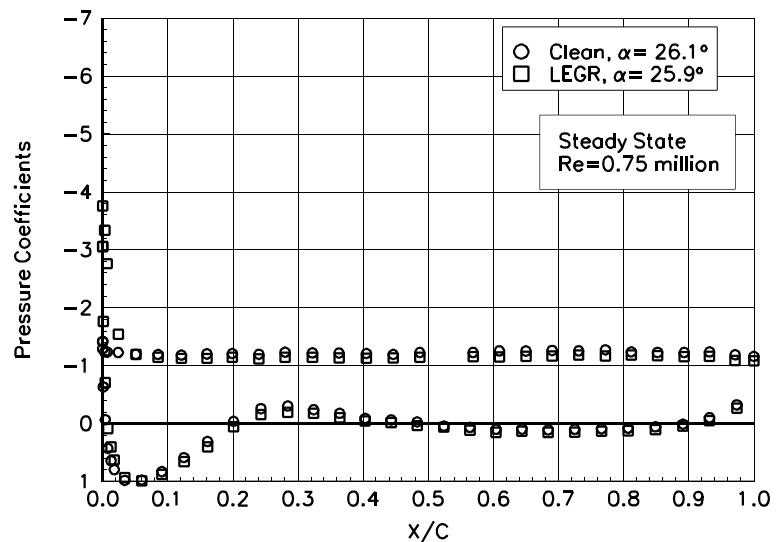


Figure 29. $\alpha = 26.1^\circ$

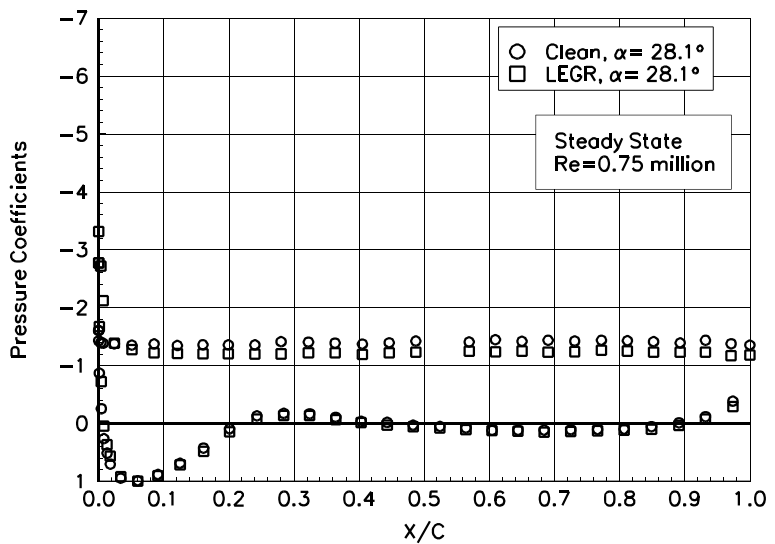


Figure 30. $\alpha = 28.1^\circ$

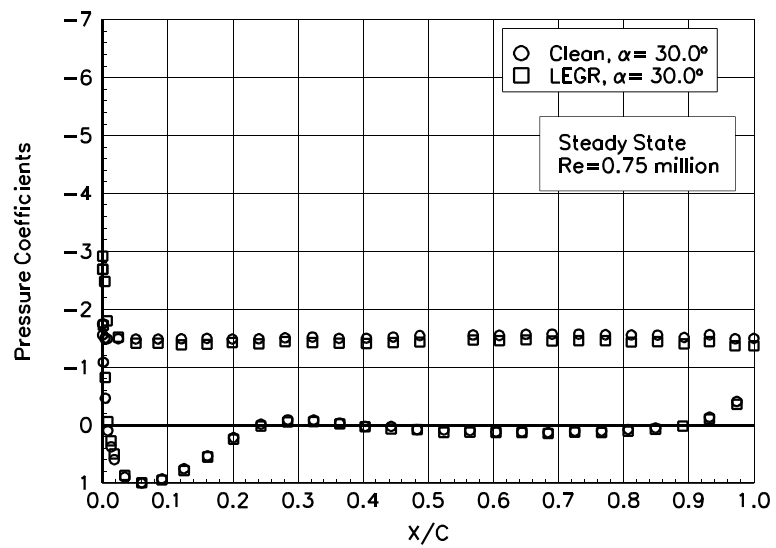


Figure 31. $\alpha = 30.0^\circ$

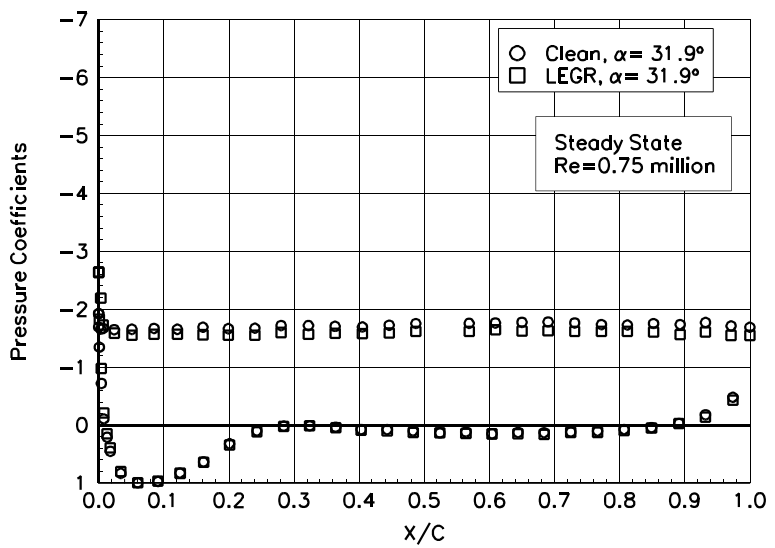


Figure 32. $\alpha = 31.9^\circ$

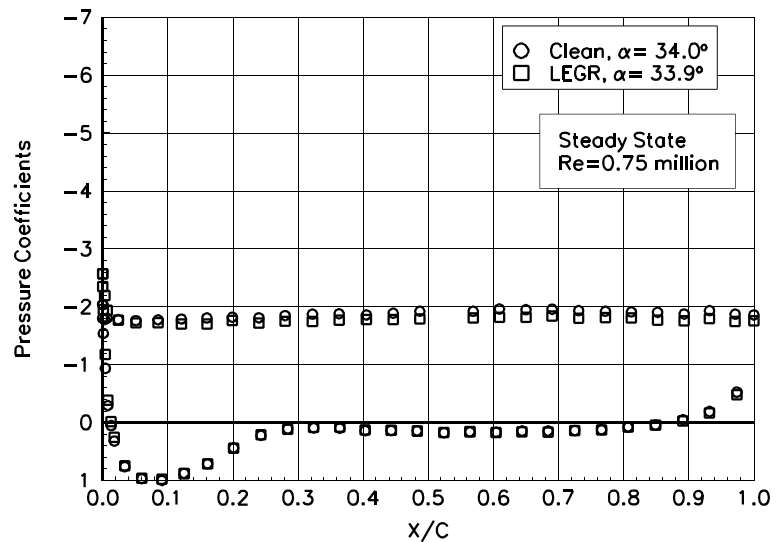


Figure 33. $\alpha = 34.0^\circ$

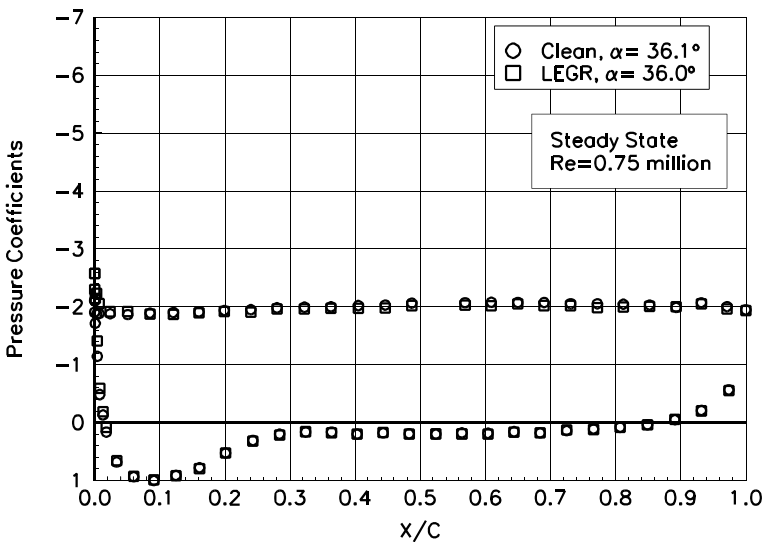


Figure 34. $\alpha = 36.1^\circ$

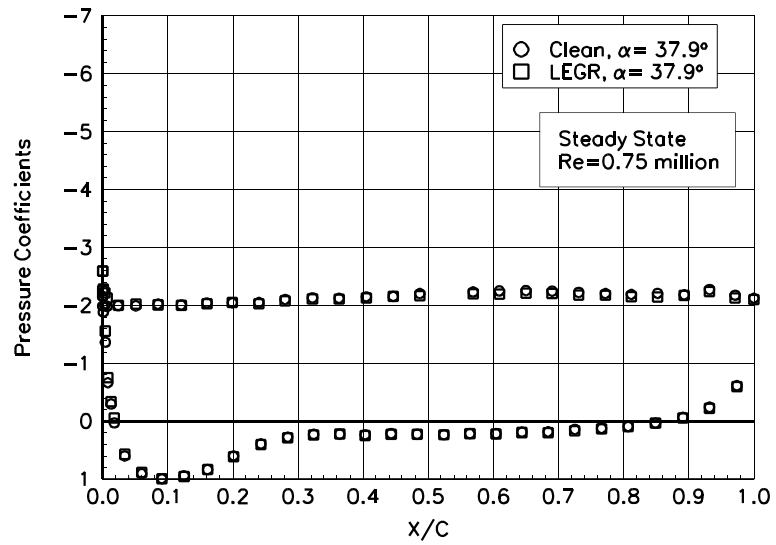


Figure 35. $\alpha = 37.9^\circ$

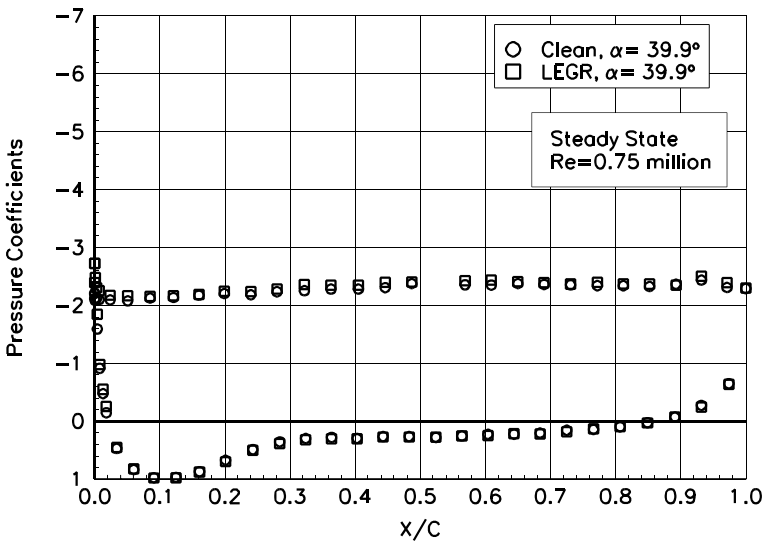


Figure 36. $\alpha = 39.9^\circ$

S814

Pressure Distributions, Steady State, Re = 1 million

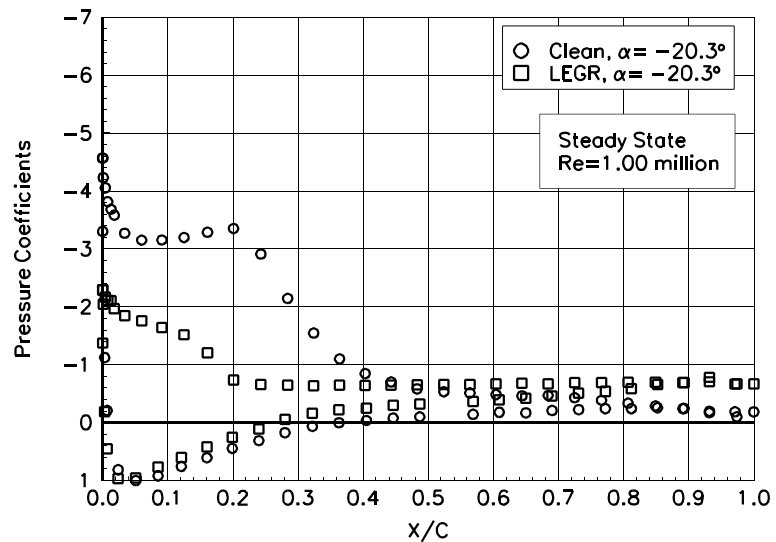


Figure 37. $\alpha = -20.3^\circ$

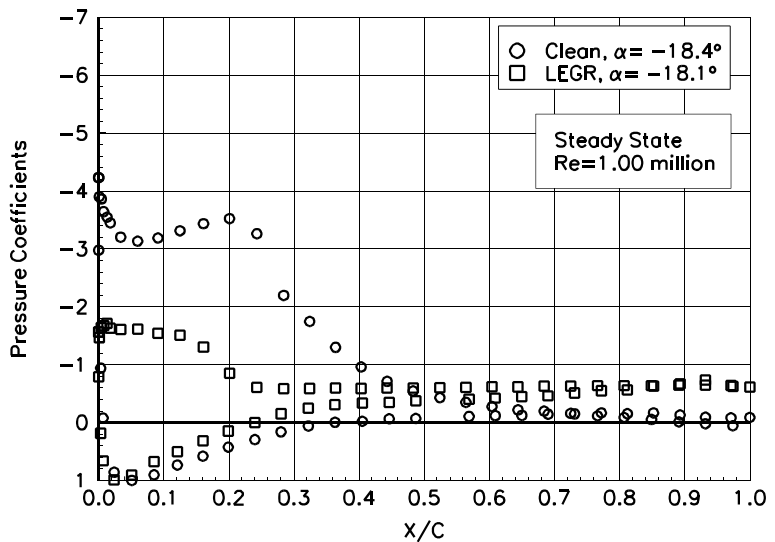


Figure 38. $\alpha = -18.4^\circ$

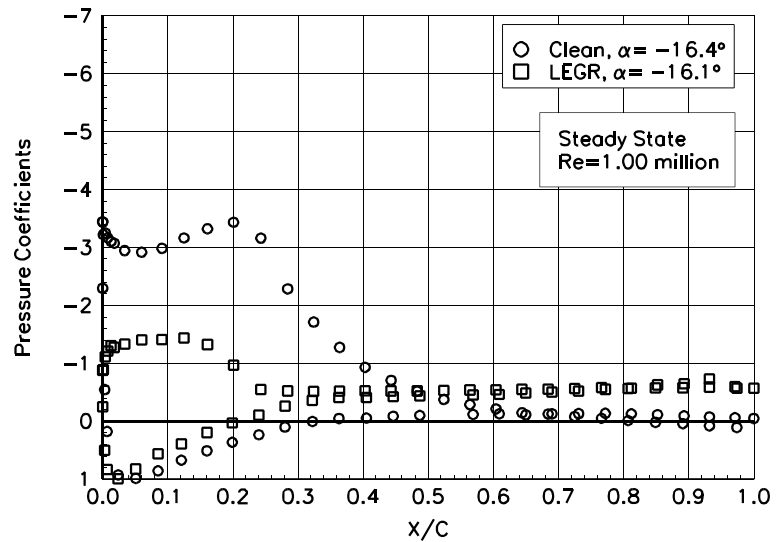


Figure 39. $\alpha = -16.4^\circ$

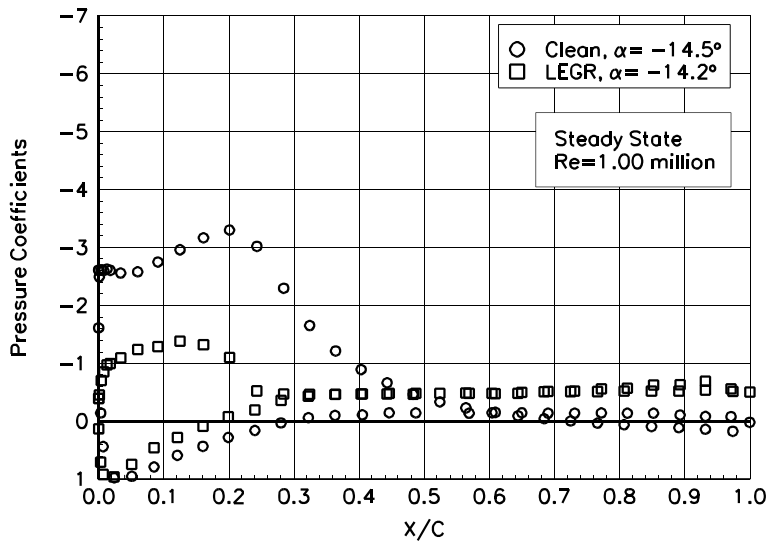


Figure 40. $\alpha = -14.5^\circ$

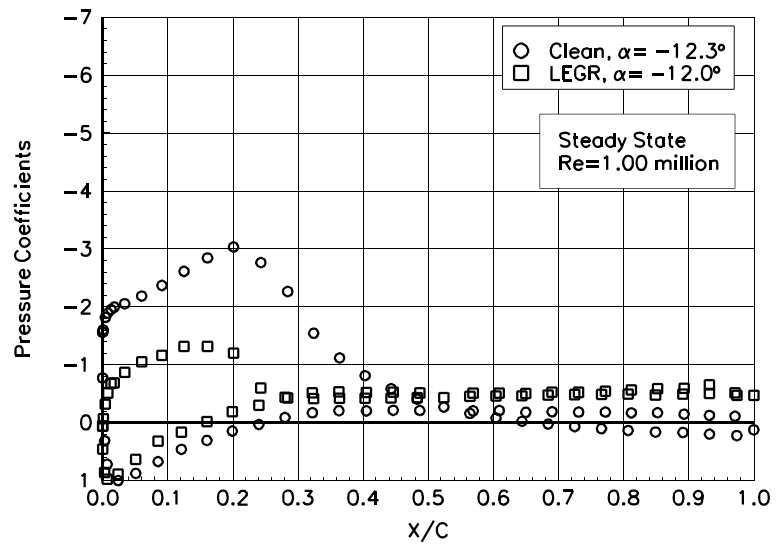


Figure 41. $\alpha = -12.3^\circ$

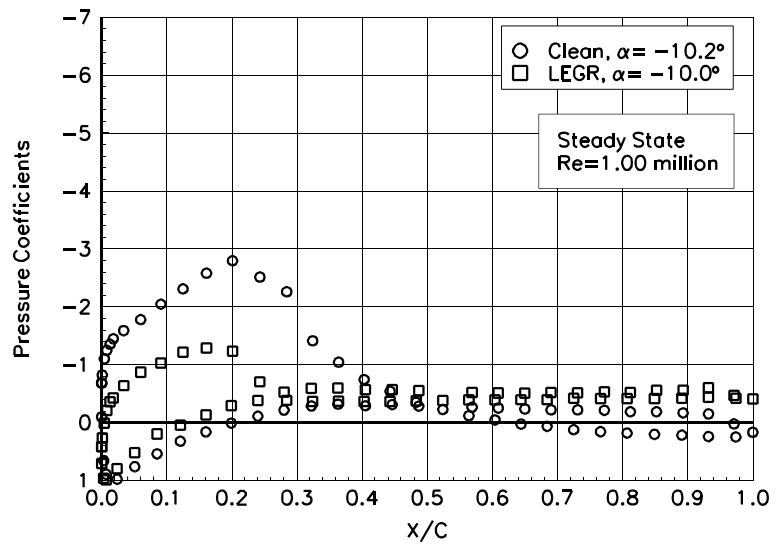


Figure 42. $\alpha = -10.2^\circ$

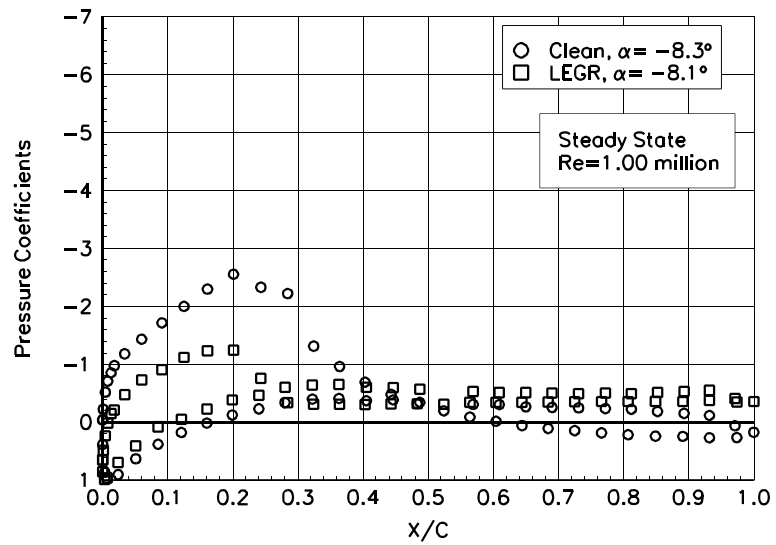


Figure 43. $\alpha = -8.3^\circ$

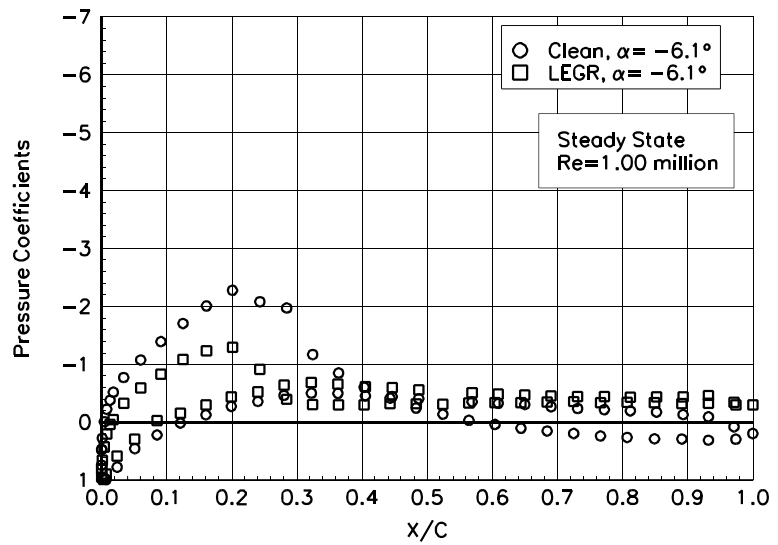


Figure 44. $\alpha = -6.1^\circ$

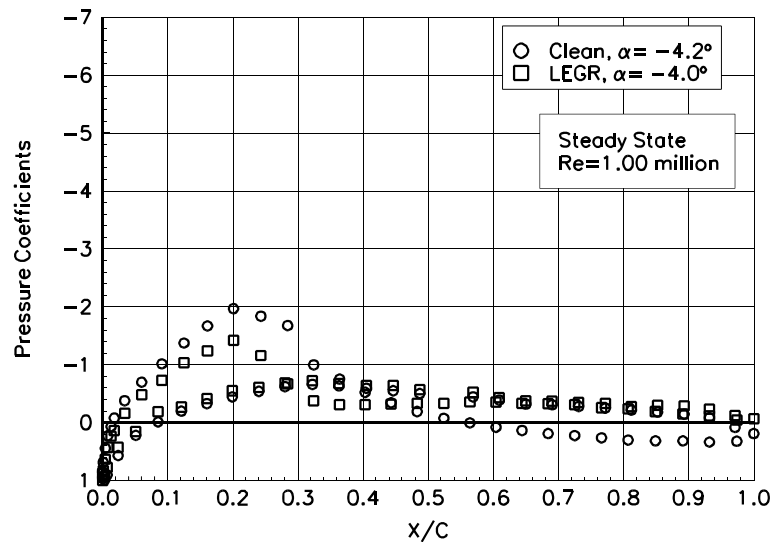


Figure 45. $\alpha = -4.2^\circ$

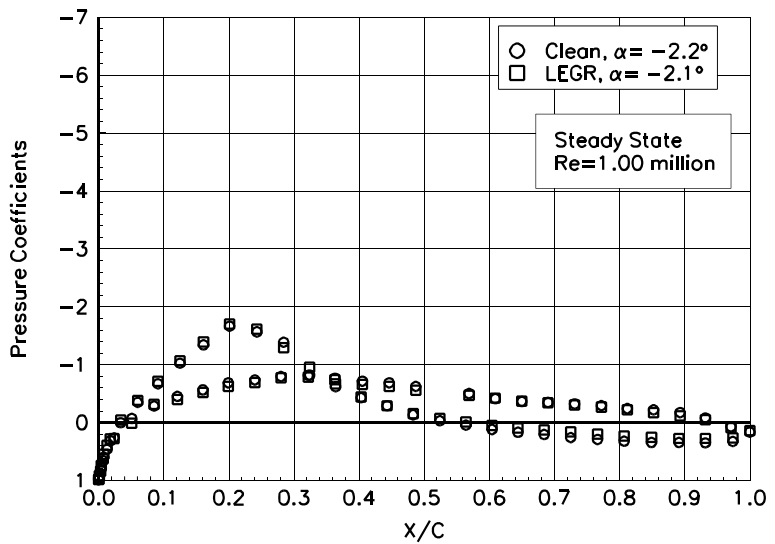


Figure 46. $\alpha = -2.2^\circ$

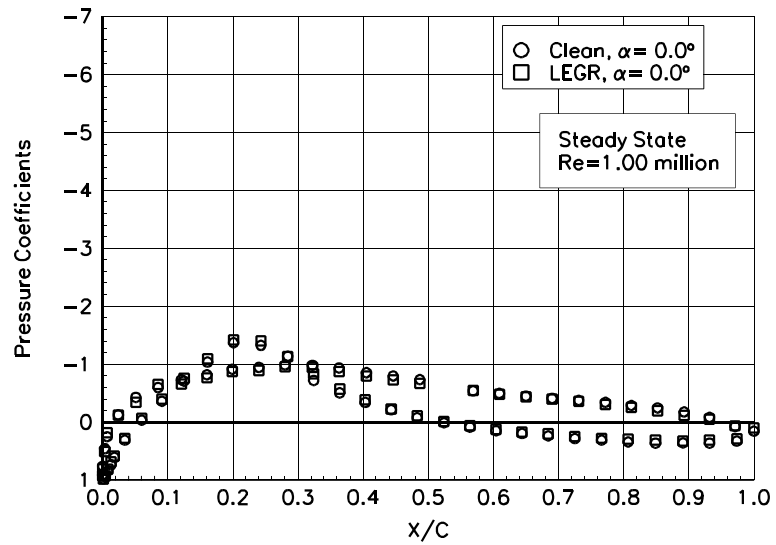


Figure 47. $\alpha = 0.0^\circ$

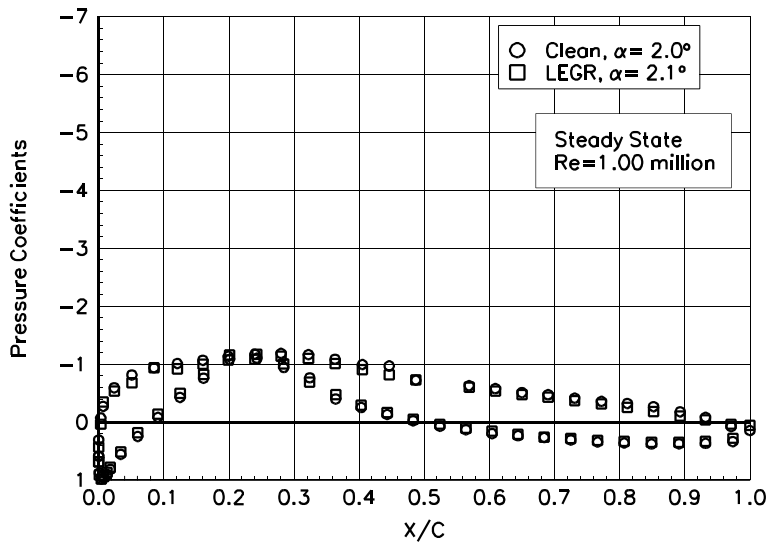


Figure 48. $\alpha = 2.0^\circ$

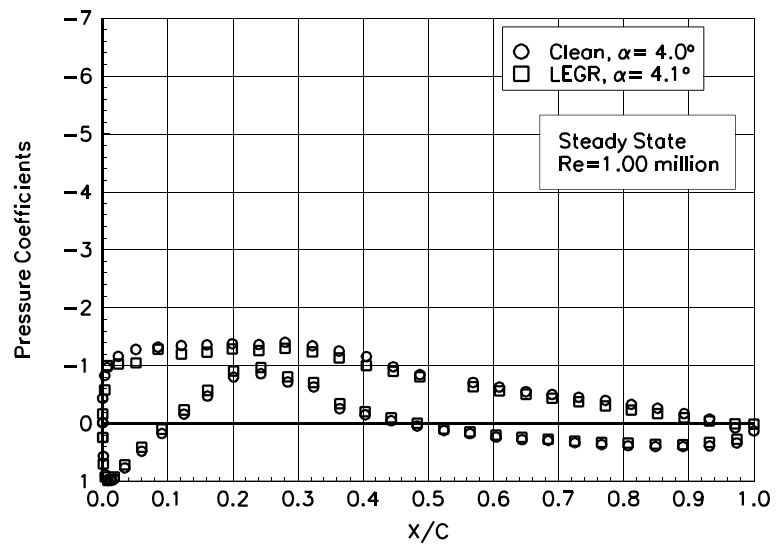


Figure 49. $\alpha = 4.0^\circ$

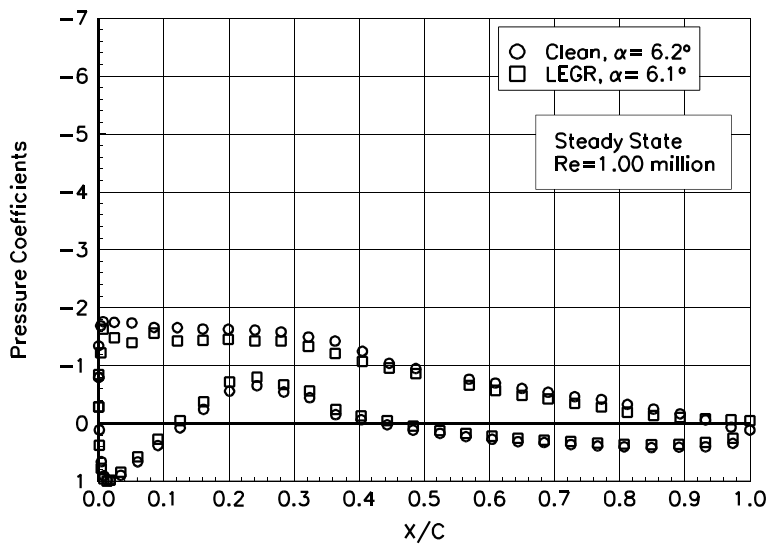


Figure 50. $\alpha = 6.2^\circ$

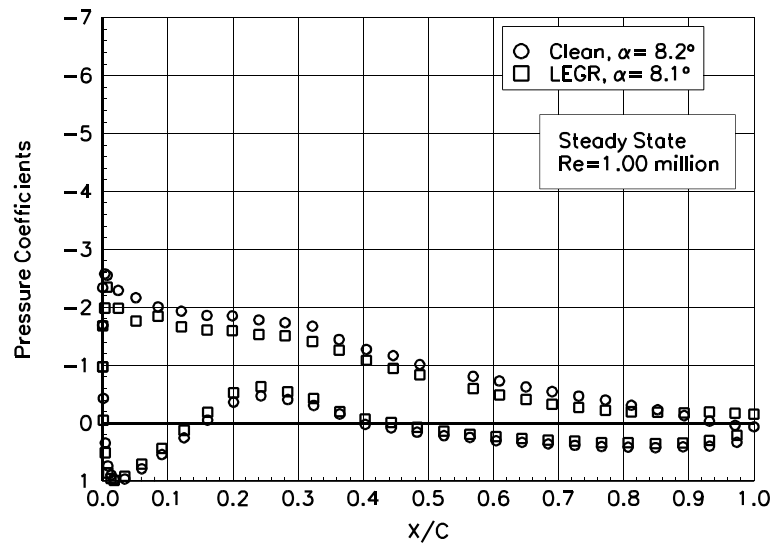


Figure 51. $\alpha = 8.2^\circ$

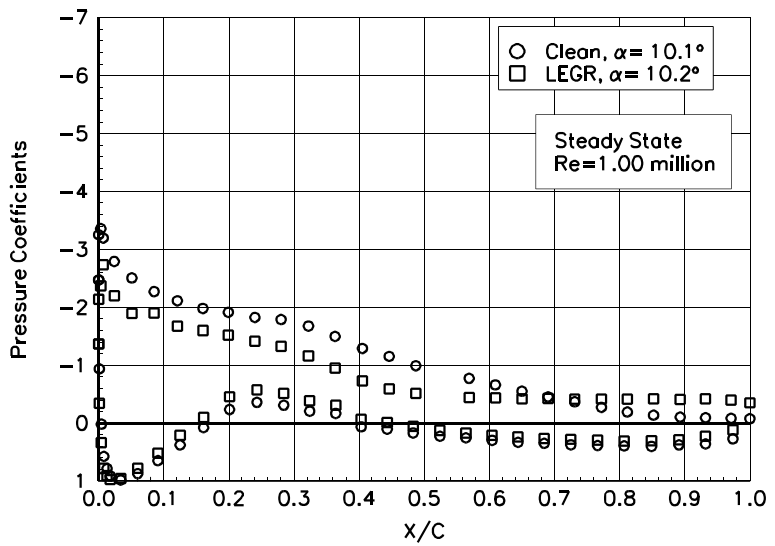


Figure 52. $\alpha = 10.1^\circ$

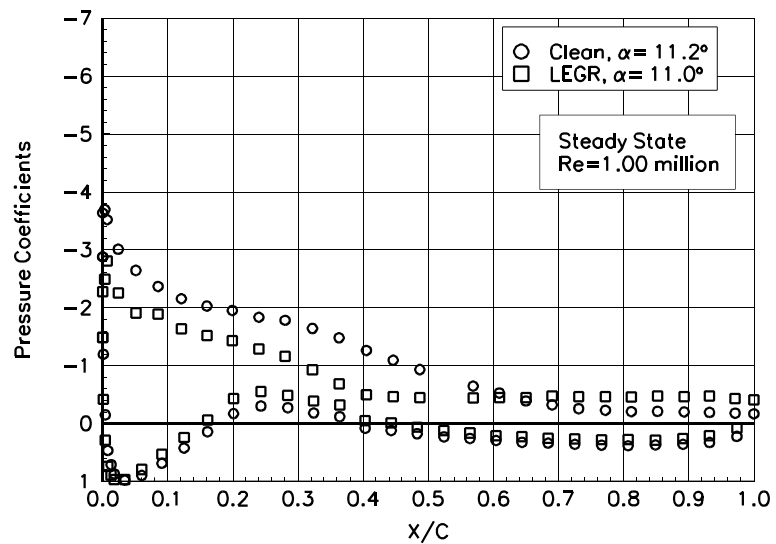


Figure 53. $\alpha = 11.2^\circ$

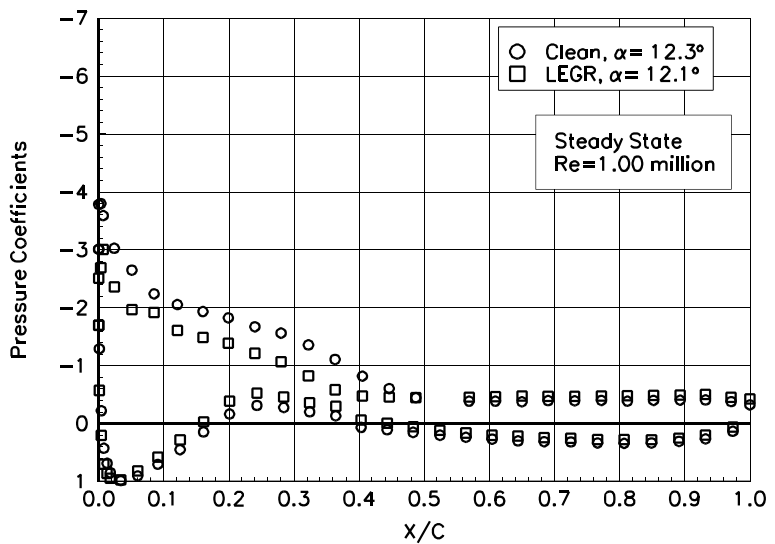


Figure 54. $\alpha = 12.3^\circ$

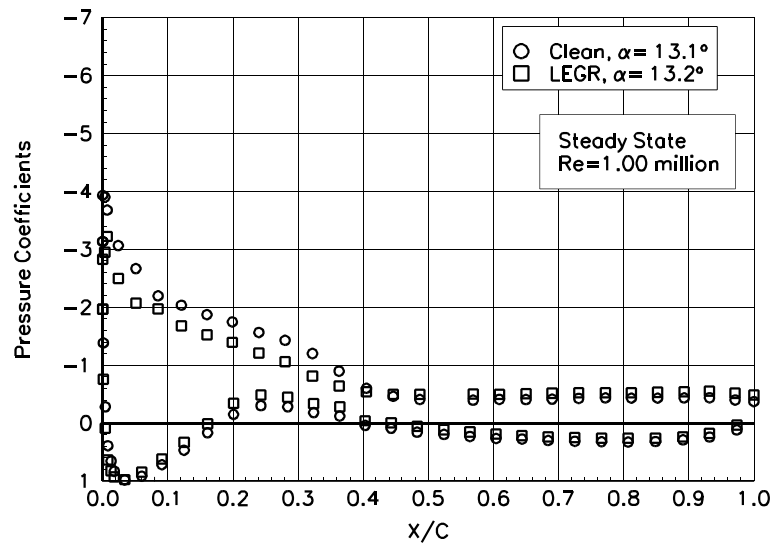


Figure 55. $\alpha = 13.1^\circ$

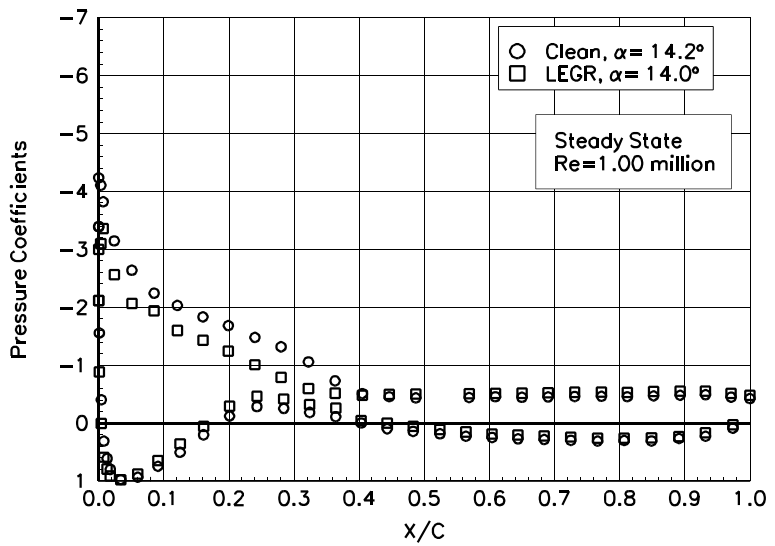


Figure 56. $\alpha = 14.2^\circ$

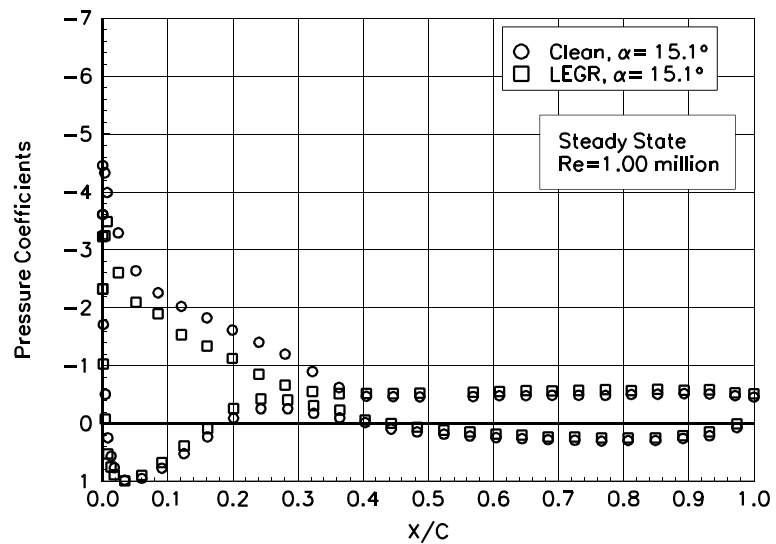


Figure 57. $\alpha = 15.1^\circ$

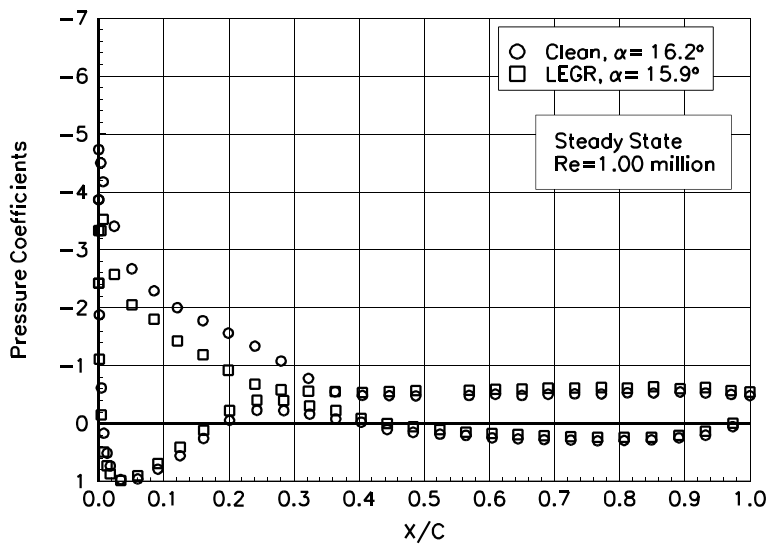


Figure 58. $\alpha = 16.2^\circ$

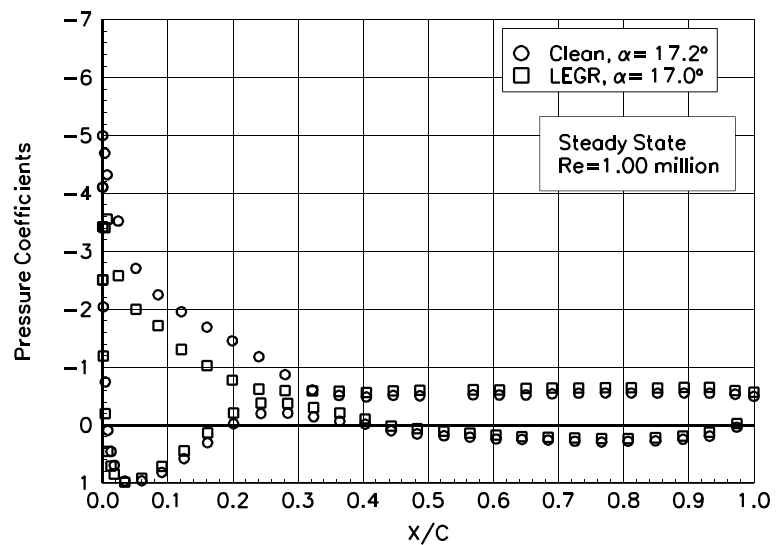


Figure 59. $\alpha = 17.2^\circ$

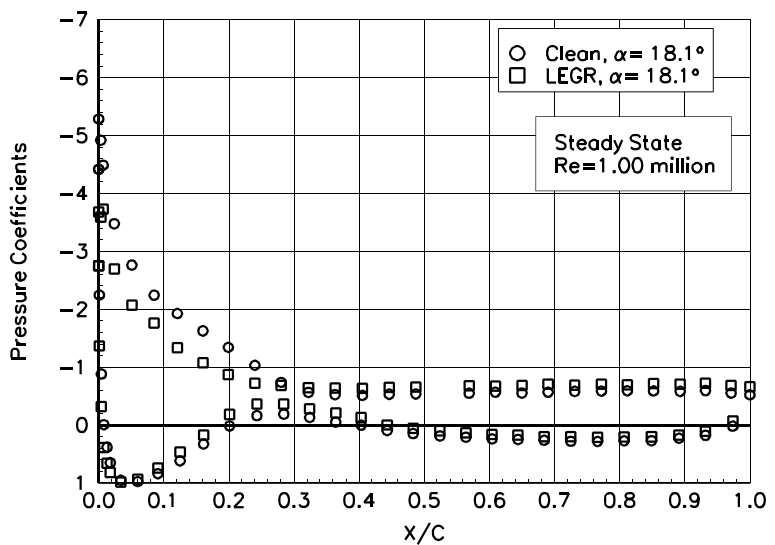


Figure 60. $\alpha = 18.1^\circ$

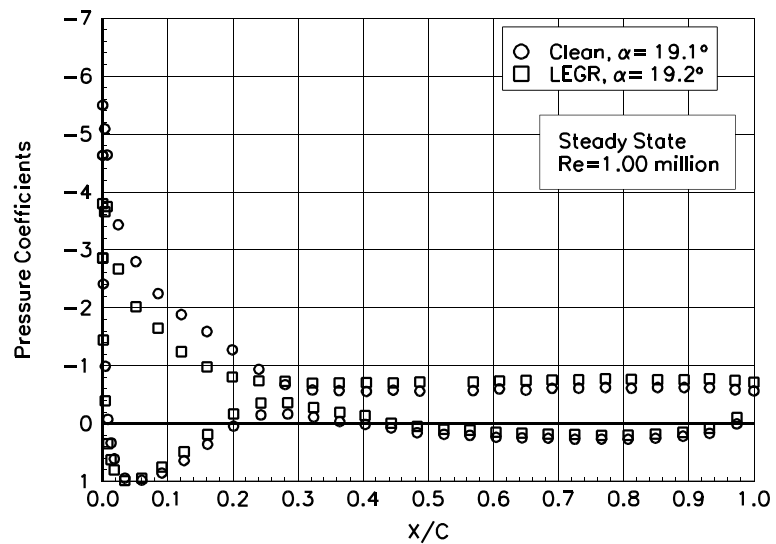


Figure 61. $\alpha = 19.1^\circ$

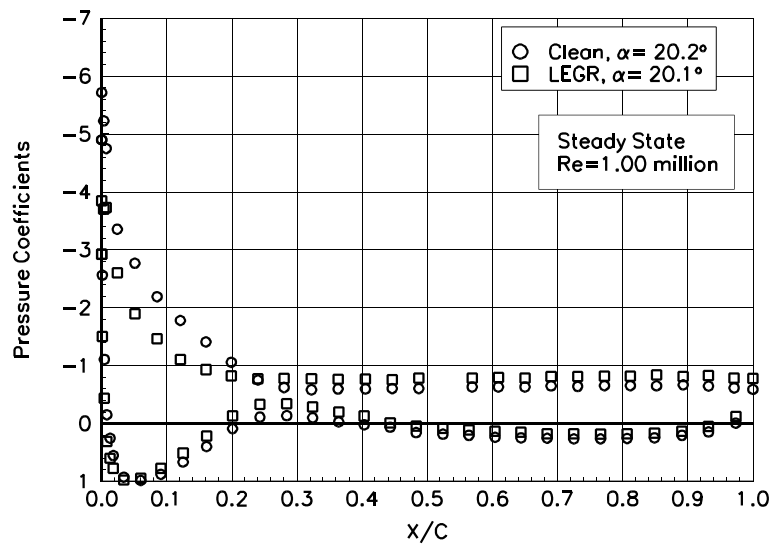


Figure 62. $\alpha = 20.2^\circ$

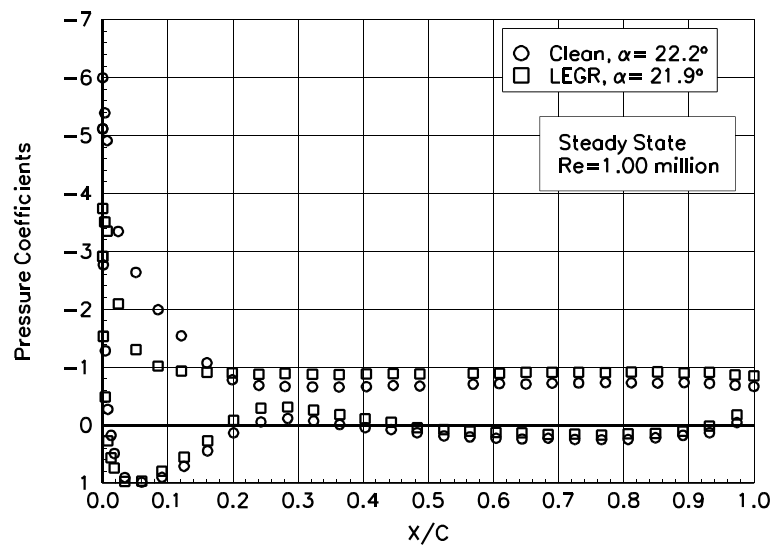


Figure 63. $\alpha = 22.2^\circ$

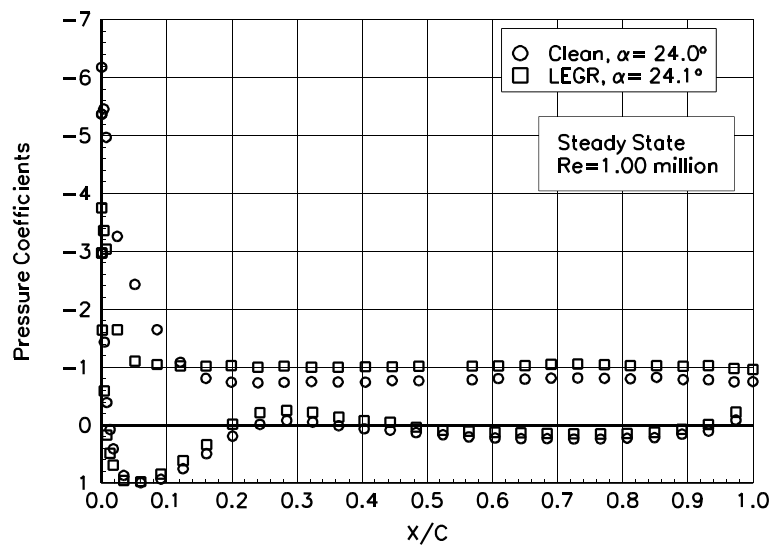


Figure 64. $\alpha = 24.0^\circ$

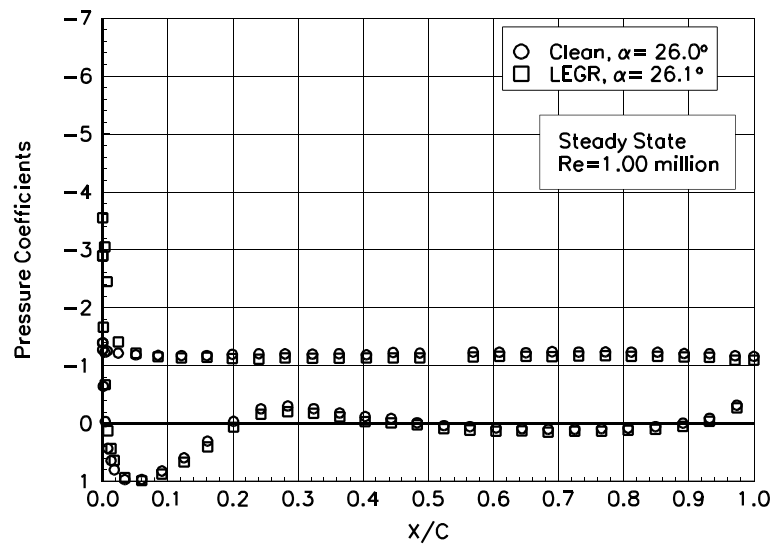


Figure 65. $\alpha = 26.0^\circ$

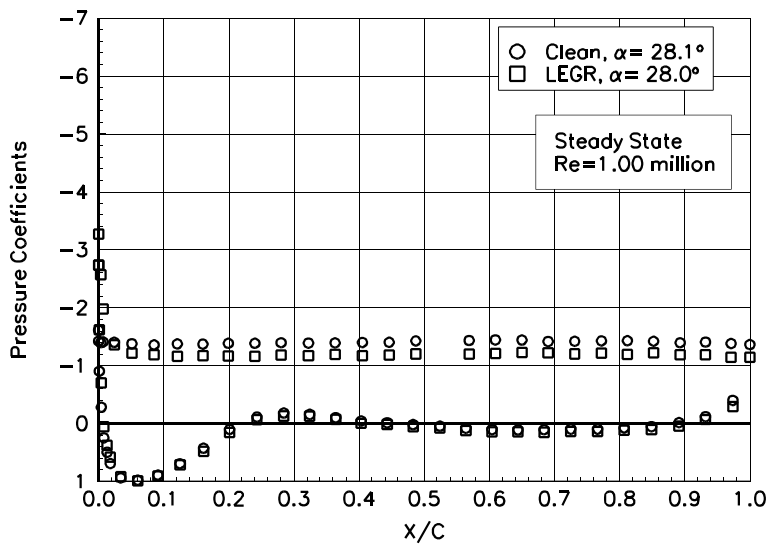


Figure 66. $\alpha = 28.1^\circ$

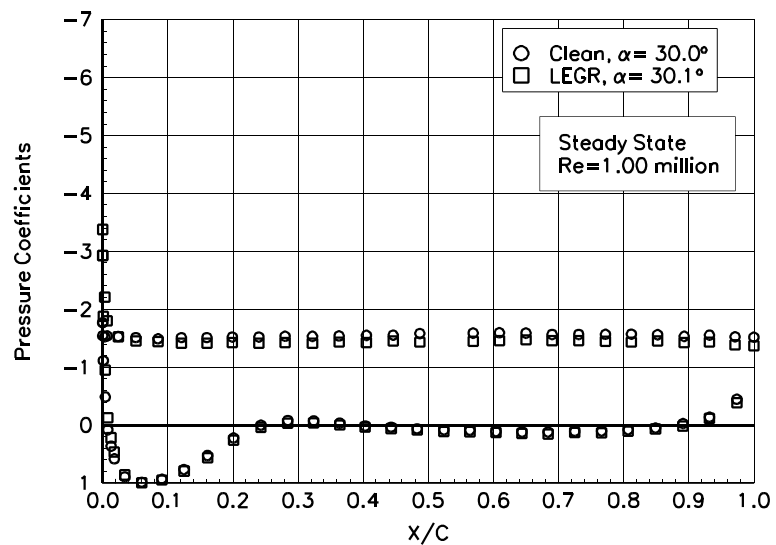


Figure 67. $\alpha = 30.0^\circ$

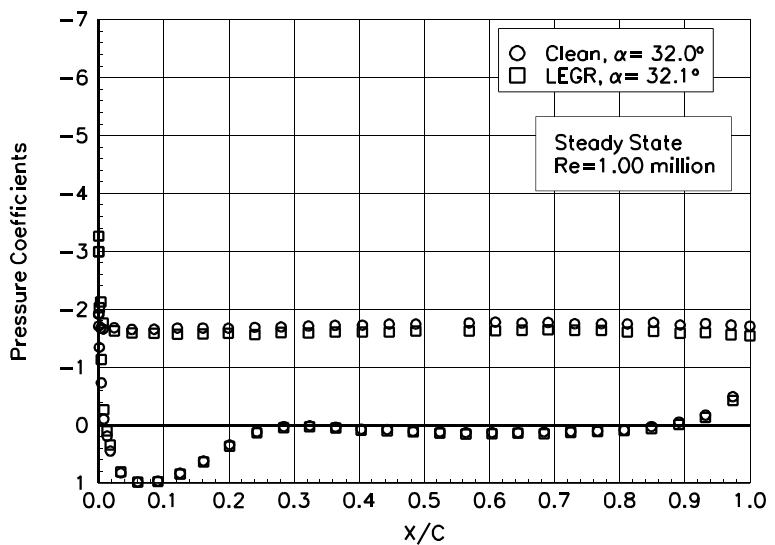


Figure 68. $\alpha = 32.0^\circ$

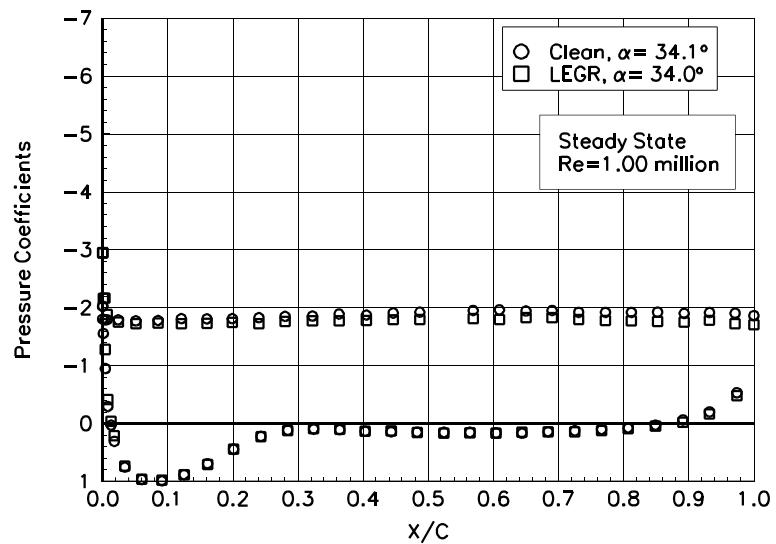


Figure 69. $\alpha = 34.1^\circ$

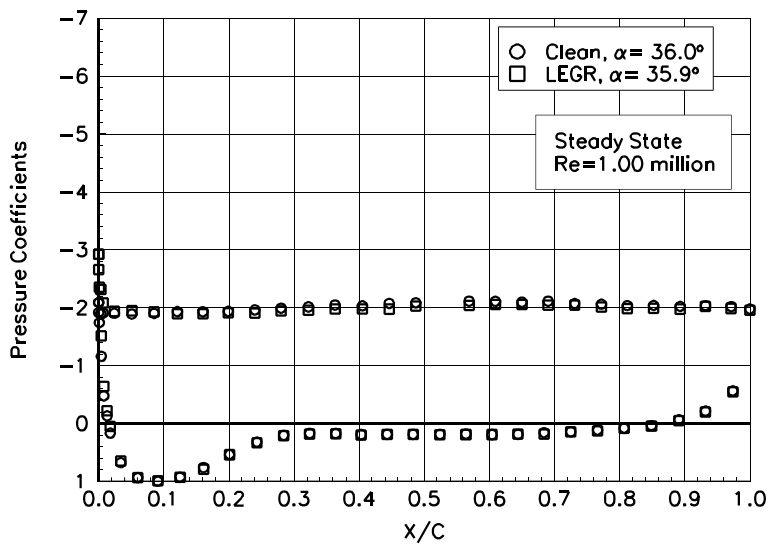


Figure 70. $\alpha = 36.0^\circ$

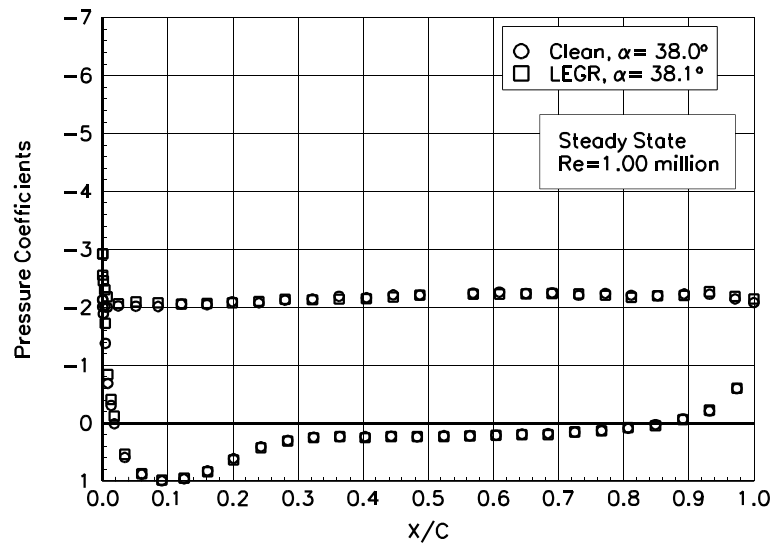


Figure 71. $\alpha = 38.0^\circ$

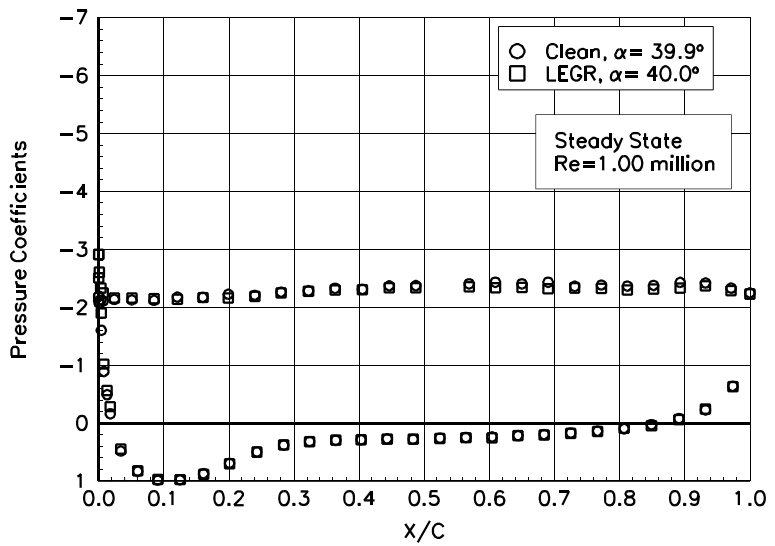


Figure 72. $\alpha = 39.9^\circ$

S814

Pressure Distributions, Steady State, Re = 1.25 million

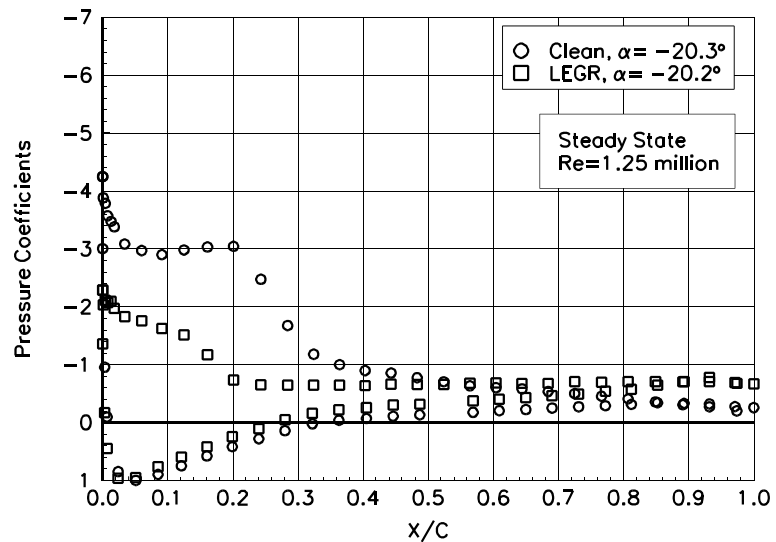


Figure 73. $\alpha = -20.3^\circ$

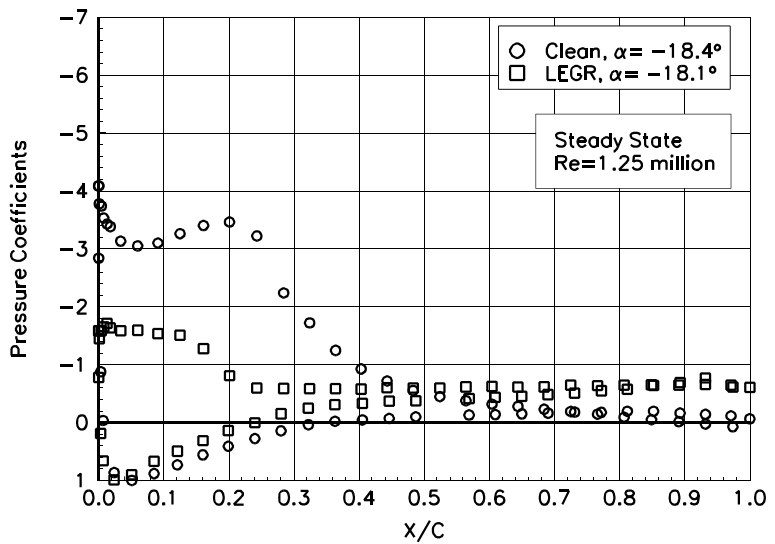


Figure 74. $\alpha = -18.4^\circ$

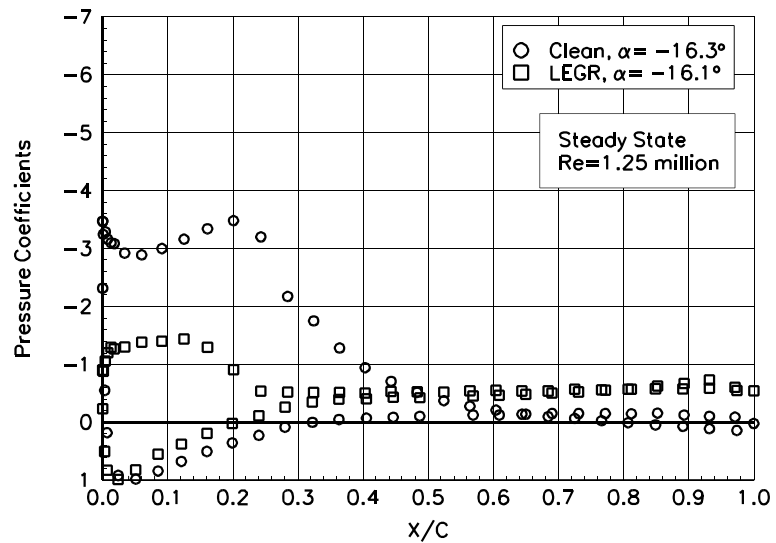


Figure 75. $\alpha = -16.3^\circ$

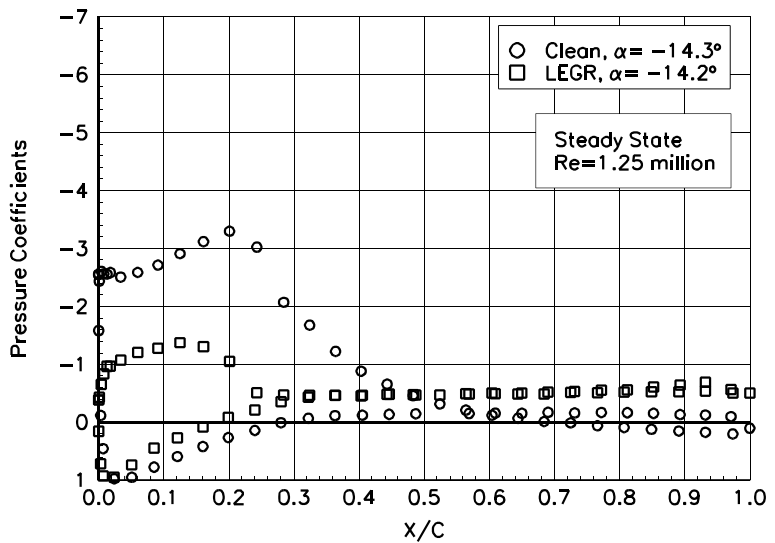


Figure 76. $\alpha = -14.3^\circ$

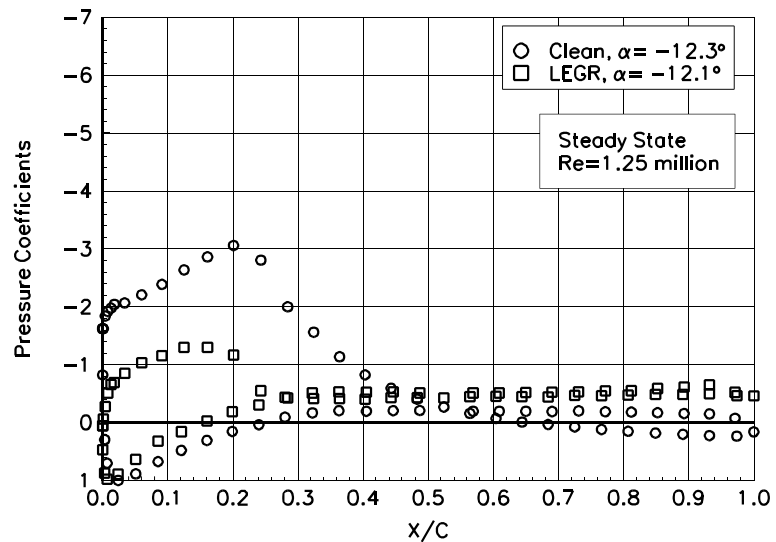


Figure 77. $\alpha = -12.3^\circ$

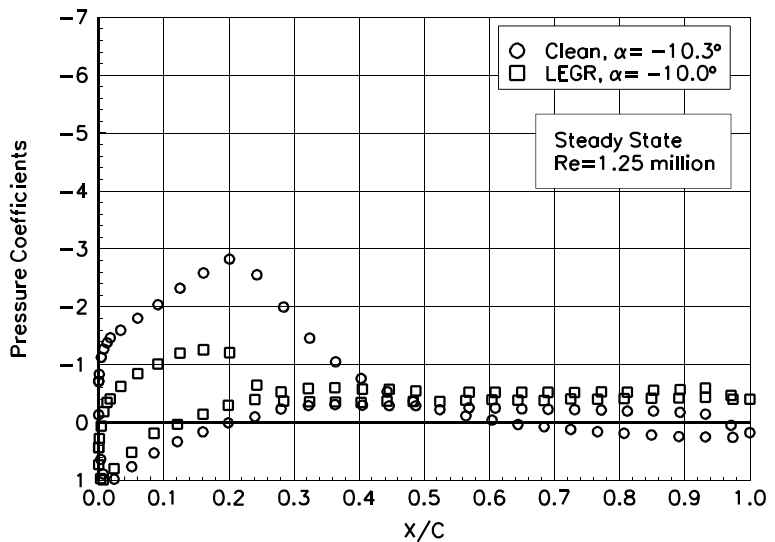


Figure 78. $\alpha = -10.3^\circ$

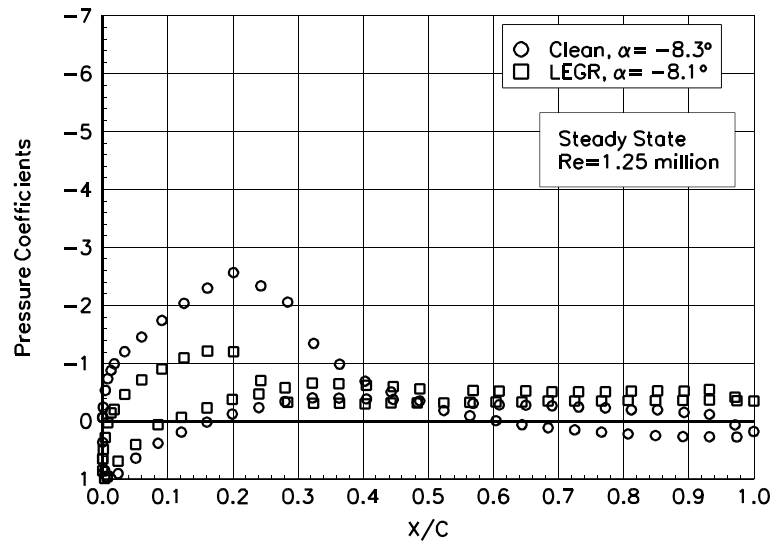


Figure 79. $\alpha = -8.3^\circ$

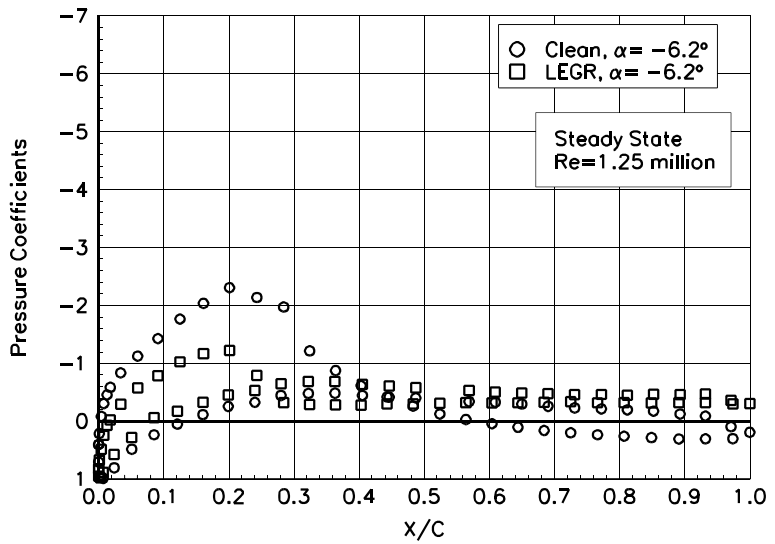


Figure 80. $\alpha = -6.2^\circ$

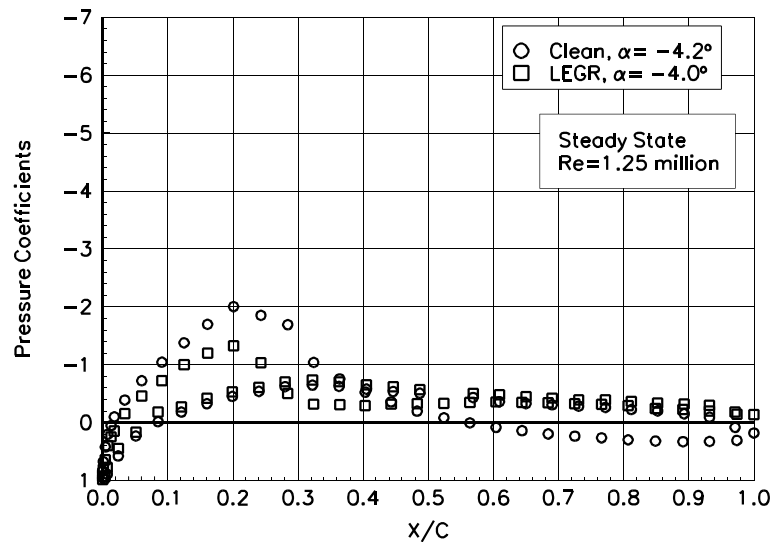


Figure 81. $\alpha = -4.2^\circ$

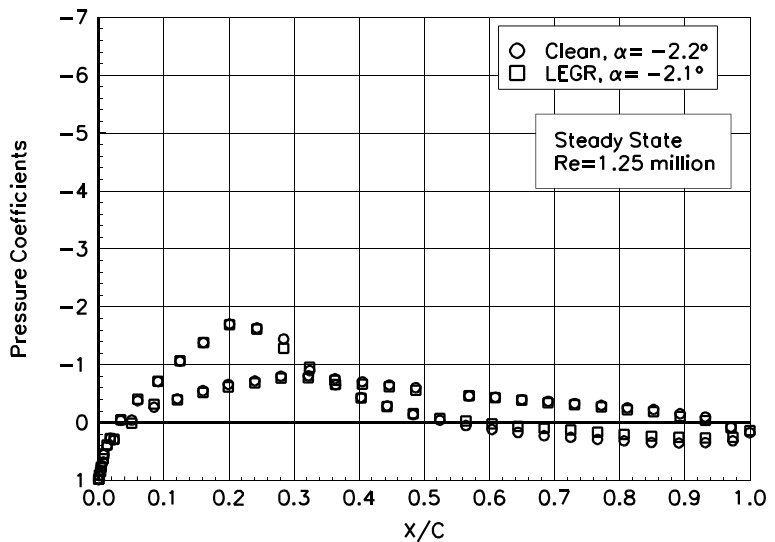


Figure 82. $\alpha = -2.2^\circ$

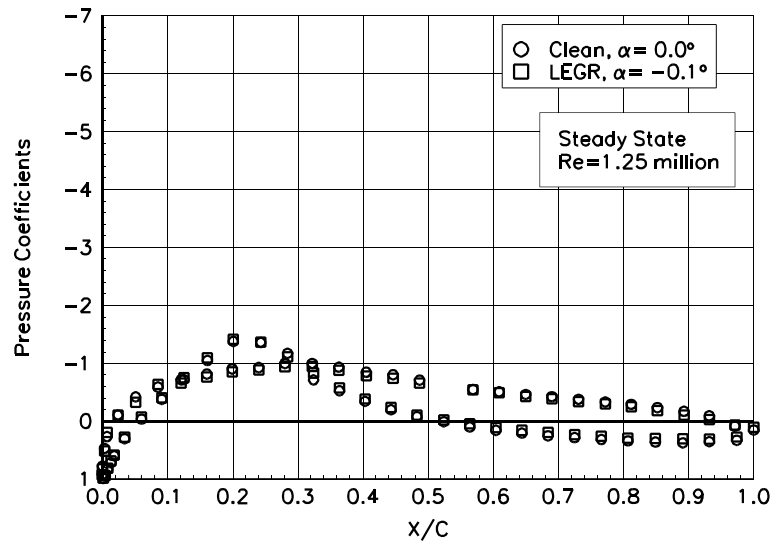


Figure 83. $\alpha = 0.0^\circ$

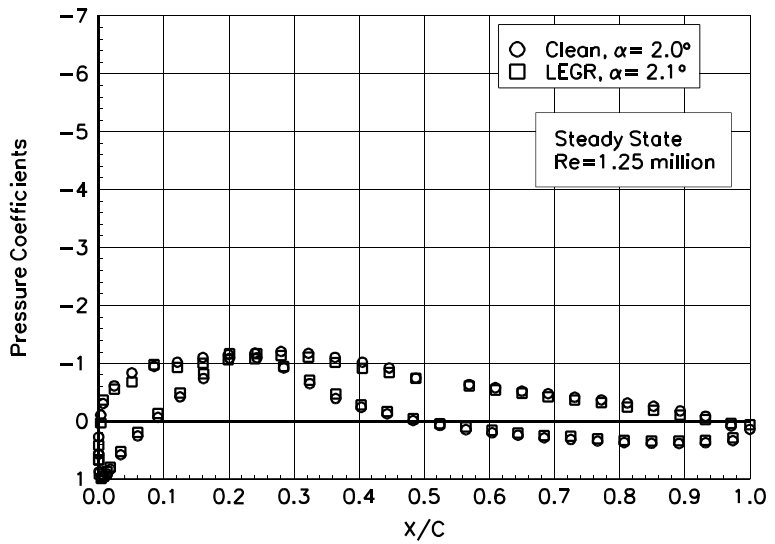


Figure 84. $\alpha = 2.0^\circ$

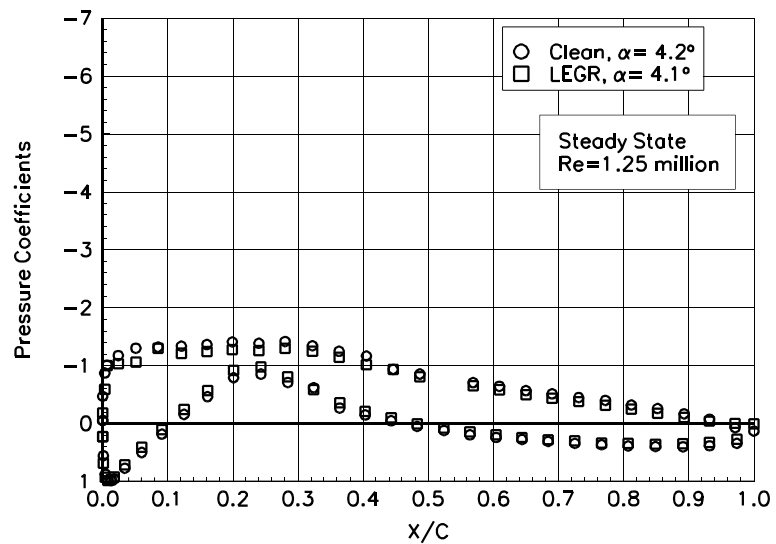


Figure 85. $\alpha = 4.2^\circ$

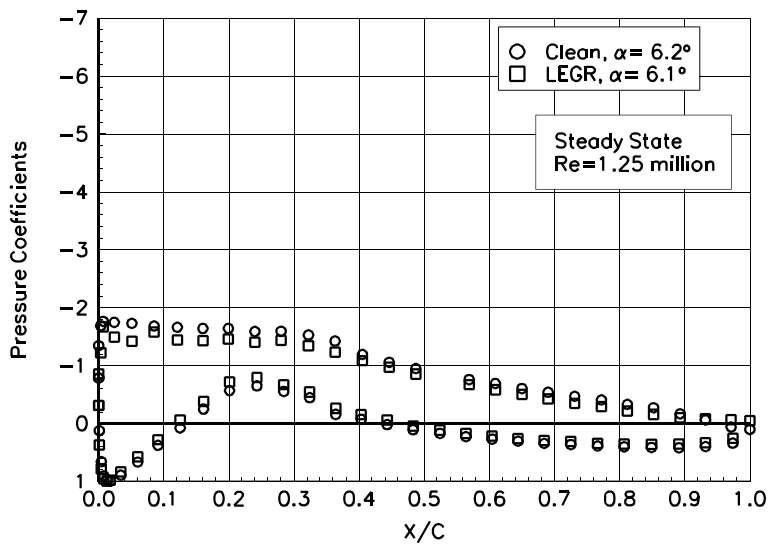


Figure 86. $\alpha = 6.2^\circ$

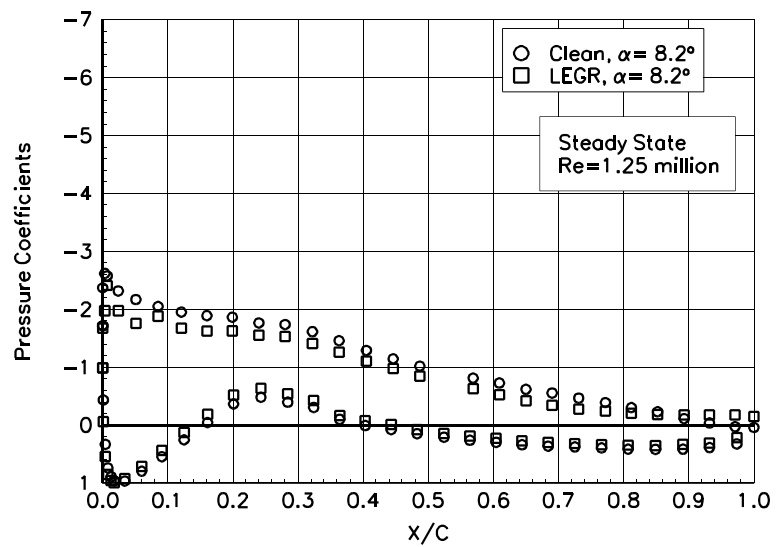


Figure 87. $\alpha = 8.2^\circ$

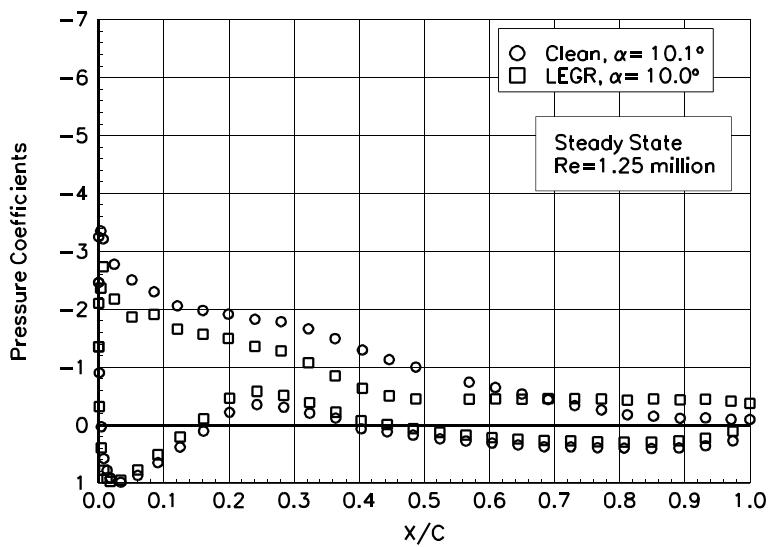


Figure 88. $\alpha = 10.1^\circ$

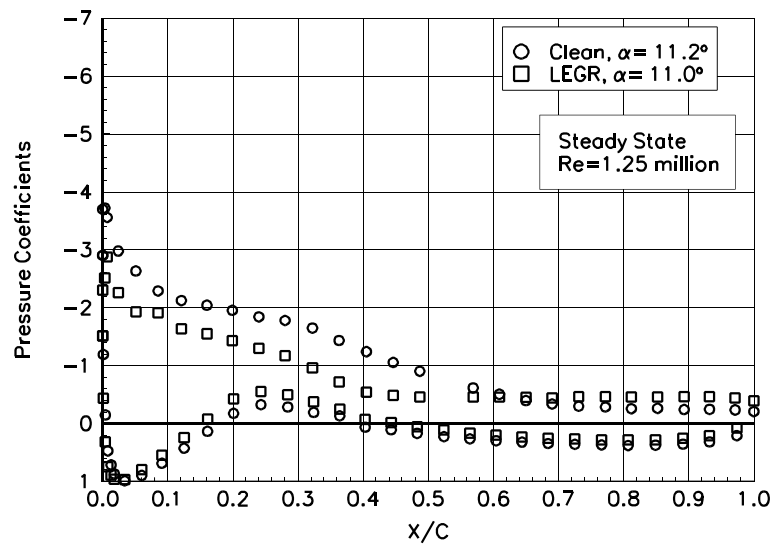


Figure 89. $\alpha = 11.2^\circ$

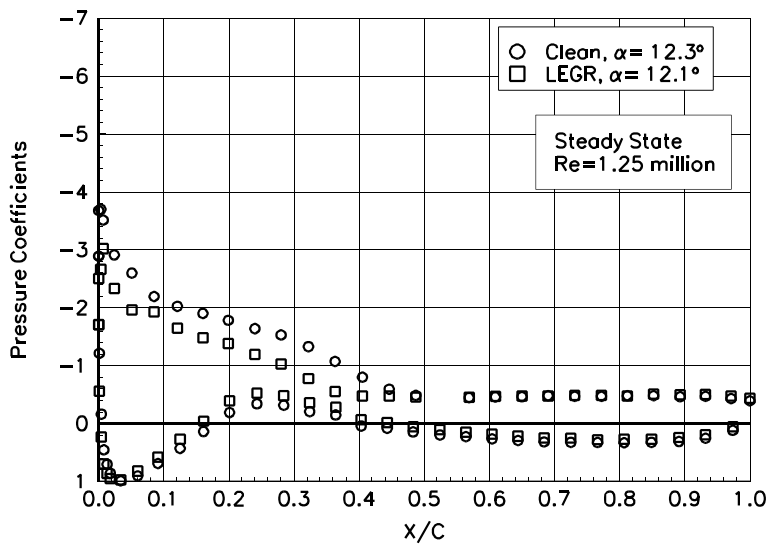


Figure 90. $\alpha = 12.3^\circ$

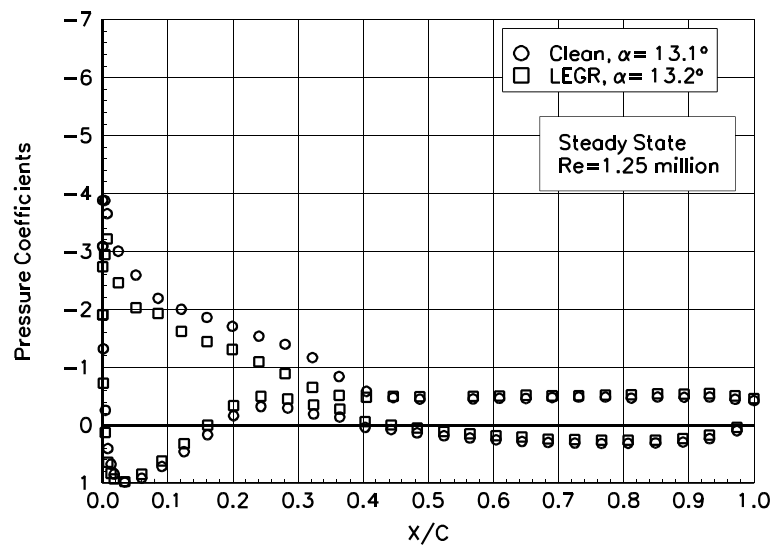


Figure 91. $\alpha = 13.1^\circ$

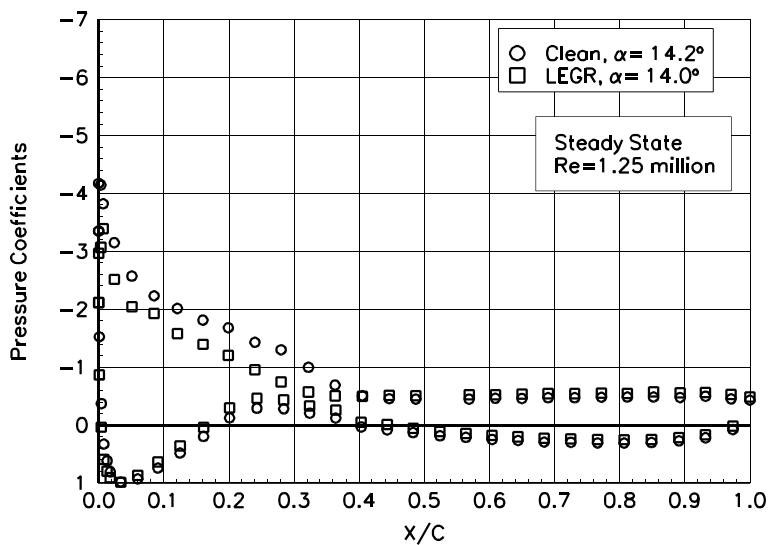


Figure 92. $\alpha = 14.2^\circ$

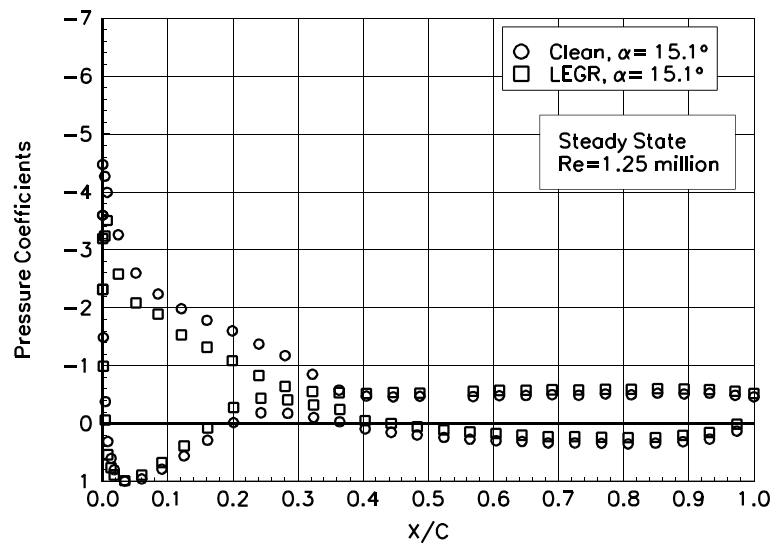


Figure 93. $\alpha = 15.1^\circ$

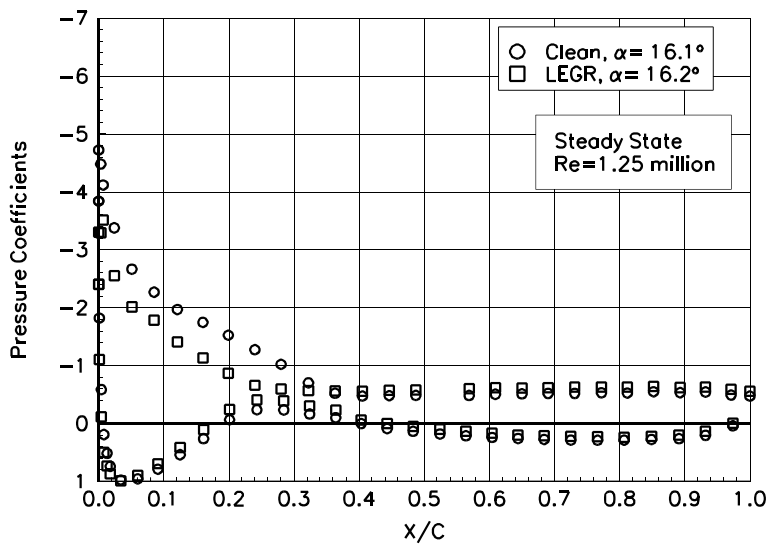


Figure 94. $\alpha = 16.1^\circ$

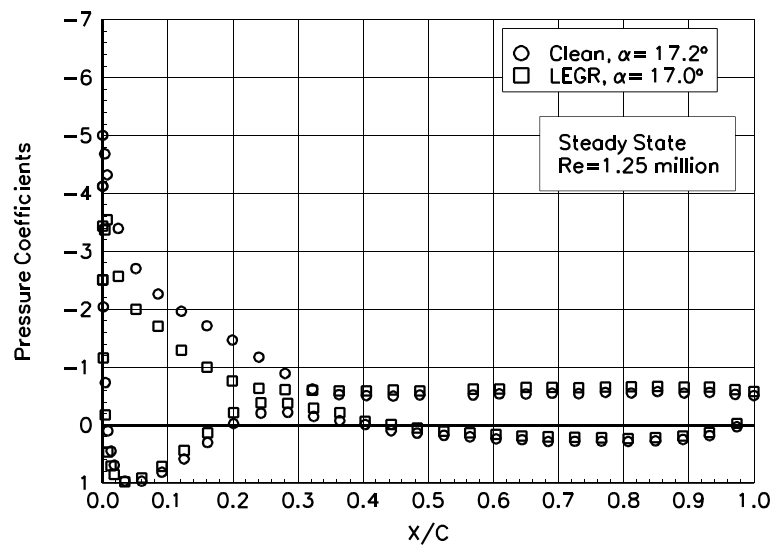


Figure 95. $\alpha = 17.2^\circ$

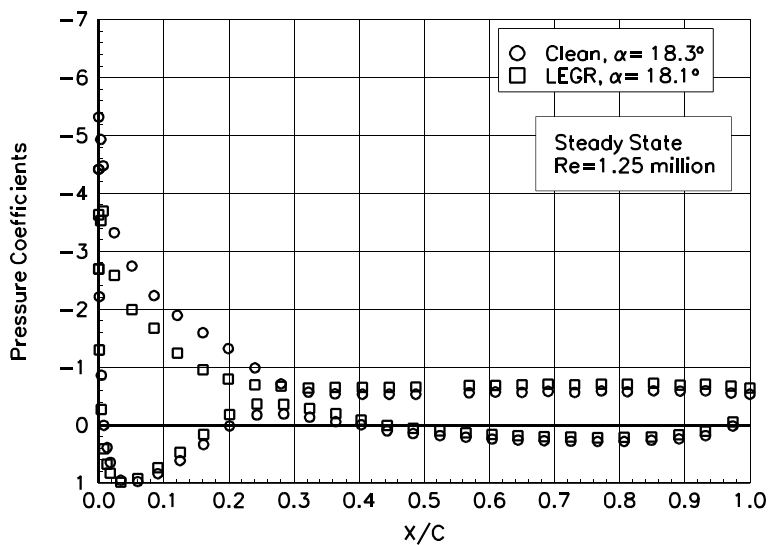


Figure 96. $\alpha = 18.3^\circ$

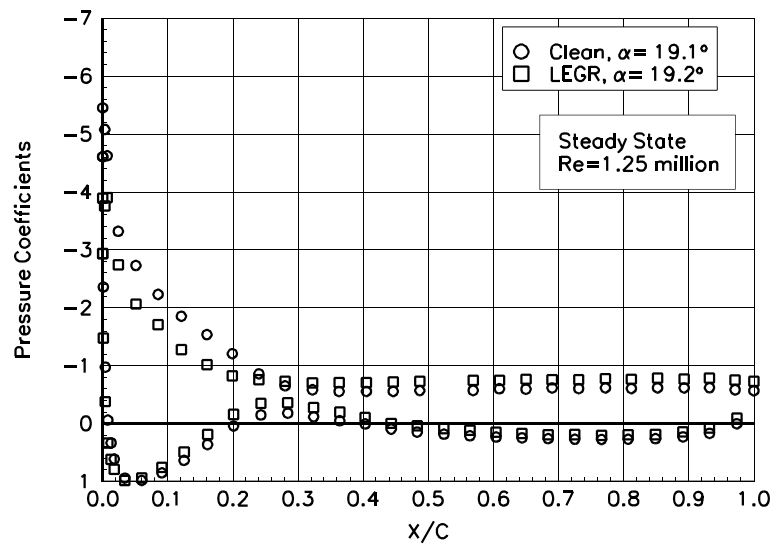


Figure 97. $\alpha = 19.1^\circ$

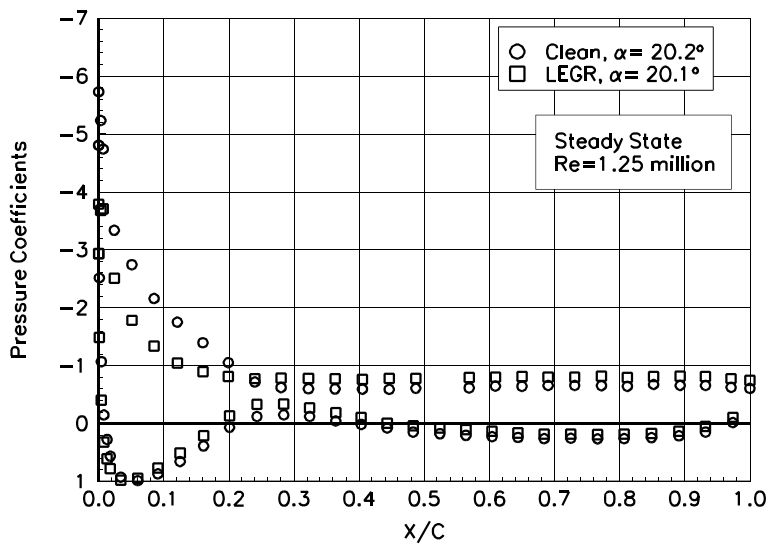


Figure 98. $\alpha = 20.2^\circ$

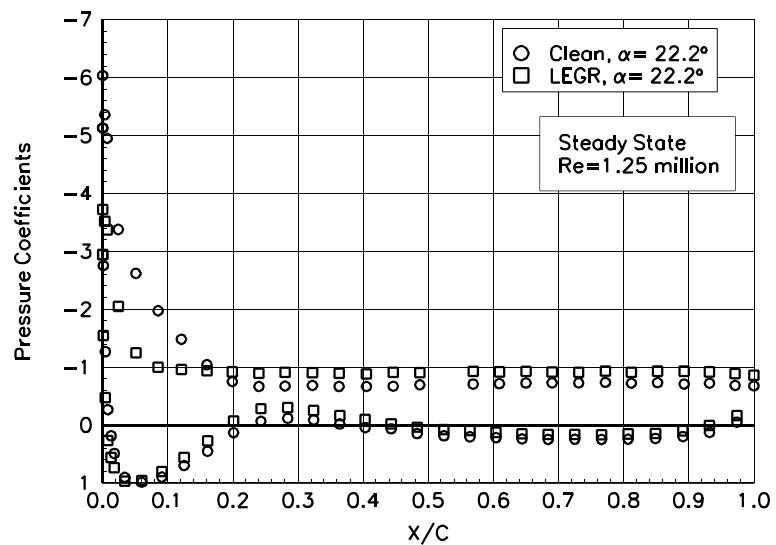


Figure 99. $\alpha = 22.2^\circ$

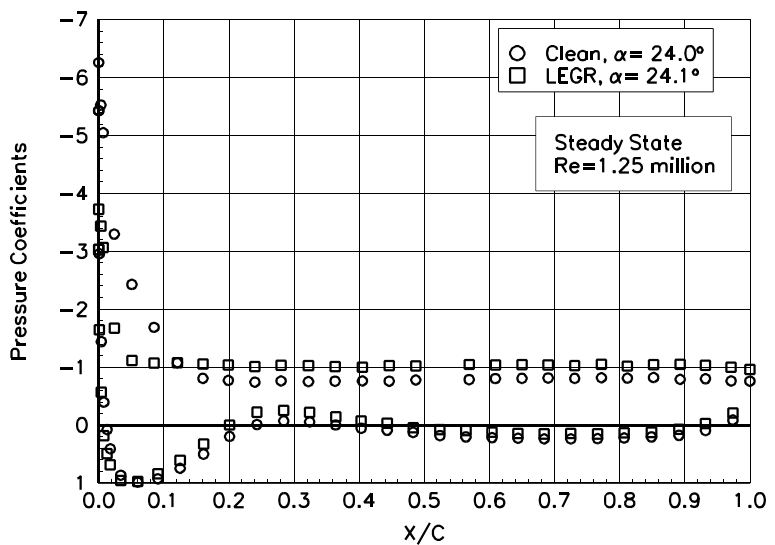


Figure 100. $\alpha = 24.0^\circ$

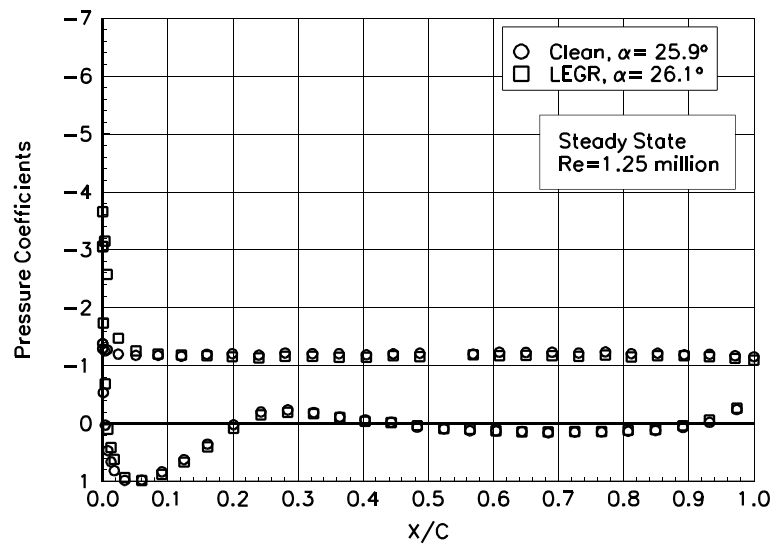


Figure 101. $\alpha = 25.9^\circ$

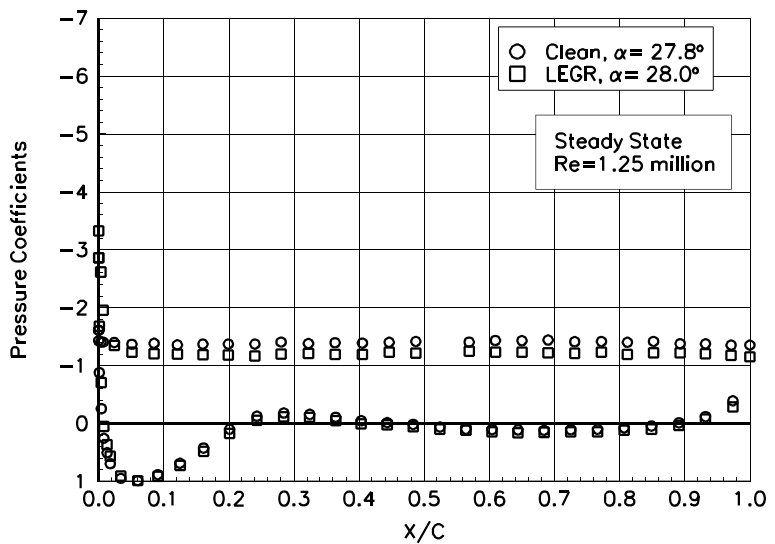


Figure 102. $\alpha = 27.8^\circ$

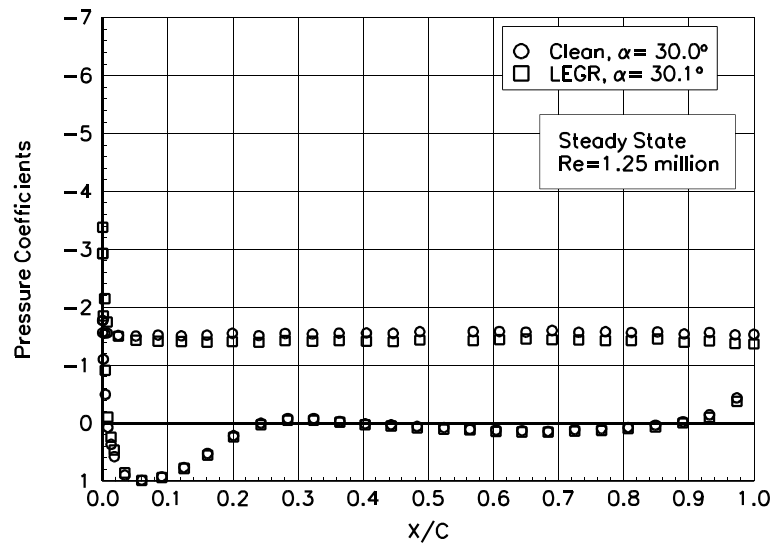


Figure 103. $\alpha = 30.0^\circ$

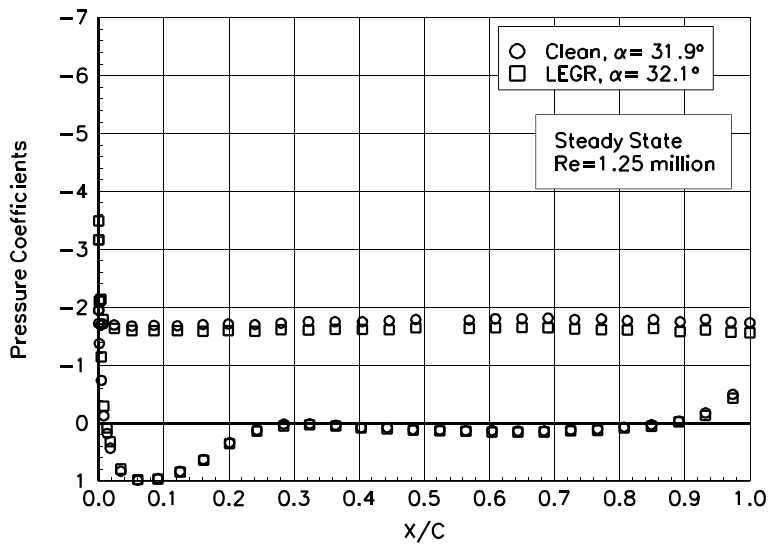


Figure 104. $\alpha = 31.9^\circ$

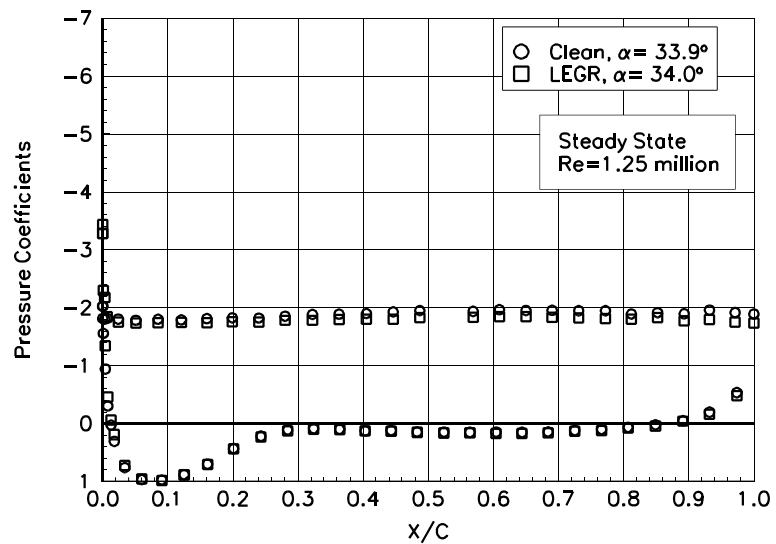


Figure 105. $\alpha = 33.9^\circ$

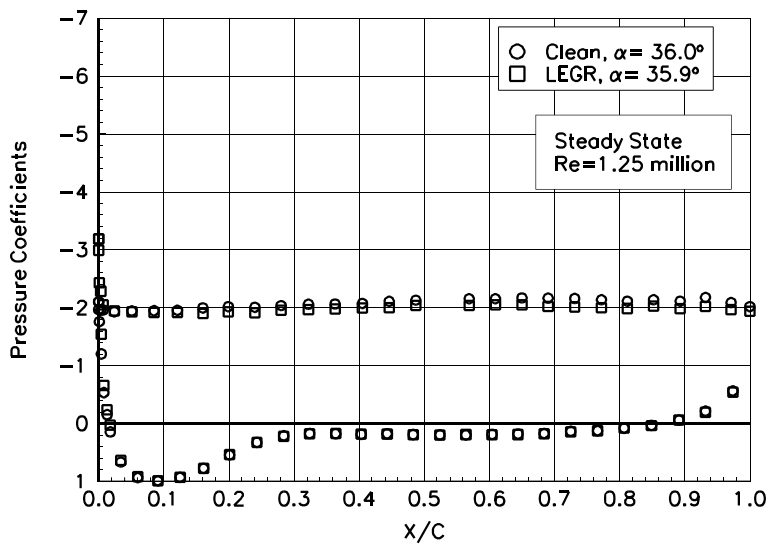


Figure 106. $\alpha = 36.0^\circ$

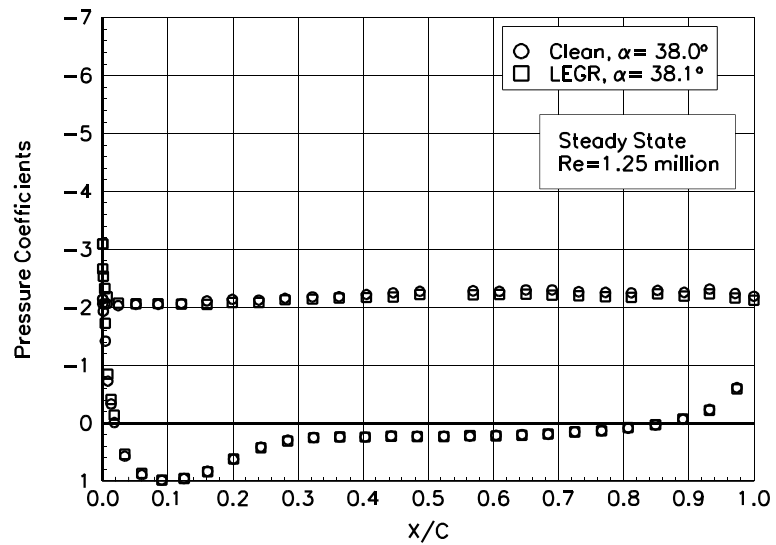


Figure 107. $\alpha = 38.0^\circ$

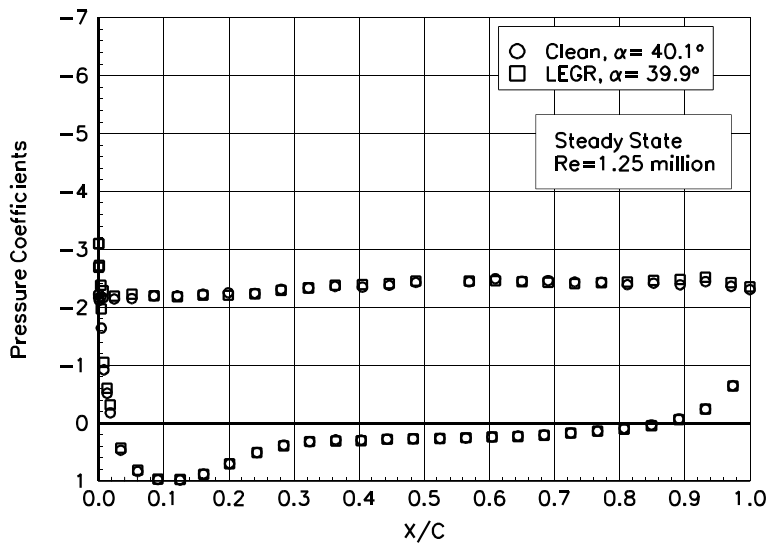


Figure 108. $\alpha = 40.1^\circ$

S814

Pressure Distributions, Steady State, Re = 1.5 million

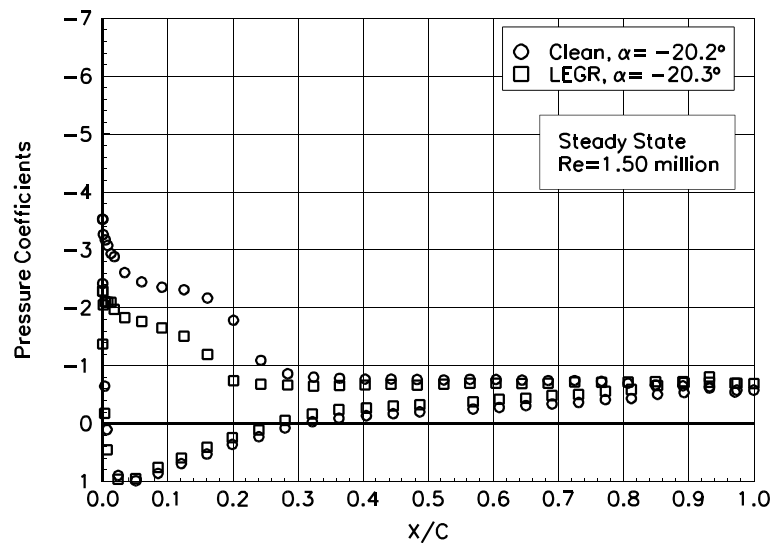


Figure 109. $\alpha = -20.2^\circ$

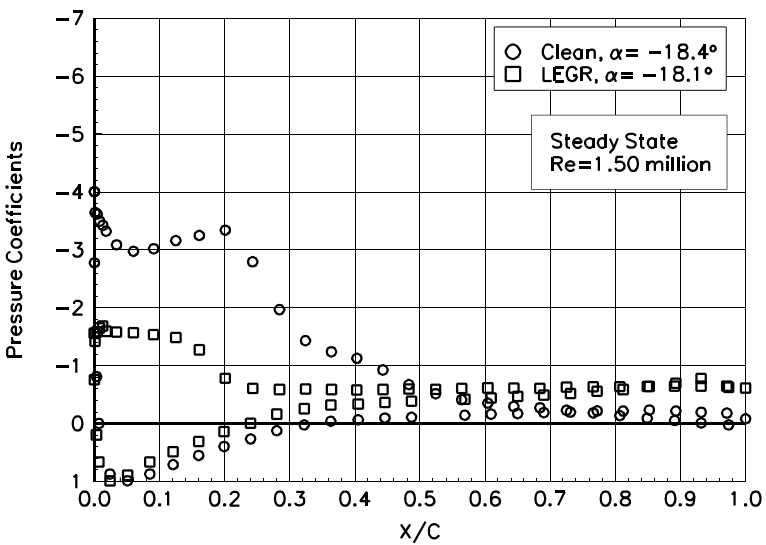


Figure 110. $\alpha = -18.4^\circ$

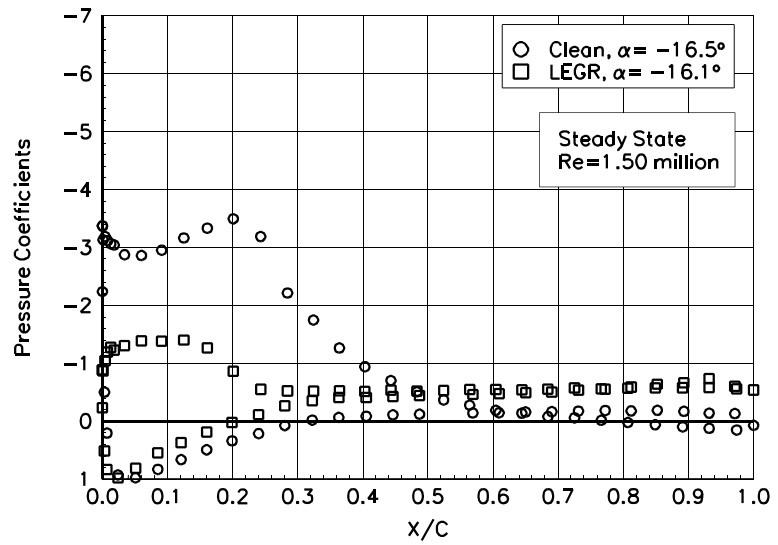


Figure 111. $\alpha = -16.5^\circ$

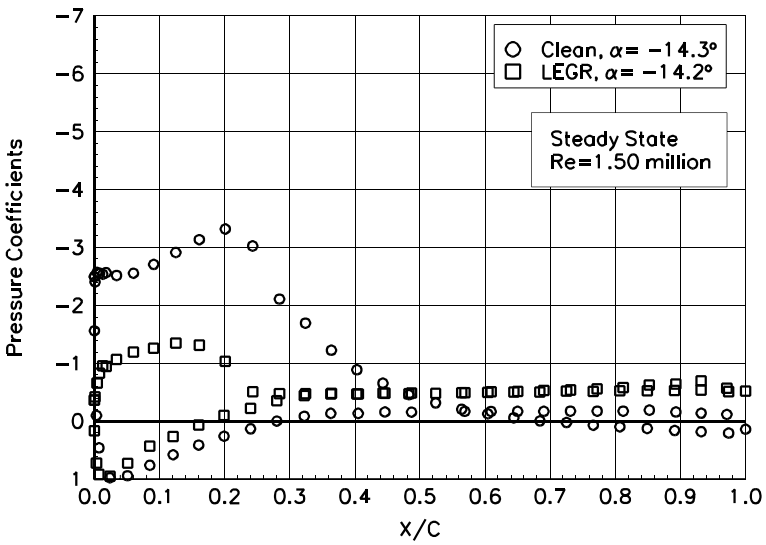


Figure 112. $\alpha = -14.3^\circ$

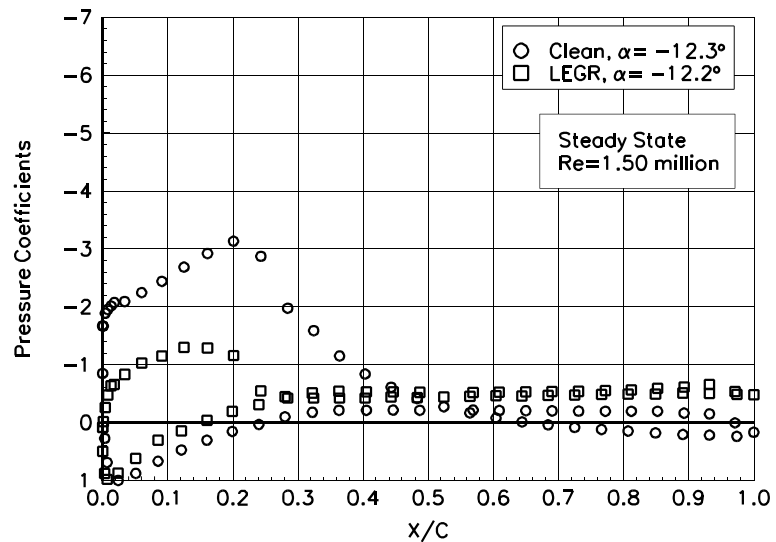


Figure 113. $\alpha = -12.3^\circ$

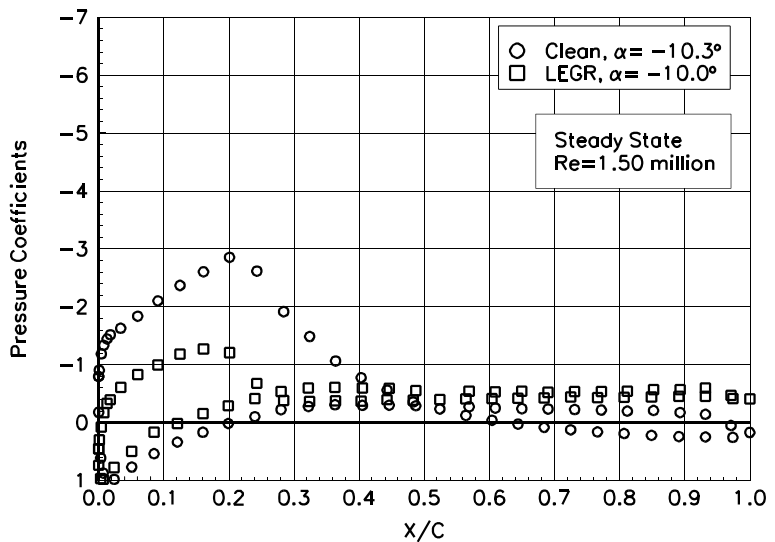


Figure 114. $\alpha = -10.3^\circ$

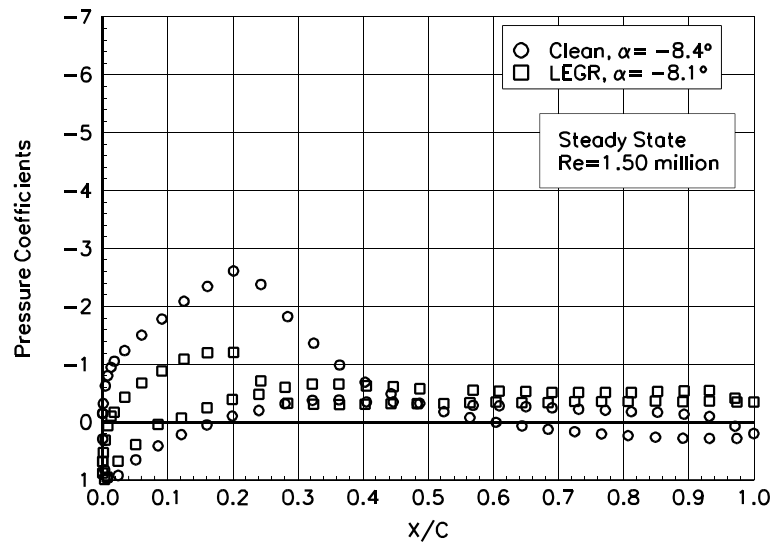


Figure 115. $\alpha = -8.4^\circ$

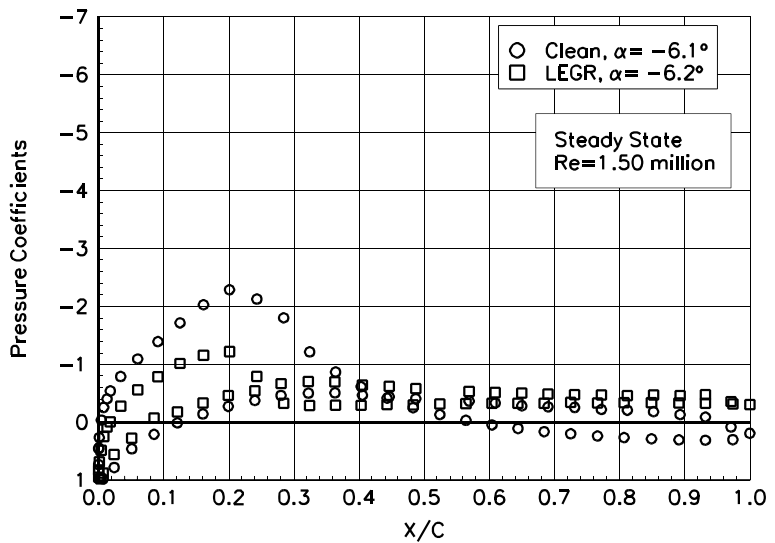


Figure 116. $\alpha = -6.1^\circ$

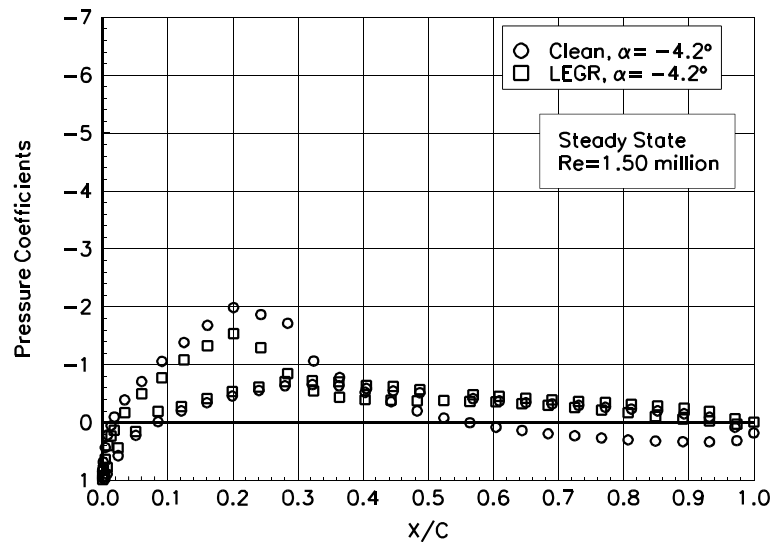


Figure 117. $\alpha = -4.2^\circ$

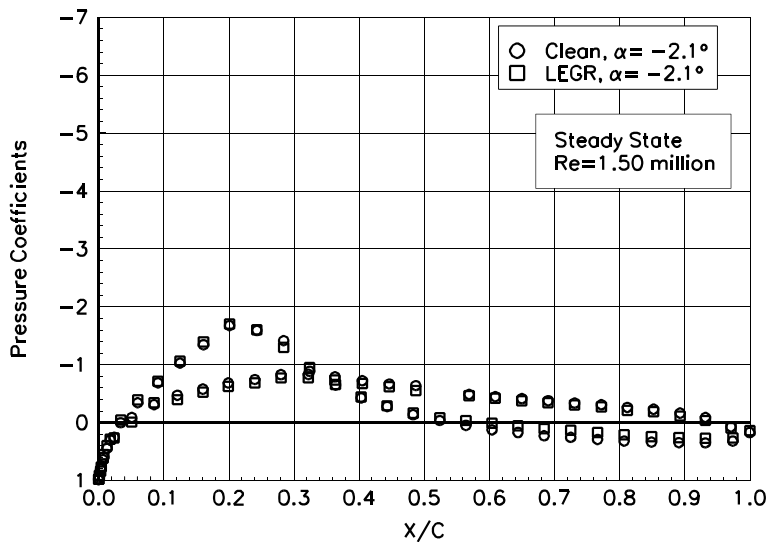


Figure 118. $\alpha = -2.1^\circ$

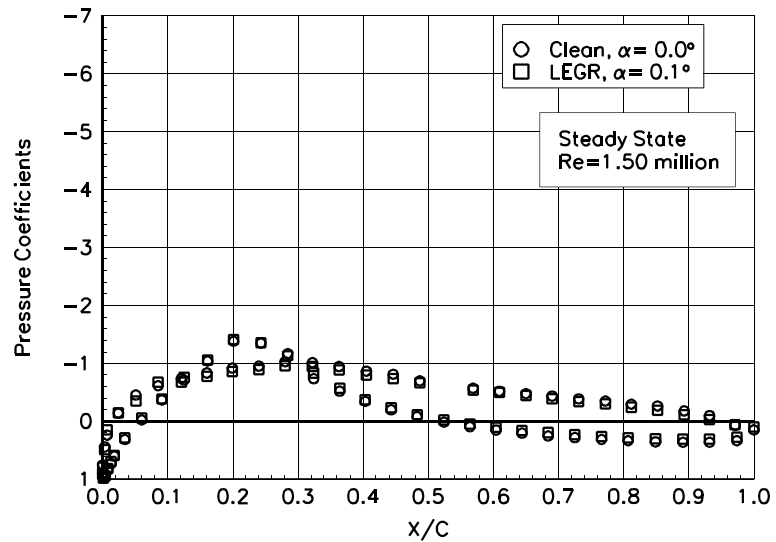


Figure 119. $\alpha = 0.0^\circ$

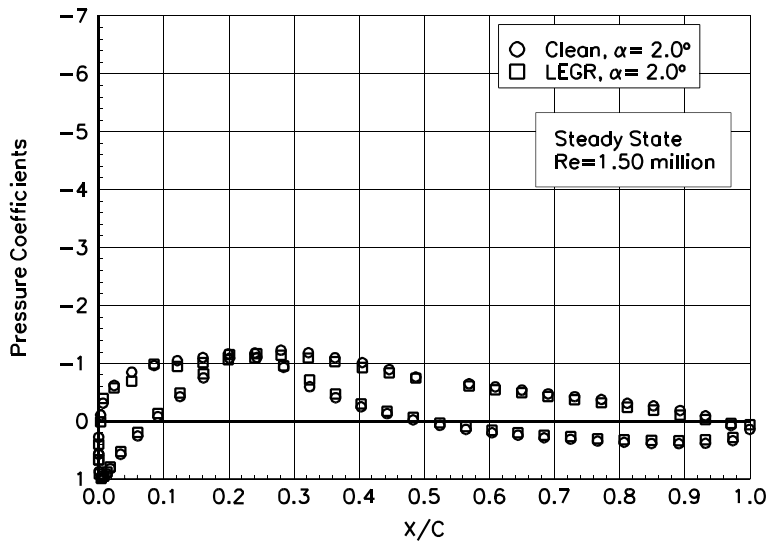


Figure 120. $\alpha = 2.0^\circ$

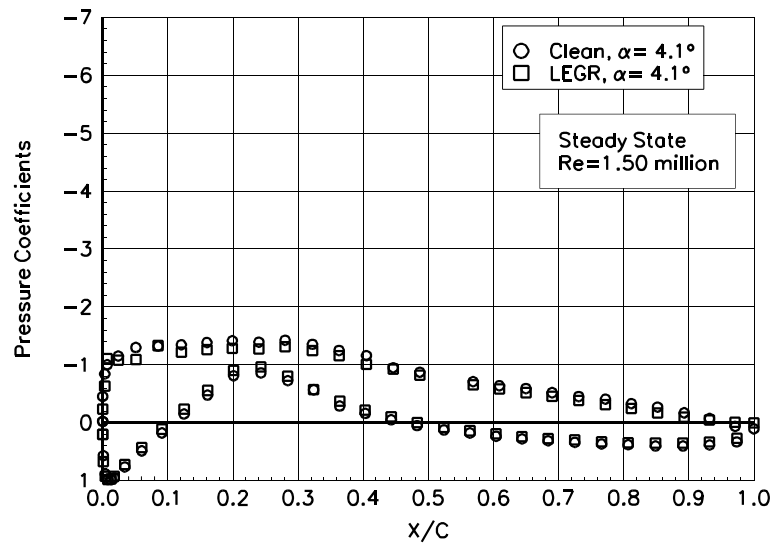


Figure 121. $\alpha = 4.1^\circ$

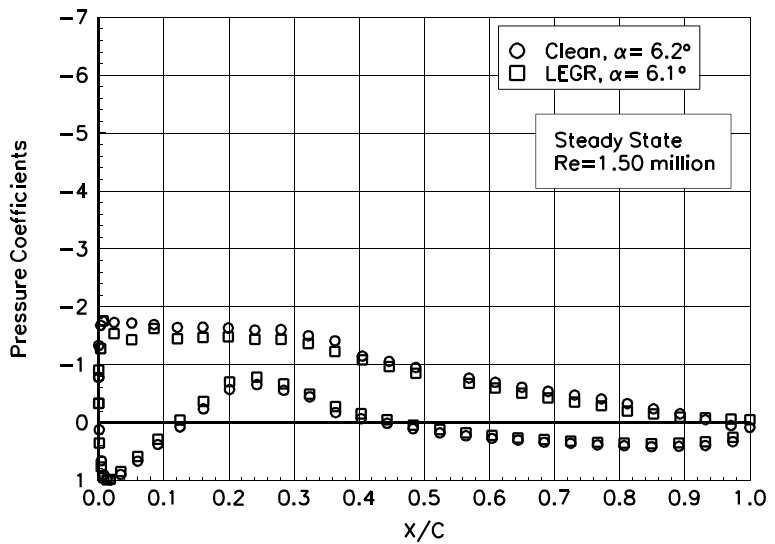


Figure 122. $\alpha = 6.2^\circ$

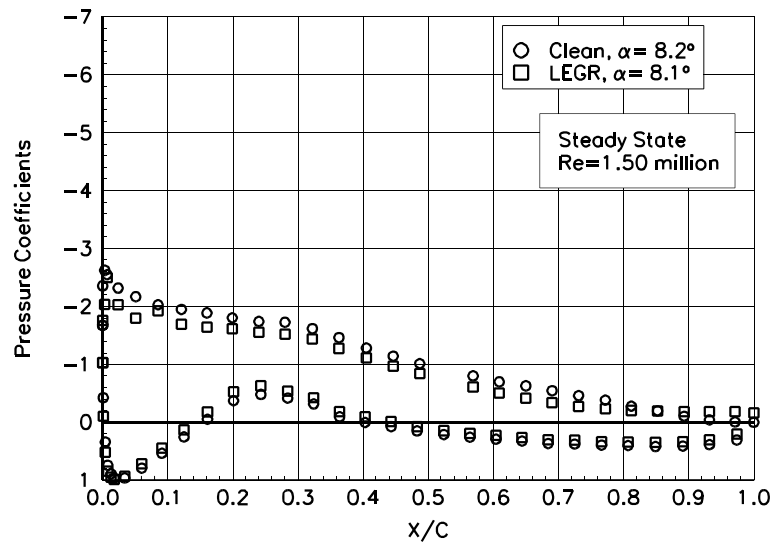


Figure 123. $\alpha = 8.2^\circ$

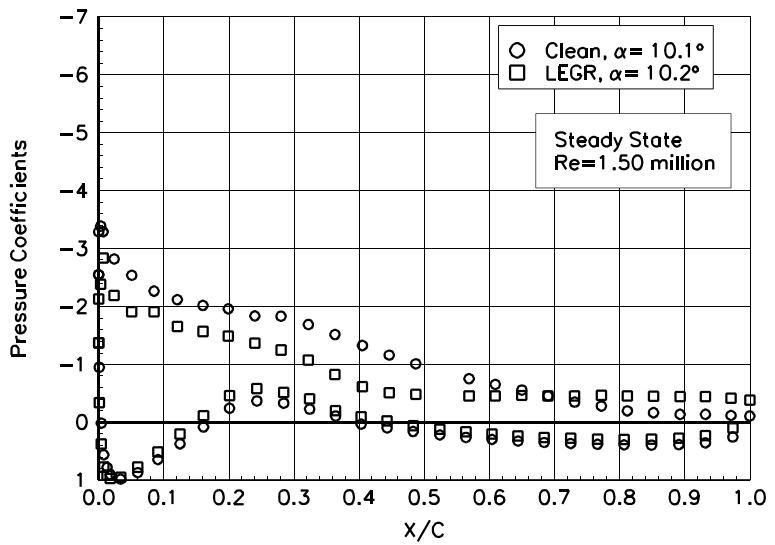


Figure 124. $\alpha = 10.1^\circ$

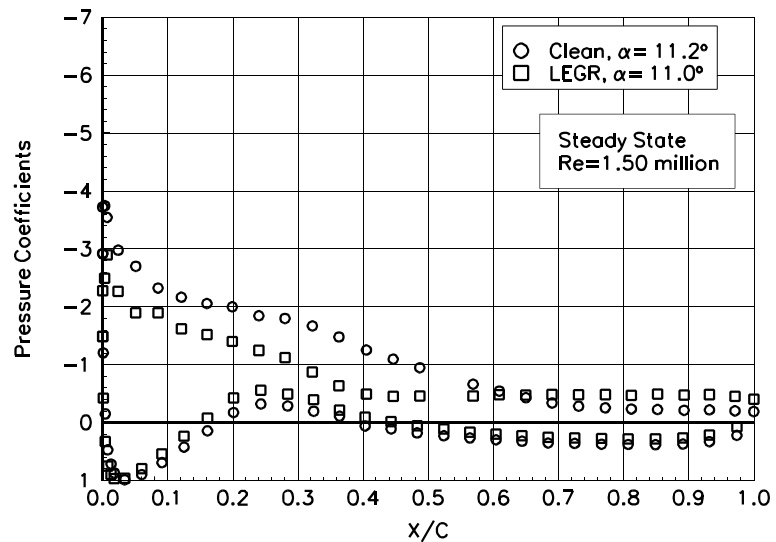


Figure 125. $\alpha = 11.2^\circ$

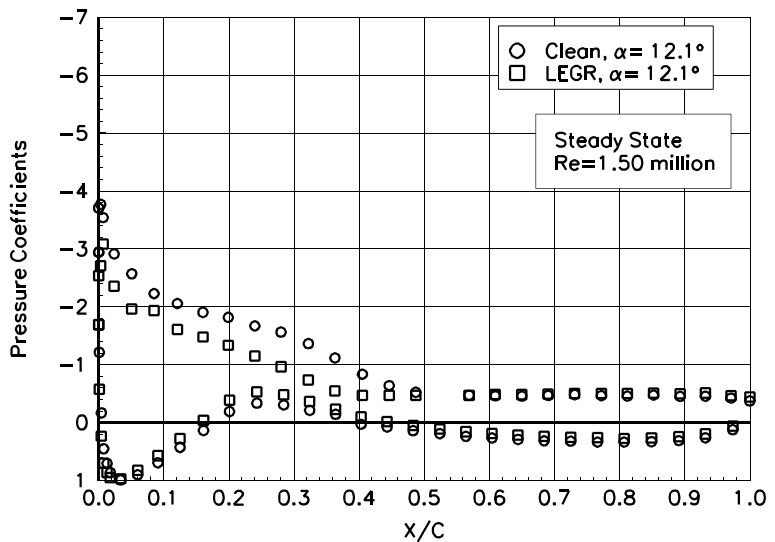


Figure 126. $\alpha = 12.1^\circ$

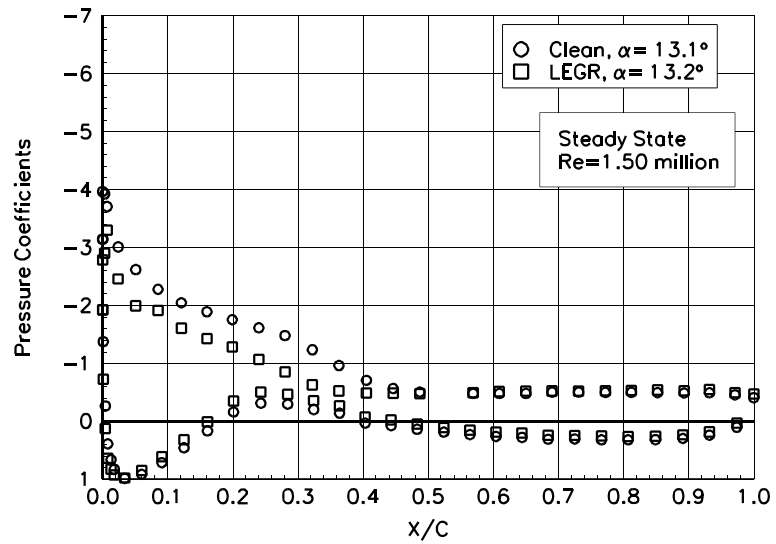


Figure 127. $\alpha = 13.1^\circ$

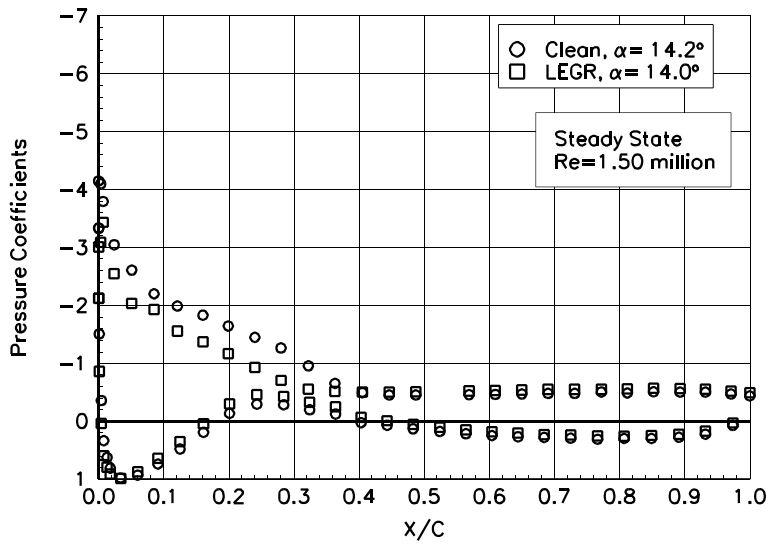


Figure 128. $\alpha = 14.2^\circ$

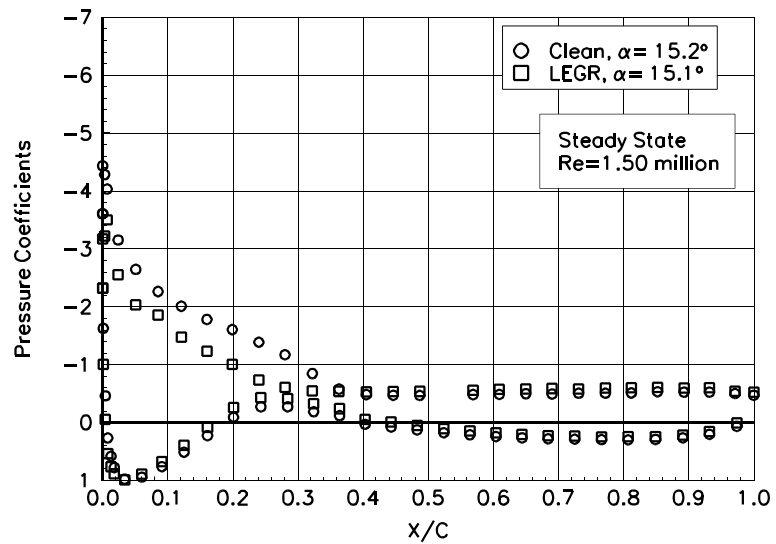


Figure 129. $\alpha = 15.2^\circ$

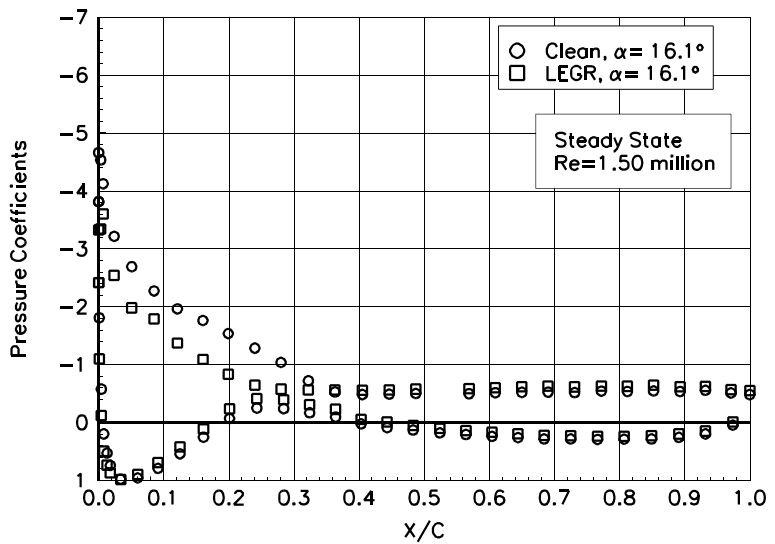


Figure 130. $\alpha = 16.1^\circ$

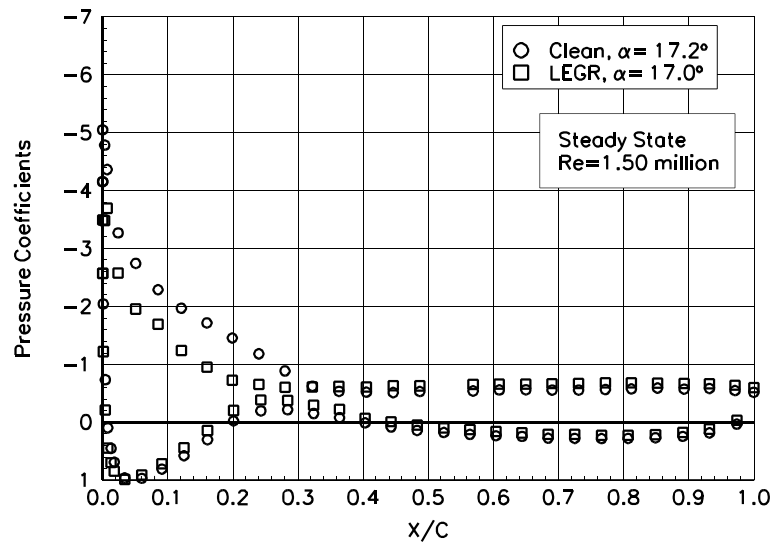


Figure 131. $\alpha = 17.2^\circ$

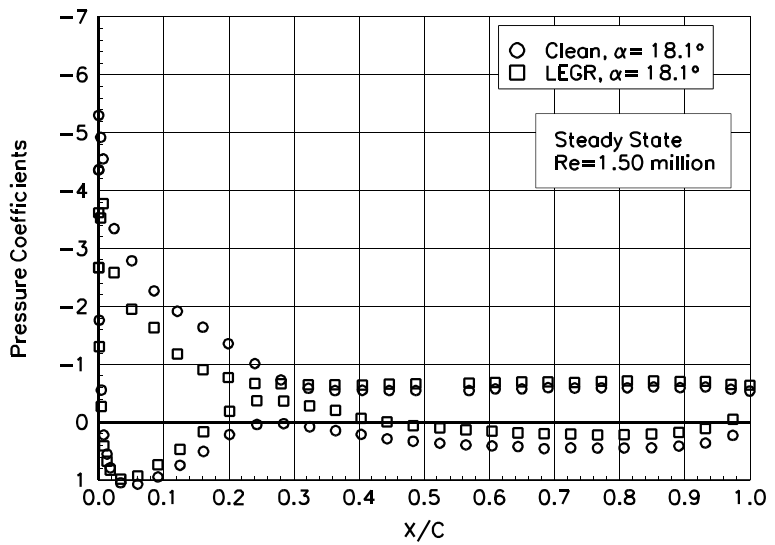


Figure 132. $\alpha = 18.1^\circ$

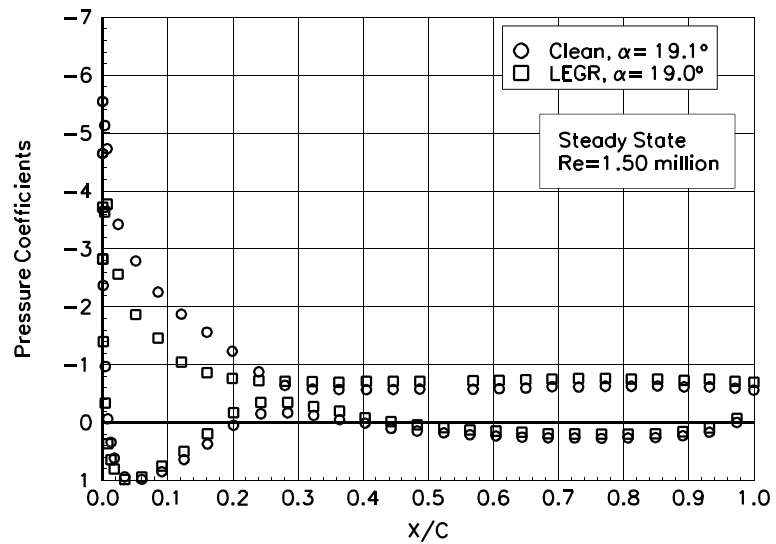


Figure 133. $\alpha = 19.1^\circ$

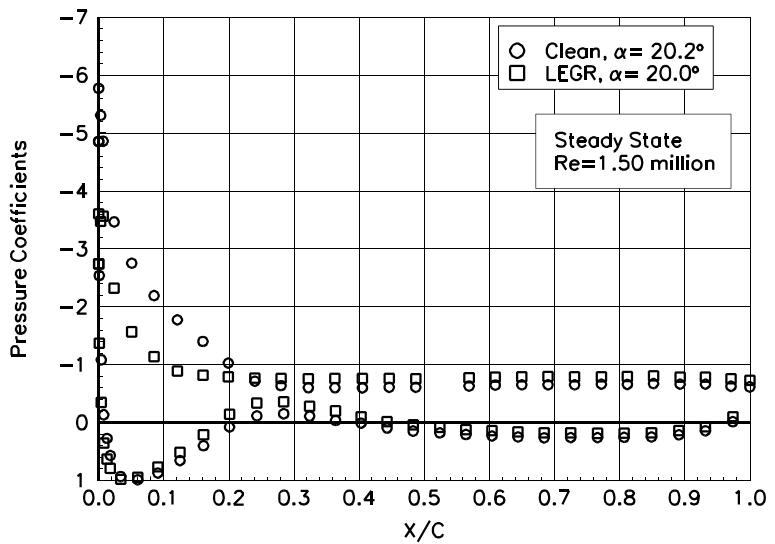


Figure 134. $\alpha = 20.2^\circ$

Appendix C: Unsteady Integrated Coefficients

List of Figures

	Page
--	-------------

±5.5° Sine, Re = 0.75 million	C-3
±5.5° Sine, Re = 1 million	C-10
±5.5° Sine, Re= 1.25 million	C-17
±5.5° Sine, Re = 1.5 million	C-24
±10° Sine, Re = 0.75 million	C-31
±10° Sine, Re = 1 million	C-38
±10° Sine, Re = 1.25 million	C-45
±10° Sine, Re = 1.5 million	C-52

Unsteady Airfoil Characteristics

$\pm 5.5^\circ$ Sine, Re = 0.75 million

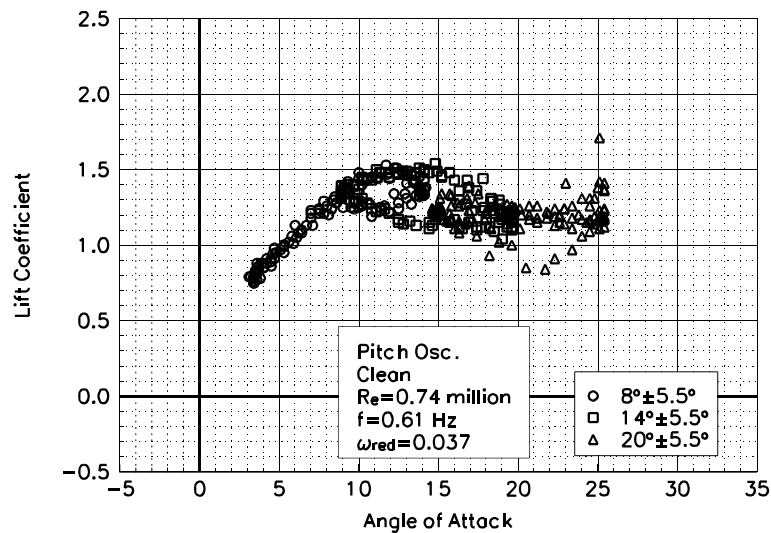


Figure C1. Lift coefficient vs α .

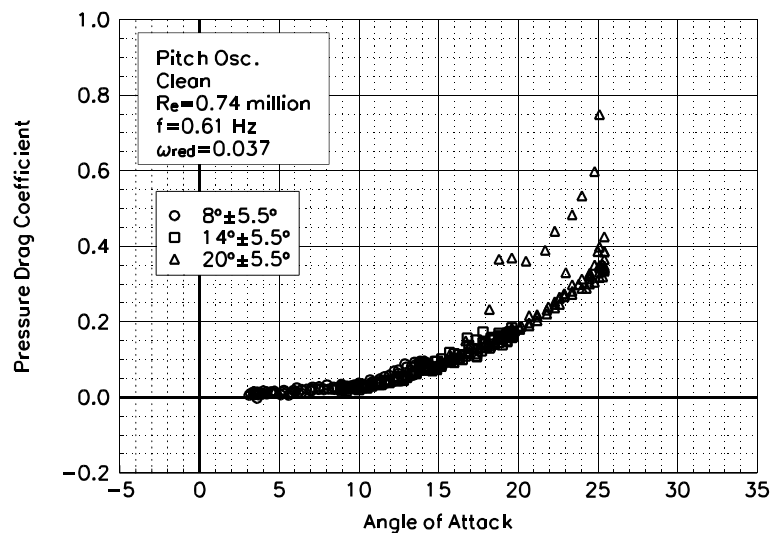


Figure C2. Pressure drag coefficient vs α .

S814
Clean
 $Re=0.74$ million
 $\omega_{red}=0.037$

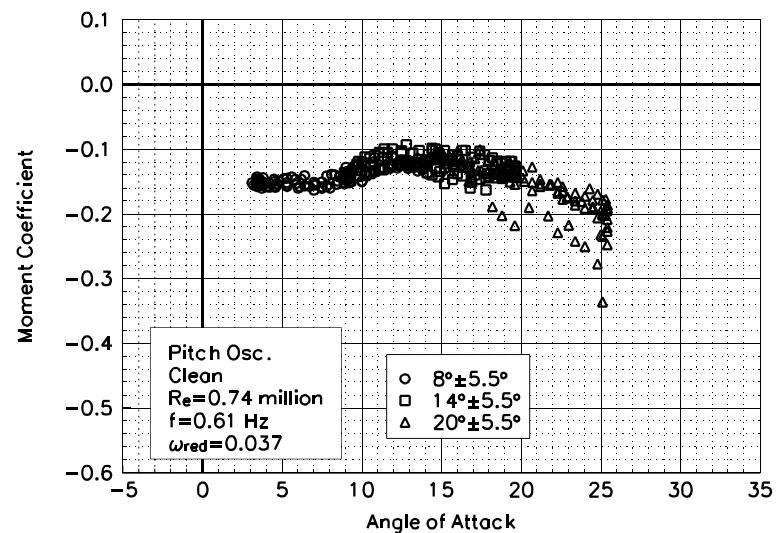


Figure C3. Moment coefficient vs α .

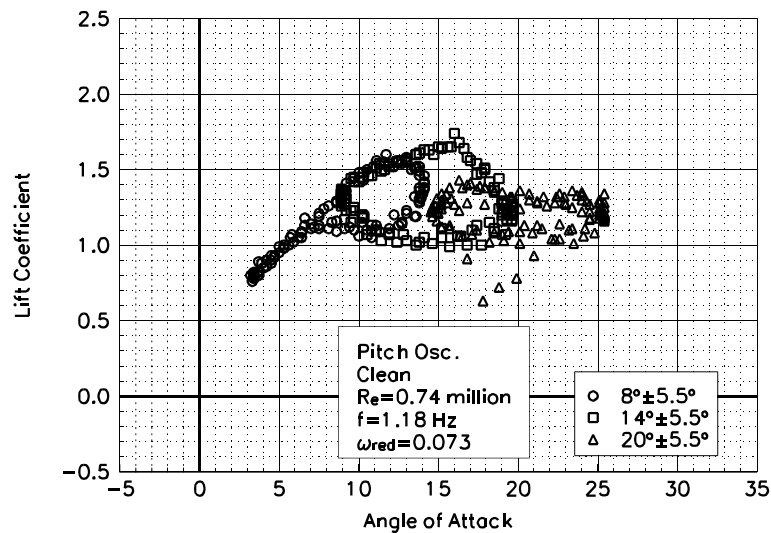


Figure C4. Lift coefficient vs α .

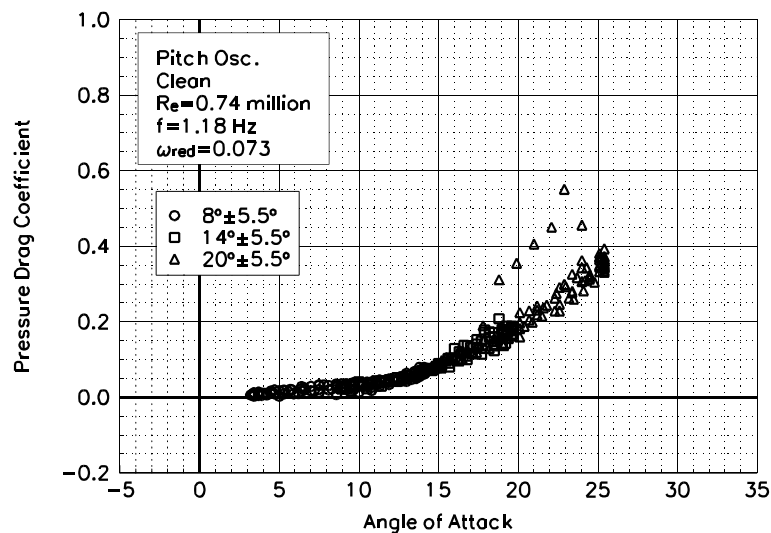


Figure C5. Pressure drag coefficient vs α .

S814
Clean
 $Re=0.74$ million
 $\omega_{red}=0.073$

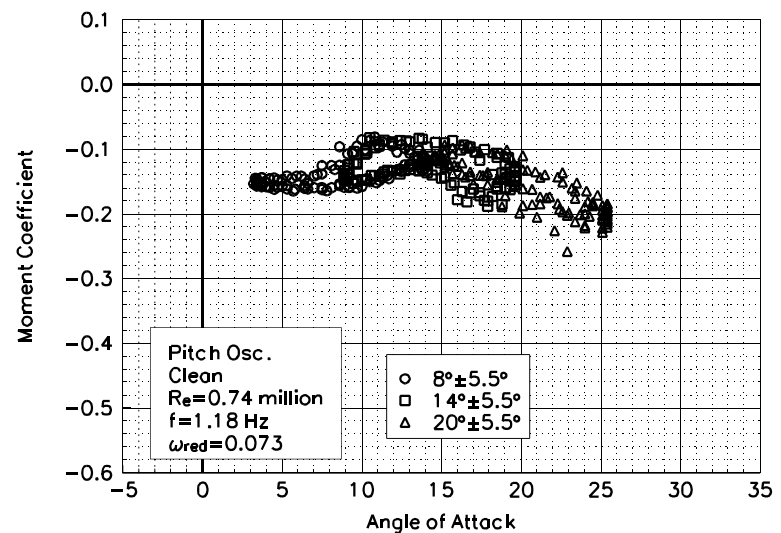


Figure C6. Moment coefficient vs α .

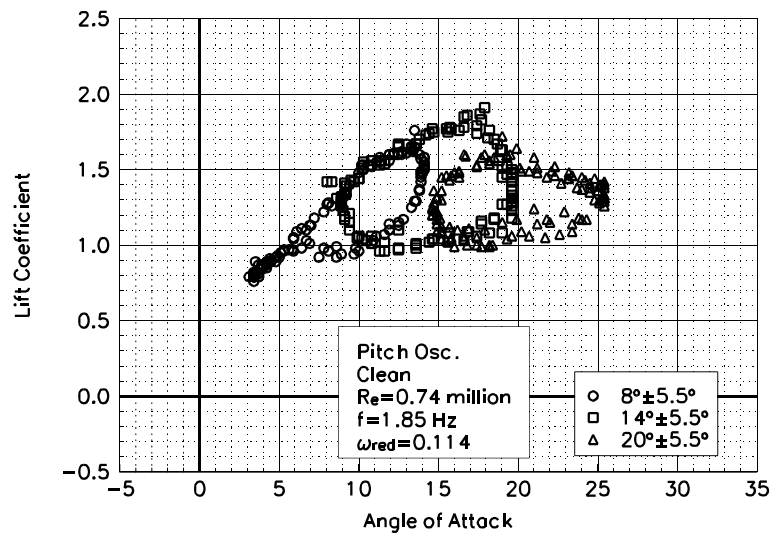


Figure C7. Lift coefficient vs α .

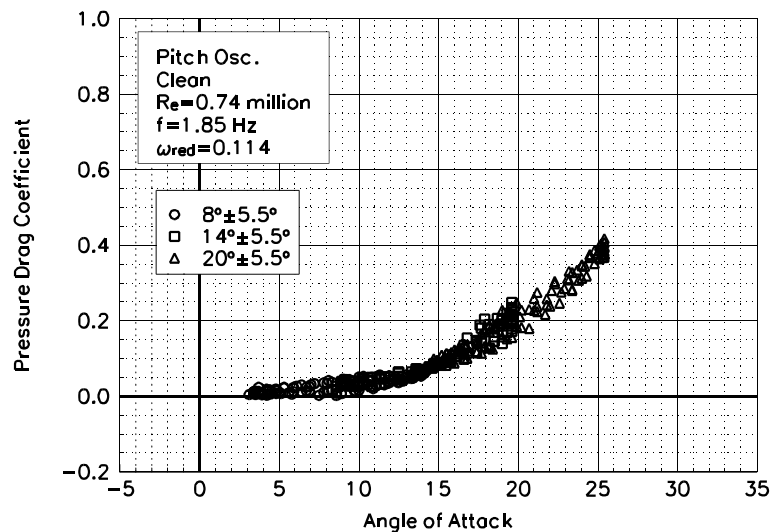


Figure C8. Pressure drag coefficient vs α .

S814
Clean
 $Re=0.74$ million
 $\omega_{red}=0.114$

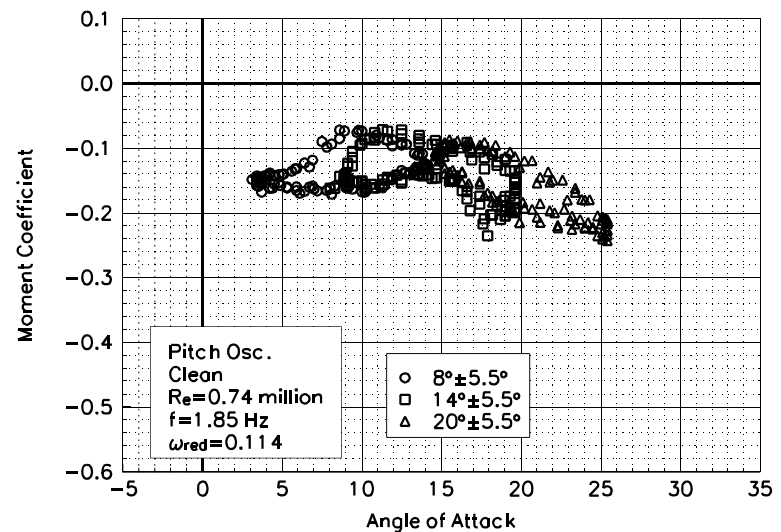


Figure C9. Moment coefficient vs α .

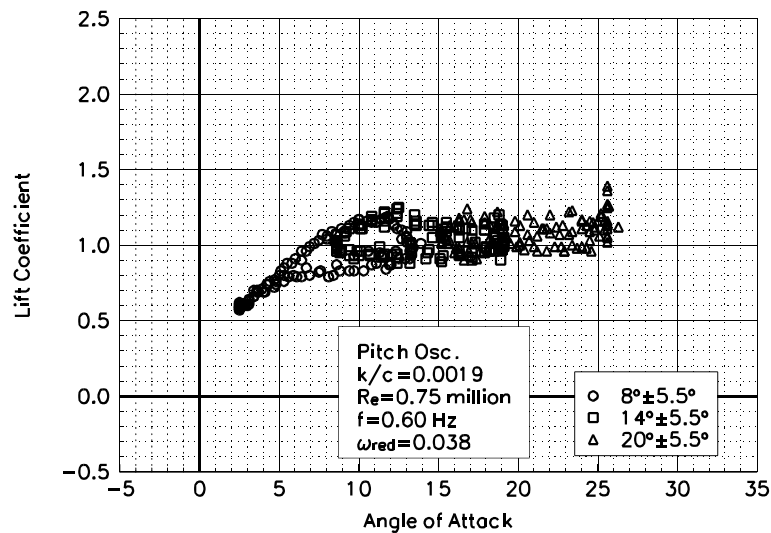


Figure C10. Lift coefficient vs α .

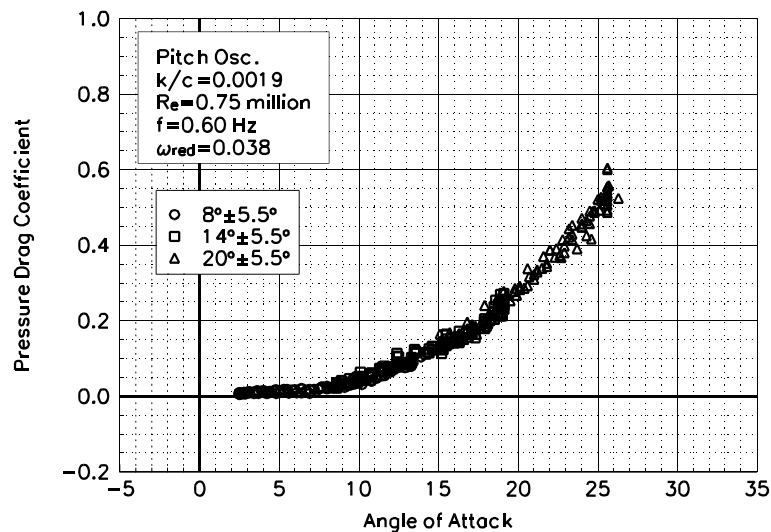


Figure C11. Pressure drag coefficient vs α .

S814
LEGR
 $Re = 0.75$ million
 $\omega_{red} = 0.038$

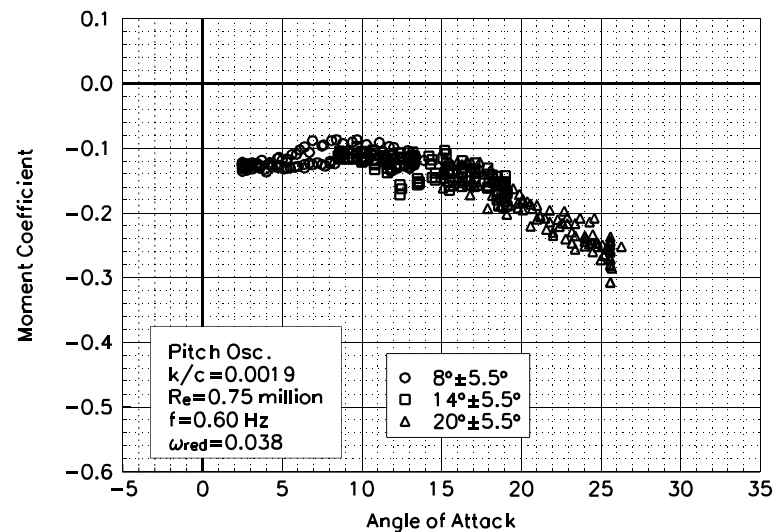


Figure C12. Moment coefficient vs α .

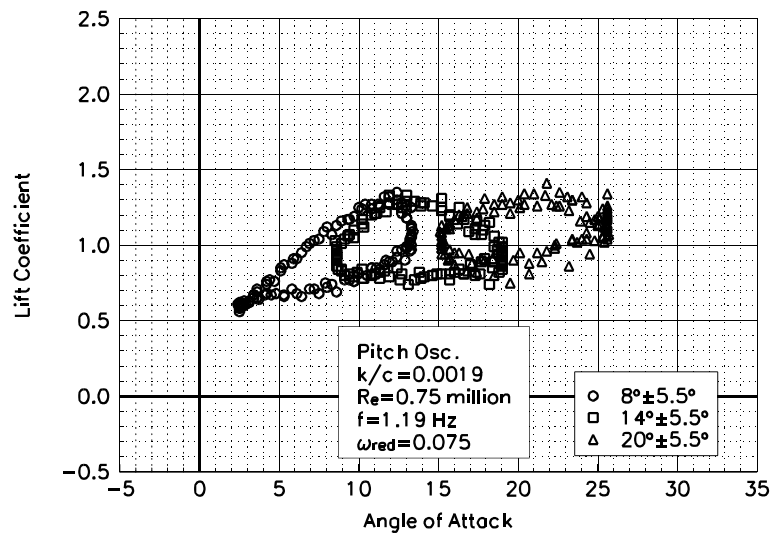


Figure C13. Lift coefficient vs α .

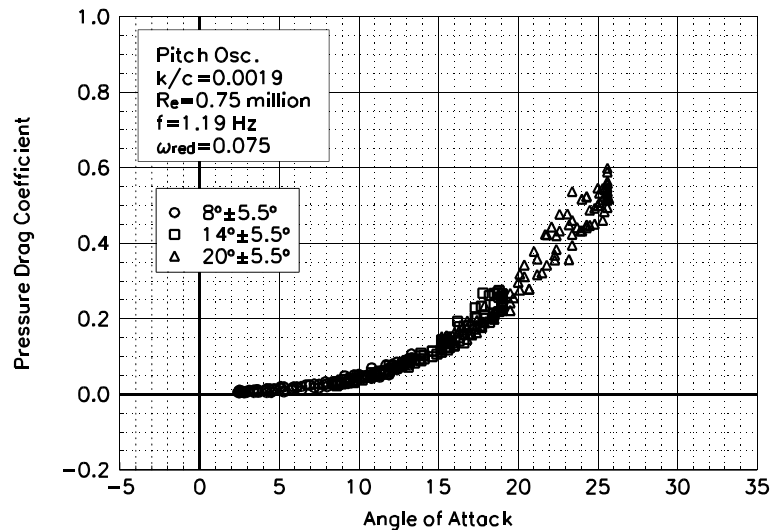


Figure C14. Pressure drag coefficient vs α .

S814
LEGR
 $Re = 0.75$ million
 $\omega_{red} = 0.075$

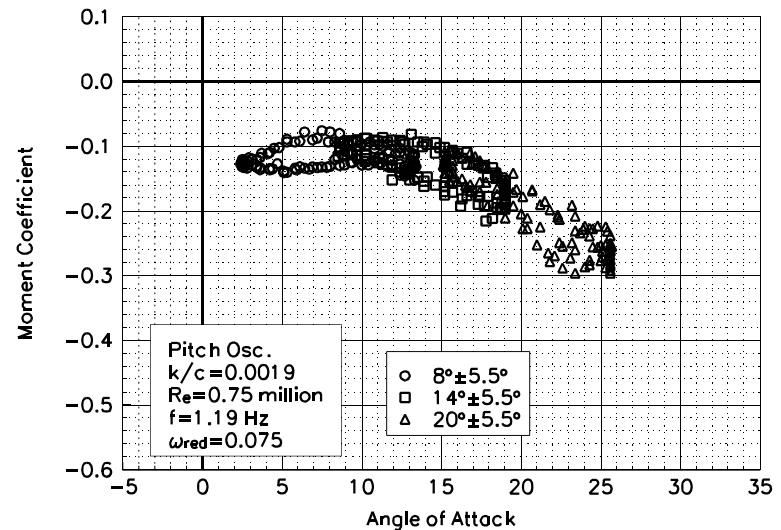


Figure C15. Moment coefficient vs α .

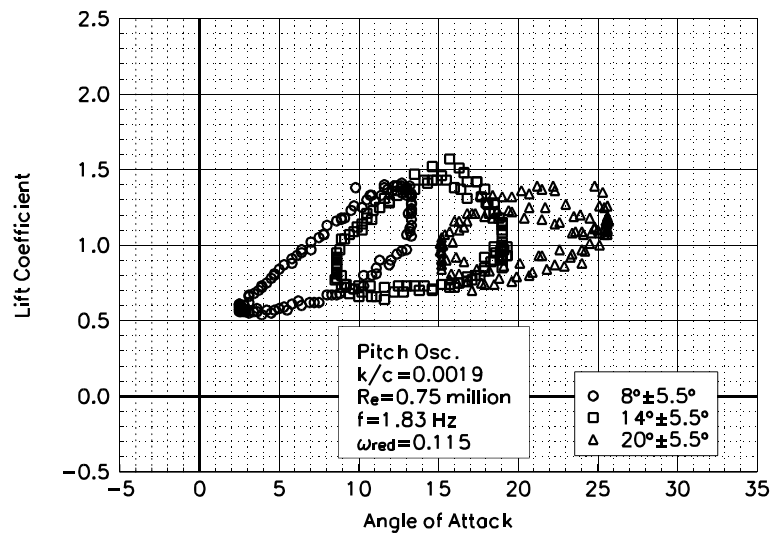


Figure C16. Lift coefficient vs α .

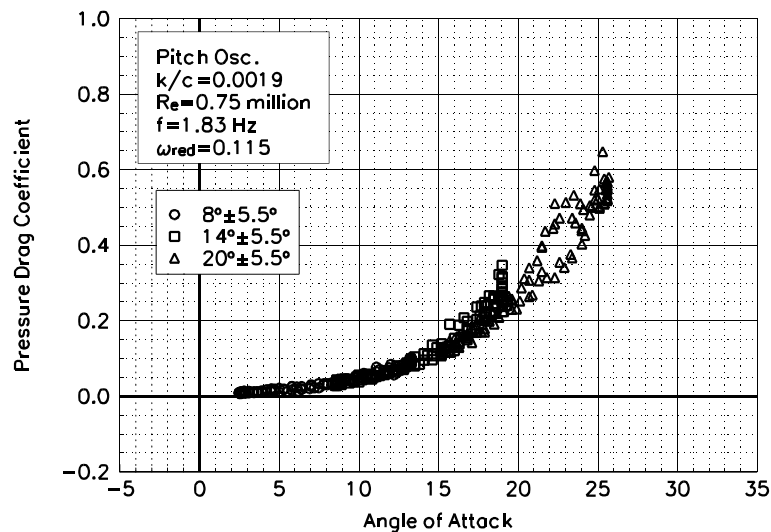


Figure C17. Pressure drag coefficient vs α .

S814
LEGR
 $Re = 0.75$ million
 $\omega_{red} = 0.115$

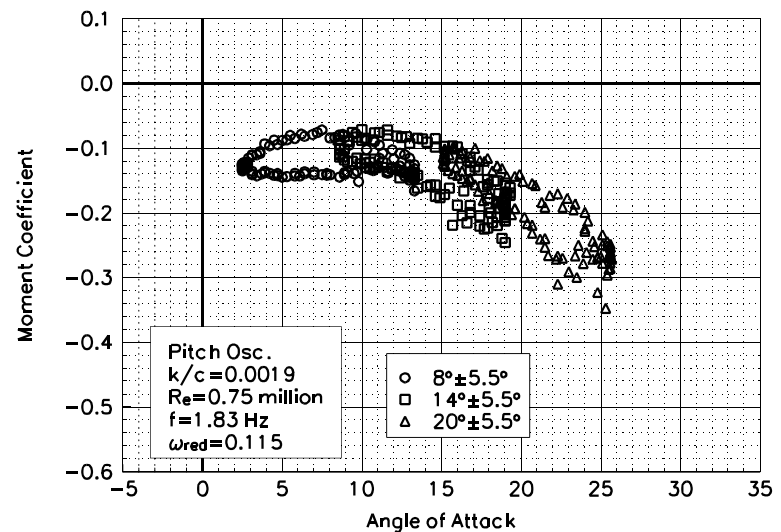


Figure C18. Moment coefficient vs α .

Unsteady Airfoil Characteristics

$\pm 5.5^\circ$ Sine, $Re = 1$ million

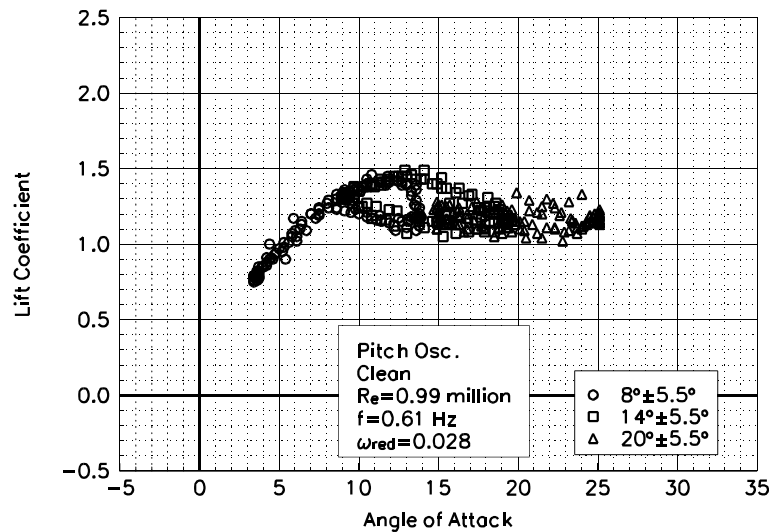


Figure C19. Lift coefficient vs α .

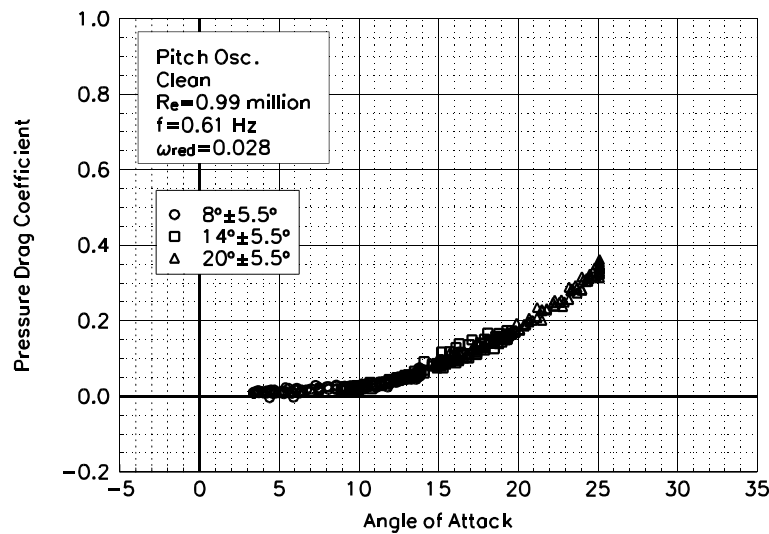


Figure C20. Pressure drag coefficient vs α .

S814
Clean
 $Re=0.99$ million
 $\omega_{reduced}=0.028$

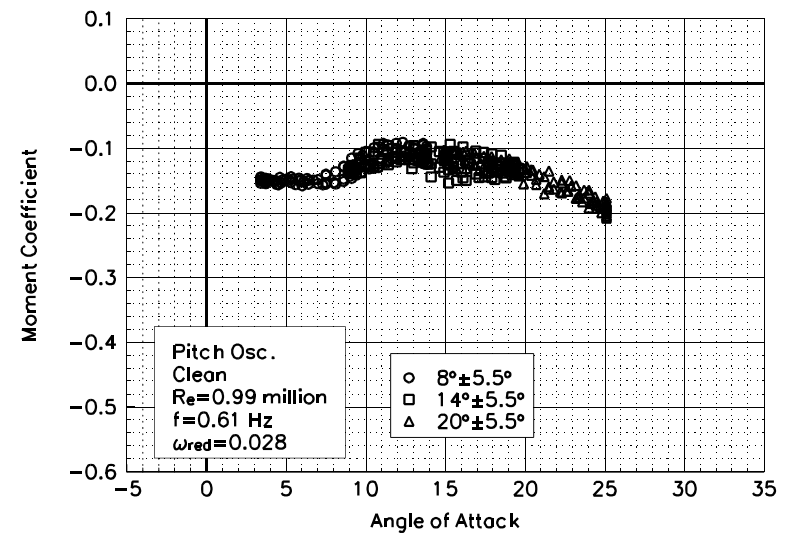


Figure C21. Moment coefficient vs α .

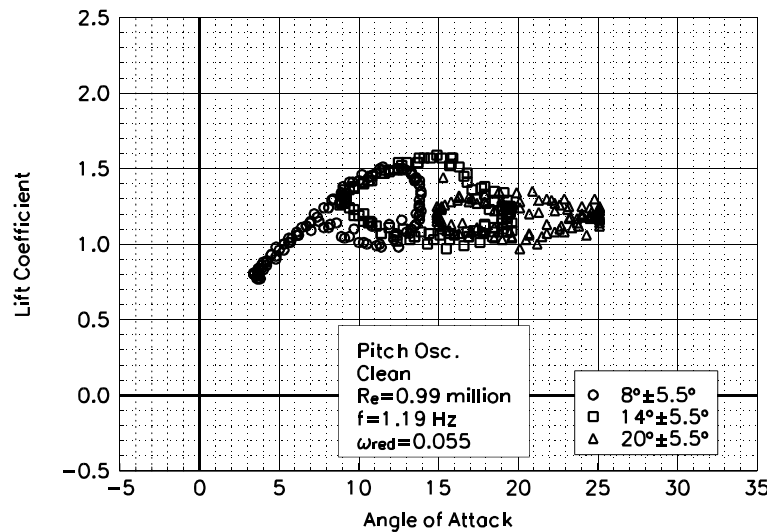


Figure C22. Lift coefficient vs α .

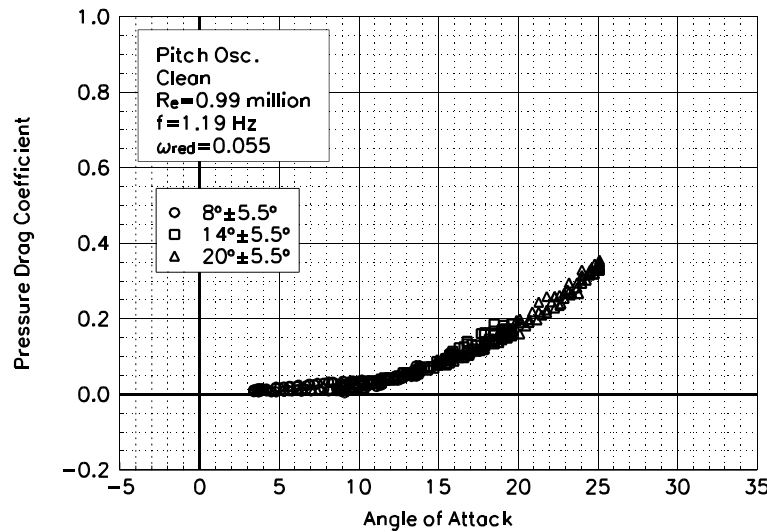


Figure C23. Pressure drag coefficient vs α .

S814
Clean
 $Re=0.99$ million
 $\omega_{reduced}=0.055$

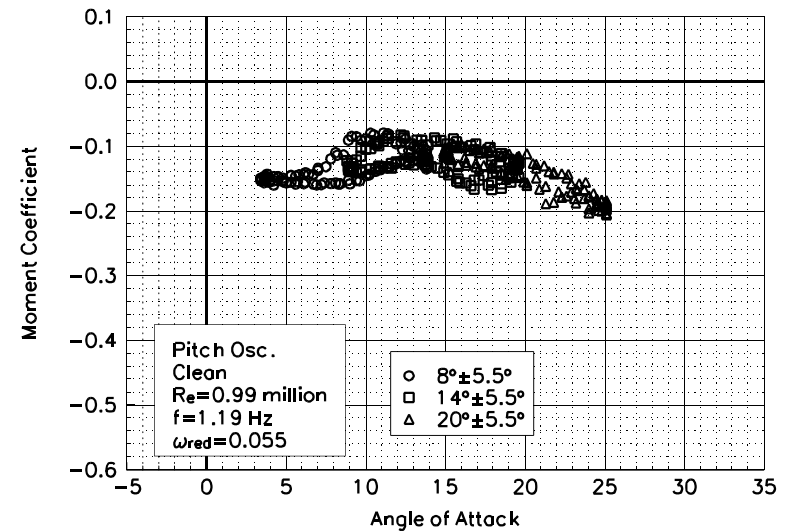


Figure C24. Moment coefficient vs α .

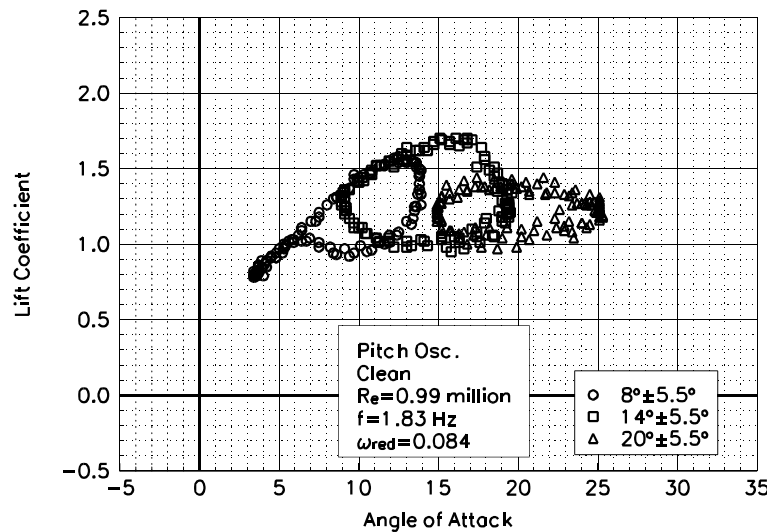


Figure C25. Lift coefficient vs α .

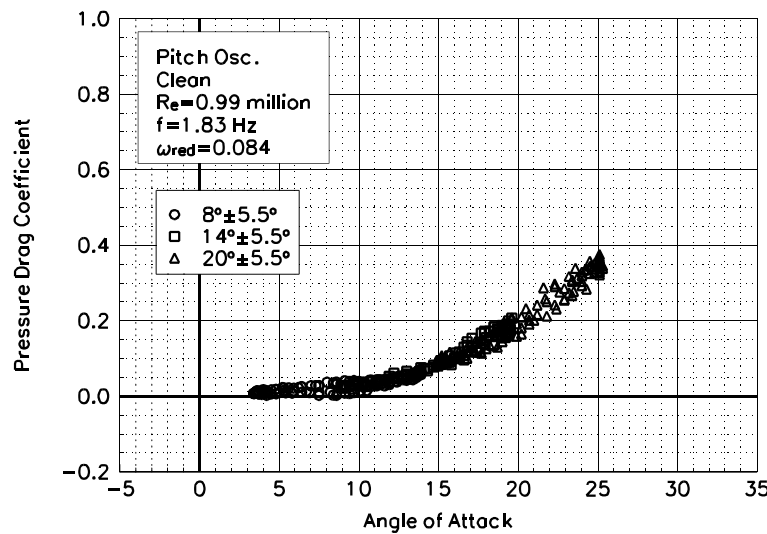


Figure C26. Pressure drag coefficient vs α .

S814
Clean
 $Re=0.99$ million
 $\omega_{red}=0.084$

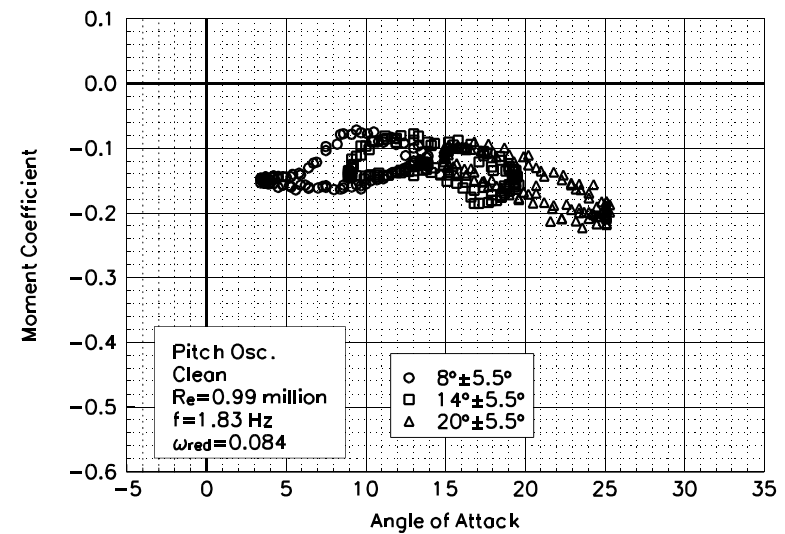


Figure C27. Moment coefficient vs α .

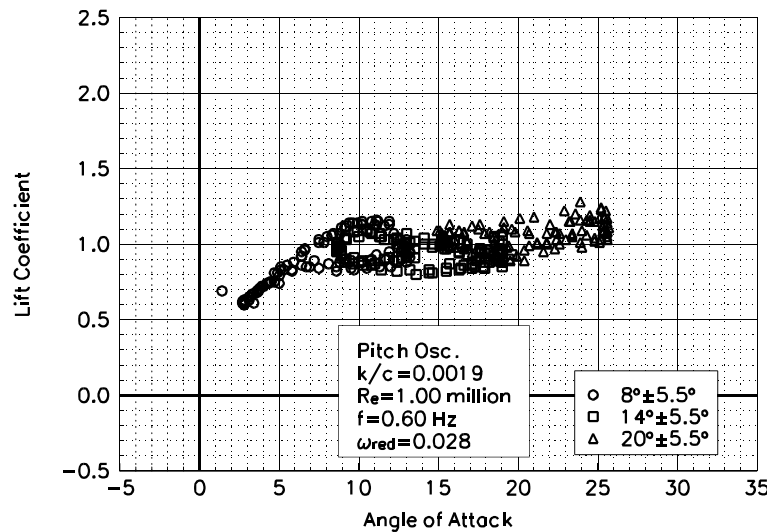


Figure C28. Lift coefficient vs α .

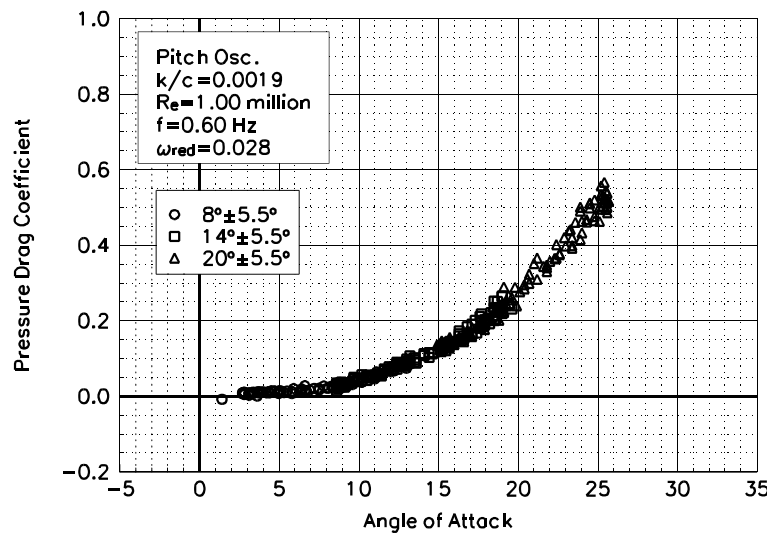


Figure C29. Pressure drag coefficient vs α .

S814
LEGR
Re=1.00 million
 $\omega_{\text{reduced}} = 0.028$

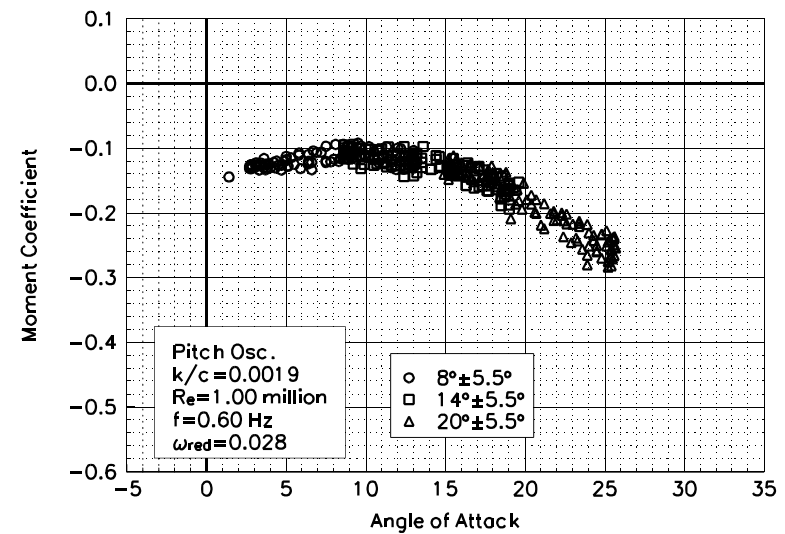


Figure C30. Moment coefficient vs α .

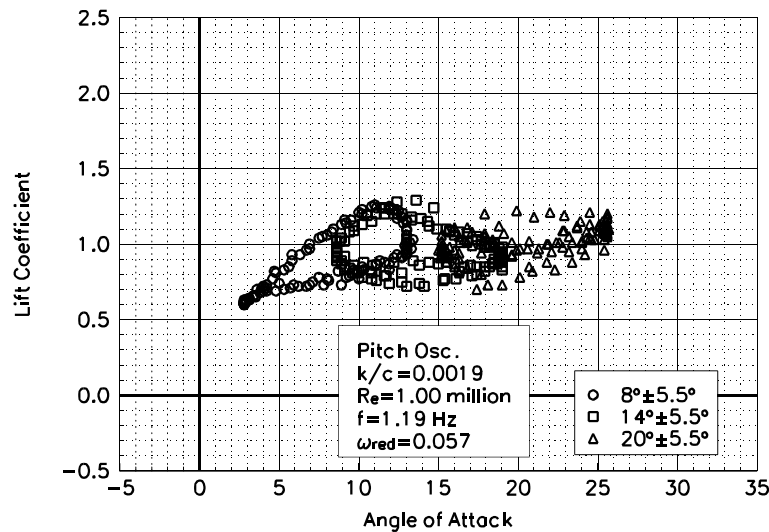


Figure C31. Lift coefficient vs α .

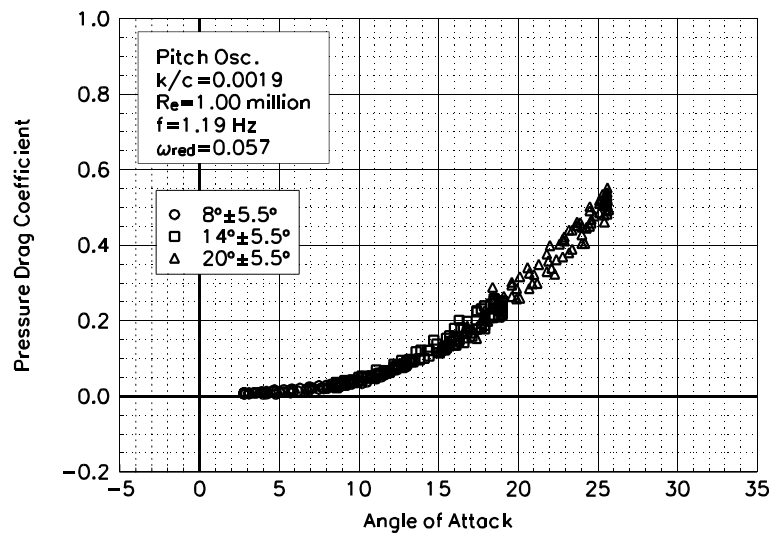


Figure C32. Pressure drag coefficient vs α .

**S814
LEGR
 $Re = 1.00 \text{ million}$
 $\omega_{\text{reduced}} = 0.057$**

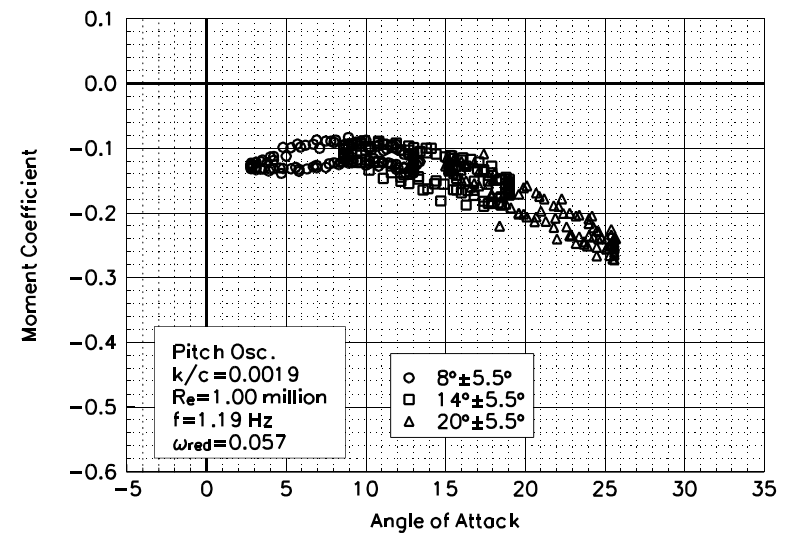


Figure C33. Moment coefficient vs α .

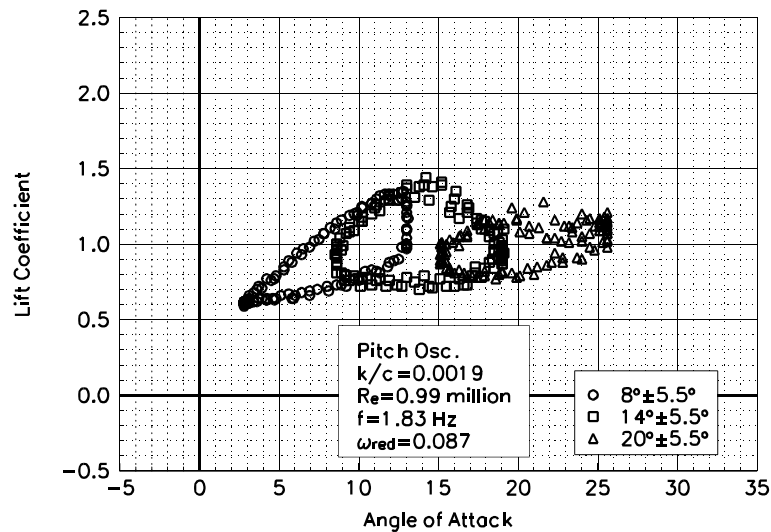


Figure C34. Lift coefficient vs α .

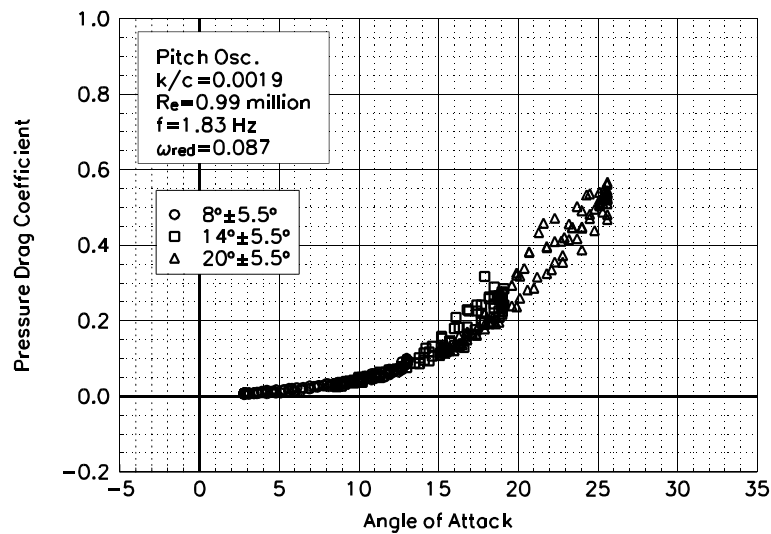


Figure C35. Pressure drag coefficient vs α .

S814
LEGR
Re=0.99 million
 $\omega_{reduced}=0.087$

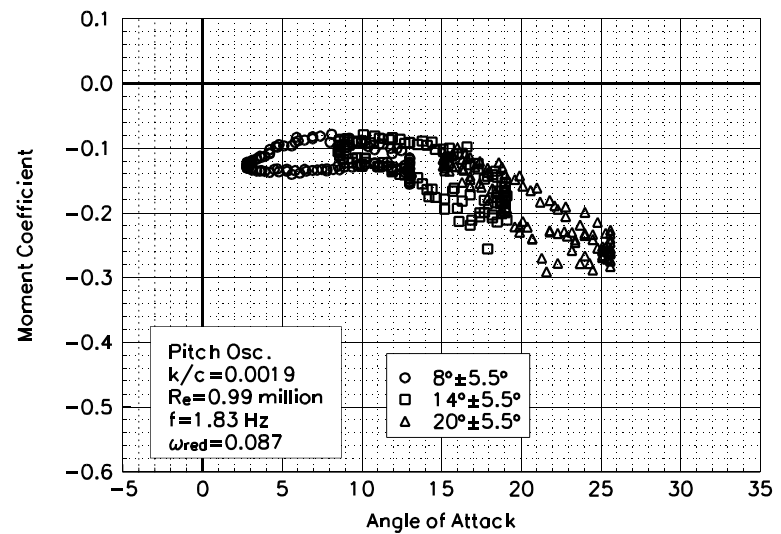


Figure C36. Moment coefficient vs α .

Unsteady Airfoil Characteristics

$\pm 5.5^\circ$ Sine, Re= 1.25 million

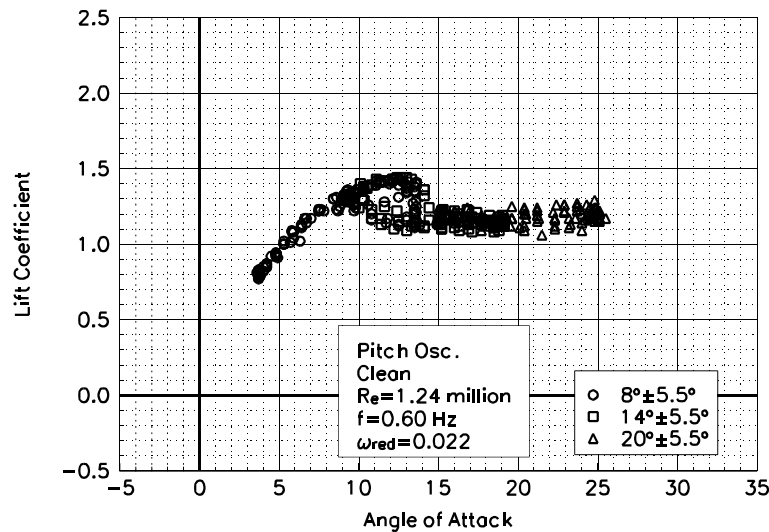


Figure C37. Lift coefficient vs α .

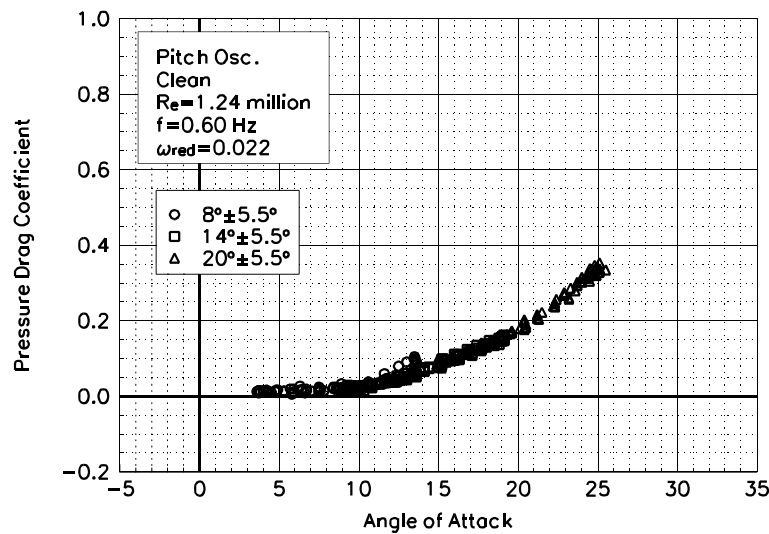


Figure C38. Pressure drag coefficient vs α .

S814
Clean
 $Re=1.24$ million
 $\omega_{reduced}=0.022$

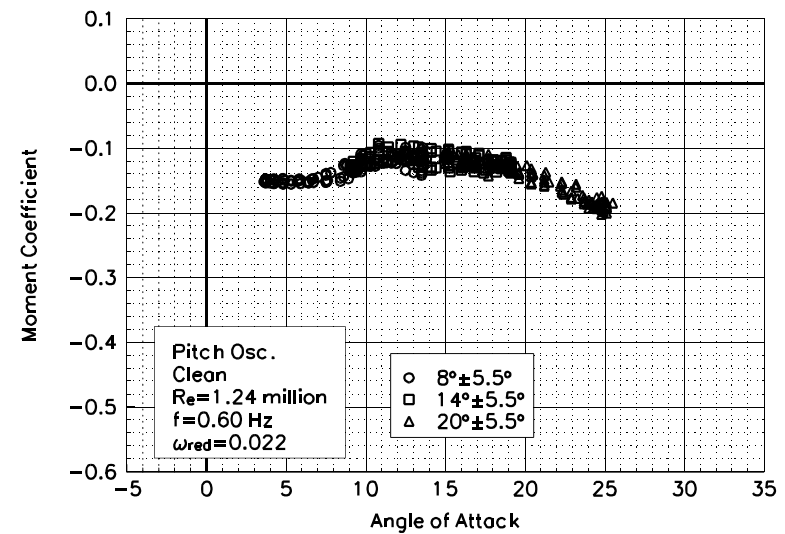


Figure C39. Moment coefficient vs α .

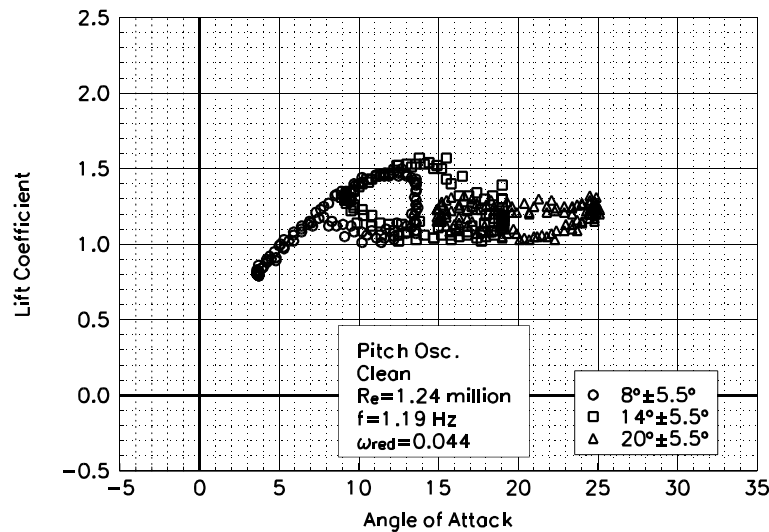


Figure C40. Lift coefficient vs α .

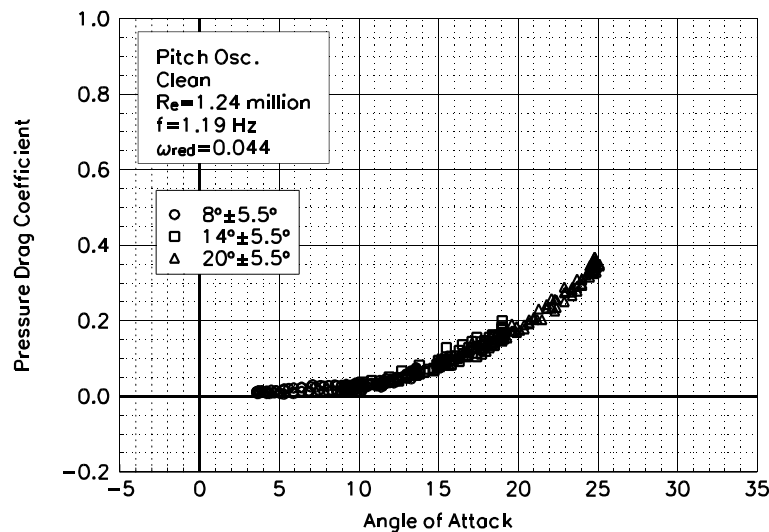


Figure C41. Pressure drag coefficient vs α .

S814
Clean
 $Re=1.24$ million
 $\omega_{reduced}=0.044$

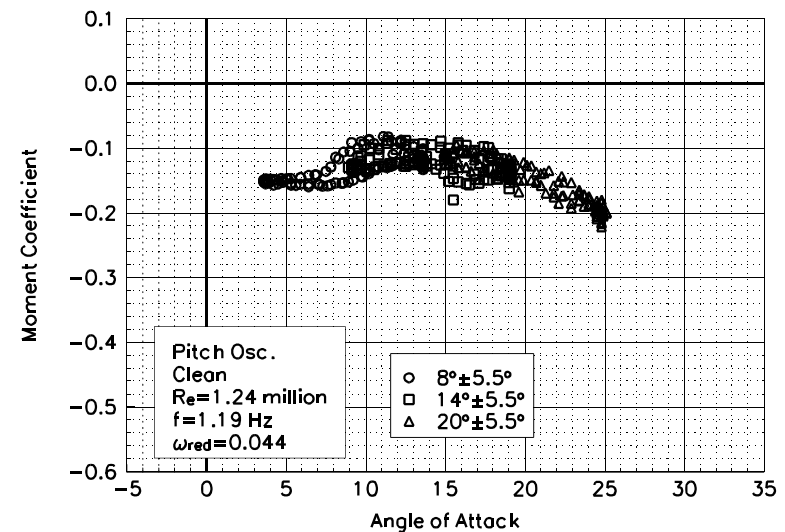


Figure C42. Moment coefficient vs α .

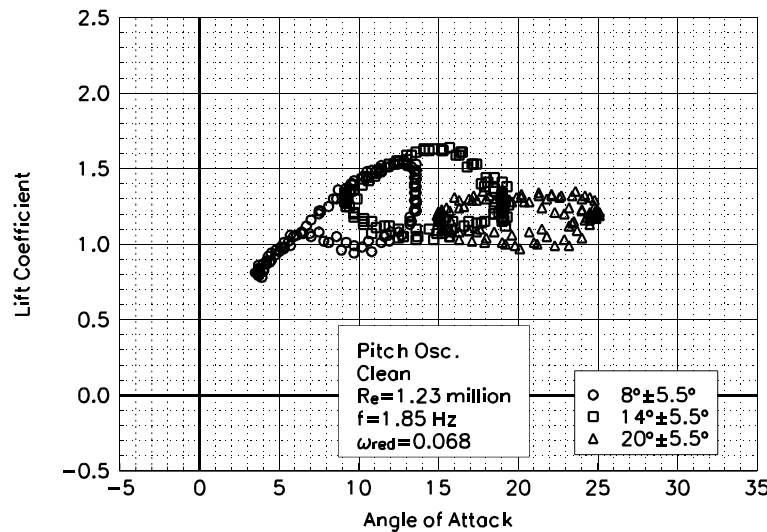


Figure C43. Lift coefficient vs α .

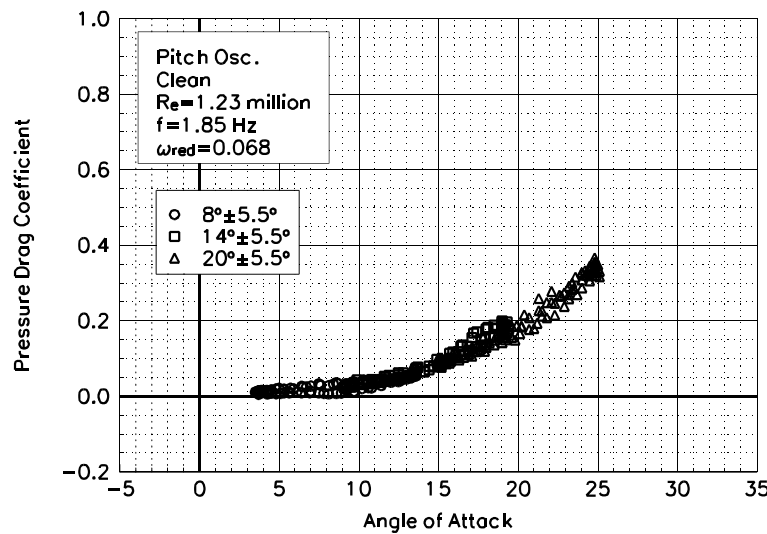


Figure C44. Pressure drag coefficient vs α .

S814
Clean
 $Re=1.23$ million
 $\omega_{reduced}=0.068$

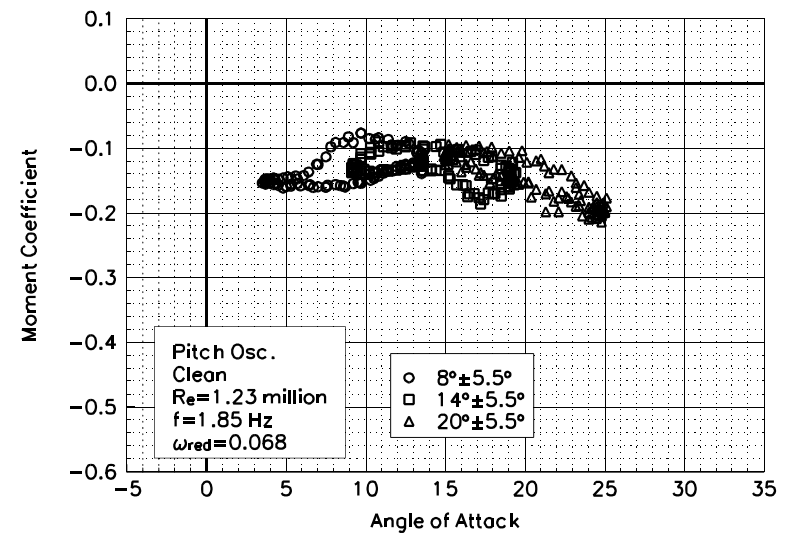


Figure C45. Moment coefficient vs α .

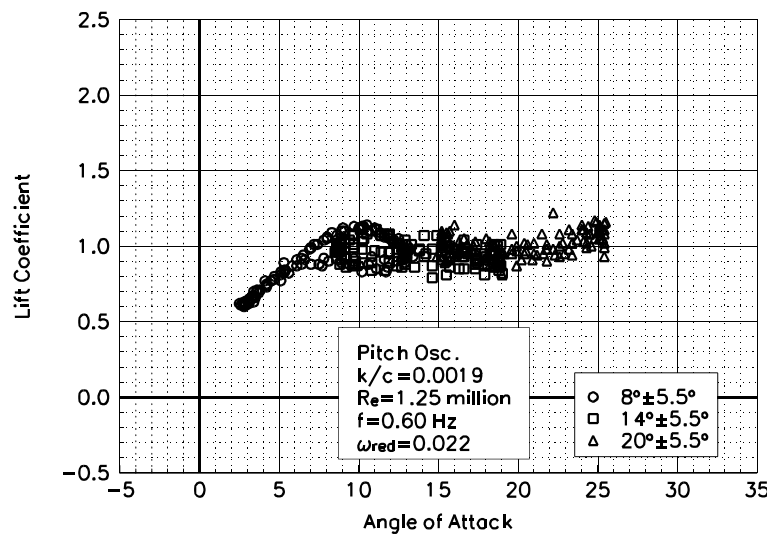


Figure C46. Lift coefficient vs α .

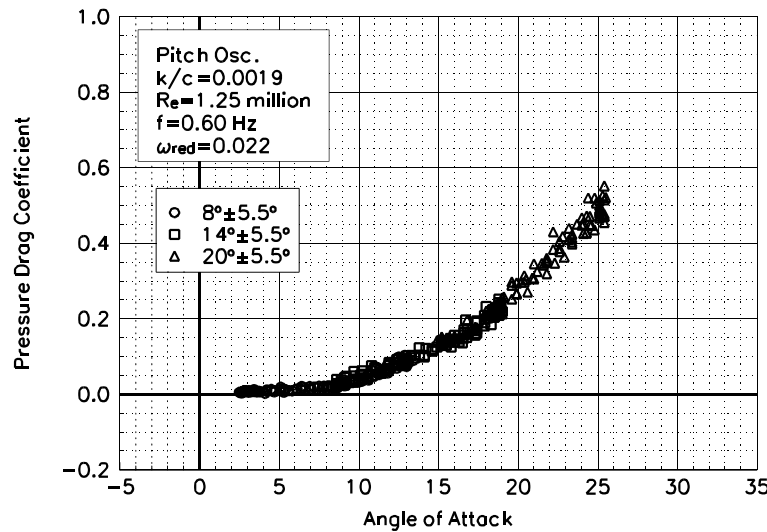


Figure C47. Pressure drag coefficient vs α .

S814
LEGR
Re=1.25 million
 $\omega_{\text{reduced}} = 0.022$

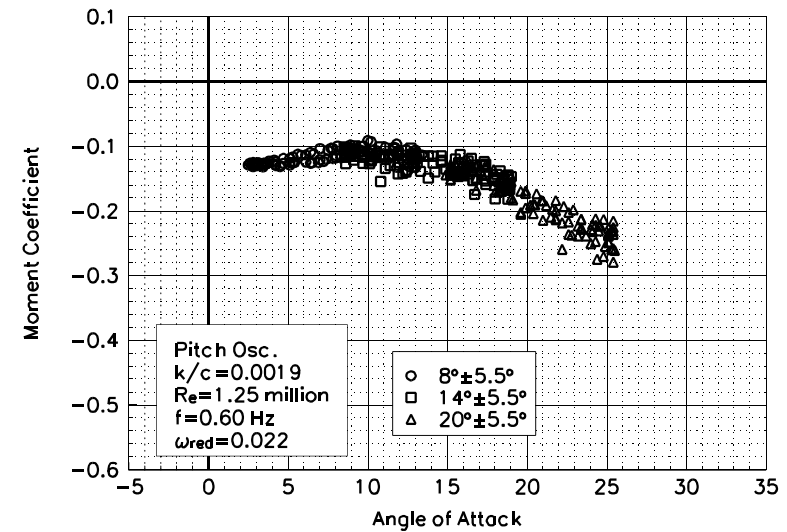


Figure C48. Moment coefficient vs α .

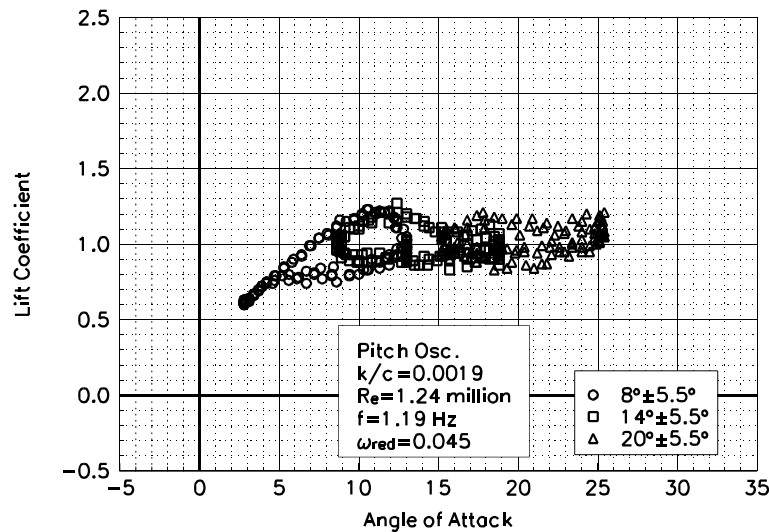


Figure C49. Lift coefficient vs α .

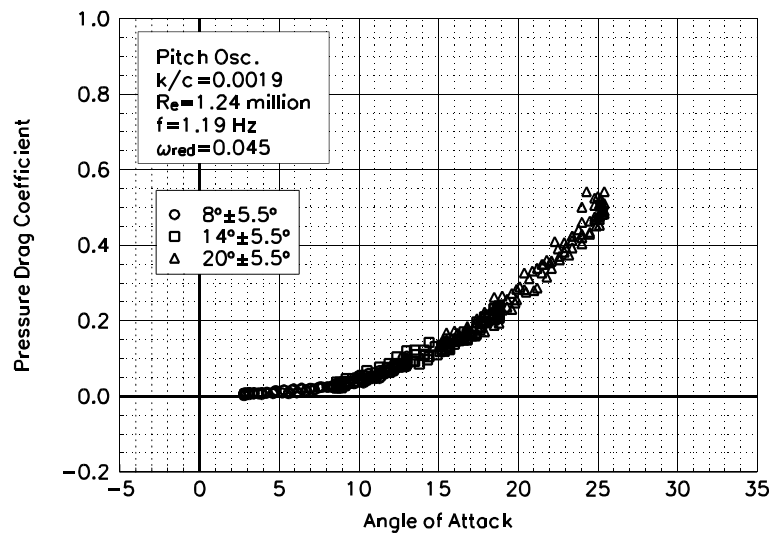


Figure C50. Pressure drag coefficient vs α .

S814
LEGR
Re=1.24 million
 $\omega_{\text{reduced}}=0.045$

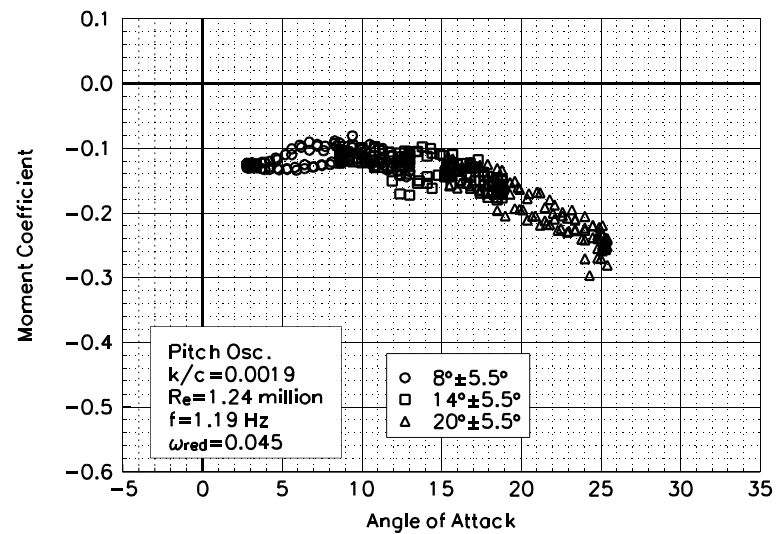


Figure C51. Moment coefficient vs α .

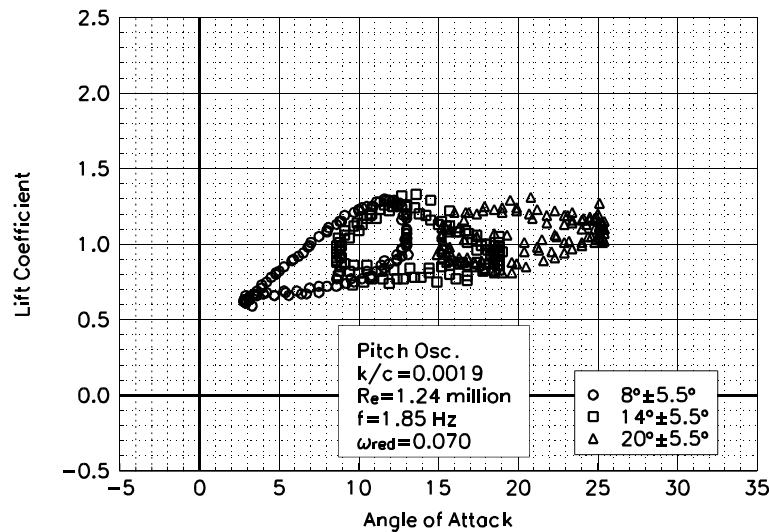


Figure C52. Lift coefficient vs α .

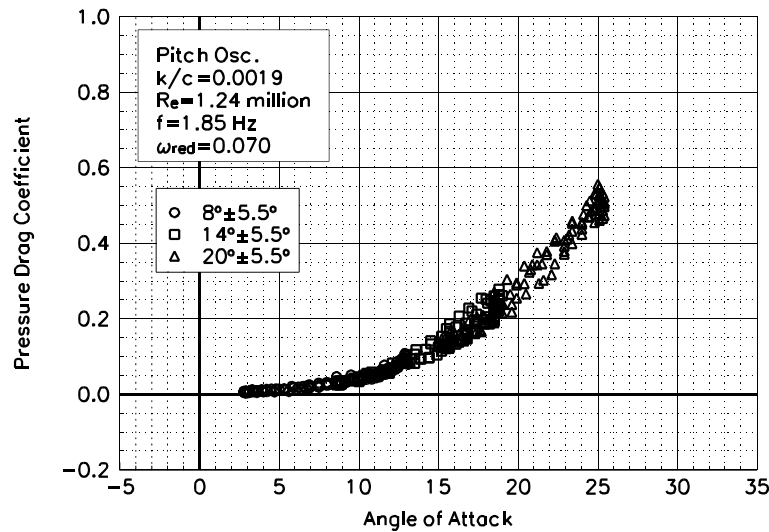


Figure C53. Pressure drag coefficient vs α .

S814
LEGR
 $Re = 1.24$ million
 $\omega_{reduced} = 0.070$

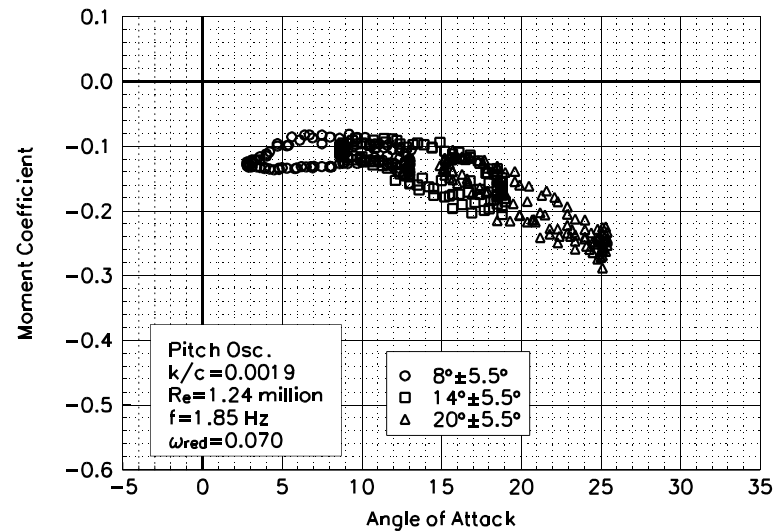


Figure C54. Moment coefficient vs α .

Unsteady Airfoil Characteristics

$\pm 5.5^\circ$ Sine, $Re = 1.5$ million

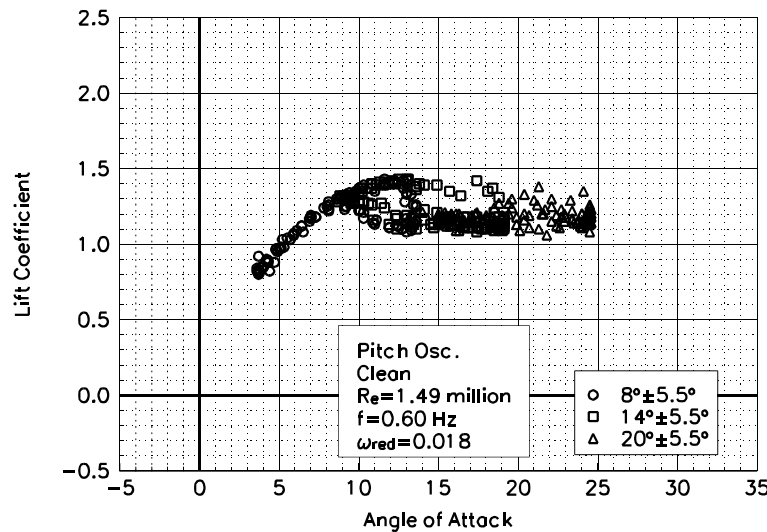


Figure C55. Lift coefficient vs α .

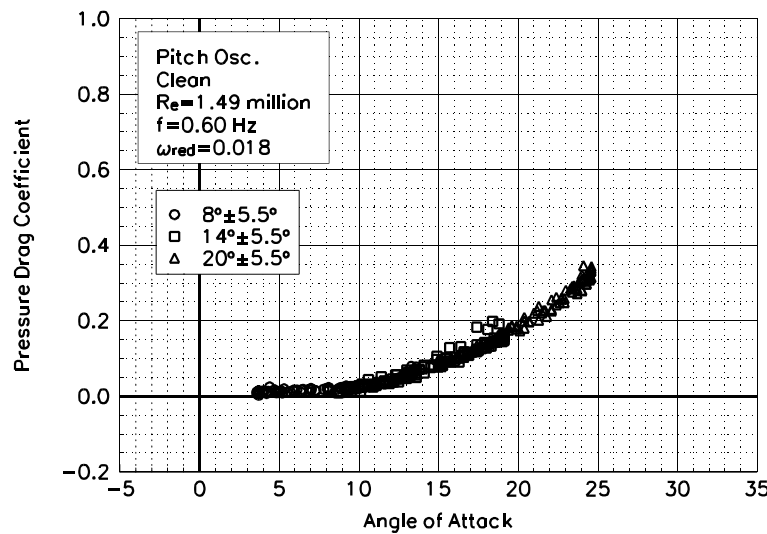


Figure C56. Pressure drag coefficient vs α .

S814
Clean
 $Re=1.49$ million
 $\omega_{reduced}=0.018$

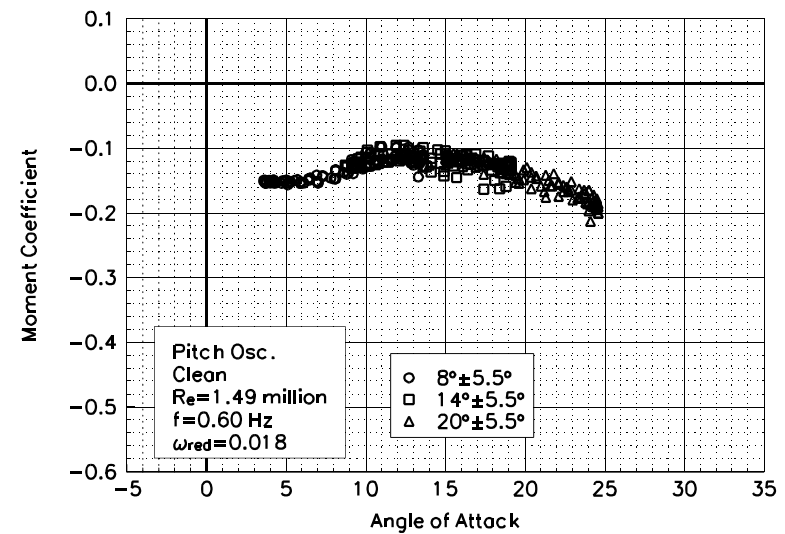


Figure C57. Moment coefficient vs α .

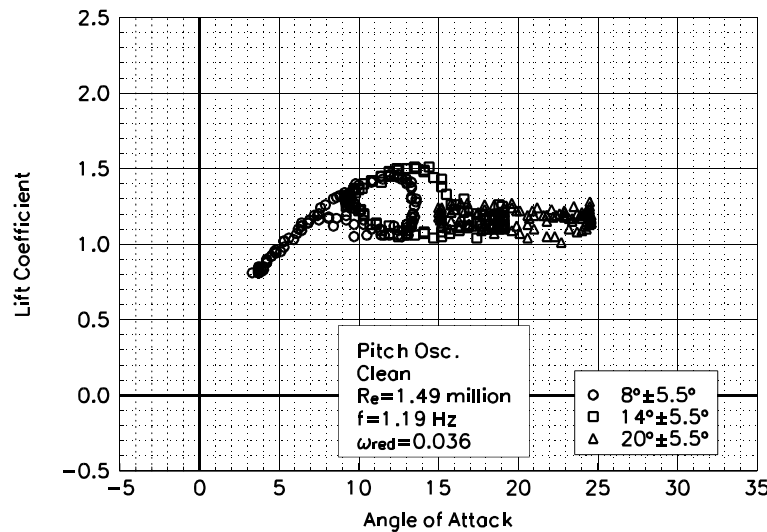


Figure C58. Lift coefficient vs α .

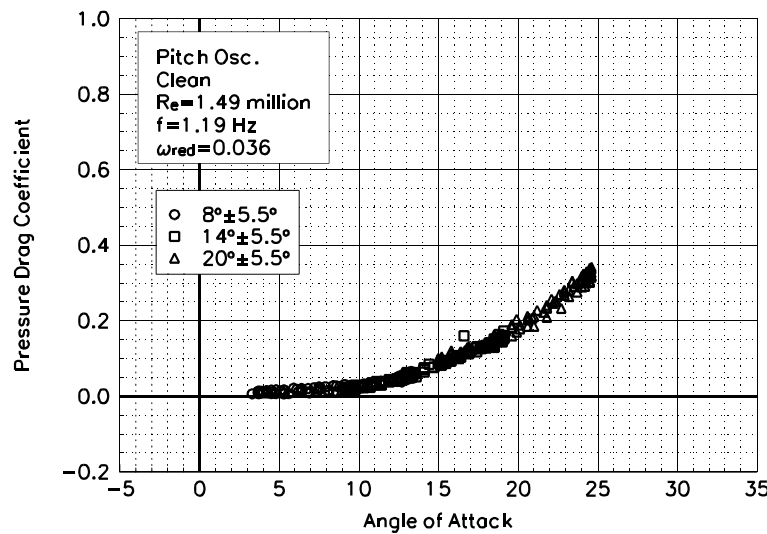


Figure C59. Pressure drag coefficient vs α .

S814
Clean
 $Re=1.49$ million
 $\omega_{reduced}=0.036$

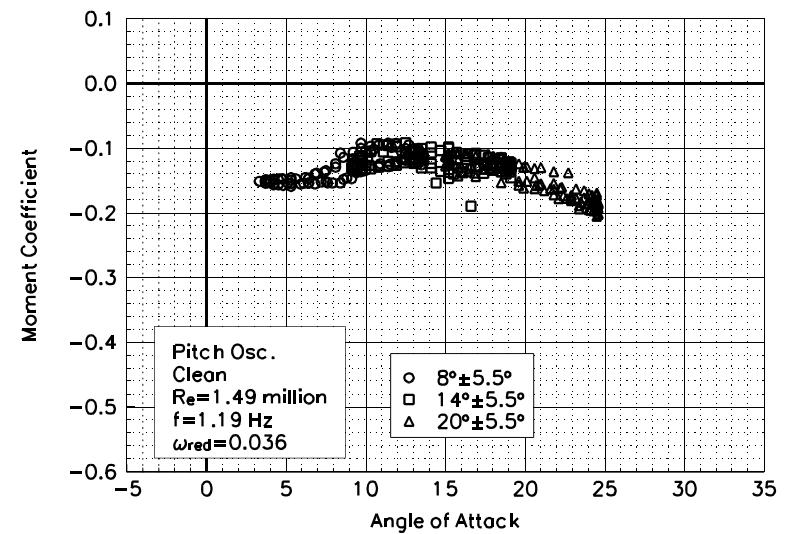


Figure C60. Moment coefficient vs α .

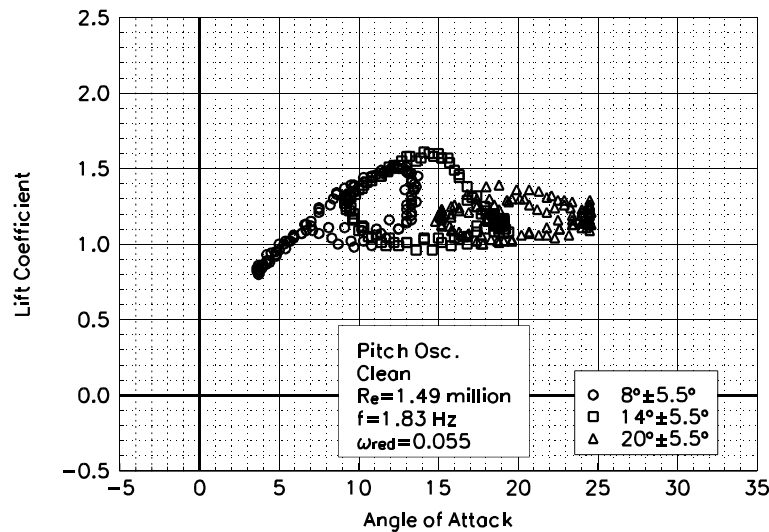


Figure C61. Lift coefficient vs α .

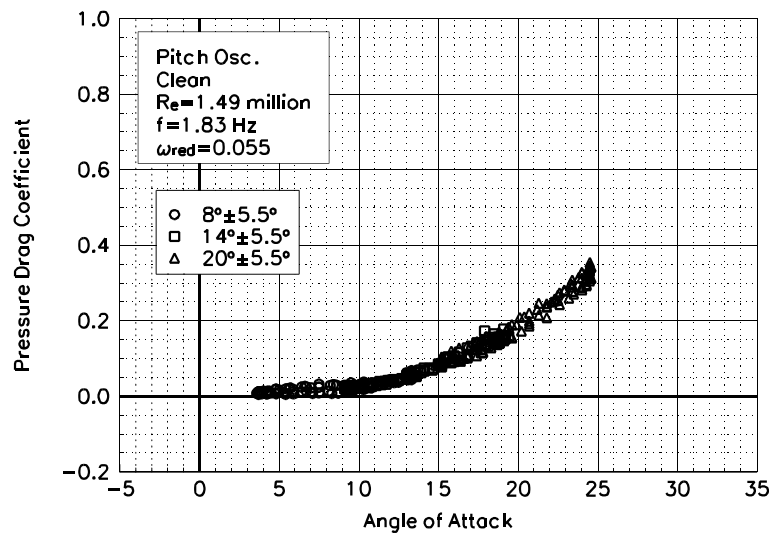


Figure C62. Pressure drag coefficient vs α .

S814
Clean
 $Re=1.49$ million
 $\omega_{reduced}=0.055$

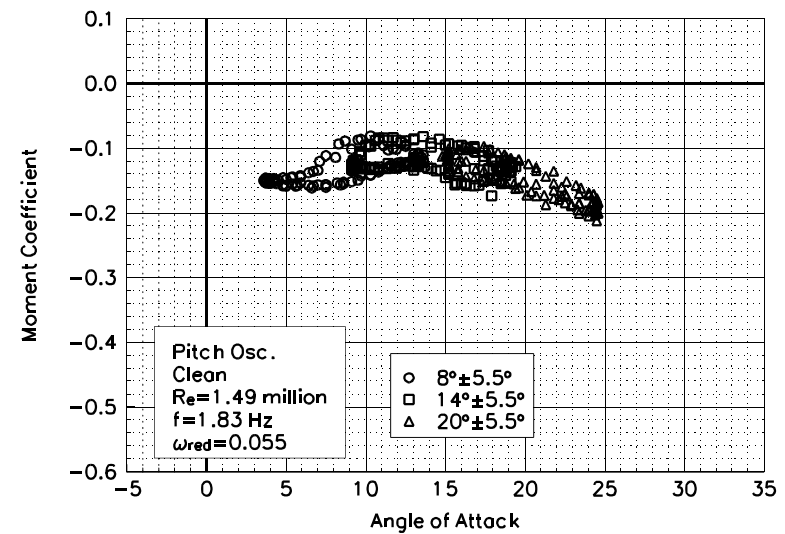


Figure C63. Moment coefficient vs α .

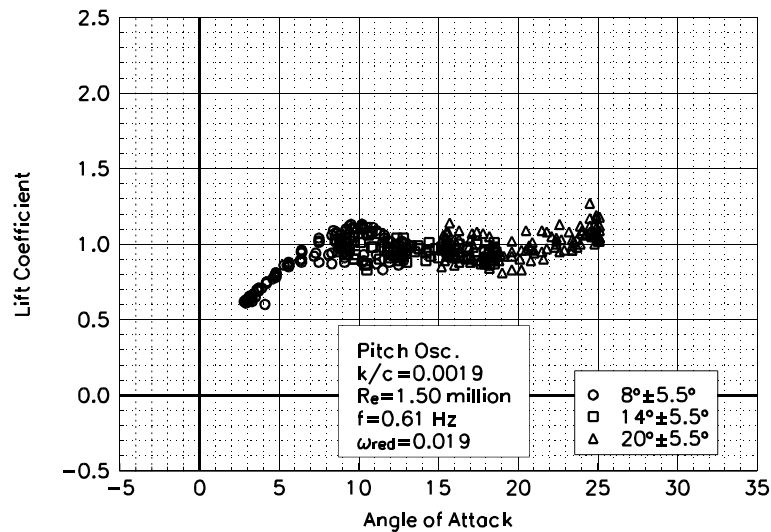


Figure C64. Lift coefficient vs α .

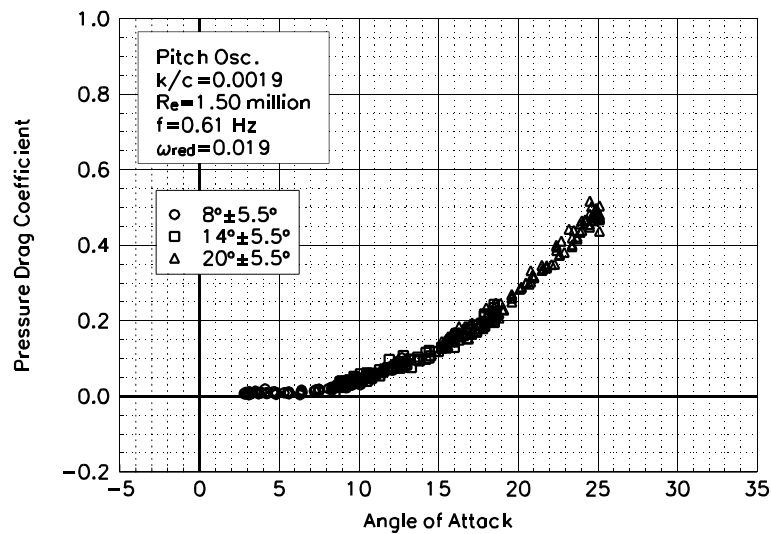


Figure C65. Pressure drag coefficient vs α .

S814
LEGR
Re=1.50 million
 $\omega_{\text{reduced}} = 0.019$

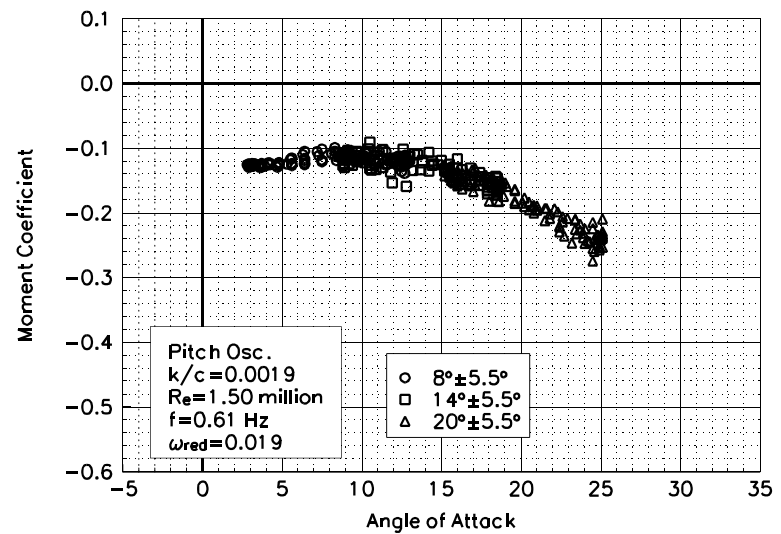


Figure C66. Moment coefficient vs α .

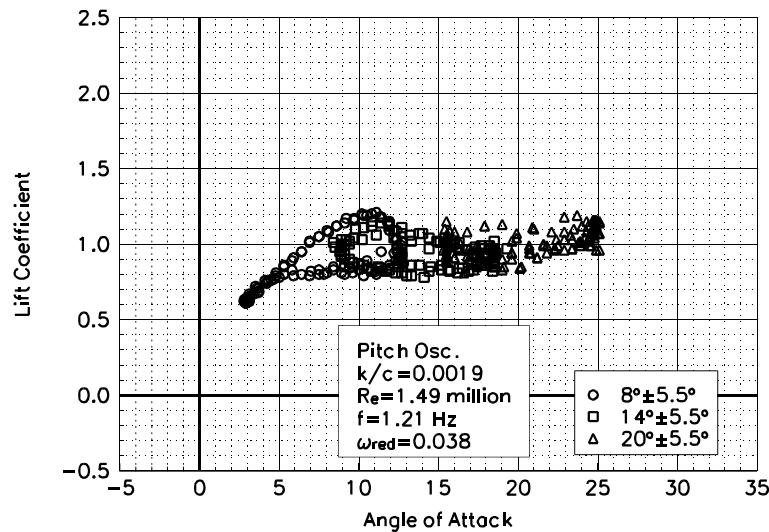


Figure C67. Lift coefficient vs α .

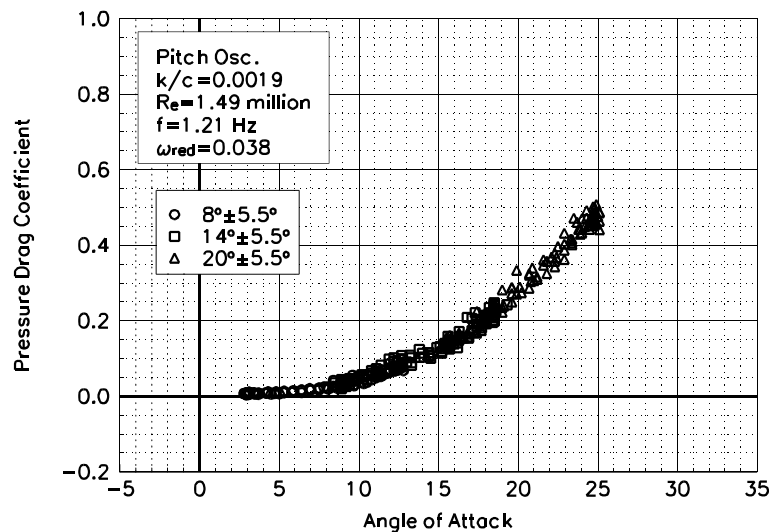


Figure C68. Pressure drag coefficient vs α .

S814
LEGR
Re=1.49 million
 $\omega_{\text{reduced}} = 0.038$

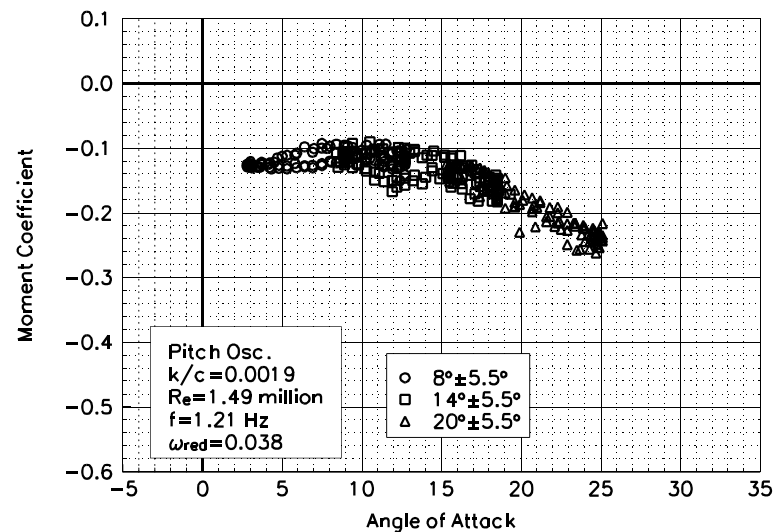


Figure C69. Moment coefficient vs α .

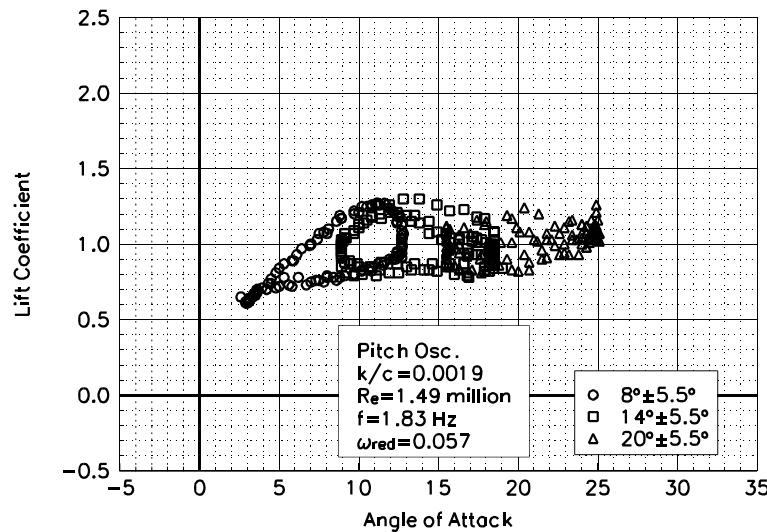


Figure C70. Lift coefficient vs α .

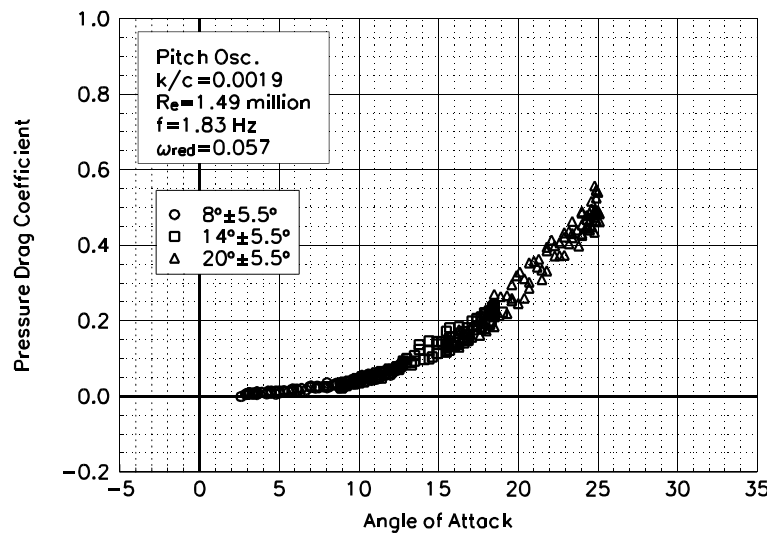


Figure C71. Pressure drag coefficient vs α .

S814
LEGR
Re=1.49 million
 ω_{red} =0.057

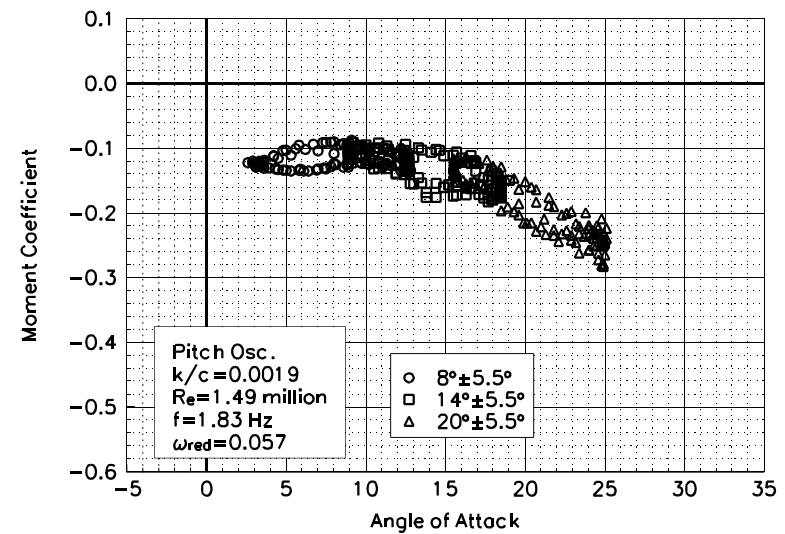


Figure C72. Moment coefficient vs α .

Unsteady Airfoil Characteristics

$\pm 10^\circ$ Sine, $Re = 0.75$ million

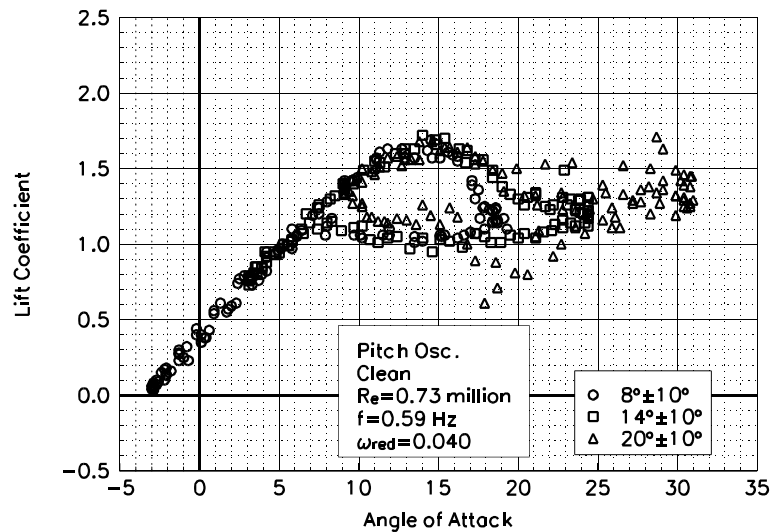


Figure C73. Lift coefficient vs α .

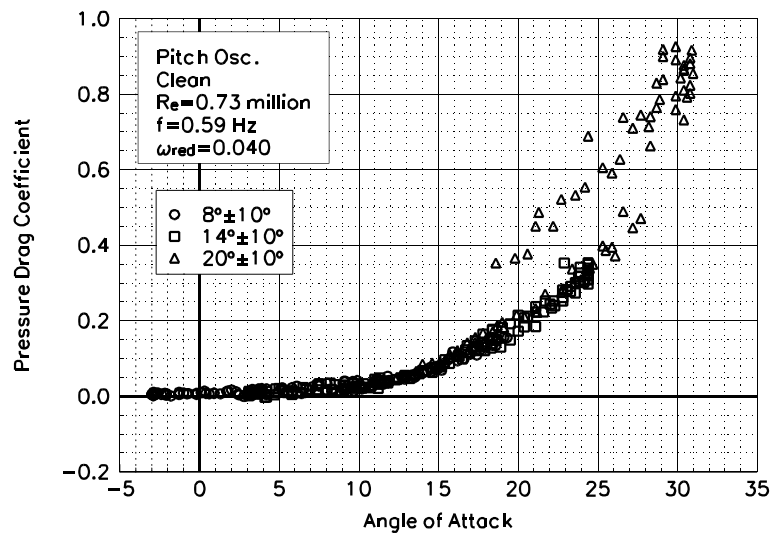


Figure C74. Pressure drag coefficient vs α .

S814
Clean
 $Re=0.73$ million
 $\omega_{reduced}=0.040$

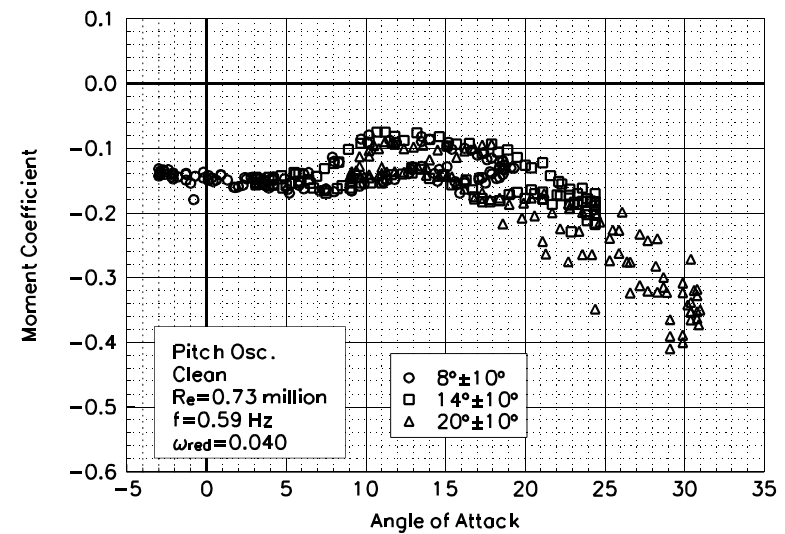


Figure C75. Moment coefficient vs α .

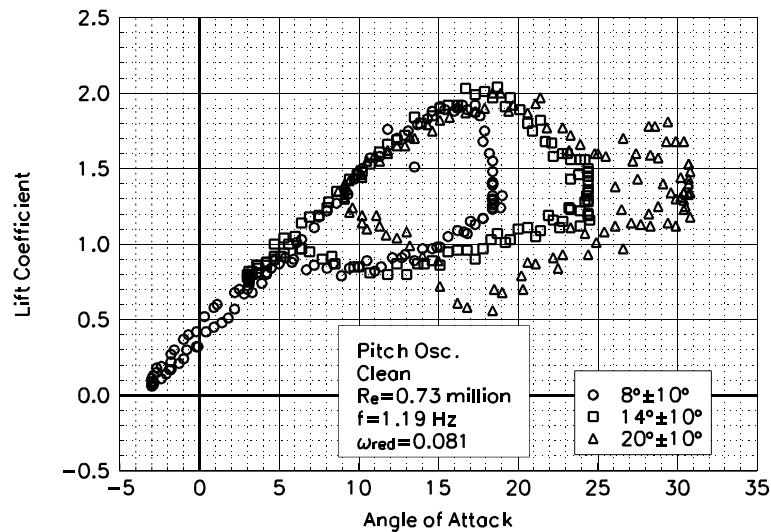


Figure C76. Lift coefficient vs α .

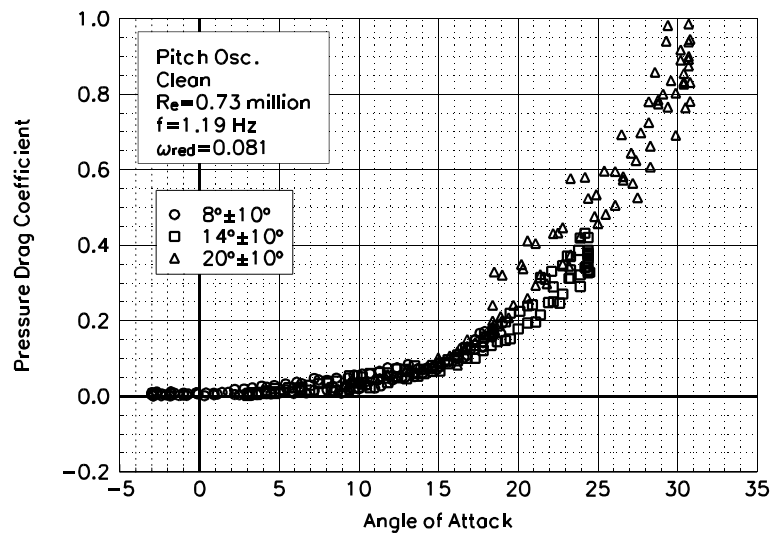


Figure C77. Pressure drag coefficient vs α .

S814
Clean
 $Re=0.73$ million
 $\omega_{red}=0.081$

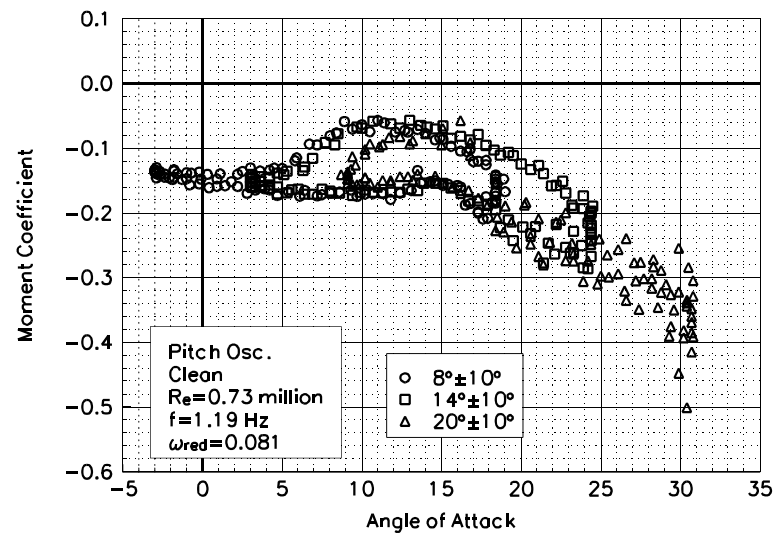


Figure C78. Moment coefficient vs α .

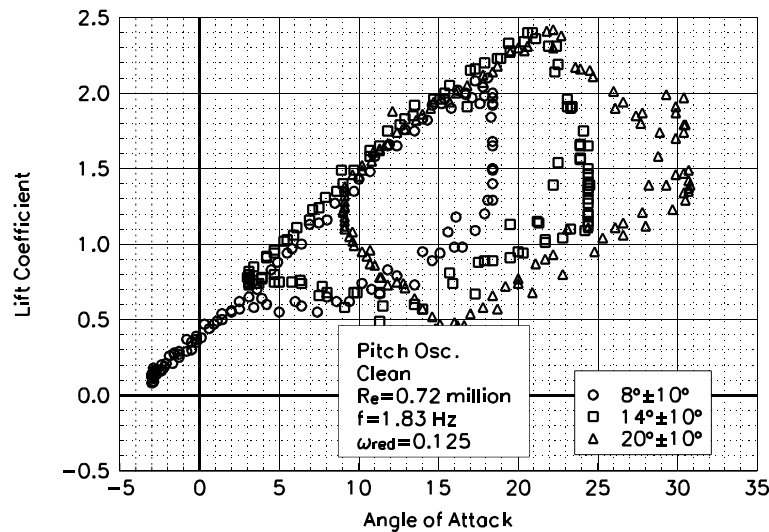


Figure C79. Lift coefficient vs α .

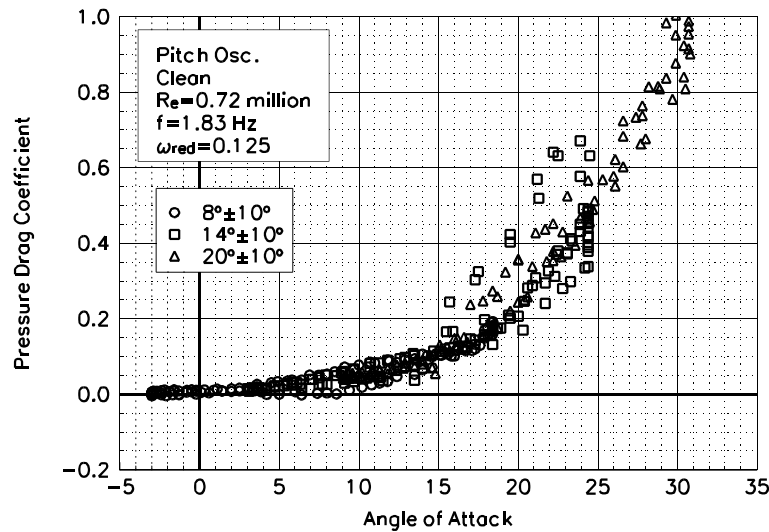


Figure C80. Pressure drag coefficient vs α .

S814
Clean
 $Re=0.72$ million
 $\omega_{reduced}=0.125$

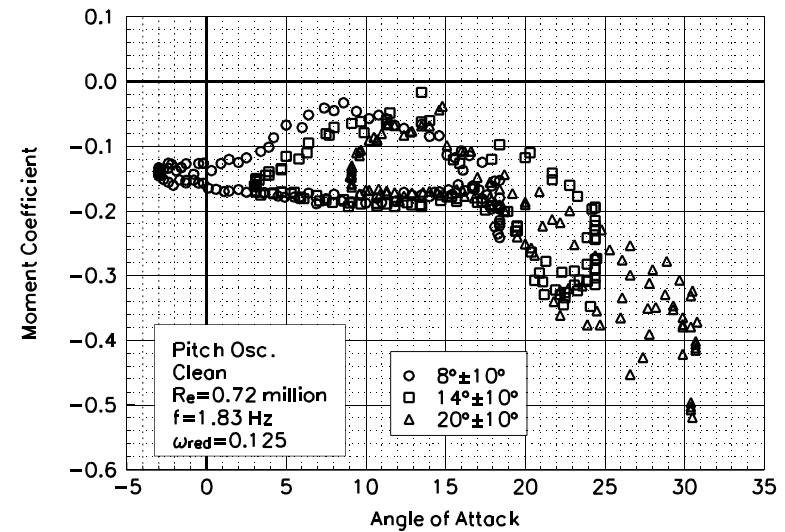


Figure C81. Moment coefficient vs α .

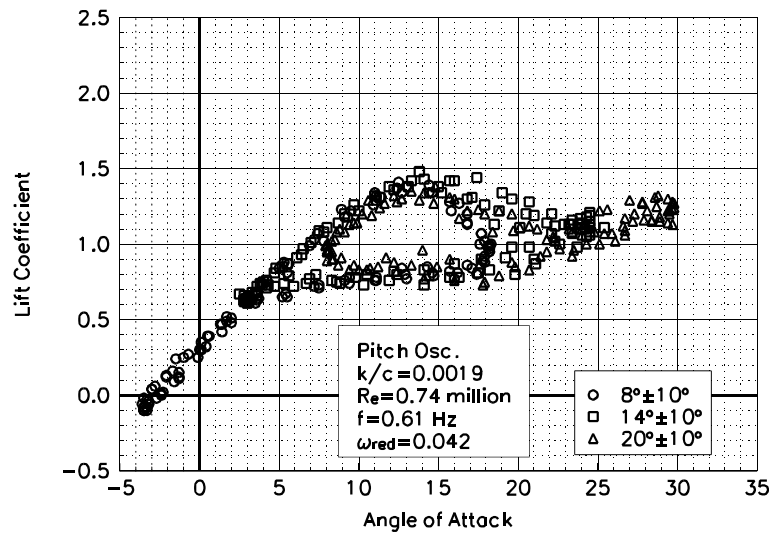


Figure C82. Lift coefficient vs α .

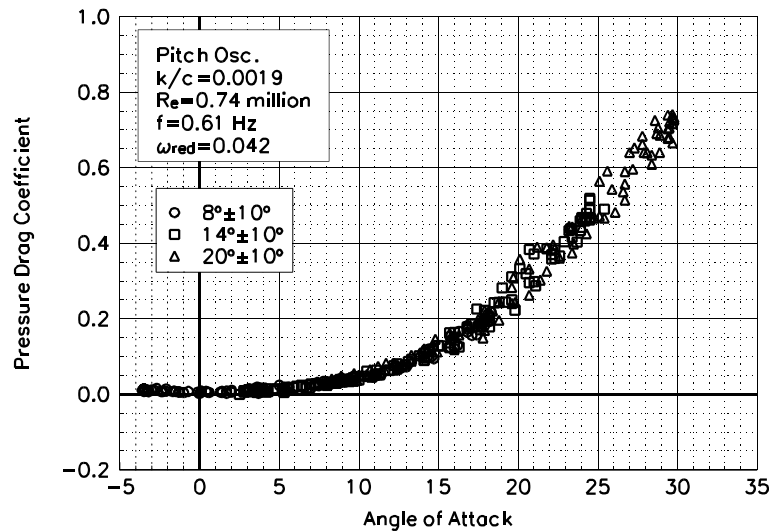


Figure C83. Pressure drag coefficient vs α .

S814
LEGR
 $Re = 0.74$ million
 $\omega_{red} = 0.042$

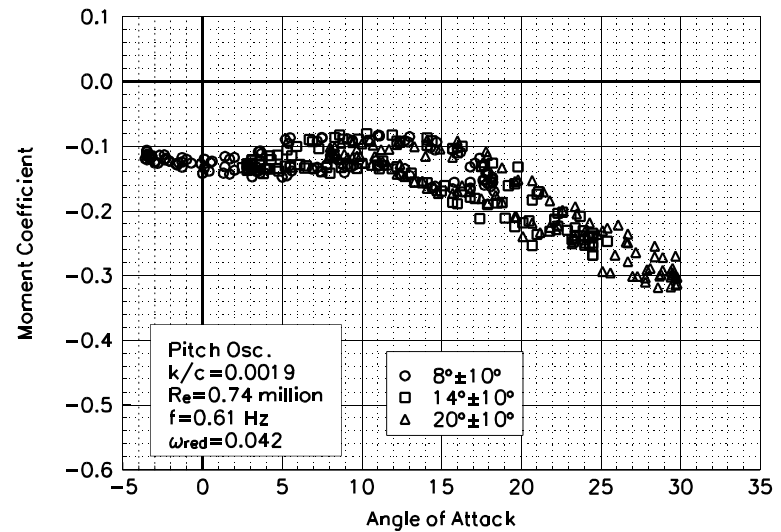


Figure C84. Moment coefficient vs α .

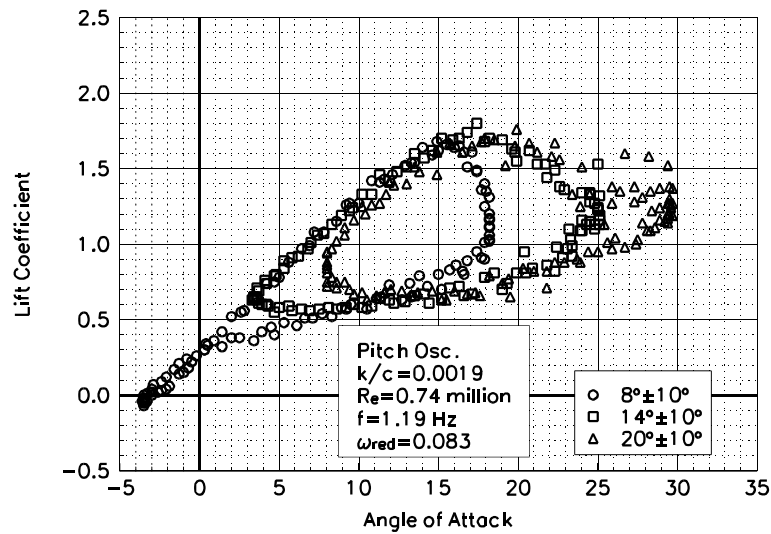


Figure C85. Lift coefficient vs α .

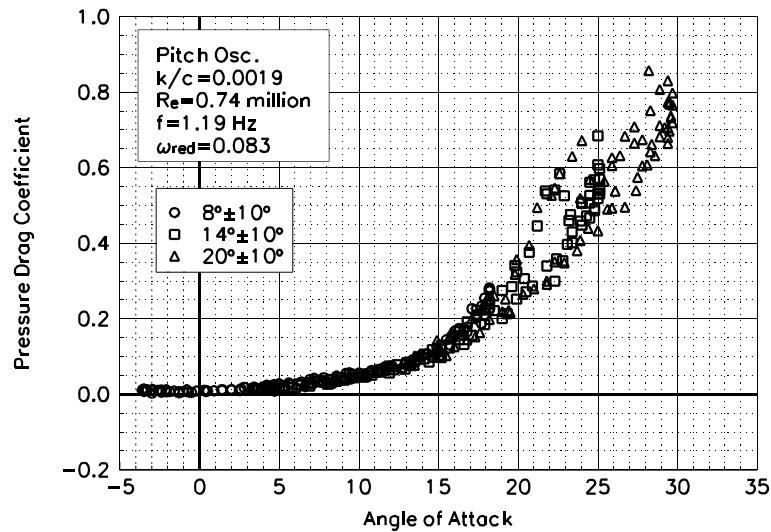


Figure C86. Pressure drag coefficient vs α .

S814
LEGR
 $Re = 0.74$ million
 $\omega_{red} = 0.083$

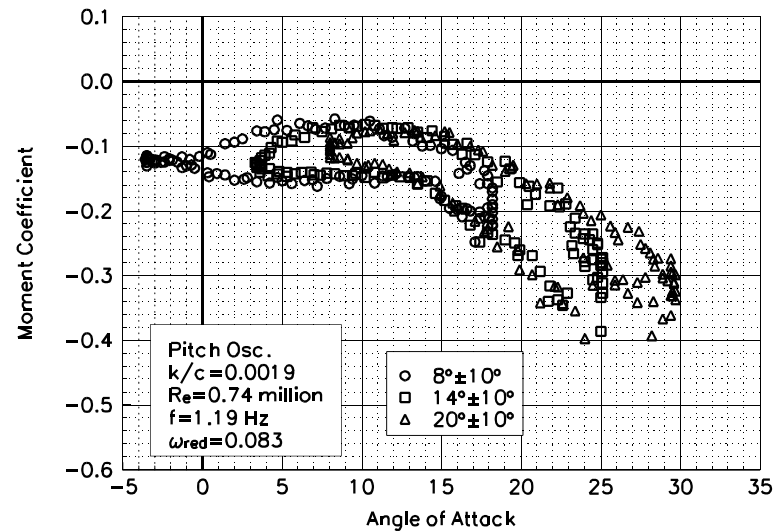


Figure C87. Moment coefficient vs α .

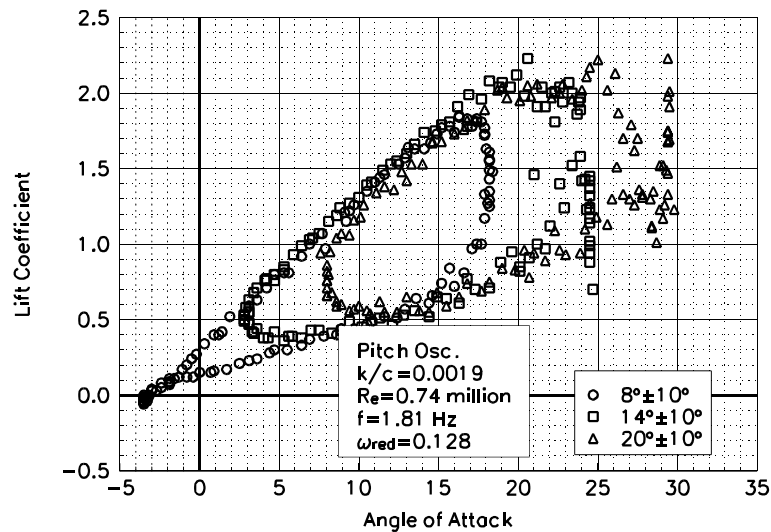


Figure C88. Lift coefficient vs α .

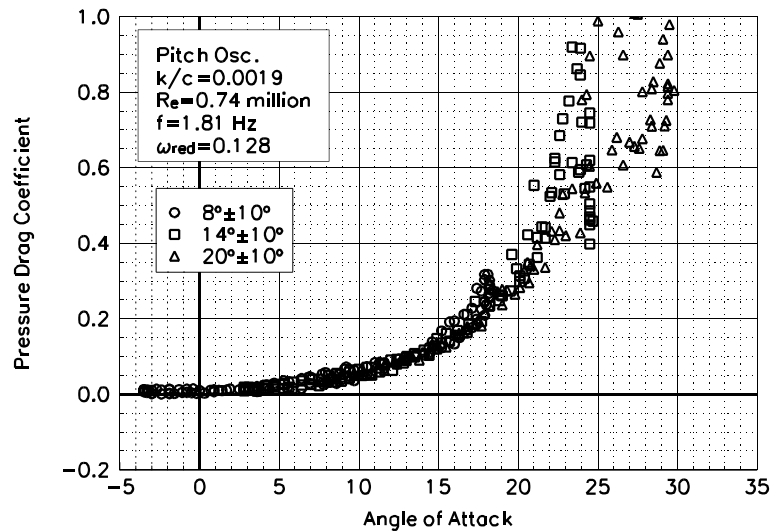


Figure C89. Pressure drag coefficient vs α .

S814
LEGR
 $Re = 0.74$ million
 $\omega_{red} = 0.128$

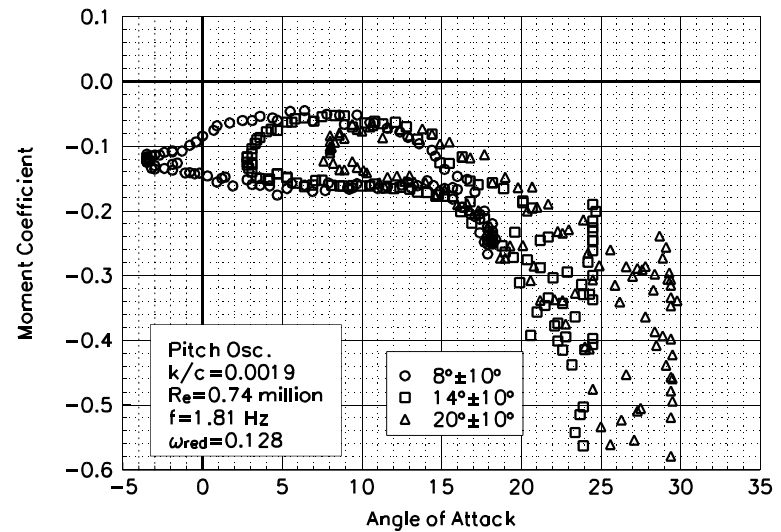


Figure C90. Moment coefficient vs α .

Unsteady Airfoil Characteristics

$\pm 10^\circ$ Sine, $Re = 1$ million

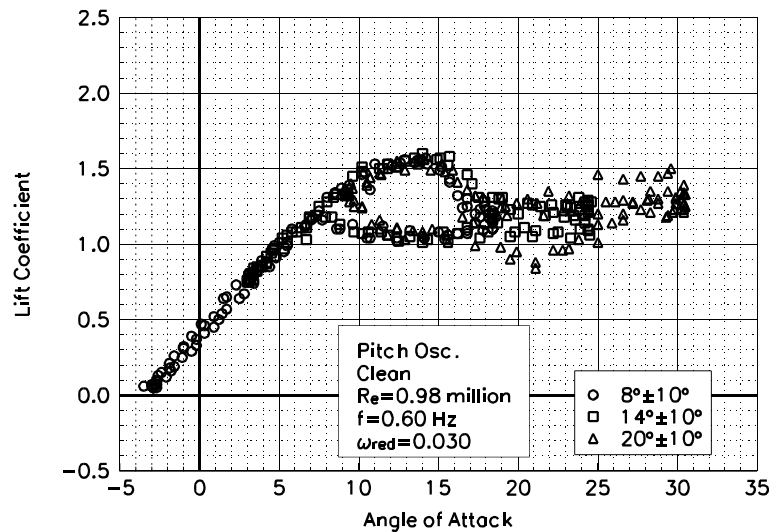


Figure C91. Lift coefficient vs α .

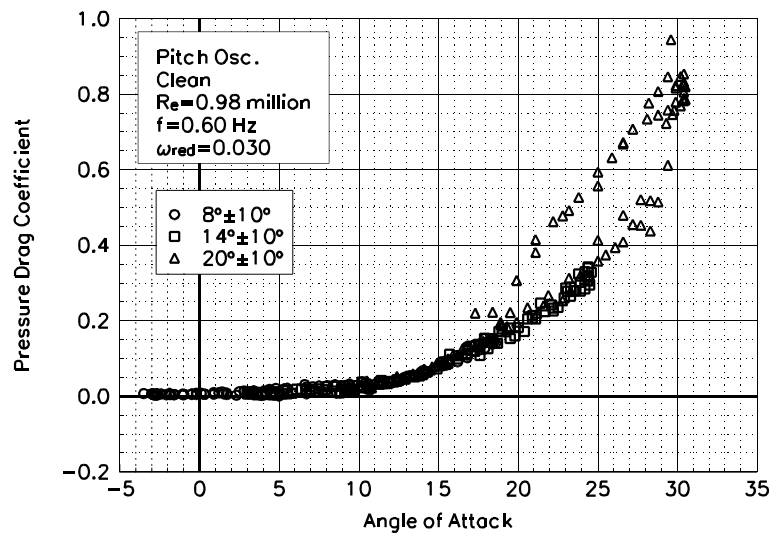


Figure C92. Pressure drag coefficient vs α .

S814
Clean
 $Re=0.98$ million
 $\omega_{reduced}=0.030$

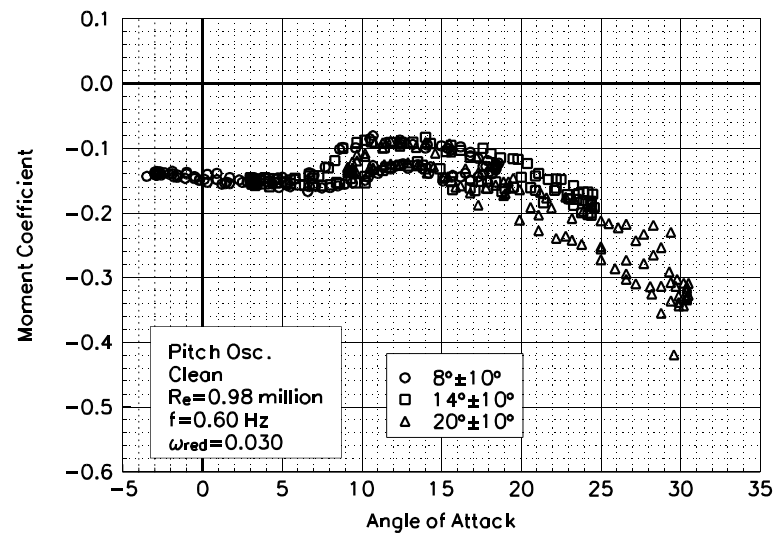


Figure C93. Moment coefficient vs α .

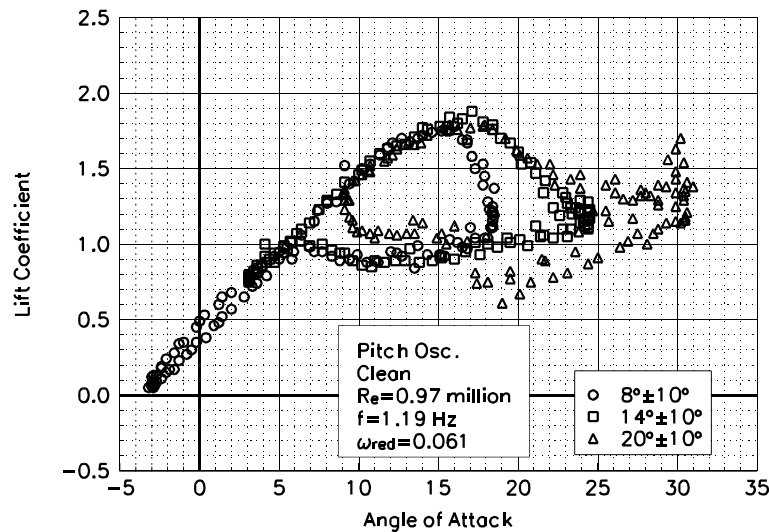


Figure C94. Lift coefficient vs α .

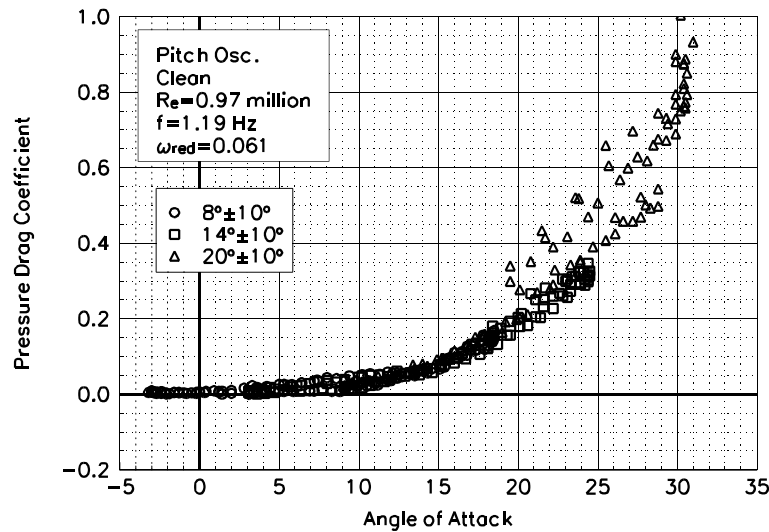


Figure C95. Pressure drag coefficient vs α .

S814
Clean
 $Re=0.97$ million
 $\omega_{red}=0.061$

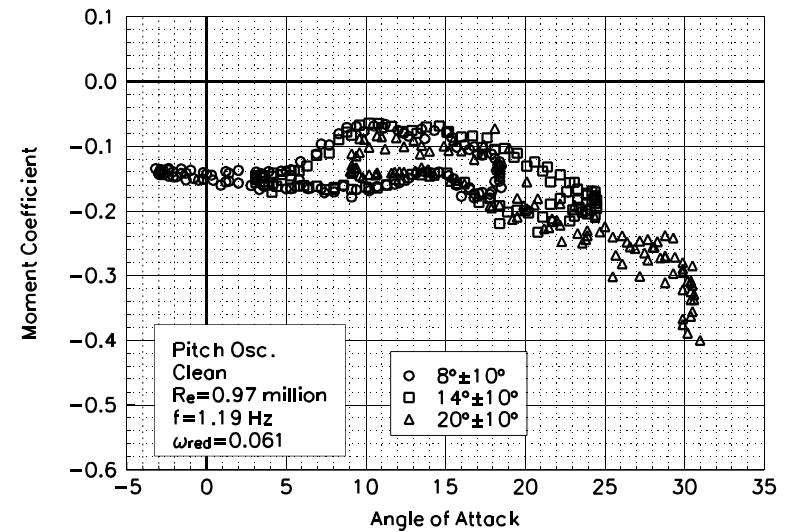


Figure C96. Moment coefficient vs α .

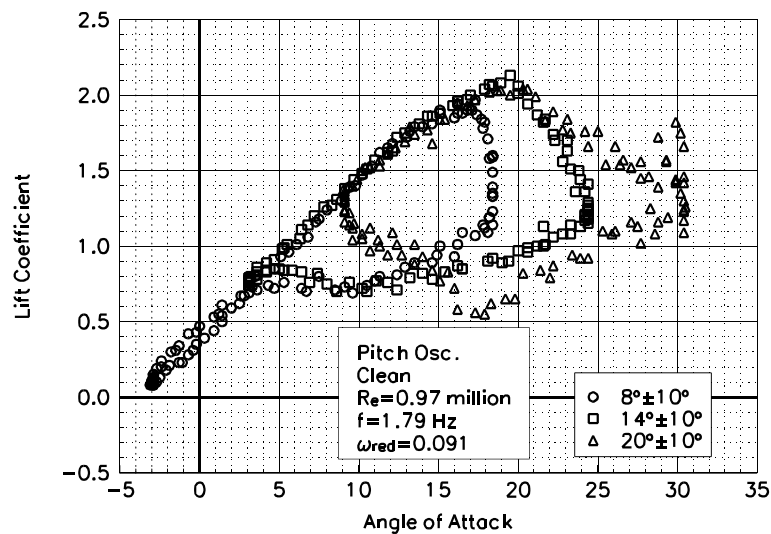


Figure C97. Lift coefficient vs α .

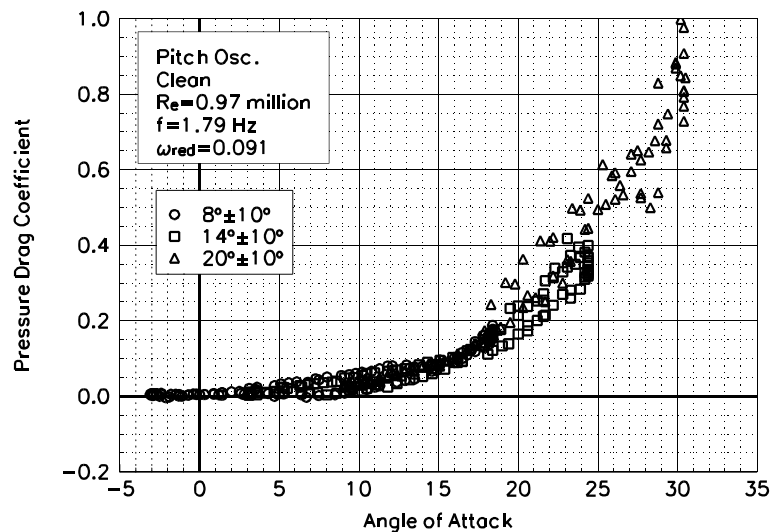


Figure C98. Pressure drag coefficient vs α .

S814
Clean
 $Re=0.97$ million
 $\omega_{reduced}=0.091$

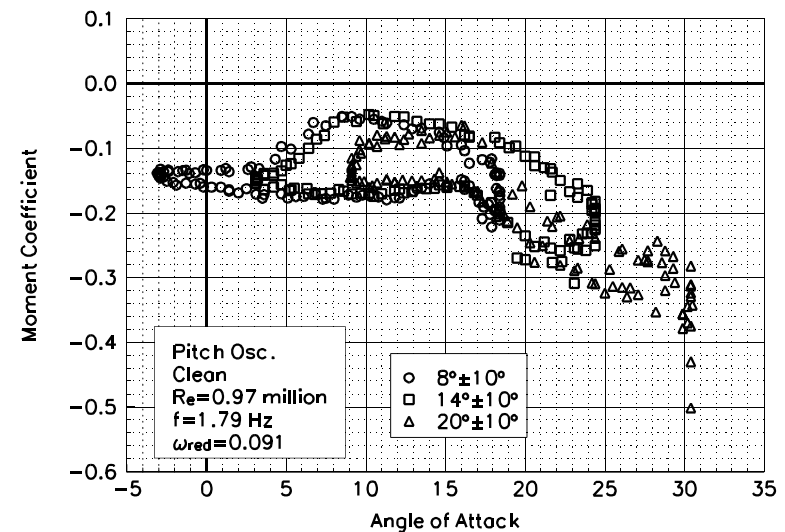


Figure C99. Moment coefficient vs α .

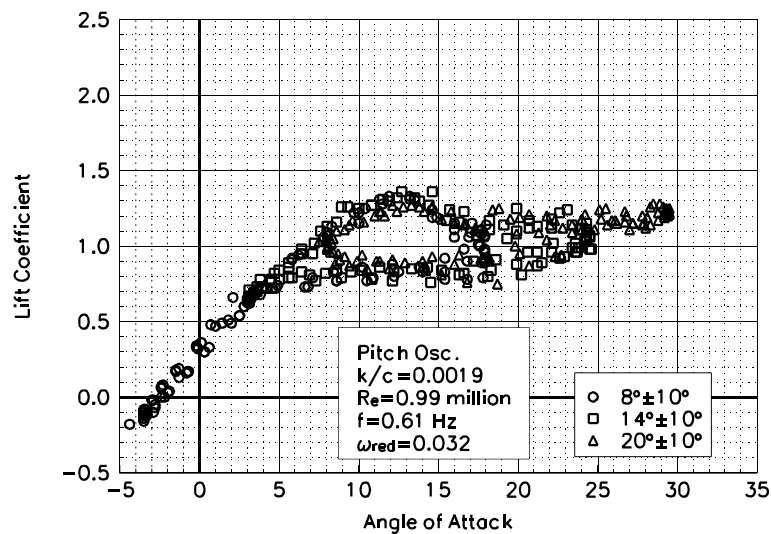


Figure C100. Lift coefficient vs α .

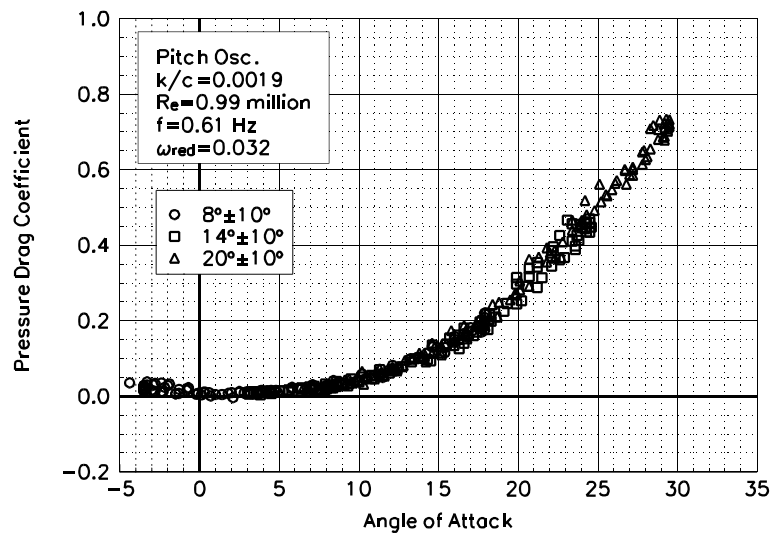


Figure C101. Pressure drag coefficient vs α .

**S814
LEGR
 $Re = 0.99 \text{ million}$
 $\omega_{\text{reduced}} = 0.032$**

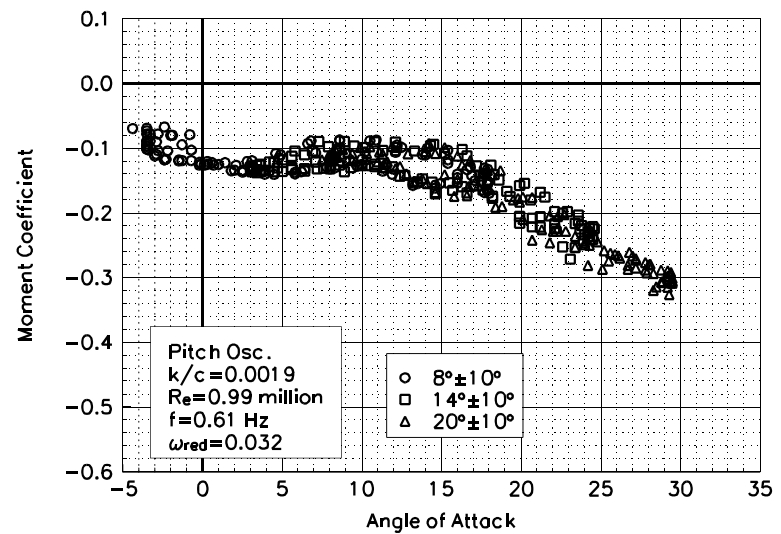


Figure C102. Moment coefficient vs α .

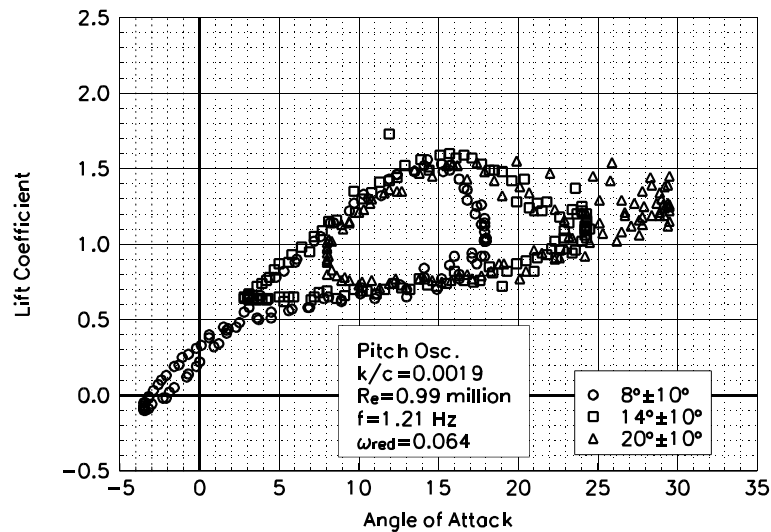


Figure C103. Lift coefficient vs α .

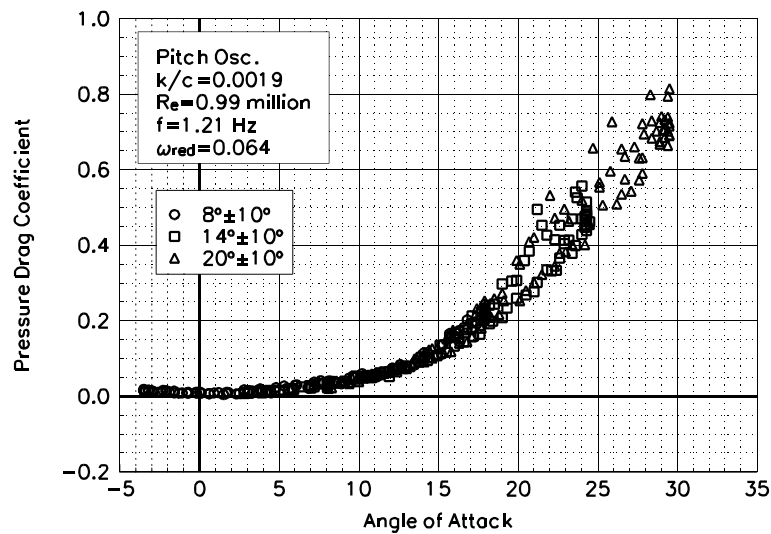


Figure C104. Pressure drag coefficient vs α .

S814
LEGR
 $Re = 0.99 \text{ million}$
 $\omega_{\text{reduced}} = 0.064$

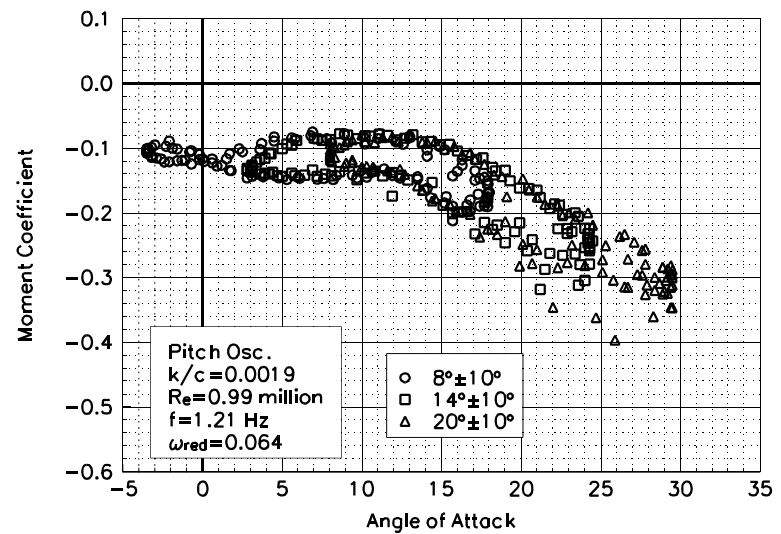


Figure C105. Moment coefficient vs α .

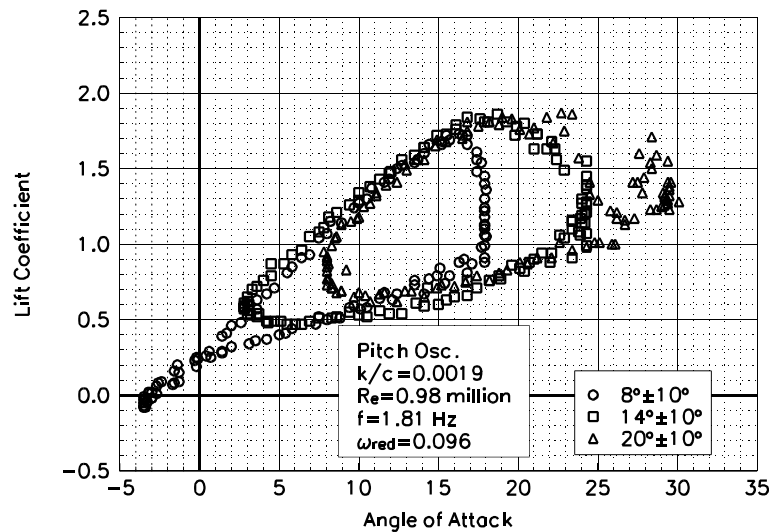


Figure C106. Lift coefficient vs α .

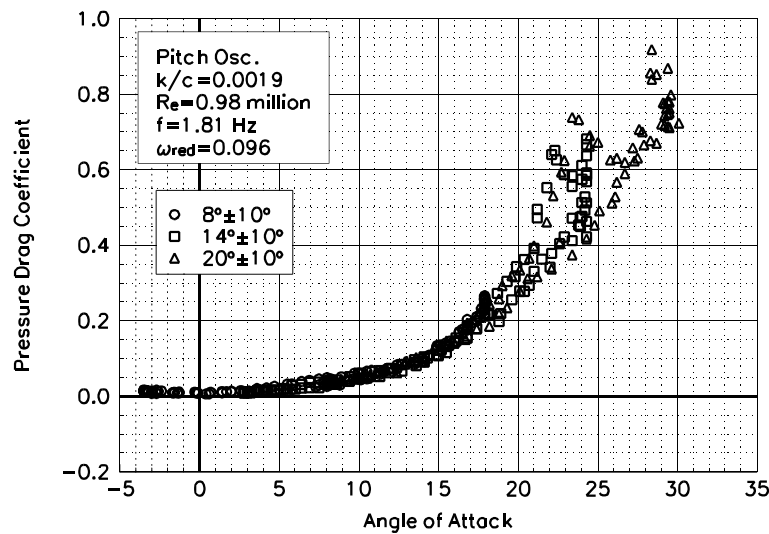


Figure C107. Pressure drag coefficient vs α .

**S814
LEGR
 $Re = 0.98 \text{ million}$
 $\omega_{\text{reduced}} = 0.096$**

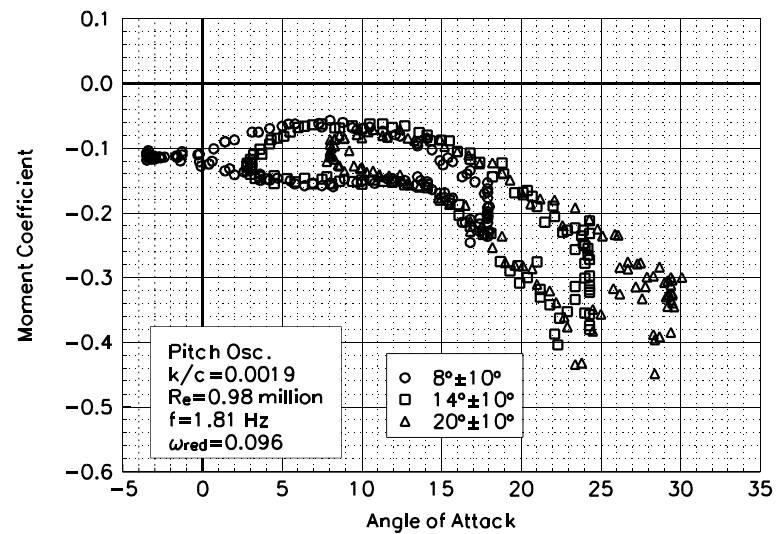


Figure C108. Moment coefficient vs α .

Unsteady Airfoil Characteristics

$\pm 10^\circ$ Sine, Re = 1.25 million

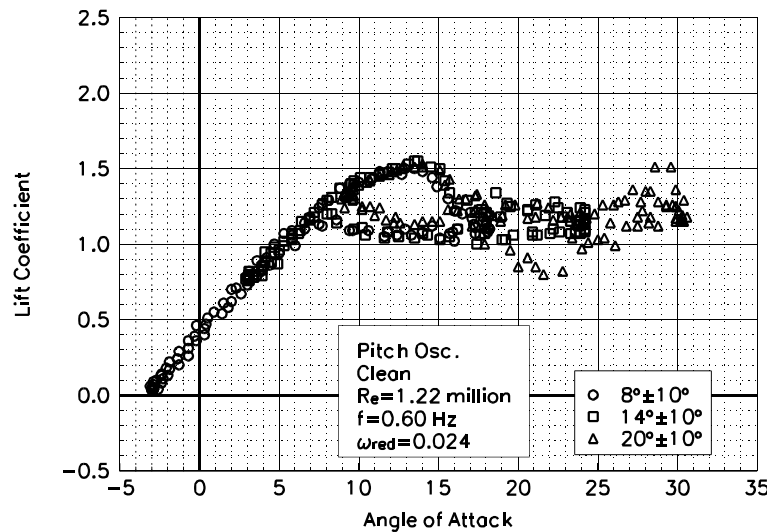


Figure C109. Lift coefficient vs α .

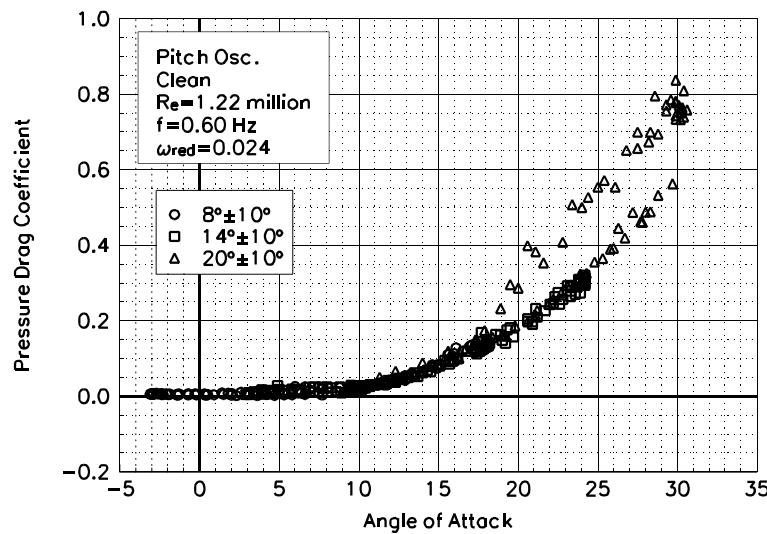


Figure C110. Pressure drag coefficient vs α .

S814
Clean
 $Re=1.22$ million
 $\omega_{reduced}=0.024$

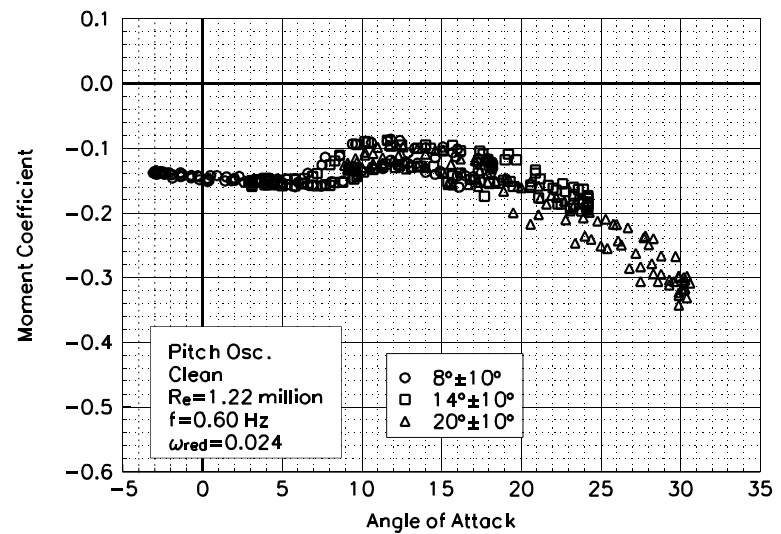


Figure C111. Moment coefficient vs α .

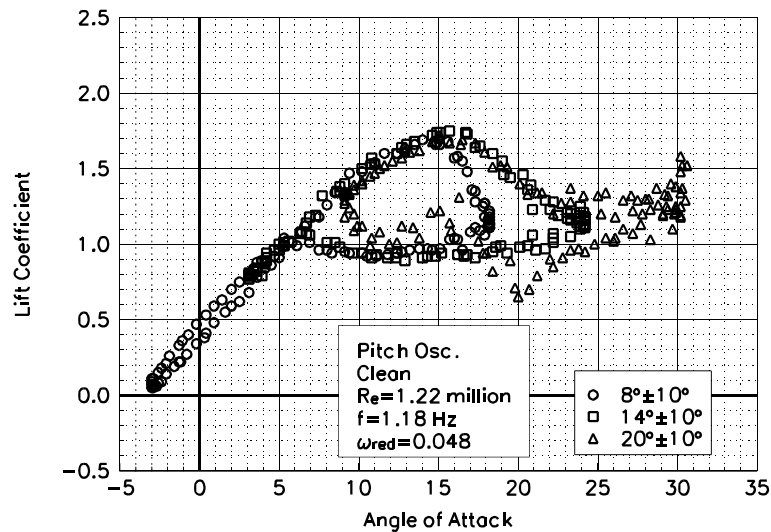


Figure C112. Lift coefficient vs α .

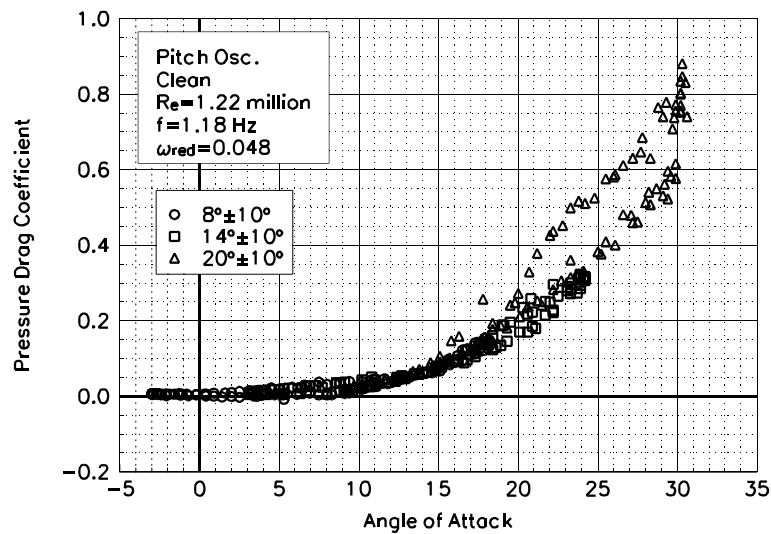


Figure C113. Pressure drag coefficient vs α .

S814
Clean
 $Re=1.22$ million
 $\omega_{reduced}=0.048$

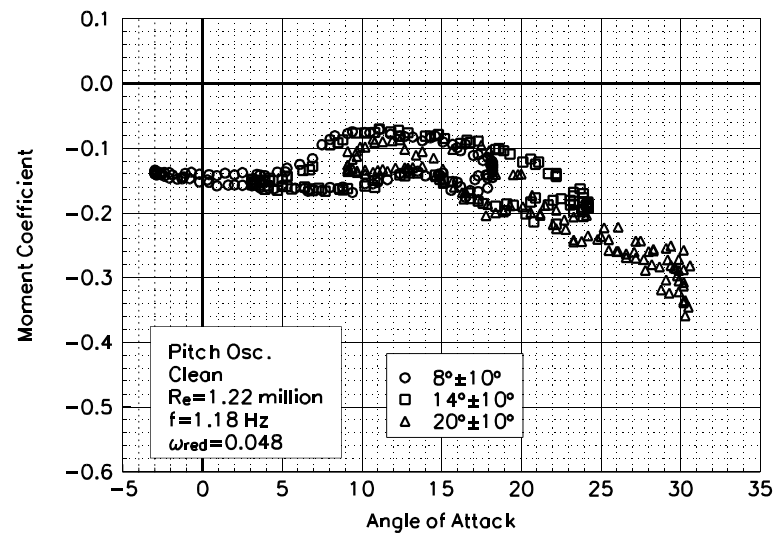


Figure C114. Moment coefficient vs α .

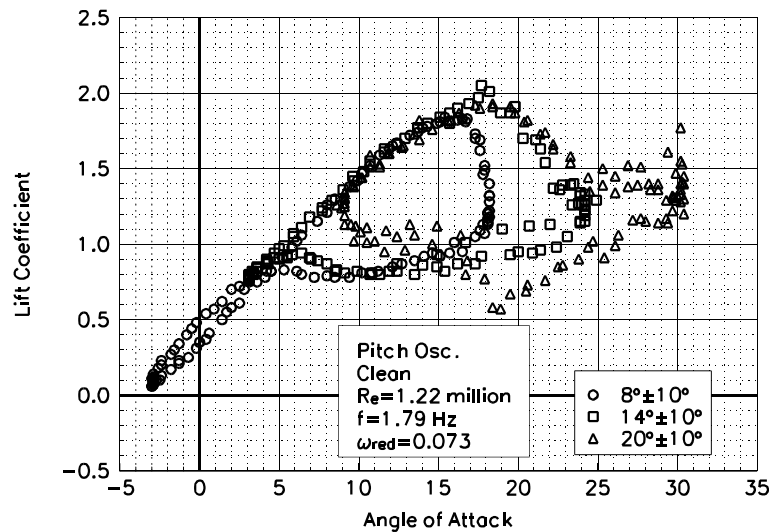


Figure C115. Lift coefficient vs α .

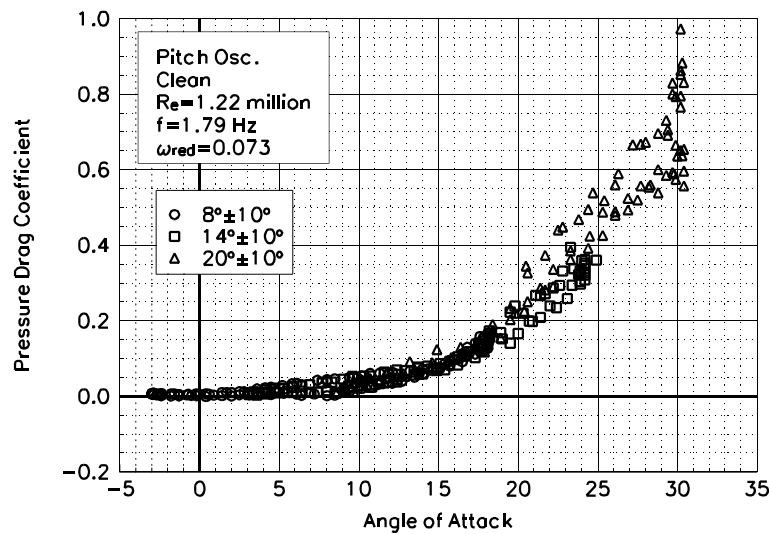


Figure C116. Pressure drag coefficient vs α .

S814
Clean
 $Re=1.22$ million
 $\omega_{reduced}=0.073$

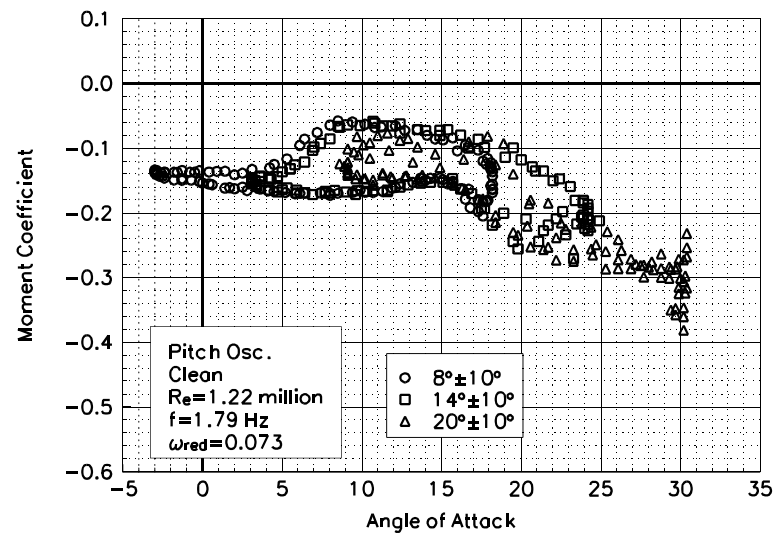


Figure C117. Moment coefficient vs α .

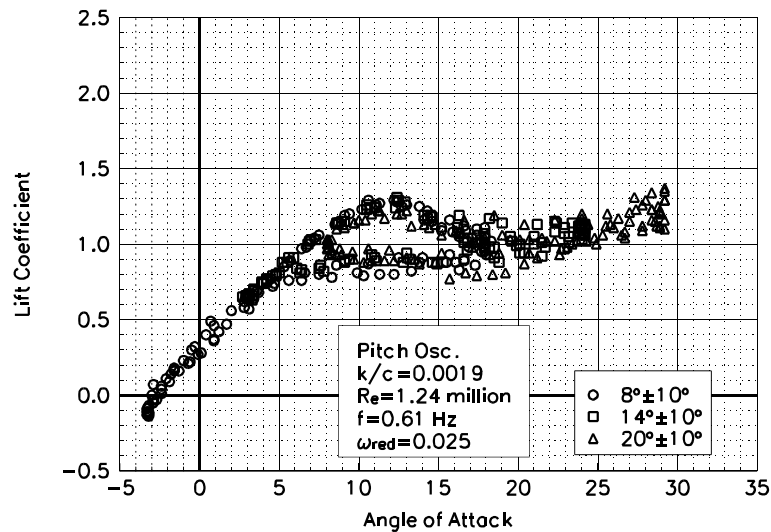


Figure C118. Lift coefficient vs α .

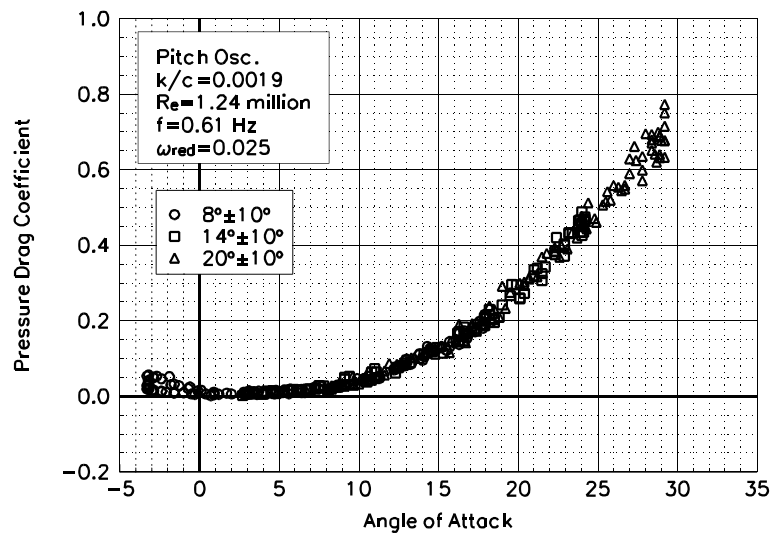


Figure C119. Pressure drag coefficient vs α .

S814
LEGR
 $Re = 1.24$ million
 $\omega_{red} = 0.025$

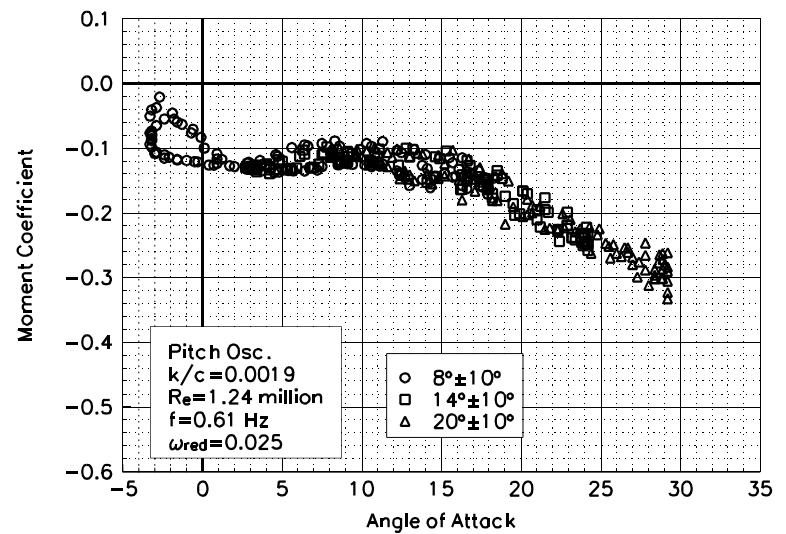


Figure C120. Moment coefficient vs α .

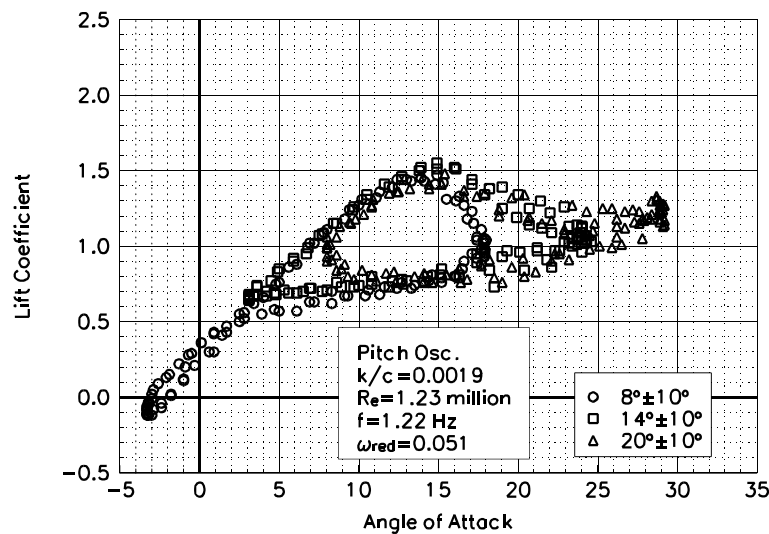


Figure C121. Lift coefficient vs α .

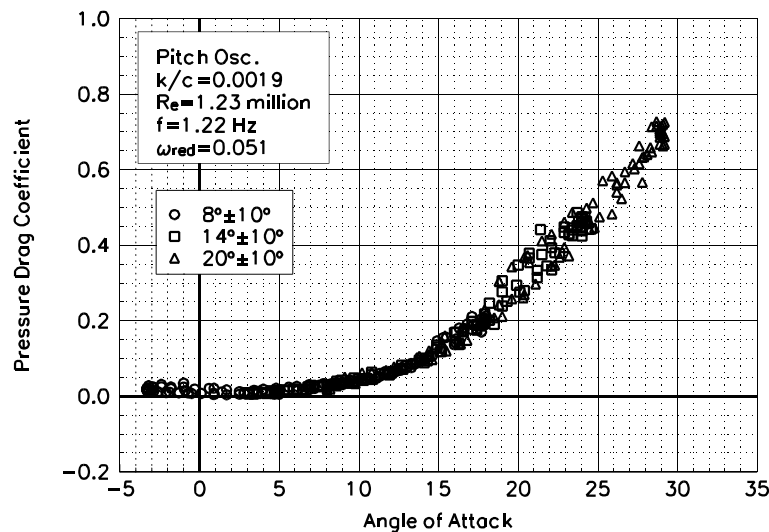


Figure C122. Pressure drag coefficient vs α .

**S814
LEGR
 $Re = 1.23 \text{ million}$
 $\omega_{\text{reduced}} = 0.051$**

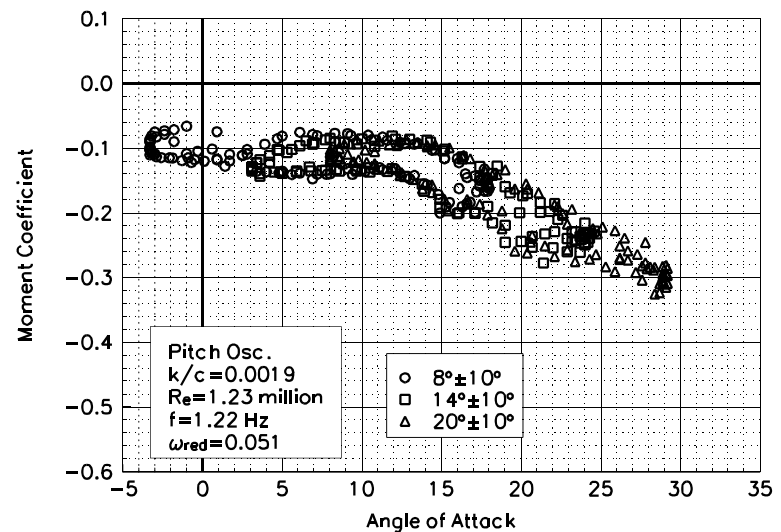


Figure C123. Moment coefficient vs α .

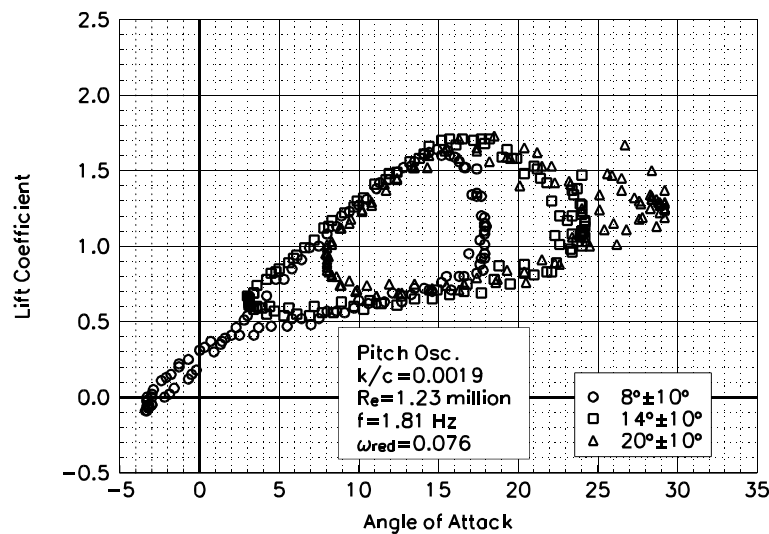


Figure C124. Lift coefficient vs α .

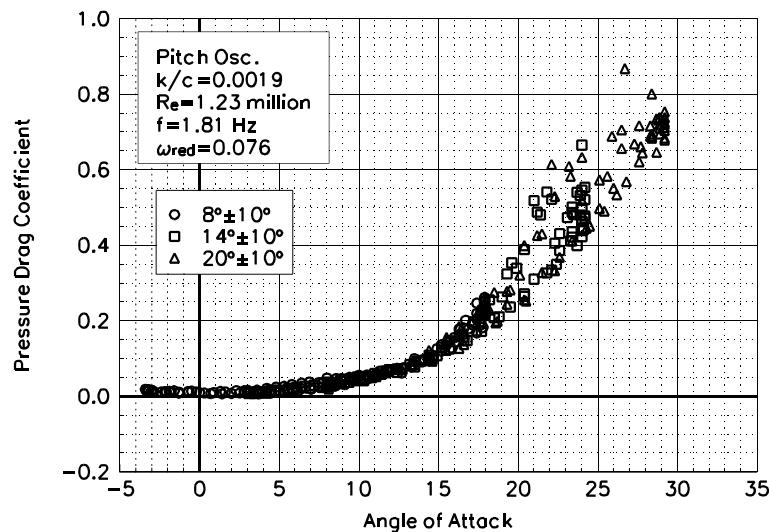


Figure C125. Pressure drag coefficient vs α .

S814
LEGR
 $Re = 1.23 \text{ million}$
 $\omega_{\text{reduced}} = 0.076$

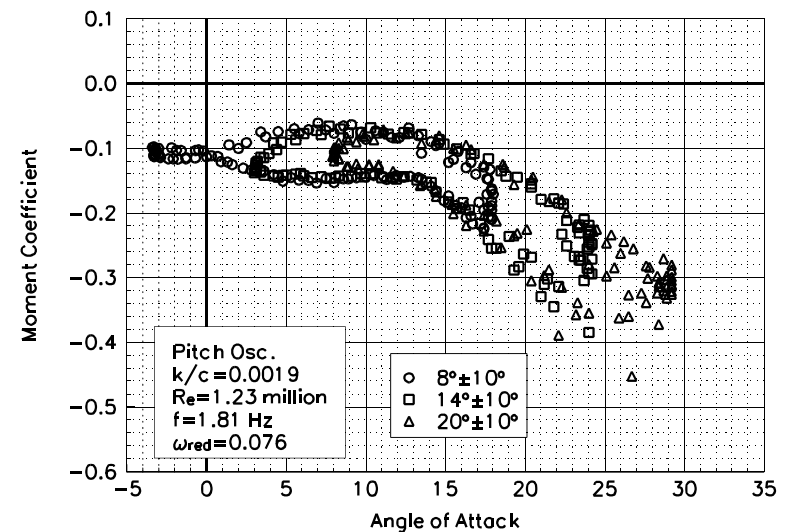


Figure C126. Moment coefficient vs α .

Unsteady Airfoil Characteristics

$\pm 10^\circ$ Sine, $Re = 1.5$ million

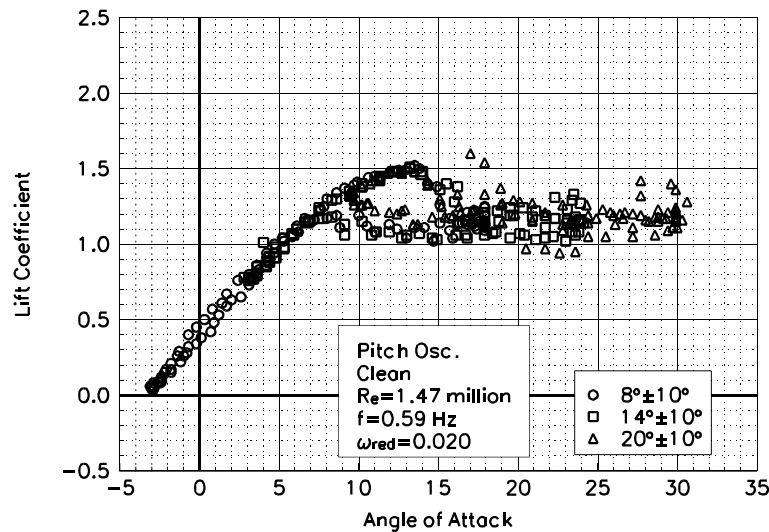


Figure C127. Lift coefficient vs α .

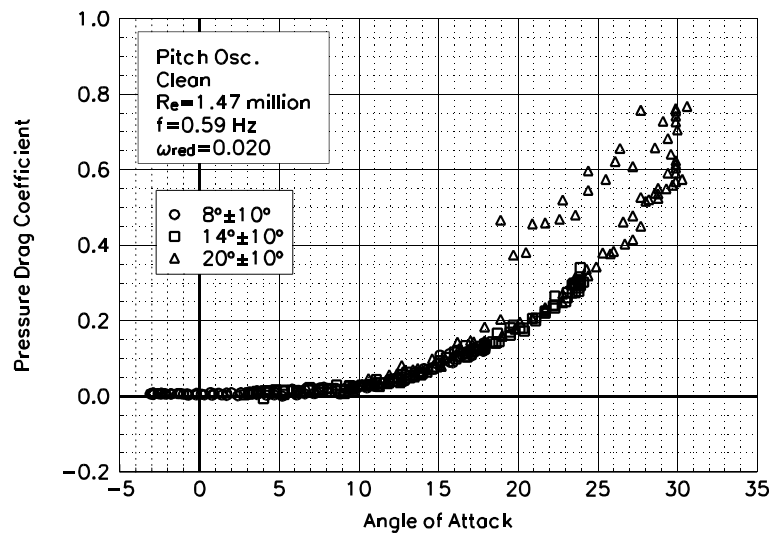


Figure C128. Pressure drag coefficient vs α .

S814
Clean
 $Re=1.47$ million
 $\omega_{reduced}=0.020$

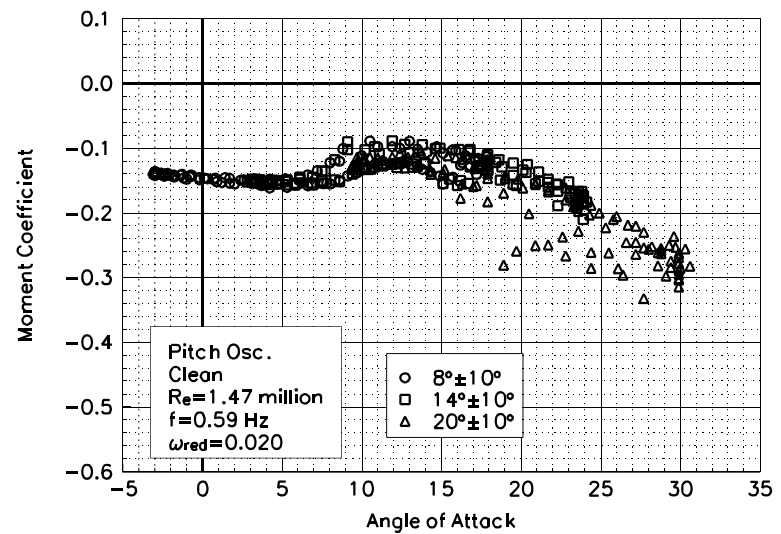


Figure C129. Moment coefficient vs α .

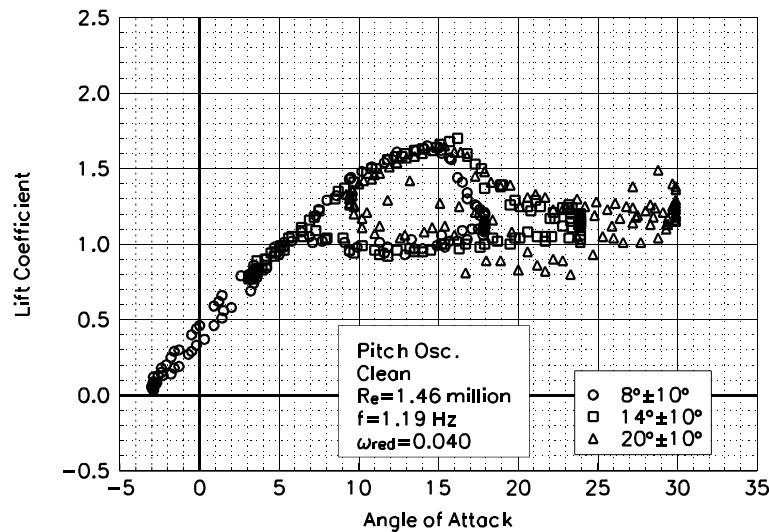


Figure C130. Lift coefficient vs α .

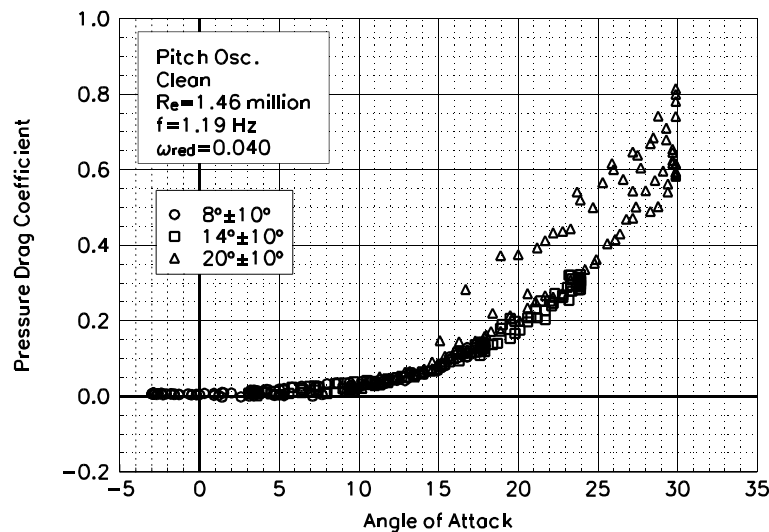


Figure C131. Pressure drag coefficient vs α .

S814
Clean
 $Re=1.46$ million
 $\omega_{reduced}=0.040$

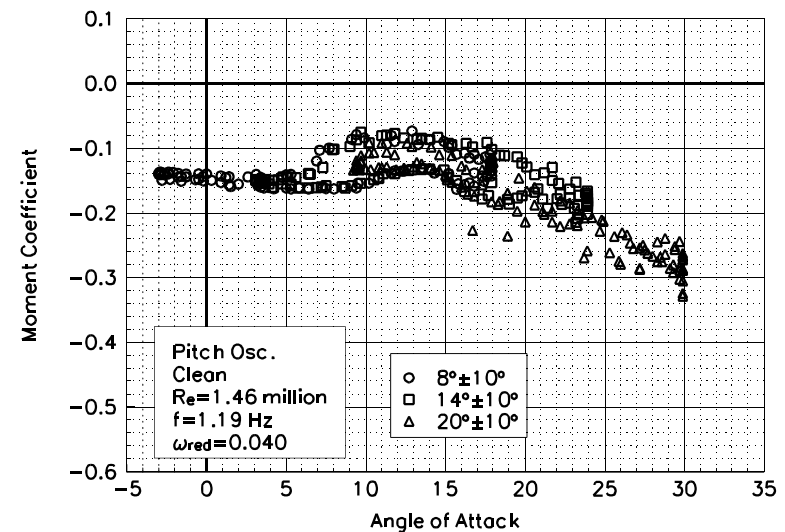


Figure C132. Moment coefficient vs α .

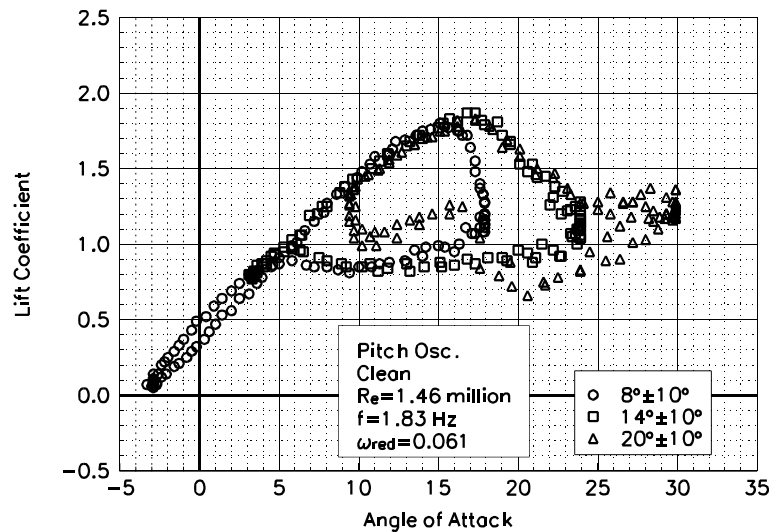


Figure C133. Lift coefficient vs α .

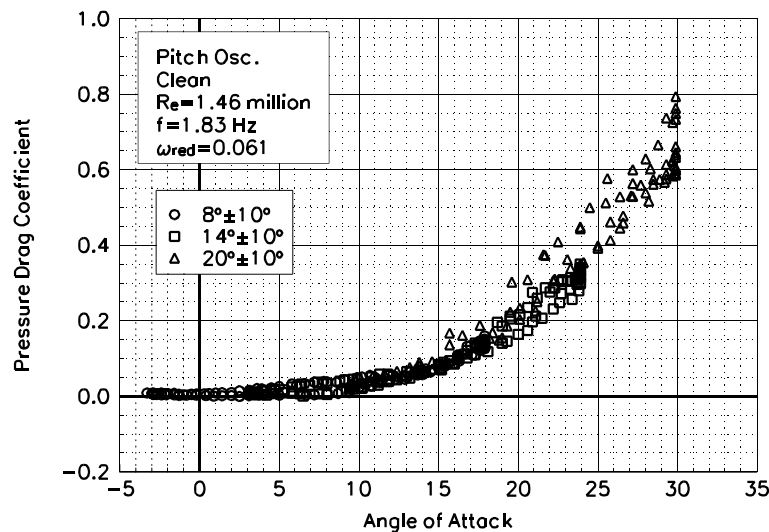


Figure C134. Pressure drag coefficient vs α .

S814
Clean
 $Re=1.46$ million
 $\omega_{red}=0.061$

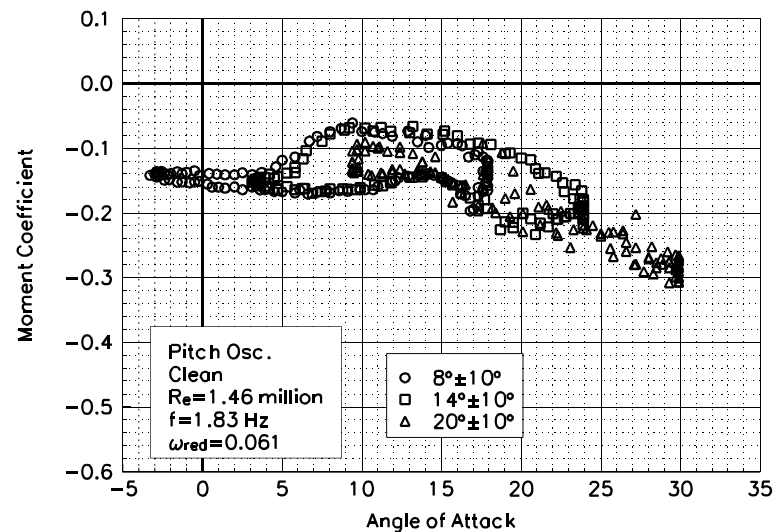


Figure C135. Moment coefficient vs α .

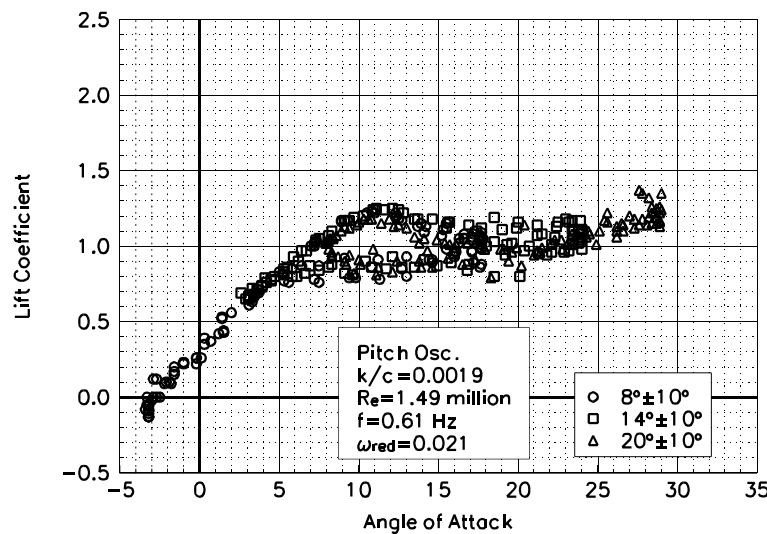


Figure C136. Lift coefficient vs α .

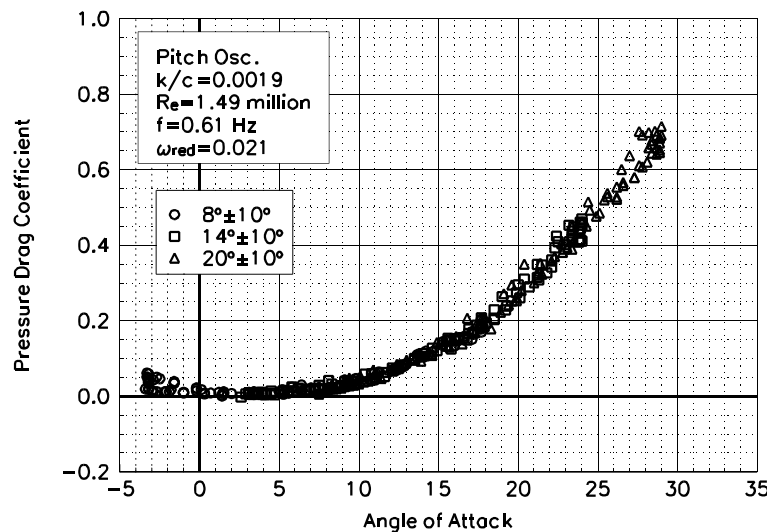


Figure C137. Pressure drag coefficient vs α .

**S814
LEGR
 $Re = 1.49 \text{ million}$
 $\omega_{\text{reduced}} = 0.021$**

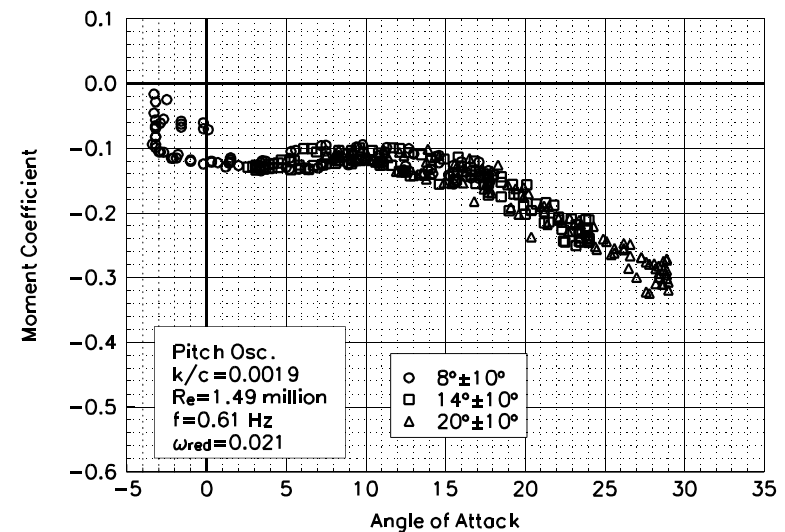


Figure C138. Moment coefficient vs α .

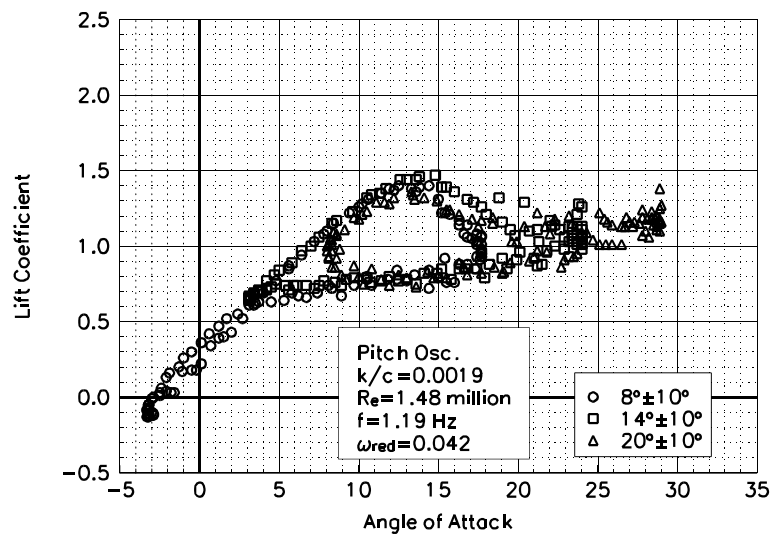


Figure C139. Lift coefficient vs α .

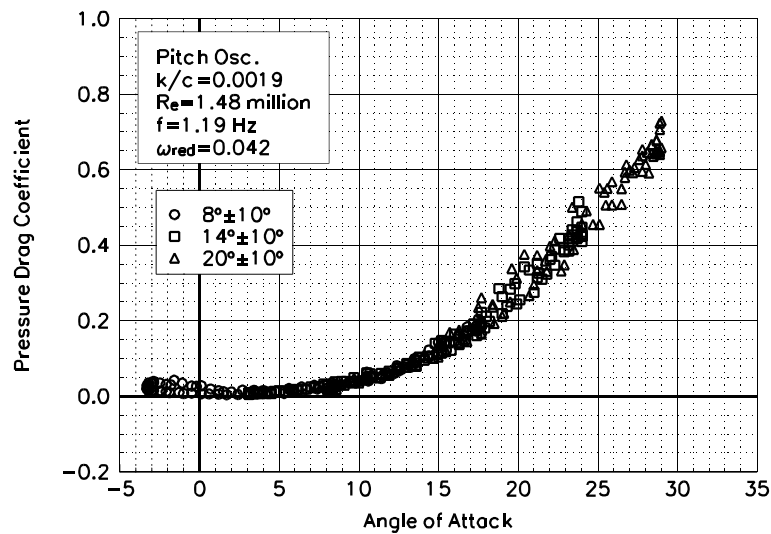


Figure C140. Pressure drag coefficient vs α .

S814
LEGR
 $Re = 1.48$ million
 $\omega_{red} = 0.042$

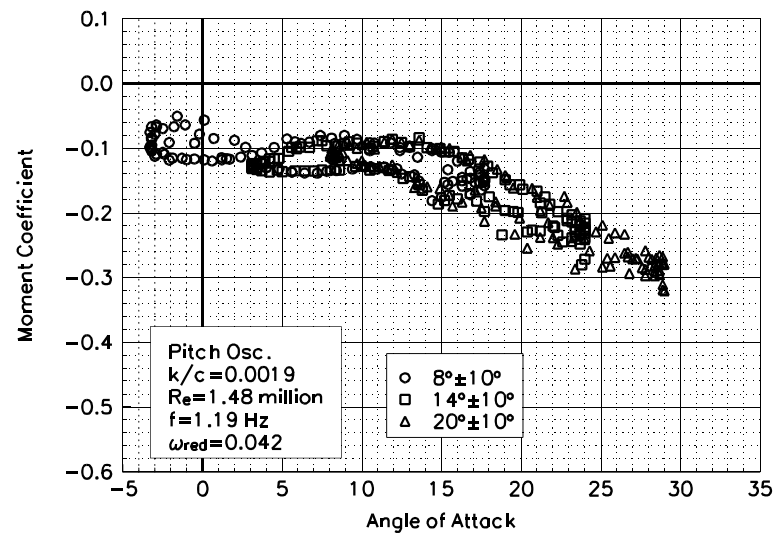


Figure C141. Moment coefficient vs α .

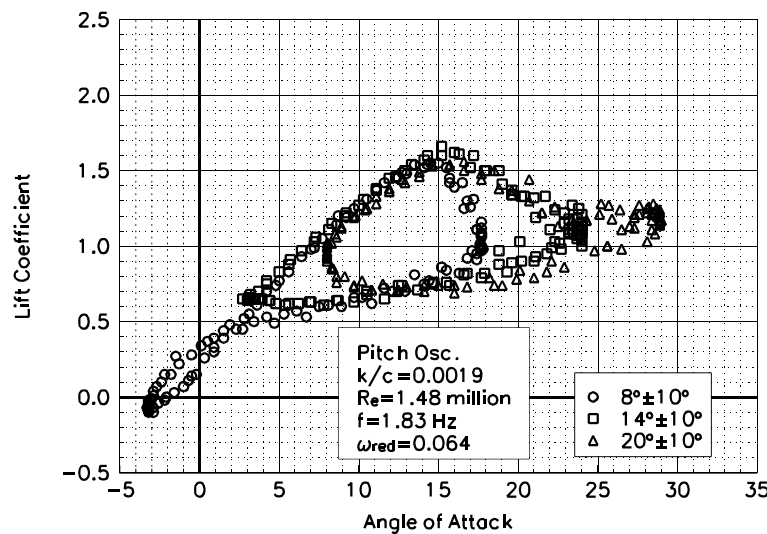


Figure C142. Lift coefficient vs α .

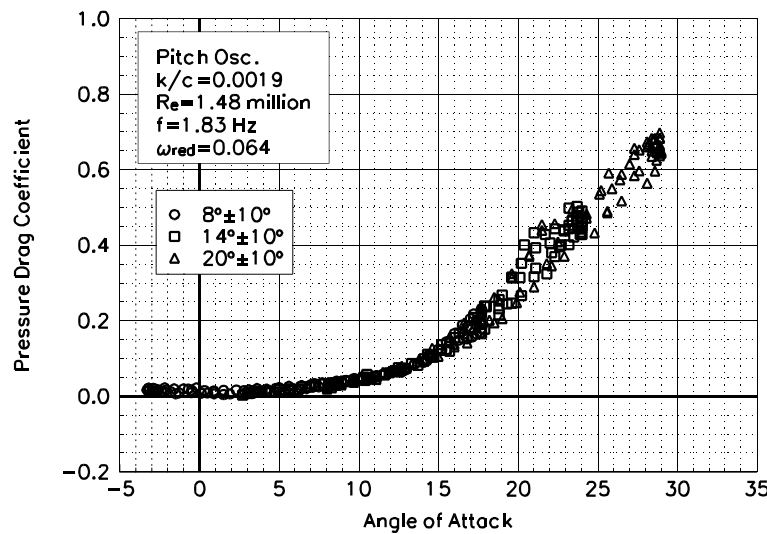


Figure C143. Pressure drag coefficient vs α .

**S814
LEGR
Re=1.48 million
 $\omega_{\text{reduced}} = 0.064$**

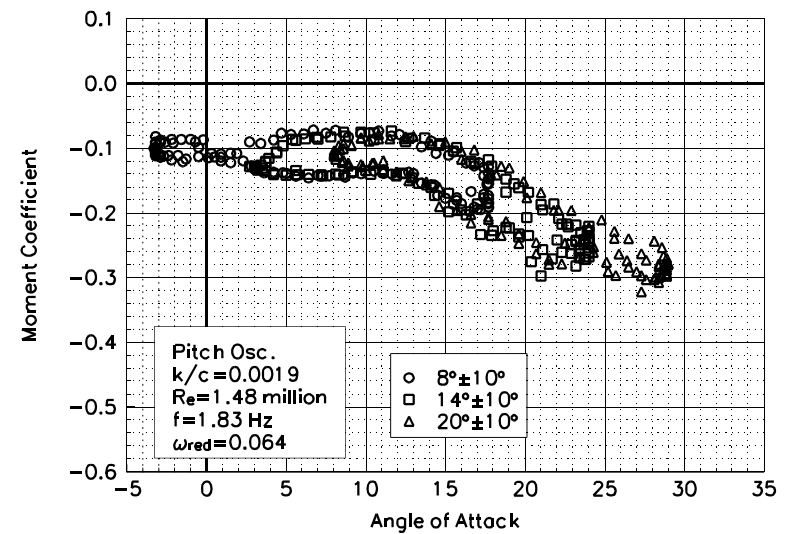


Figure C144. Moment coefficient vs α .